3rd of 3 files

Chapters 5 to 8 and Appendix

High Pressure Diffraction Studies of Gallosilicate Natrolite: Applications to Pressure-Induced Cation Trapping

By
Gemma Louise Hill
(nee Little)

A thesis submitted to
The University of Birmingham
For the degree of
DOCTOR OF PHILOSOPHY (PhD)

School of Chemistry
The University of Birmingham
2010

CHAPTER FIVE

High Pressure Synchrotron X-Ray Diffraction

In the previous chapter, high pressure neutron diffraction data were collected which was used to elucidate the crystallographic nature of both the tetragonal and the orthorhombic gallosilicate natrolites over a range of pressures, including ambient. These data provided details of framework structure, pore content (i.e. OW2 occupancy) and hydrogen atom positioning. This gave the first details of hydrogen bonding both at ambient and during high pressures for both gallosilicate analogues. The study of tetragonal gallosilicate was particularly useful as it was the first high pressure structural characterisation and the first evidence of PIH occurring for this form. To date no other high pressure study of tetragonal Na-GaSi-NAT has been published.

In this chapter synchrotron X-ray diffraction was used to perform studies over a greater number of pressure points in order to gain a more complete picture of the evolution of the superhydrated phase and its subsequent compression. During neutron diffraction studies, only 4 high pressure steps were possible due to the lengthy preparation and data collection times. With synchrotron X-ray diffraction a Diamond Anvil Cell (DAC) is used, which is quick and easy to load and data collections times are as little as 5 minutes. Studying the evolution of the high pressure phase and subsequent compression should elucidate more details of the mechanism by which pressure-induced hydration (PIH) occurs; for example giving enough data to be able to fit an accurate equation of state to the superhydrated phase.

Experiments were first done at the X7A beamline, Brookhaven NY, with subsequent studies performed on the 9.5HPT beamline at Daresbury. Details of the experimental conditions and set up at each of the beamlines are given in Chapter 2.

5.1 Synchrotron X-Ray Diffraction Studies (X7A)

Experiments began with an ambient pressure data collection for comparison with subsequent high pressure collections. The ambient pressure studies were performed using a rotating capillary tube and the high pressure data collections were performed by using a diamond anvil cell. Pressure increments were achieved by manual tightening of the cell. Pressures were determined using ruby chips included when packing the DAC. The shift in the R1 emission line was used to calculate the pressure. Further details of experimental set up and conditions are given in Chapter 2.

5.1.1 Capillary Data Results

Rietveld refinement of Na-GaSi-NAT capillary data for both the tetragonal and orthorhombic samples gave very poor fits with a significant amount of poorly fitting intensities. As discussed in full later in the chapter, when comparing these results to those achieved at the 9.5HPT beamline, Daresbury (MAR345 image plate rather than a psd detector), we can assume that the poor quality of these results is due to: a) pattern spotting (a consequence of large sample grains) and b) the nature of the data collection (1D strip psd detector rather than a MAR345 image plate). At 9.5HPT we observed more significant grain issues in the orthorhombic, rather than the tetragonal form, this is reflected in the Rietveld refinement output values for the ambient pressure collection from X7A data: orthorhombic (χ^2=12.0 and R_{F2}=0.4240) and tetragonal (χ^2=4.39 and R_{F2}=0.1011).

Although rotating capillary data goes some way to limiting the effect of these large grains, the use of a limited beam (200μm pin hole) and in particular the use of a strip detector has resulted in very poor averaging. Thus, we see significant intensity

discrepancies during refinement. We would expect that these effects should become more pronounced in high pressure runs as use of a diamond anvil cell results in even poorer averaging.

As a consequence of these poor data, Rietveld refinements at both ambient and high pressures were not possible and therefore no accurate information on the water content was gained. In order to retrieve some cell parameter information Le Bail refinements were performed. These used a manually fitted background with refinement of zero point, unit cell and profile parameters *LY* and *GW*. The results of these refinements are summarised in Table 1 with refinement profile plots displayed in Figure 1 and Figure 2.

Table 1: Le Bail refinement data for capillary runs performed upon tetragonal and orthorhombic Na-GaSi-NAT

		Na-GaSi-NAT	
		Orthorhombic	Tetragonal
Space group		*Fdd2*	*I-42d*
χ^2		3.111	3.010
R_{wp}		0.0426	0.0312
R_p		0.0360	0.0257
Cell parameters (Å)	*a*	18.3741(4)	13.23609(28)
	b	18.86036(33)	13.23609(28)
	c	6.65319(15)	6.66053(17)
Cell Volume (Å^3)		2305.61(8)	1166.89(5)

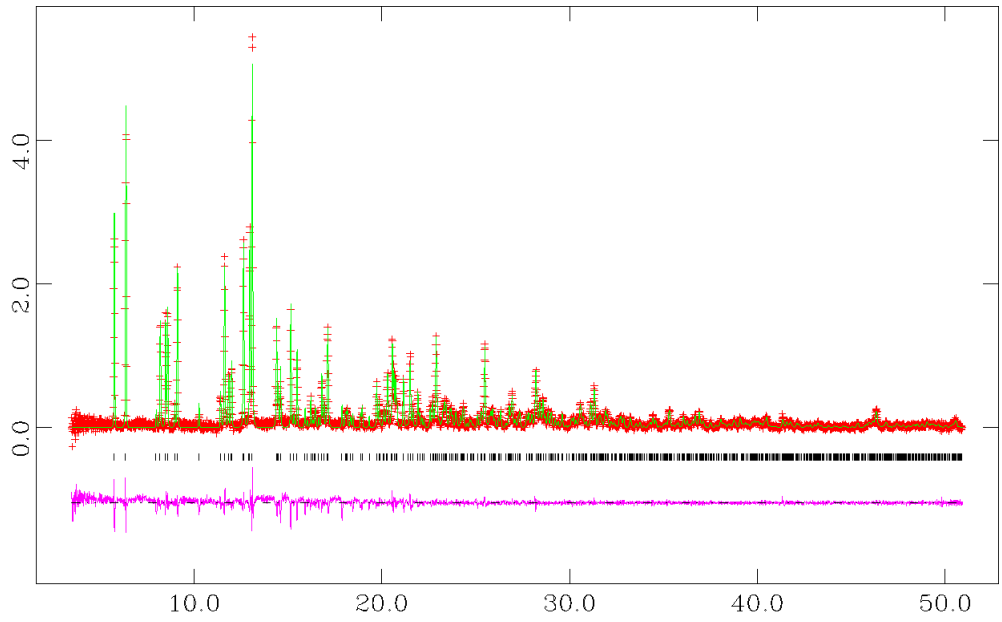

Figure 1: Le Bail refinement fit of orthorhombic Na-GaSi-NAT capillary data. Black, vertical tick marks indicated allowed reflections for Na-GaSi-NAT phase.

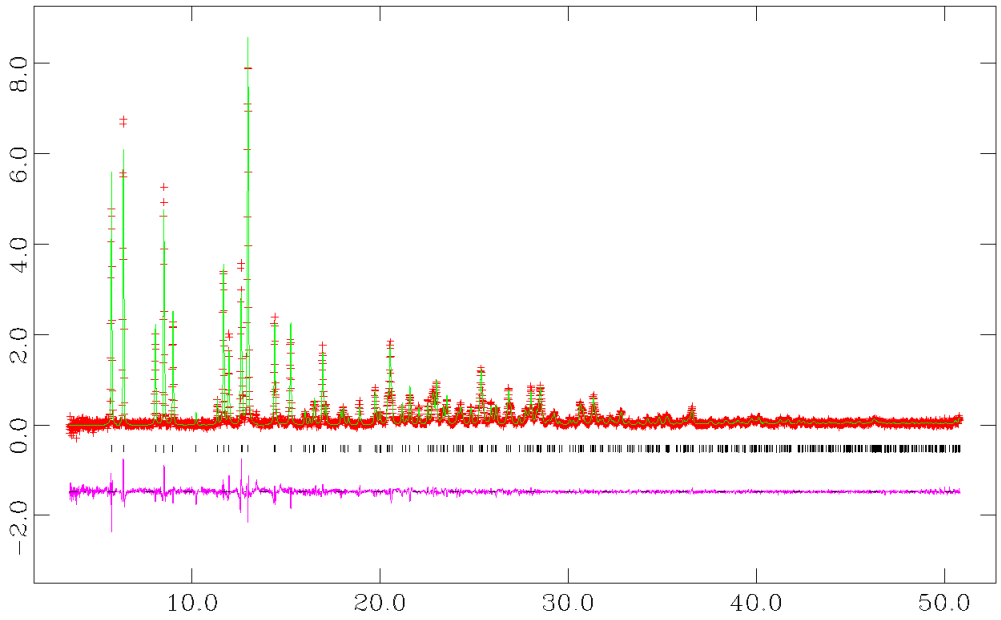

Figure 2: Le Bail refinement fit of tetragonal, Na-GaSi-NAT capillary data. Black, vertical tick marks indicated allowed reflections for Na-GaSi-NAT phase.

5.1.2 High Pressure Data

High pressure experiments were performed in a diamond anvil cell, over an estimated range of 0-5 GPa. The pressure medium (MeOH:EtOH:H_2O, 16:3:1), is included in the DAC cavity in order to induce and maintain hydrostatic pressures. Much effort was made to minimise the pressure increments so that a greater number of data collections could be performed in and around the region at which PIH occurs (superhydrating pressures).

5.1.2.1 Tetragonal Na-GaSi-NAT

A high pressure sequence, as described above, was initiated for the tetragonal form of Na-GaSi-NAT. Experiments were soon terminated, as it became very clear that each data set gave patterns with considerable peak broadening (Figure 3). The collected data was unrefinable. This was likely due to a non-hydrostatic loading of the cell, but due to time limitations it was not possible to reload and start a second data collection. However, as discussed later in this chapter the experiment was successfully rerun at beamline 9.5HPT at Daresbury.

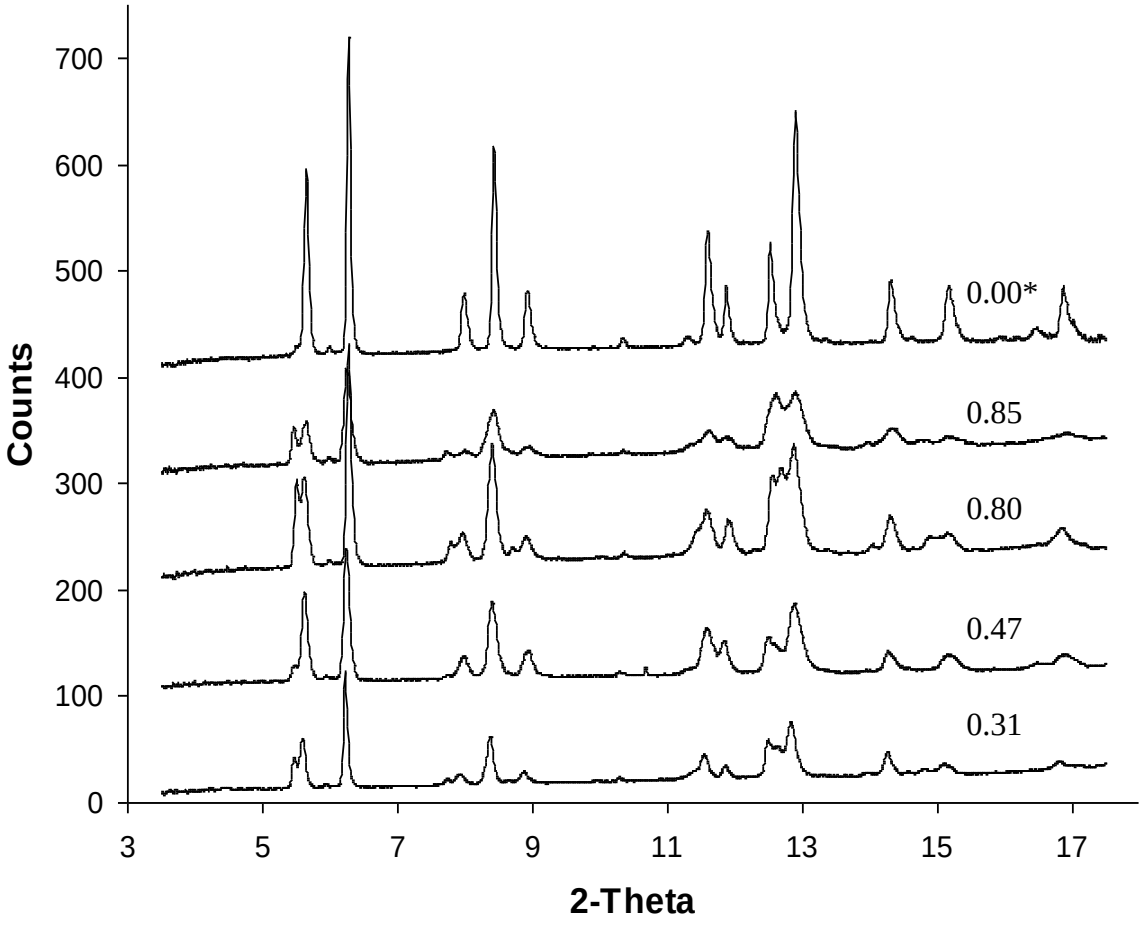

Figure 3: Synchrotron X-ray diffraction patterns of tetragonal Na-Na-GaSi-NAT collected at beamline X7A, pressures are given in GPa.

***Data collected when pressure has been released and allowed to drop down to ambient values.**

5.1.2.2 Orthorhombic Na-GaSi-NAT

A high pressure sequence was also performed with the orthorhombic form of Na-GaSi-NAT, with much more success than the previous tetragonal gallosilicate study. Pressures range from 0.52 to 5.42 GPa. The raw diffraction patterns collected are displayed in Figure 4. Data were refined using the EXPGUI GSAS software suite. Unfortunately the data was not of adequate quality for a full, Rietveld structural refinement (as seen in the previous ambient capillary experiments). A Le Bail intensity fit was performed for each pressure increment; a summary of the volume and cell parameter values is given in Table 2, with an exemplar refinement profile given in Figure 5 with profile plots for all pressures shown in appendices 1.2.1.

During the experiments, the orthorhombic phase showed evidence of a transition to a paranatrolite phase (evident from observed peak splitting at 0.52 and 0.60 GPa). This is the first evidence of the existence of a paranatrolite phase for gallosilicate natrolite, as seen in previous reports of paranatrolite formation from the aluminosilicate analogue, Al-NAT.[1,2]

At 0.83 GPa a sudden cell volume expansion of 1.43% (1.41% from V_0), is observed. This is slightly less than, but in good agreement with, the value refined from the neutron diffraction data discussed in chapter 4 (2.044%). This expansion is characteristic of PIH/superhydration. During unit cell expansion there is an increase in the *a*- and *b*-cell parameters of 0.76% and 1.22%, respectively. These values are in very good agreement with those refined from neutron data (0.79% and 1.37%, respectively).

Following transition to the superhydrated phases, a smooth compression curve is observed. The pressure dependence of the cell volume and cell parameters is shown in Figure 7 and Figure 6.

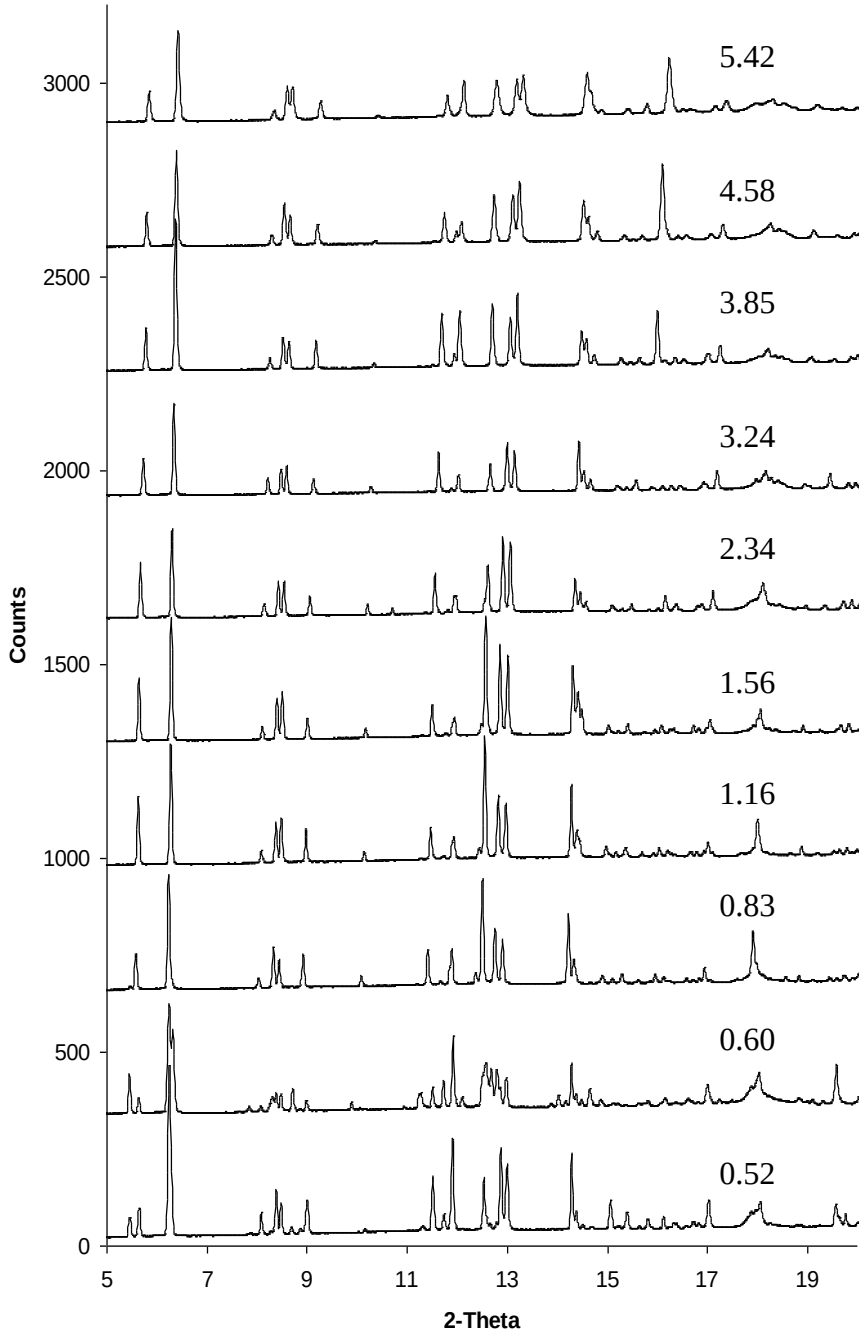

Figure 4: Synchrotron X-ray diffraction patterns of orthorhombic Na-Na-GaSi-NAT collected at X7A with pressures given in GPa.

Table 2: Summary of unit cell parameters and volume of orthorhombic Na-GaSi-NAT as a function of pressure.

Pressure (GPa)	Cell Parameters (Å) a	b	c	Volume ($Å^3$)	V/V_0
0.00	18.3741(4)	18.86036(33)	6.65319(15)	2305.61(8)	1.0000
0.52	18.3368(21)	18.8246(18)	6.6402(7)	2292.1(4)	0.9941
0.60	18.375(5)	18.911(5)	6.6334(16)	2305.1(10)	0.9998
0.83	18.4768(7)	19.0550(7)	6.64098(23)	2338.12(15)	1.0141
1.16	18.4137(5)	18.9946(5)	6.63304(16)	2319.98(11)	1.0062
1.56	18.3519(6)	18.9276(7)	6.62491(19)	2301.22(14)	0.9981
2.34	18.2663(9)	18.8288(10)	6.61203(33)	2274.09(20)	0.9863
3.24	18.1733(7)	18.7199(8)	6.59873(24)	2244.90(15)	0.9737
3.85	18.1295(10)	18.6793(8)	6.5948(4)	2233.31(20)	0.9686
4.58	18.0620(10)	18.5651(7)	6.57832(30)	2205.86(18)	0.9567
5.42	18.0063(22)	18.5121(18)	6.5763(7)	2192.1(4)	0.9508

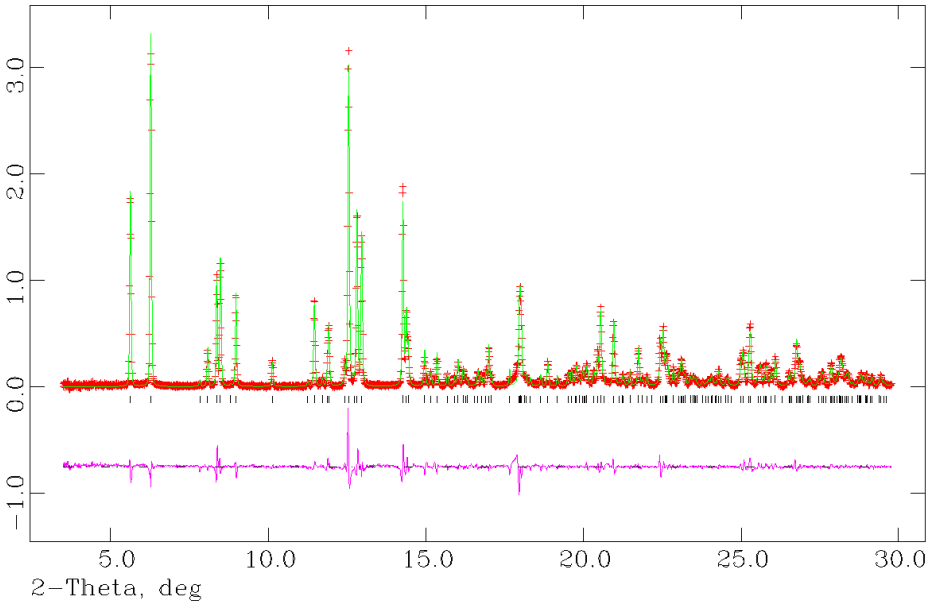

Figure 5: Example of a Le Bail refinement profile obtained for orthorhombic Na-GaSi-NAT within the high pressure series of experiments from data collected at X7A. The profile shown is that of superhydrated Na-GaSi-NAT at 1.16 GPa.

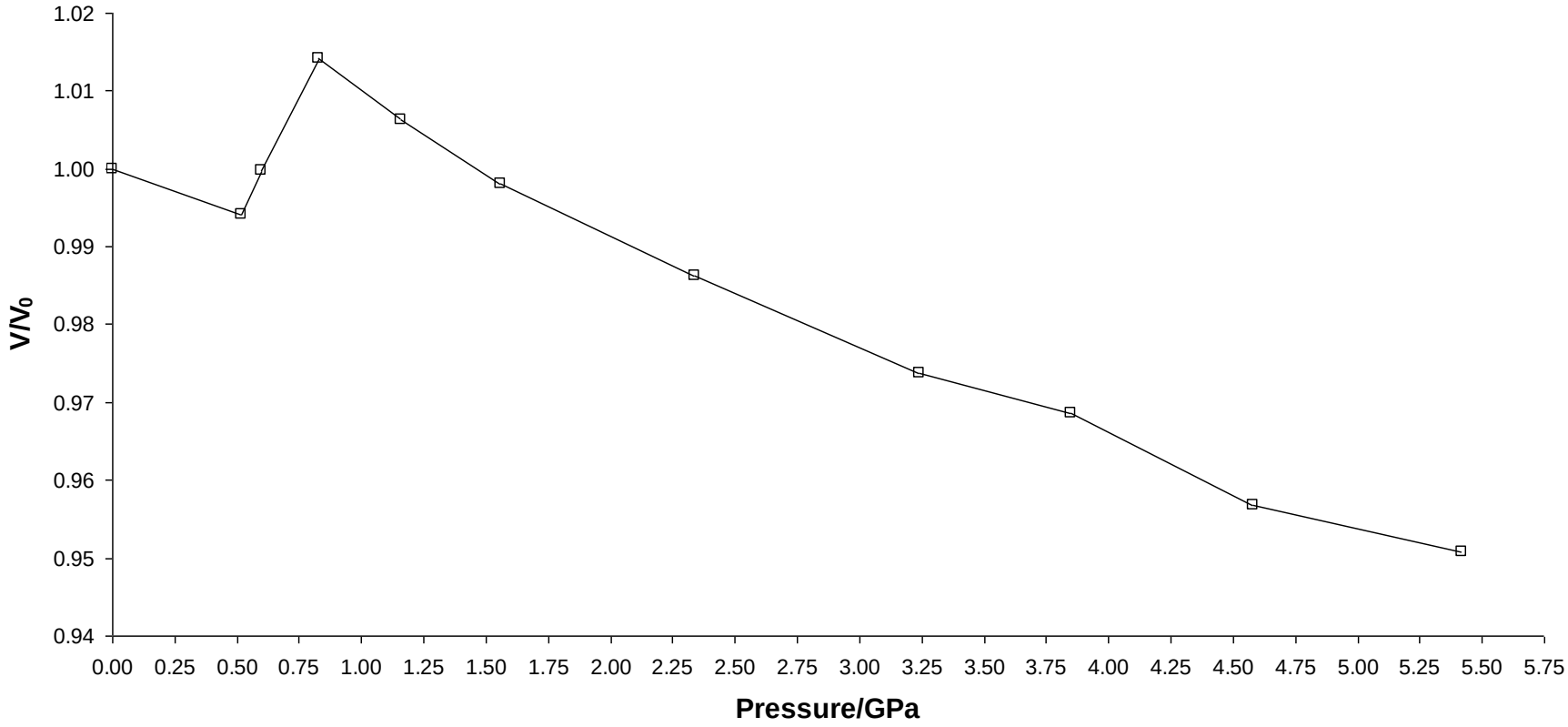

Figure 6: Normalised cell volumes of orthorhombic Na-GaSi-NAT as a function of pressure from le Bail refinements of X7A data.

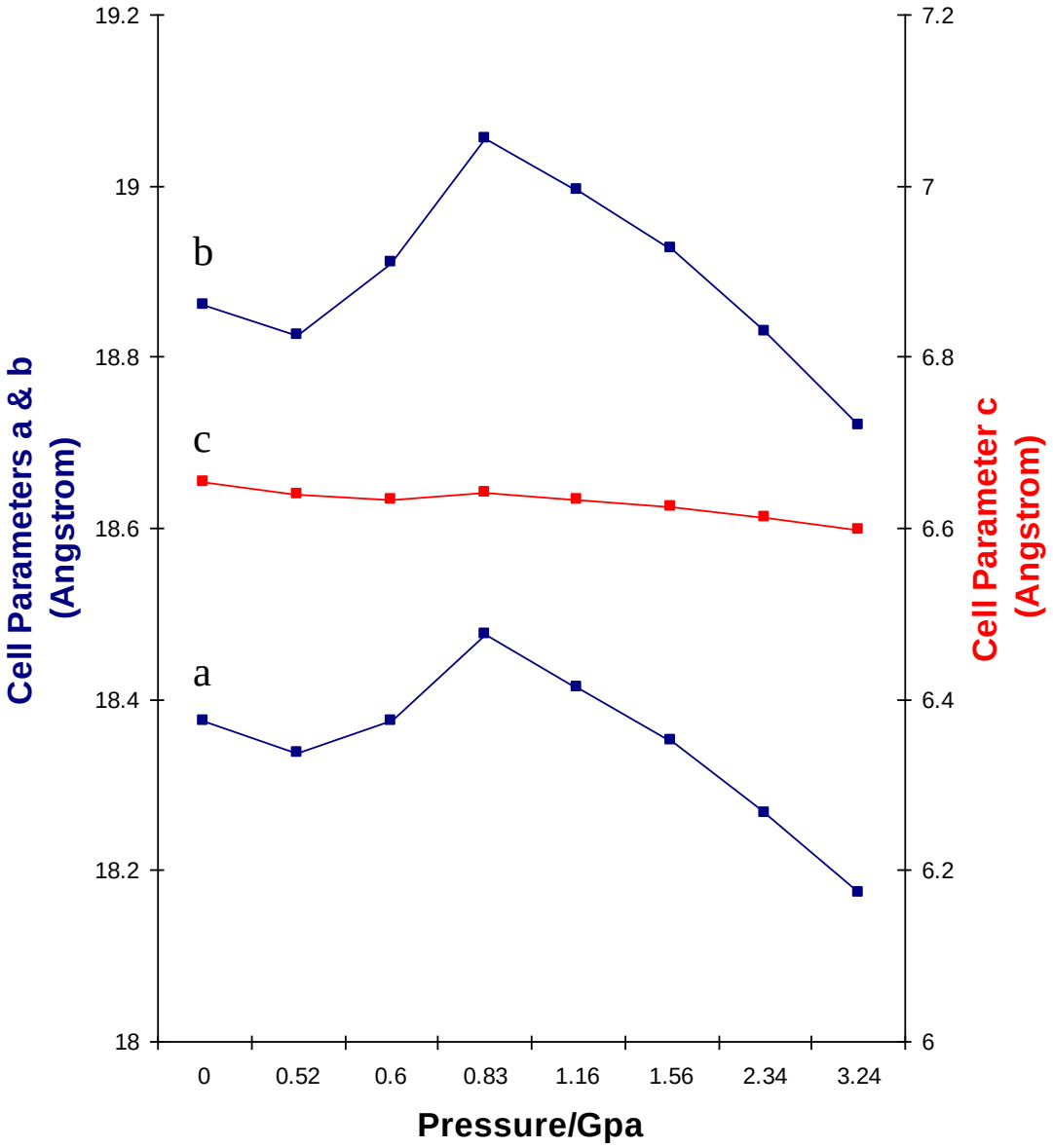

Figure 7: Changes in the unit cell parameters of orthorhombic Na-GaSi-NAT as a function of pressure from the X7A data. For clarity, values >3.5 GPa are not included. The unit cell axes *a* and *b* are shown in blue (left scale) and *c* in red (right scale).

5.2 Fitting an Equation of State

The compression of the superhydrated phase gave data which was fit to an equation of state using EoSFIT version 5.2.[3] A Murnaghan equation of state was used to fit the data and the bulk moduli (*K*), pressure derivative (*K*') and a theoretical V_0 for the superhydrated phase of orthorhombic Na-GaSi-NAT were calculated in this way. Other methods, including fixing *K*' at 4 in a Murnaghan equation or applying a 2nd order Birch-Murnaghan equation, gave similar but poorer fits.

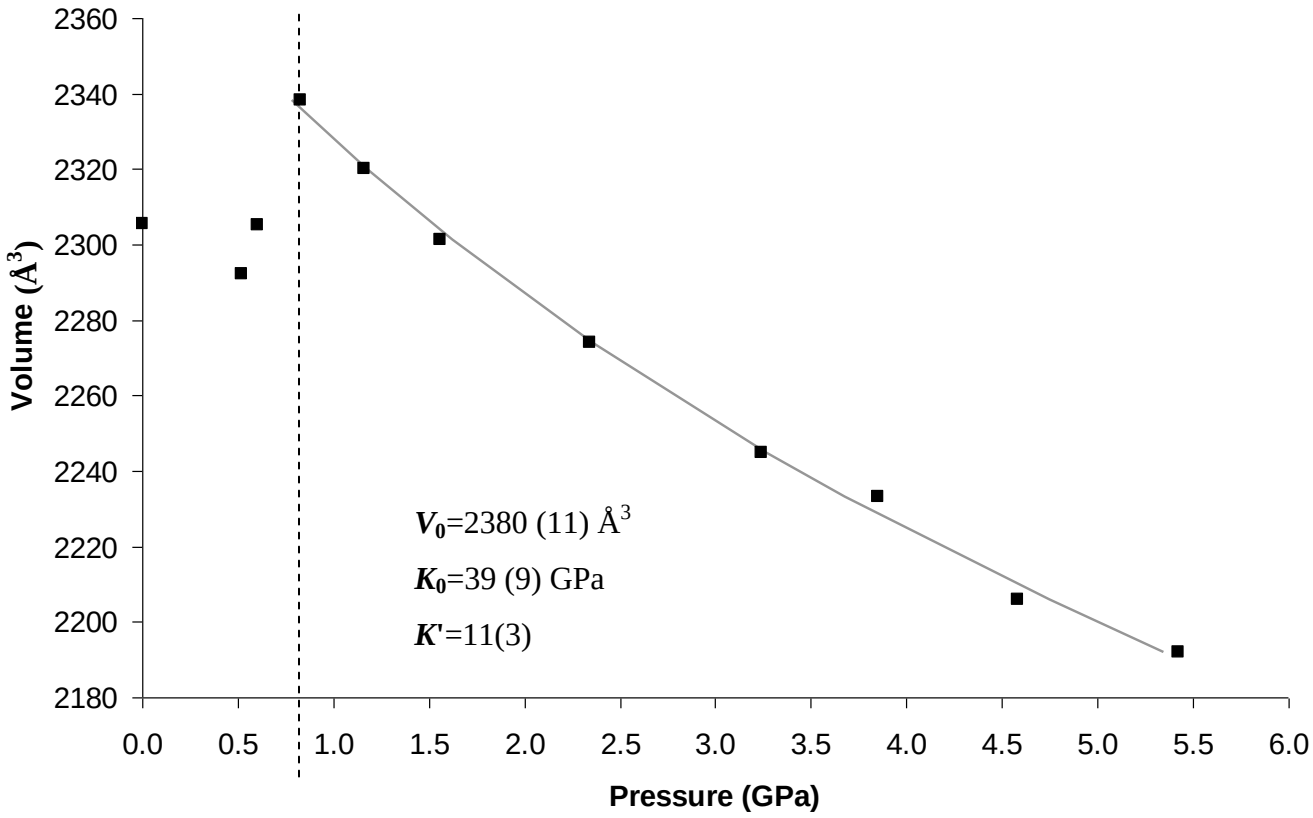

Figure 8: Pressure dependence of the unit cell volume of orthorhombic Na-GaSi-NAT and the equation of state fit (solid grey line), for the high pressure superhydrated form. The dashed black line indicates the transition to the expanded/superhydrated form.

The refined V_0 value for the superhydrated phase was 2380(11) Å^3. This is a difference of 74.9 Å^3, 3.3% larger than that of the normal, ambient condition phase. This is larger, but similar to the EoS refined value given in a report by Lee *et. al.*,[4] of 2365.(4) Å^3, 58 Å^3 larger than the normal state. The difference in V_0 values calculated for the two phases acts to estimate the increase in space required to incorporate OW2 water into the pores.

The bulk modulus for the superhydrated phase was refined to 50(12) GPa. Similar values were refined during the neutron diffraction study of orthorhombic Na-GaSi-NAT, discussed in chapter 4 (V_0= 2389(4) and K=49(3)).

The values refined using these data shall be used for comparative purposes, later in this chapter, when discussing further high pressure measurements of orthorhombic Na-GaSi-NAT.

5.3 Synchrotron X-Ray Diffraction Studies (9.5HPT)

As explained in the previous section, synchrotron X-ray diffraction of the two gallosilicate natrolite forms offers the benefit of collecting many pressure points with small pressure increments. In the hope of gaining ambient and high pressure data which enables full structural refinement (rather than just Le Bail fitting); experiments were performed using synchrotron X-ray diffraction at 9.5HPT, Daresbury. The set up of this particular beamline has distinct advantages over that of X7a (for the purposes of these experiments). Full experimental set up and conditions for each of these methods are given in chapter 2.

Use of the 9.5HPT beamline offers some solution to the problems encountered during the previous synchrotron X-ray diffraction study at X7a. Problems arose for two main reasons:

- **Sample Nature**

Both the gallosilicate samples were particularly grainy in nature, made up of large glass-like particles. This graininess remains even with hours of extensive grinding. Due to the nature of these particles, a well averaged powder diffraction data collection was impaired by spotting from these (which reduces powder averaging as these particles can act as small single crystals within the powder). This effects data by giving a false representation of relative intensities and in some cases significant peak broadening (as seen in the tetragonal Na-GaSi-NAT X7A study).

- **Data detection method**

A two-dimension strip psd detector was used in X7A experiments. This detector collects a ‘slice’ from the diffraction rings to give 1-dimensional data. Problems with spotting, as well as the presence of ruby peaks or diamond reflections, are exaggerated due to the

poor averaging that emerges from the use of this technique. Use of a psd detector represents the true diffraction pattern only when the nature of the sample is such that well defined rings with little/no spotting are observed.

By the use of the 9.5HPT beamline some solution to these problems is offered. This is mainly in the form of a change in data collection method and selective removal of spots prior to data integration. In addition a new sample preparation technique was implemented to reduce the occurrence of spotting.

Implemented Solutions:

- **Data detection method**

Detection via a MAR345 image plate, rather than a PSD detector; gives a full 2-dimensional data i.e. the full 360 deg of the diffraction rings are collected. This significantly increases structural averaging as well as signal-to-noise ratios.

- **Sample preparation method**

For these experiments, preparation techniques were modified in the hope of reducing the occurrence of data spotting due to particle nature. In this method samples were ground extensively under H_2O to produces a fine particle suspension which is then removed and dried to give much finer particles than was possible with normal sample grinding.

- **Fit2d software**

The use of this software allows analysis of the diffraction rings and the ability to selectively mask spots or reflections from the image prior to data integration. This excludes a great number of spots/reflections without affecting the powder diffraction rings. Example Images of the diffraction patterns collected using a MAR345 image plate and the use of Fit2d software to mask some spots/reflections are displayed in Figure 9.

Implementing these solutions, collectively, gave a significant increase in the quality of the ambient and high pressure data so that all data collects were Rietveld refinable. In

particular the significant peak broadening observed for tetragonal Na-GaSi-NAT, was addressed. So for the first time, refinable synchrotron X-ray data was collected for the tetragonal form. Full experimental details of these methods are given in chapter 2.

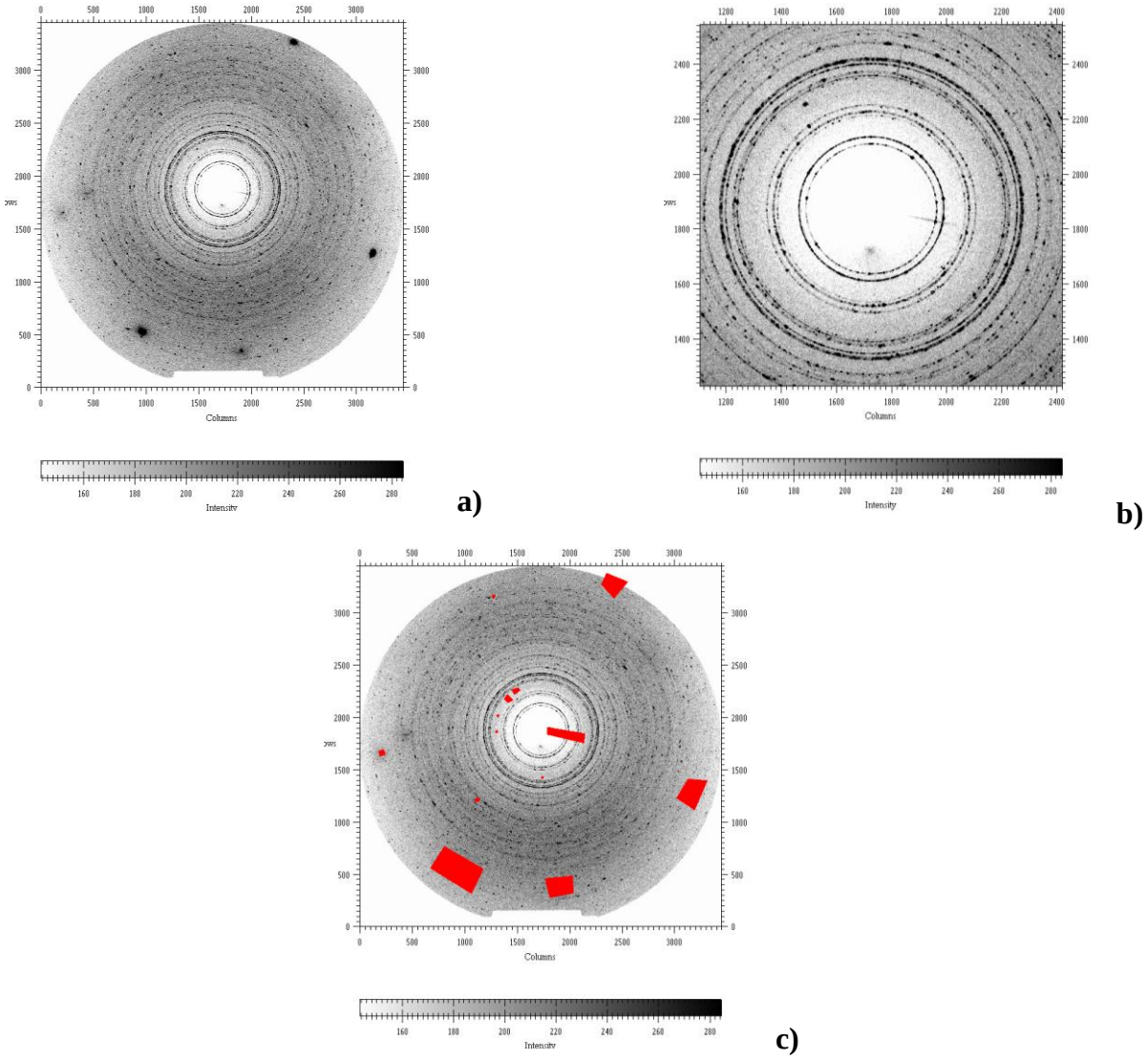

Figure 9: Image plate data from experiments using synchrotron X-ray diffraction at 9.5 HPT beamline, Daresbury. Images are displayed and manipulated using Fit2d software. A) Image of diffraction rings from orthorhombic Na-GaSi-NAT, showing diamond reflections and spotting from ruby chips. The granular nature of the sample is shown via intense spotting throughout the image. B) A zoomed in image showing clear evidence of wide spread spotting within the pattern. C) An image with masked regions to exclude some of the reflection/spots.

5.3.1 Ambient Pressure Studies

An ambient pressure control (to which the high pressure data will be compared), was performed with the sample mounted on tape. The ambient pressure data collected for orthorhombic Na-GaSi-NAT, at 9.5HPT gave a good diffraction pattern with well resolved peaks. Rietveld refinement gave a good fit, with little/no intensity difference within the refinement, Figure 10. Full atomic coordinates and selected bond distances and angles included in Table 3 and Table 4 respectively.

A similar ambient pressure run was performed for tetragonal Na-GaSi-NAT, with comparable success. The Rietveld fit for this ambient run is shown in Figure 11; full atomic coordinates are included in Table 5 with selected bond distances and angles given in Table 6. The orthorhombic Na-GaSi-NAT measured volume (2303.67(27)) and OW2 content (0.0) compare very well to neutron values presented in Chapter 4 (2309.75(11) and 0.048(4), respectively), as does the tetragonal Na-GaSi-NAT measured volume (1167.40(33) vs. (1163.77(12)) and OW2 content (0.323(43) vs. 0.118(19)), The small discrepancy in OW2 water content between methods can be attributed to sample differences and/or environmental humidity.

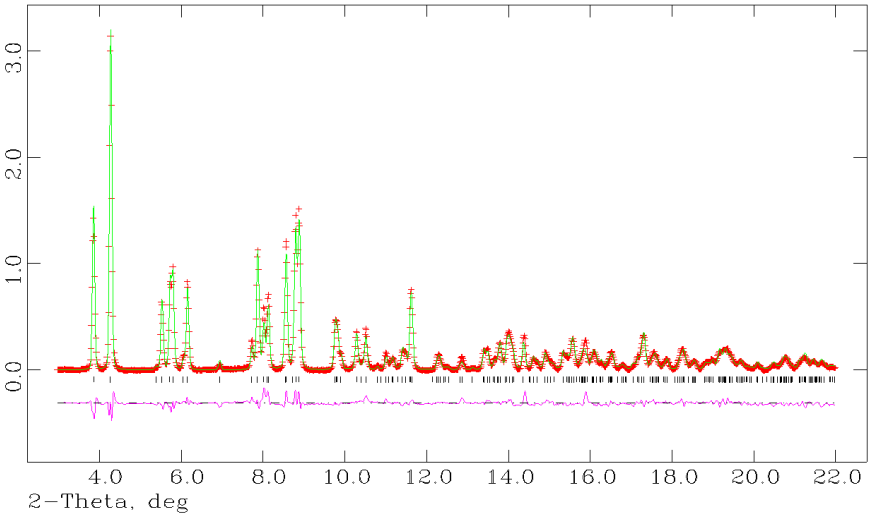

Figure 10: Rietveld refinement of data collected from 9.5 HPT for orthorhombic Na-GaSi-NAT, at ambient pressure (using mounting tape).

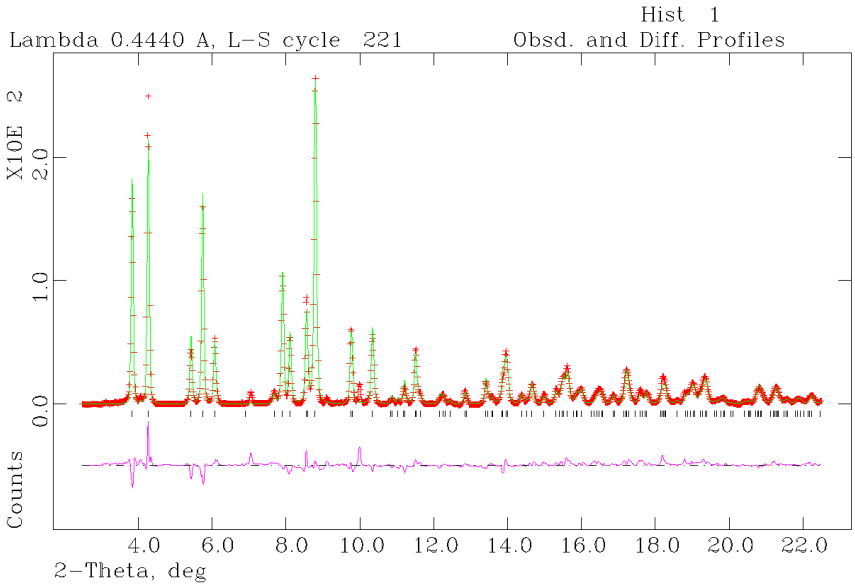

Figure 11: Rietveld refinement of data collected from 9.5 HPT for tetragonal Na-GaSi-NAT, at ambient pressure (using mounting tape).

5.3.2 High Pressure Studies

The aim was to collect good quality, high pressure data at small increments of pressure and over a good pressure range. This should give a fuller understanding of the structural changes during PIH and also cell compression, with more accurate pressure-onset values.

5.3.3.1 Orthorhombic Na-GaSi-NAT

High pressure data were collected using a diamond anvil cell from 0-2.89 GPa inclusive. Experimental set up and specifications are discussed in chapter two. The pressure was increased at small increments for each data collection. At about 3GPa the pressure was released at increments so that pressure release steps were also used in data collection. Raw diffraction patterns are shown in Figure 12. Rietveld refinement of diffraction data was performed using the GSAS suite (EXPGUI). Table 3 gives full listings of atomic coordinates and Table 4 shows selected bond distances and angles for each pressure step. Rietveld refinement profile plots, along with atoms structural schematics at each pressure step can be found in the appendices 1.2.2.1. and 1.3.1.

Upon application of pressure, the changes in unit cell volume and parameters follow the expected pattern, based upon the evolution of a superhydrated/expanded phase. From 0-0.906 GPa cell compression is observed (Figure 14). This is seen in other high pressure work for orthorhombic Na-GaSi-NAT, discussed in this thesis and reported by Lee *et. al.*[4], all of which show cell compression at very low pressures. The compression is accompanied by contraction along the *a*- and *b*-axes (Figure 13).

At ambient pressure, only one water site is occupied (OW1). As pressure is increased a second water site (OW2) is partially filled at increasing increments with pressure (Figure 14). Insertion of the OW2 water molecule begins at pressures as low as 0.35 GPa and increases to full occupancy once the superhydrated phase is reached. At low pressure,

OW2 increases in occupancy, but does not show any bonding with the sodium cation until the pressure approaches values where the superhydrated phase appears. In this case, Na-OW2 bonding is not observed until 0.714 GPa, with full superhydration occurring at the next pressure step, 0.906 GPa. This is in excellent agreement with a reported high pressure study performed upon orthorhombic Na-GaSi-NAT, in which Lee *et. al*. observe superhydration occurring a 0.90(5).[4] This result is also in good agreement with the high pressure neutron diffraction study discussed in chapter 4. In the neutron study, Na-OW2 bonds are not observed until pressures above 0.74 GPa.

Results obtained for the pressure step at 0.906 GPa are, very fortuitously, unique. At this pressure we observe a two phase system, the transition between orthorhombic Na-GaSi-NAT and superhydrated orthorhombic Na-GaSi-NAT (51.10% and 48.90 % respectively). Other formulations were tried, but refinements involving a single phase system were very poor. The raw diffraction pattern at this pressure is clearly very different to others in the series (Figure 12). Looking at peaks in the 2-theta region 7.5-9.0, it looks very likely that the pattern is created by contributions form a Na-GaSi-NAT phase and a superhydrated Na-GaSi-NAT phase. A good Rietveld refinement fit was achieved for this two phase system. These data give a unique insight into the specific point of transition during PIH and cell expansion. Phase one, Na-GaSi-NAT, sits on the low pressure compression curve with a contracted cell volume of 2256.9(8) $Å^3$. From phase one (Na-GaSi-NAT) to phase two (superhydrated Na-GaSi-NAT), the characteristic cell volume expansion associated with the formation of a superhydrated phase is observed. A volume increase of 2.42%, up to 2311.4(7) $Å^3$ (0.62% increase from V_0), is accompanied by a 0.99% and 1.46% increase in the *a*- and *b*-axes respectively (Figure 13 and Figure 14). This volume increase compares well with that observed during high pressure neutron diffraction studies of orthorhombic Na-GaSi-NAT, where the volume expansion step is 2.04%. The formation of the superhydrated phase occurs at 0.906 GPa, a slightly high pressure than that observed in high pressure neutron studies (0.714GPa). Samples from different sources were used in these two experiments which could attribute for the difference in the superhydration pressure value. However, a difference of ~0.2 GPa could be within the errors of the pressure measurement.

Following the formation of the superhydrated phase, the unit cell (whilst maintaining full OW2 occupancy), progresses down a compression curve as the pressure is increased. The pressure and volume data obtained from this compression curve can be used to fit an equation of state to the superhydrated phase. In doing so, both the bulk modulus and an extrapolated 'V_0' were obtained for the superhydrated phase. A value for V_0 is not possible to determine experimentally due to the reversibility of the pressure-induced hydration step. Results from EoS fitting are discussed in later sections within this chapter.

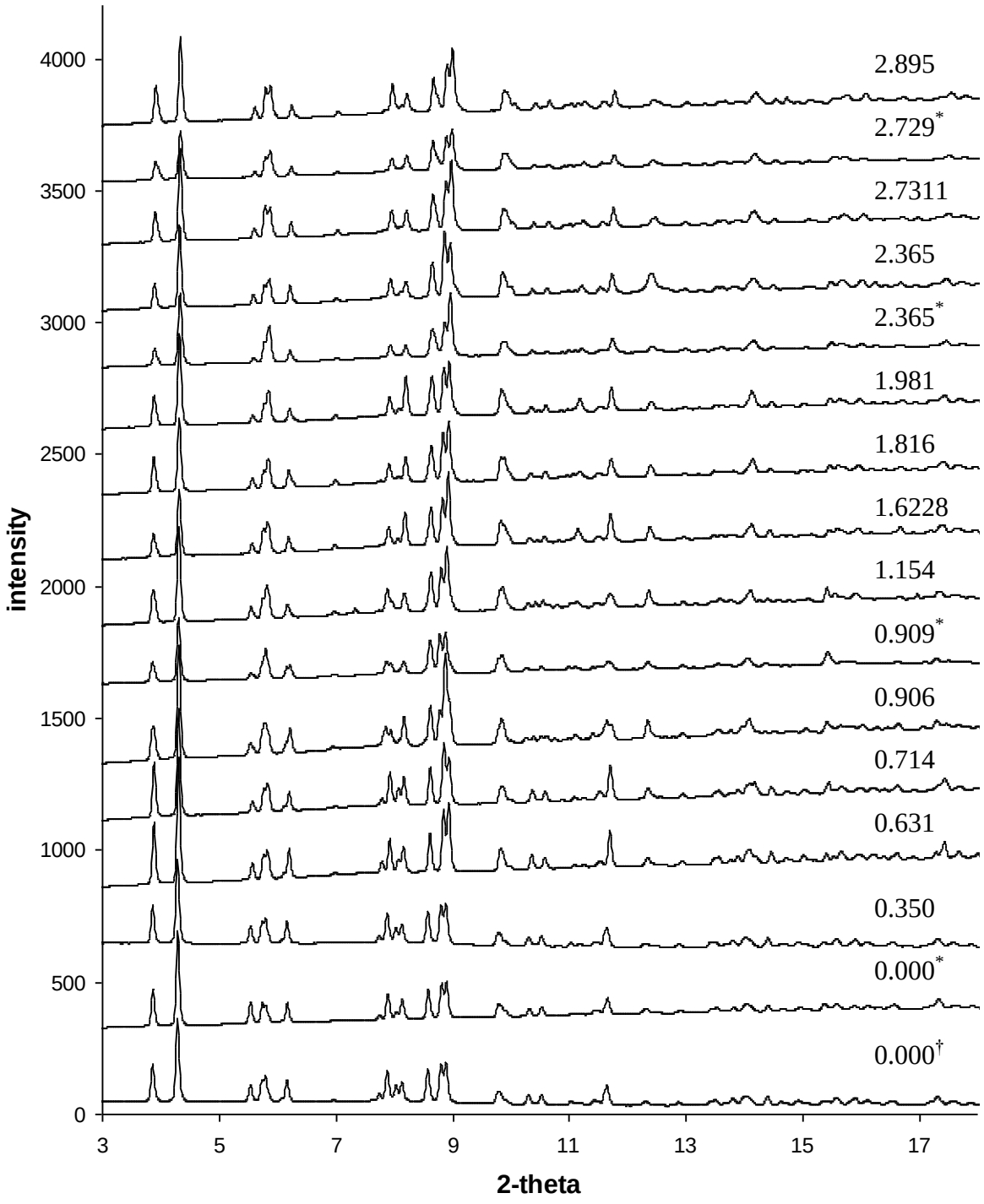

Figure 12: Synchrotron X-ray diffraction patterns collected for orthorhombic Na-GaSi-NAT in sequential steps from ambient to 2.89 GPa and back again, data collected during high pressure release steps noted with a *. †Data collected at ambient pressure, using mounting tape rather than a DAC, for comparison with high pressure results.

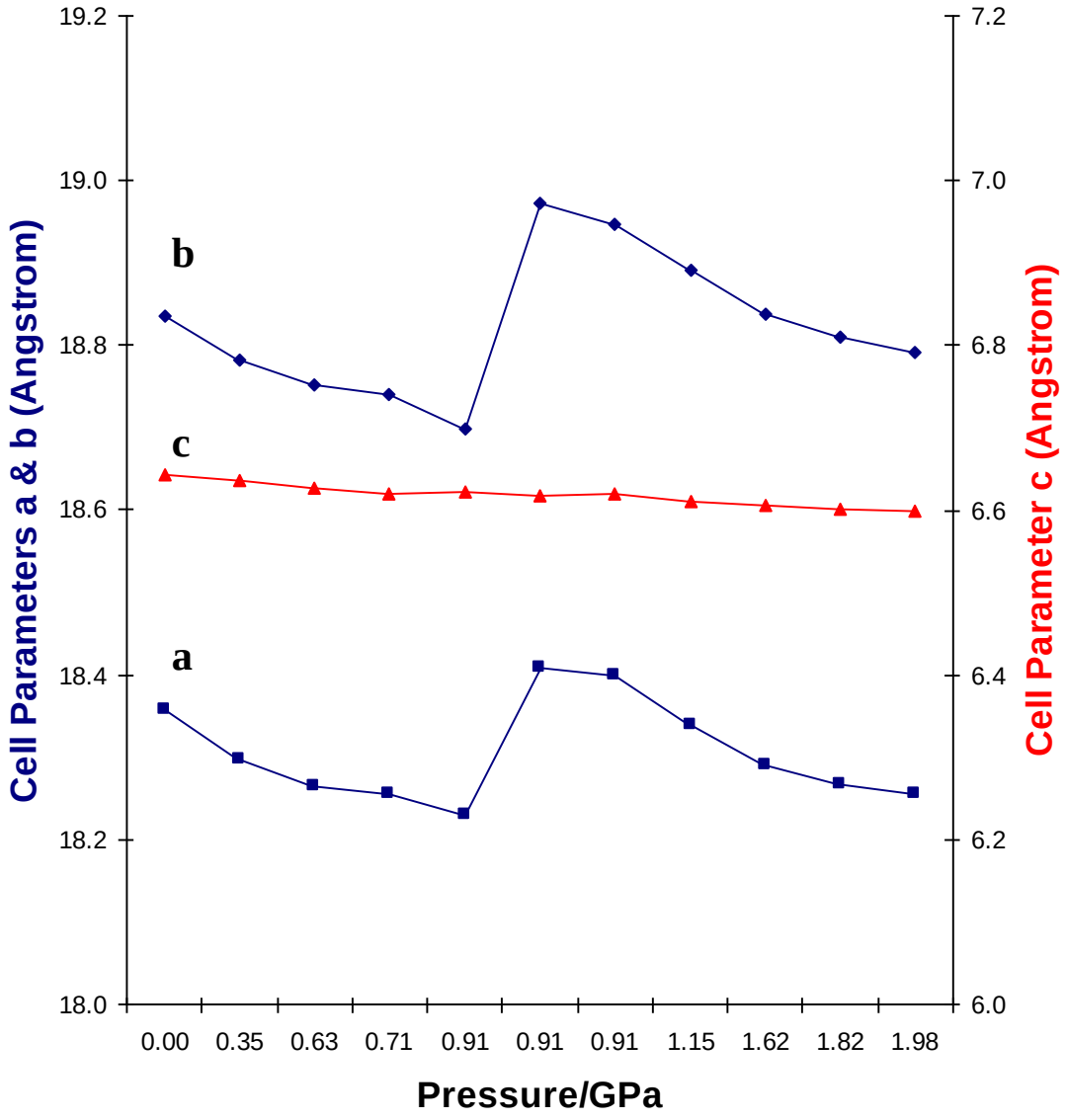

Figure 13: Changes in the cell parameters of orthorhombic Na-GaSi-NAT as a function of pressure. For clarity, values >2 GPa are not included. Unit cell axes *a* and *b* shown in blue (left scale), and *c* in red (right scale).

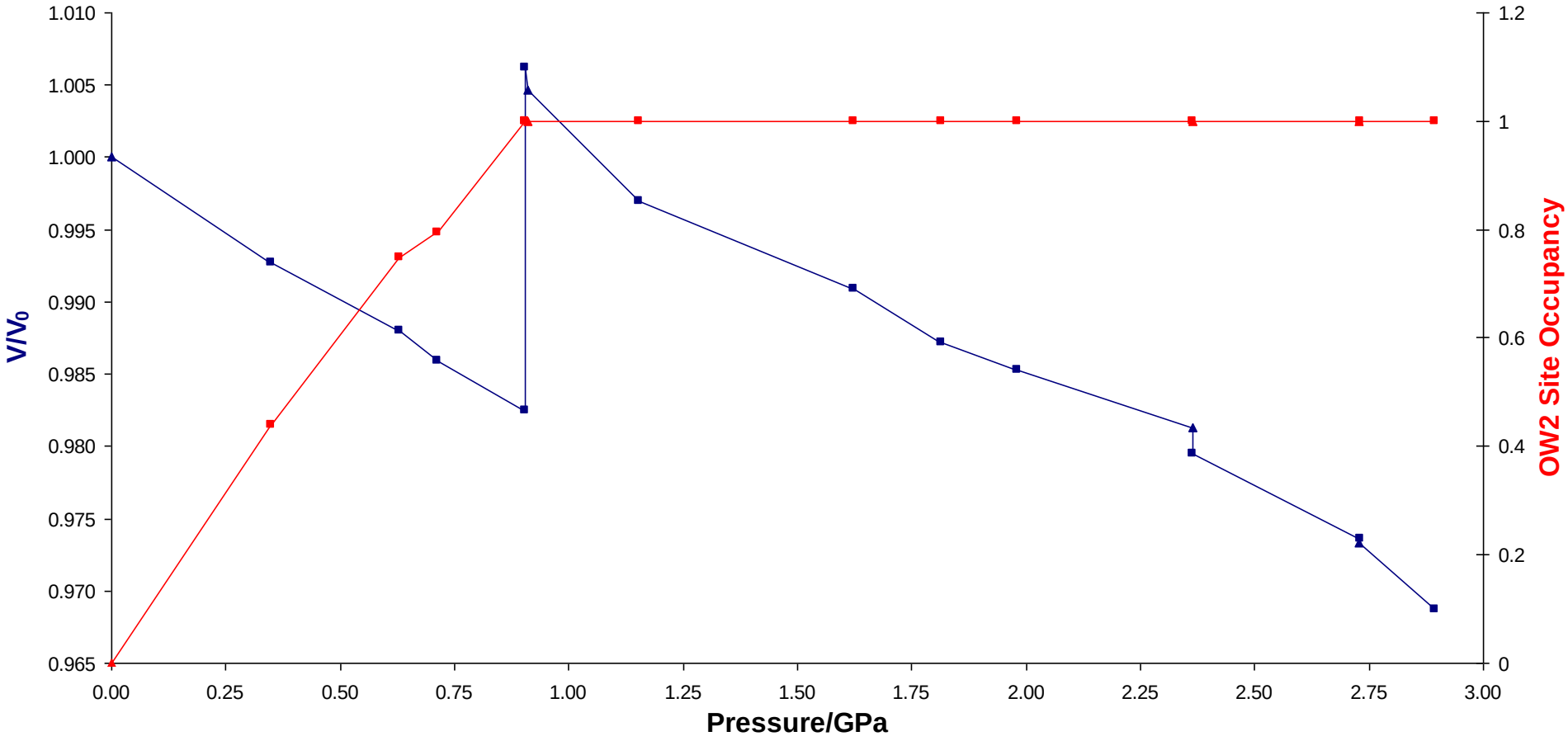

Figure 14: High pressure superhydration and volume expansion of orthorhombic Na-GaSi-NAT. The blue points are unit cell volumes normalized to ambient pressure and the red points are the OW2 site occupancy. Triangular data points are those collected during pressure release steps.

Table 3: Refined atomic coordinates for orthorhombic Na-GaSi-NAT (Fdd2) from ambient to 2.90 GPa, inclusive. Data were collected using beamline 9.5 HPT, Daresbury. †

Reference		Mounting Tape I‡	23c§	1b	3	4	5K phase 1	5K phase 2	22§	6	7	8	9	21d§	10	11b	20§	12
Pressure		0	0	0.35	0.631	0.714	0.906		0.909	1.154	1.6228	1.816	1.981	2.365	2.365	2.7311	2.729	2.8945
R_{wp}		0.0378	0.0214	0.0173	0.0188	0.0237	0.0187		0.0311	0.0293	0.0311	0.0242	0.0306	0.0265	0.0294	0.0199	0.0214	0.0187
R_p		0.0277	0.0152	0.0107	0.0137	0.0173	0.0128		0.018	0.0182	0.0198	0.0152	0.019	0.0181	0.017	0.0123	0.0122	0.0119
cell parameters	*a*	18.3696(12)	18.3584(18)	18.2980(14)	18.2639(15)	18.2552(22)	18.2288(33)	18.4086(32)	18.400(4)	18.3393(28)	18.2900(29)	18.2664(23)	18.2546(28)	18.2242(26)	18.2094(28)	18.1730(18)	18.1613(28)	18.1287(18)
	b	18.8551(12)	18.8354(17)	18.7810(14)	18.7525(15)	18.7408(21)	18.698(4)	18.9719(30)	18.947(4)	18.8924(31)	18.8377(31)	18.8097(24)	18.7906(28)	18.7660(31)	18.7447(28)	18.6877(20)	18.6911(29)	18.6495(19)
	c	6.6510(5)	6.6434(8)	6.6360(6)	6.6265(6)	6.6200(8)	6.6212(16)	6.6184(14)	6.6201(16)	6.6101(12)	6.6068(12)	6.6004(9)	6.5984(11)	6.5916(13)	6.5924(12)	6.5854(8)	6.5866(12)	6.5823(8)
volume		2303.67(27)	2297.2(4)	2280.49(33)	2269.54(33)	2264.8(5)	2256.9(8)	2311.4(7)	2307.9(9)	2290.2(7)	2276.3(7)	2267.8(5)	2263.4(6)	2254.3(7)	2250.2(6)	2236.5(4)	2235.8(6)	2225.4(4)
Si1	*x*	0	0	0	0	0	0	0	0	0	0	0	0	0	0	0	0	0
8a	*y*	0	0	0	0	0	0	0	0	0	0	0	0	0	0	0	0	0
	z	0	0	0	0	0	0	0	0	0	0	0	0	0	0	0	0	0
	U_{iso} *100	1.11(9)	2.5	2.5	2.5	2.5	2.5	2.5	2.5	2.5	2.5	2.5	2.5	2.5	2.5	2.5	2.5	2.5
Si2	*x*	0.1489(5)	0.1473(9)	0.1524(7)	0.1450(8)	0.1501(10)	0.1474(18)	0.1549(18)	0.1501(14)	0.1515(14)	0.1545(12)	0.1533(9)	0.1529(11)	0.1482(12)	0.1524(13)	0.152832	0.1494(11)	0.1547(8)
16b	*y*	0.2124(5)	0.2113(8)	0.2142(7)	0.2172(8)	0.2209(10)	0.2225(18)	0.2104(15)	0.2065(16)	0.2062(13)	0.2090(13)	0.2117(11)	0.2088(13)	0.2120(13)	0.2091(16)	0.209865	0.2119(13)	0.2114(9)
	z	0.6048(23)	0.6108(33)	0.5967(33)	0.5932(34)	0.588(5)	0.626(6)	0.602(7)	0.598(6)	0.601(5)	0.590(6)	0.595(5)	0.594(6)	0.5909(32)	0.622(5)	0.596914	0.589(5)	0.5946(34)
	U_{iso} *100	1.11(9)	2.5	2.5	2.5	2.5	2.5	2.5	2.5	2.5	2.5	2.5	2.5	2.5	2.5	2.5	2.5	2.5
Ga	*x*	0.03533(24)	0.0328(4)	0.0353(4)	0.03357(35)	0.0316(6)	0.0393(9)	0.0371(8)	0.0430(7)	0.0414(6)	0.0402(6)	0.0388(5)	0.0405(6)	0.0421(6)	0.0398(6)	0.039072	0.0373(5)	0.0369(4)
16b	*y*	0.09346(23)	0.0935(4)	0.09388(33)	0.0960(4)	0.0928(4)	0.0977(8)	0.0937(7)	0.0949(6)	0.0932(5)	0.0953(6)	0.0915(4)	0.0939(5)	0.0982(6)	0.0950(6)	0.095574	0.0946(5)	0.0947(4)
	z	0.6097(24)	0.597(4)	0.5900(33)	0.5913(35)	0.593(5)	0.604(8)	0.585(6)	0.593(5)	0.592(6)	0.599(6)	0.603(5)	0.593(6)	0.5807(18)	0.603(5)	0.586751	0.595(6)	0.5842(31)
	U_{iso} *100	1.11(9)	2.5	2.5	2.5	2.5	2.5	2.5	2.5	2.5	2.5	2.5	2.5	2.5	2.5	2.5	2.5	2.5

O1	*x*	0.0138(9)	0.0157(13)	0.0168(13)	0.0134(15)	0.0143(16)	0.0340(32)	0.0251(34)	0.0303(24)	0.0174(21)	0.0370(19)	0.0348(16)	0.0274(22)	0.0217(23)	0.0465(18)	0.032348	0.0309(17)	0.0257(14)
16b	*y*	0.0705(7)	0.0672(14)	0.0633(13)	0.0636(15)	0.0675(18)	0.0611(30)	0.0574(32)	0.0577(27)	0.0638(22)	0.0633(16)	0.0639(16)	0.0640(19)	0.0462(19)	0.0516(25)	0.05499	0.0620(20)	0.0584(15)
	z	0.8692(32)	0.857(5)	0.844(5)	0.843(5)	0.855(7)	0.857(11)	0.837(10)	0.844(8)	0.846(8)	0.865(7)	0.869(7)	0.856(8)	0.804(4)	0.852(8)	0.835919	0.854(7)	0.837(5)
	U_{iso} *100	1.40(32)	2.5	2.5	2.5	2.5	2.5	2.5	2.5	2.5	2.5	2.5	2.5	2.5	2.5	2.5	2.5	2.5
O2	*x*	0.0659(6)	0.0630(9)	0.0728(9)	0.0643(10)	0.0723(13)	0.0665(21)	0.0747(18)	0.0644(15)	0.0687(13)	0.0674(13)	0.0711(10)	0.0682(13)	0.0655(12)	0.0677(13)	0.069449	0.0656(10)	0.0718(8)
16b	*y*	0.1850(4)	0.1850(5)	0.1818(6)	0.1865(7)	0.1809(8)	0.1896(12)	0.1796(12)	0.1883(10)	0.1832(9)	0.1881(8)	0.1818(6)	0.1856(7)	0.1894(9)	0.1866(9)	0.185643	0.1868(7)	0.1839(6)
	z	0.5932(55)	0.626(13)	0.574(8)	0.634(7)	0.603(10)	0.642(15)	0.637(13)	0.608(11)	0.641(11)	0.567(13)	0.598(12)	0.590(12)	0.634(8)	0.646(11)	0.632054	0.608(15)	0.623(7)
	U_{iso} *100	1.40(32)	2.5	2.5	2.5	2.5	2.5	2.5	2.5	2.5	2.5	2.5	2.5	2.5	2.5	2.5	2.5	2.5
O3	*x*	0.0984(7)	0.0979(9)	0.1035(8)	0.1003(9)	0.1008(11)	0.1074(25)	0.0997(20)	0.1026(22)	0.1020(16)	0.0981(17)	0.1022(13)	0.0983(17)	0.1062(15)	0.1064(16)	0.103236	0.1020(14)	0.0997(10)
16b	*y*	0.0346(7)	0.0308(11)	0.0359(10)	0.0310(11)	0.0291(12)	0.0292(27)	0.0378(21)	0.0284(21)	0.0296(18)	0.0349(20)	0.0308(16)	0.0217(16)	0.0349(18)	0.0332(19)	0.034724	0.0329(16)	0.0414(11)
	z	0.4831(37)	0.499(6)	0.478(5)	0.504(5)	0.517(6)	0.557(9)	0.448(9)	0.482(9)	0.474(8)	0.454(10)	0.485(8)	0.509(8)	0.469(6)	0.492(9)	0.465949	0.478(8)	0.434(5)
	U_{iso} *100	1.40(32)	2.5	2.5	2.5	2.5	2.5	2.5	2.5	2.5	2.5	2.5	2.5	2.5	2.5	2.5	2.5	2.5
O4	*x*	0.2031(6)	0.1992(9)	0.2039(8)	0.2069(9)	0.1944(10)	0.2047(23)	0.2112(20)	0.2067(12)	0.2021(11)	0.2076(14)	0.2016(10)	0.1984(10)	0.2078(11)	0.2019(13)	0.201175	0.1994(9)	0.1971(6)
16b	*y*	0.1561(7)	0.1511(11)	0.1527(10)	0.1626(14)	0.1613(14)	0.1661(27)	0.1494(21)	0.1548(23)	0.1509(18)	0.1494(19)	0.1567(18)	0.1573(21)	0.1570(18)	0.1475(19)	0.149492	0.1568(18)	0.1497(11)
	z	0.7083(38)	0.704(7)	0.686(5)	0.670(5)	0.714(8)	0.717(14)	0.662(10)	0.711(8)	0.723(8)	0.692(9)	0.724(8)	0.741(9)	0.682(5)	0.724(9)	0.7084	0.715(8)	0.718(5)
	U_{iso} *100	1.40(32)	2.5	2.5	2.5	2.5	2.5	2.5	2.5	2.5	2.5	2.5	2.5	2.5	2.5	2.5	2.5	2.5
O5	*x*	0.1788(7)	0.1831(13)	0.1786(10)	0.1793(12)	0.1720(11)	0.1856(32)	0.1825(23)	0.1824(18)	0.1862(18)	0.1812(18)	0.1885(14)	0.1823(16)	0.1855(14)	0.1905(21)	0.184494	0.1836(14)	0.1811(9)
16b	*y*	0.2316(10)	0.2311(14)	0.2221(14)	0.2196(15)	0.2347(21)	0.2324(37)	0.2178(22)	0.2176(21)	0.2115(16)	0.2090(19)	0.2063(13)	0.2111(18)	0.2078(15)	0.2140(18)	0.20988	0.2093(13)	0.2132(10)
	z	0.3819(30)	0.396(5)	0.366(4)	0.368(4)	0.355(6)	0.408(10)	0.372(9)	0.373(8)	0.376(7)	0.354(8)	0.371(6)	0.361(7)	0.368(4)	0.400(7)	0.368036	0.363(7)	0.362(4)
	U_{iso} *100	1.40(32)	2.5	2.5	2.5	2.5	2.5	2.5	2.5	2.5	2.5	2.5	2.5	2.5	2.5	2.5	2.5	2.5
Na	*x*	0.2202(6)	0.2273(12)	0.2270(11)	0.2208(12)	0.2199(13)	0.2404(25)	0.2373(24)	0.2257(21)	0.2287(17)	0.2224(19)	0.2262(15)	0.2119(16)	0.2307(16)	0.2382(18)	0.227653	0.2318(17)	0.2278(11)
16b	*y*	0.0281(6)	0.0250(10)	0.0245(9)	0.0294(11)	0.0242(13)	0.0269(25)	0.0253(17)	0.0268(20)	0.0324(15)	0.0245(15)	0.0204(12)	0.0286(15)	0.0293(16)	0.0170(18)	0.027656	0.0164(14)	0.0259(11)
	z	0.6217(34)	0.607(6)	0.600(5)	0.606(5)	0.584(7)	0.543(11)	0.602(11)	0.569(10)	0.588(9)	0.652(9)	0.639(7)	0.648(7)	0.619(5)	0.574(9)	0.622565	0.611(8)	0.612(5)
	U_{iso} *100	0.2(4)	2.5	2.5	2.5	2.5	2.5	2.5	2.5	2.5	2.5	2.5	2.5	2.5	2.5	2.5	2.5	2.5

OW1	*x*	0.0563(9)	0.0610(14)	0.0629(15)	0.0560(16)	0.0608(20)	0.0600(37)	0.0643(32)	0.0733(24)	0.0696(21)	0.0653(24)	0.0666(19)	0.0604(25)	0.0677(21)	0.0622(24)	0.065952	0.0748(17)	0.0662(14)
16b	*y*	0.1904(9)	0.1902(15)	0.1872(14)	0.1784(12)	0.1814(18)	0.1772(27)	0.1889(29)	0.1770(22)	0.1784(18)	0.1856(23)	0.1791(17)	0.1782(19)	0.2008(18)	0.1813(20)	0.188837	0.1852(19)	0.1938(14)
	z	0.0836(54)	0.112(12)	0.115(7)	0.057(7)	0.051(10)	0.103(17)	0.034(13)	0.069(14)	0.067(11)	0.031(13)	0.070(11)	0.065(11)	0.087(11)	0.068(10)	0.077444	0.087(15)	0.097(8)
	U_{iso} *100	0.16(36)	2.5	2.5	2.5	2.5	2.5	2.5	2.5	2.5	2.5	2.5	2.5	2.5	2.5	2.5	2.5	2.5
OW2	*x*			0.1431(36)	0.1267(20)	0.1696(20)	0.1583(36)	0.1744(25)	0.1859(22)	0.1824(18)	0.1798(18)	0.1804(14)	0.1839(17)	0.1738(17)	0.1750(18)	0.174407	0.1752(15)	0.1729(10)
16b	*y*			0.0306(36)	0.1165(18)	0.0724(26)	0.0615(33)	0.0716(30)	0.0678(25)	0.0648(20)	0.0714(24)	0.0640(17)	0.0573(21)	0.0682(19)	0.0793(26)	0.068352	0.0672(20)	0.0720(14)
	z			-0.029(9)	-0.048(5)	0.030(8)	0.001(12)	0.068(15)	0.081(13)	0.091(12)	0.148(10)	0.125(9)	0.145(9)	0.115(9)	0.104(12)	0.082445	0.085(10)	0.086(7)
	U_{iso} *100			2.5	2.5	2.5	2.5	2.5	2.5	2.5	2.5	2.5	2.5	2.5	2.5	2.5	2.5	2.5
	Occ			0.441(26)	0.750(34)	0.793(36)	1	1	1	1	1	1	1	1	1	1	1	1

† Weights in parenthesis. Isotropic displacement factors (U_{iso} * 100) were fixed at 2.5 for all models (excluding ambient pressure data collected using mounting tape).

‡ Data collected at ambient pressure, using mounting tape rather than a DAC.

§ Data points collected during pressure release steps.

Table 4: A summary of selected bond distances and angles from the Rietveld refinement of orthorhombic Na-GaSi-NAT. Part A) 0-1.154 GPa inclusive. Part B) 1.62-2.89 GPa inclusive

Part A

	Pressure (GPa)								
	0	0	0.35	0.631	0.714	0.906 (phase 1)	0.906 (phase 2)	0.909	1.154
Si-O Tetrahedra									
Bond Length (Å)									
SI1_O1 × 2	1.60819(8)	1.60981(11)	1.60471(9)	1.60200(9)	1.60874(13)	1.60625(21)	1.60336(20)	1.60570(23)	1.60891(19)
SI1_O5 × 2	1.61247(8)	1.60528(11)	1.60542(9)	1.61224(9)	1.61009(15)	1.60687(22)	1.60452(19)	1.60907(23)	1.61012(16)
SI2_O2	1.61210(10)	1.62790(15)	1.58617(11)	1.60574(11)	1.60929(15)	1.60352(25)	1.60383(24)	1.61579(32)	1.60135(22)
SI2_O3	1.60700(8)	1.60135(12)	1.60888(10)	1.60441(10)	1.60795(14)	1.60401(25)	1.60263(22)	1.62470(27)	1.60788(21)
SI2_O4	1.61034(6)	1.60788(10)	1.60440(8)	1.60901(8)	1.60963(11)	1.60448(19)	1.60512(18)	1.61267(21)	1.61228(16)
SI2_O5	1.62147(10)	1.61449(15)	1.60855(13)	1.62123(13)	1.61674(19)	1.60972(31)	1.60679(31)	1.61743(33)	1.61974(25)
Ga-O Tetrahedra									
Bond Length (Å)									
GA_O1	1.82307(12)	1.82550(19)	1.81455(14)	1.81188(14)	1.82489(21)	1.8161(4)	1.81399(34)	1.8144(4)	1.82491(28)
GA_O2	1.81784(11)	1.82061(15)	1.79072(12)	1.80882(13)	1.81130(17)	1.80546(32)	1.80295(24)	1.8150(4)	1.80231(27)
GA_O3	1.81243(7)	1.79997(11)	1.81438(9)	1.81837(9)	1.81051(14)	1.80965(23)	1.81130(19)	1.82699(24)	1.81246(18)
GA_O4	1.81533(9)	1.80505(14)	1.80600(11)	1.81111(11)	1.80993(17)	1.80580(26)	1.81017(25)	1.81512(31)	1.82092(24)
T-O-T Bond Angles (°)									
SI1_O1_GA	137.974(1)	143.479(2)	150.374(1)	151.568(1)	142.974(2)	146.346(3)	155.756(2)	153.838(2)	149.199(3)
SI2_O2_GA	126.465(0)	124.790(0)	134.459(0)	126.498(1)	141.667(0)	127.477(2)	130.869(2)	114.690(0)	119.225(1)
SI2_O3_GA	141.678(2)	141.236(3)	132.675(3)	138.330(3)	130.209(4)	123.944(7)	134.636(6)	141.242(8)	139.918(6)
SI2_O4_GA	138.441(2)	131.830(4)	131.923(3)	142.953(2)	135.712(3)	147.046(5)	127.202(7)	141.840(7)	133.968(6)
SI1_O5_SI2	145.069(1)	153.813(1)	136.860(1)	139.946(1)	131.233(1)	157.220(2)	139.085(2)	143.160(1)	142.111(2)
Na Environment									
Bond Length (Å)									
NA_O2	2.63736(12)	2.49950(18)	2.68857(15)	2.59145(15)	2.71498(21)	2.7672(5)	2.62100(35)	2.6002(4)	2.67813(31)
NA_O2	2.39684(11)	2.40173(16)	2.43869(13)	2.36917(13)	2.44753(19)	2.17699(27)	2.57496(28)	2.30433(33)	2.43961(27)
NA_O3	2.42297(14)	2.48342(22)	2.41047(17)	2.30310(17)	2.22020(25)	2.4260(4)	2.7436(4)	2.3370(5)	2.44559(34)
NA_O4	2.50123(15)	2.51405(21)	2.51081(18)	2.54469(20)	2.74849(27)	2.9191(5)	2.4353(4)	2.6243(5)	2.46084(34)
NA_OW1	2.55410(13)	2.43202(17)	2.51107(14)	2.64246(16)	2.63770(21)	2.9187(4)	2.6265(4)	2.6680(4)	2.63568(29)
NA_OW1	2.22633(10)	2.33273(17)	2.32970(13)	2.36599(14)	2.32371(18)	1.98484(25)	2.24548(25)	2.5969(4)	2.55385(28)
NA_OW2					2.73487(22)	2.49460(32)	2.46415(29)	2.4213(4)	2.45549(28)
NA_NA	3.65714(23)	3.5524(4)	3.54462(29)	3.65102(28)	3.6040(4)	3.4779(7)	3.4770(7)	3.5757(7)	3.6091(5)
Bond Angle (°)									
OW1_NA10_OW1					145.745(2)	157.5(25)	147.904(3)	150.270(3)	147.029(3)
OW1_NA10_OW2					69.668(6)	75.102(11)	76.248(8)	78.830(12)	77.907(8)
OW1_NA10_OW2					76.238(6)	83.5(23)	77.584(11)	71.462(12)	70.171(10)

Part B

	Pressure (GPa)							
	1.6228	1.816	1.981	2.365	2.365	2.7311	2.729	2.8945
Si-O Tetrahedra								
Bond Length (Å)								
SI1_O1 × 2	1.63698(17)	1.60988(14)	1.61181(17)	1.60541(21)	1.61354(15)	1.60287(11)	1.60559(17)	1.59959(11)
SI1_O5 × 2	1.62826(17)	1.60479(13)	1.61231(16)	1.61773(16)	1.61485(16)	1.60732(10)	1.60782(16)	1.60353(11)
SI2_O2	1.64800(24)	1.60217(18)	1.60602(23)	1.59060(21)	1.60625(23)	1.59832(14)	1.59637(23)	1.59984(14)
SI2_O3	1.61749(22)	1.59972(15)	1.60798(18)	1.60972(21)	1.60920(19)	1.60739(14)	1.61248(20)	1.60536(14)
SI2_O4	1.63117(16)	1.60345(12)	1.60114(15)	1.61428(16)	1.61390(15)	1.60741(10)	1.60587(15)	1.60464(10)
SI2_O5	1.63334(28)	1.61506(19)	1.62957(24)	1.61810(26)	1.62013(24)	1.61335(17)	1.61507(26)	1.60643(18)
Ga-O Tetrahedra								
Bond Length (Å)								
GA_O1	1.85440(31)	1.83708(24)	1.84177(27)	1.80496(25)	1.83969(27)	1.81179(18)	1.82020(30)	1.80570(18)
GA_O2	1.82948(27)	1.79841(21)	1.79663(25)	1.79827(27)	1.81323(24)	1.79635(17)	1.80188(26)	1.79820(16)
GA_O3	1.82575(18)	1.80145(14)	1.80357(18)	1.82160(18)	1.82604(17)	1.81264(11)	1.81653(18)	1.80553(11)
GA_O4	1.83574(22)	1.80665(19)	1.81099(24)	1.82568(21)	1.81508(23)	1.80955(15)	1.80978(23)	1.80342(15)
T-O-T Bond Angles (°)								
SI1_O1_GA	140.044(2)	137.699(2)	145.402(2)	177.677(0)	140.385(5)	154.641(2)	145.620(2)	155.098(1)
SI2_O2_GA	118.759(1)	129.680(0)	122.011(0)	116.324(1)	120.144(1)	122.186(1)	123.266(0)	127.632(1)
SI2_O3_GA	141.136(5)	136.366(5)	138.854(5)	137.252(6)	132.717(7)	135.716(4)	138.815(6)	132.846(3)
SI2_O4_GA	133.368(6)	136.270(4)	135.589(4)	143.189(5)	129.270(6)	131.303(4)	138.727(5)	127.221(4)
SI1_O5_SI2	129.367(2)	134.682(3)	133.923(2)	135.960(4)	149.729(2)	135.728(2)	134.459(3)	132.671(1)
Na Environment								
Bond Length (Å)								
NA_O2	2.8427(4)	2.68313(24)	2.73673(30)	2.44302(27)	2.71260(32)	2.48959(18)	2.39318(26)	2.53342(18)
NA_O2	2.16780(24)	2.39327(20)	2.41152(27)	2.40168(28)	2.16493(21)	2.48464(18)	2.39412(26)	2.49467(17)
NA_O3	2.63157(33)	2.48834(27)	2.27225(30)	2.47828(31)	2.4785(4)	2.48866(21)	2.53469(35)	2.61707(21)
NA_O4	2.3832(4)	2.66373(31)	2.50856(35)	2.4669(4)	2.72161(33)	2.39480(23)	2.7752(4)	2.47532(22)
NA_OW1	3.0741(4)	2.83930(26)	2.95101(32)	2.47406(31)	2.45231(25)	2.59695(20)	2.63482(29)	2.43662(18)
NA_OW1	2.00274(24)	2.23402(19)	2.22313(26)	2.23799(24)	2.36678(25)	2.28108(16)	2.35861(24)	2.31612(16)
NA_OW2	2.54237(29)	2.33126(21)	2.49290(27)	2.52533(28)	2.40859(26)	2.54102(18)	2.30684(25)	2.56802(18)
NA_NA	3.5750(6)	3.4974(4)	3.7375(5)	3.5450(6)	3.3850(6)	3.5454(4)	3.4142(6)	3.5229(4)
Bond Angle (°)								
OW1_NA10_OW1	137.3(19)	149.1(13)	135.6(14)	146.565(4)	161.624(2)	146.382(2)	158.821(2)	149.070(2)
OW1_NA10_OW2	77.1(14)	77.0(13)	73.0(15)	70.069(7)	89.527(8)	70.100(5)	73.237(9)	69.940(5)
OW1_NA10_OW2	69.647(10)	75.725(8)	66.106(8)	78.583(9)	72.555(9)	77.939(6)	86.052(10)	79.375(6)

Structural Changes during High Pressure Studies

The contraction and expansion of the Na-GaSi-NAT framework, as a function of pressure, is facilitated by the flexibility of the T-O-T (Si-O-Al for Al-NAT, Si-O-Ga for orthorhombic Na-GaSi-NAT and Si/Ga-O-Si/Ga for tetragonal Na-GaSi-NAT) bond which connects neighbouring fibrous chains. The angle of this flexible bond varies with pressure, according to the respective contraction or expansion response of the system. Changes in this T-O-T angle accompany the pore opening mechanism. The effect this has on pore shape is to decrease the length and increase the width, making the pore much less elliptical.

With this mechanism in mind, examination of the changes in T-O-T bond angle, pore dimensions and chain rotation (Ψ) as a function of pressure should elucidate the behaviour of the orthorhombic Na-GaSi-NAT framework under hydrostatic pressure.

Compression 0-0.906 GPa

From ambient pressure up to 0.906 GPa (phase 1), we see a compression of the unit cell so that the volume and unit cell parameters *a* and *b* decrease with increasing pressure (shown in Figure 13 and Figure 14). During this period, pore width and length remain relatively constant (Figure 16(b) and (c)), although there is a very slight decrease in both pore width and pore length which is easily explained by the overall reduction in cell dimensions with sample compression.

If we assume that the pore shape remains intact and within ambient pressure dimensions during this compression period, we can assume that this is due to a lack of chain rotation and T-O-T bond flex. Figure 16(a) shows a relatively constant (Ψ) chain rotation parameter, which increases very slightly as compression reaches its maximum. Again, this could indicate a very slight closing of the pore during cell compression.

The T-O-T angles (Figure 15) do not show any of the expected signs of cell compression i.e. a fractional reduction in angle as the pore closes down slightly. In fact they show a slight increase, suggesting that the pore is opening slightly. Although the whole framework is being compressed (reduction in cell parameter and pore size reflect this), this angle change suggests that although the pore may be reducing in size it could also be changing shape due to T-O-T deformation. This shape change may account for the fact that, even under cell compression, we see the OW2 site filling. The OW2 site fills progressively from pressures as low as 0.35 GPa (where OW2=0.44) up to 0.906 GPa (OW2=1). Figure 14 shows the pressure dependence of the OW2 site filling and unit cell volume change. See Table 3 for the exact OW2 occupancy at each pressure point.

The chain rotation angle (Ψ) is a two dimensional measurement based only upon changes within the *a*,*b*-plane, whereas the T-O-T angle is a three dimensional measurement. Although an increase in the T-O-T angle and an increase in chain rotation angle may seem very contradictory, the two are similar but separate forms of the framework distortion measurement. This contradictory trend has also been seen in previously reported work by Lee *et. al.*[5], in which a high pressure study of Al-NAT showed an increasing T-O-T angle as well as an increasing chain rotation angle.

To summarise, the application of pressures between 0 and 0.906 GPa to orthorhombic Na-GaSi-NAT induces a unit cell volume reduction and a contraction in the *a*,*b*-plane. The pore reduces in size slightly with the application of pressure (reflected in pore dimensions and in Ψ). The T-O-T angle increases, which may account for increasing OW2 site filling as a function of pressure even though the system is being compressed.

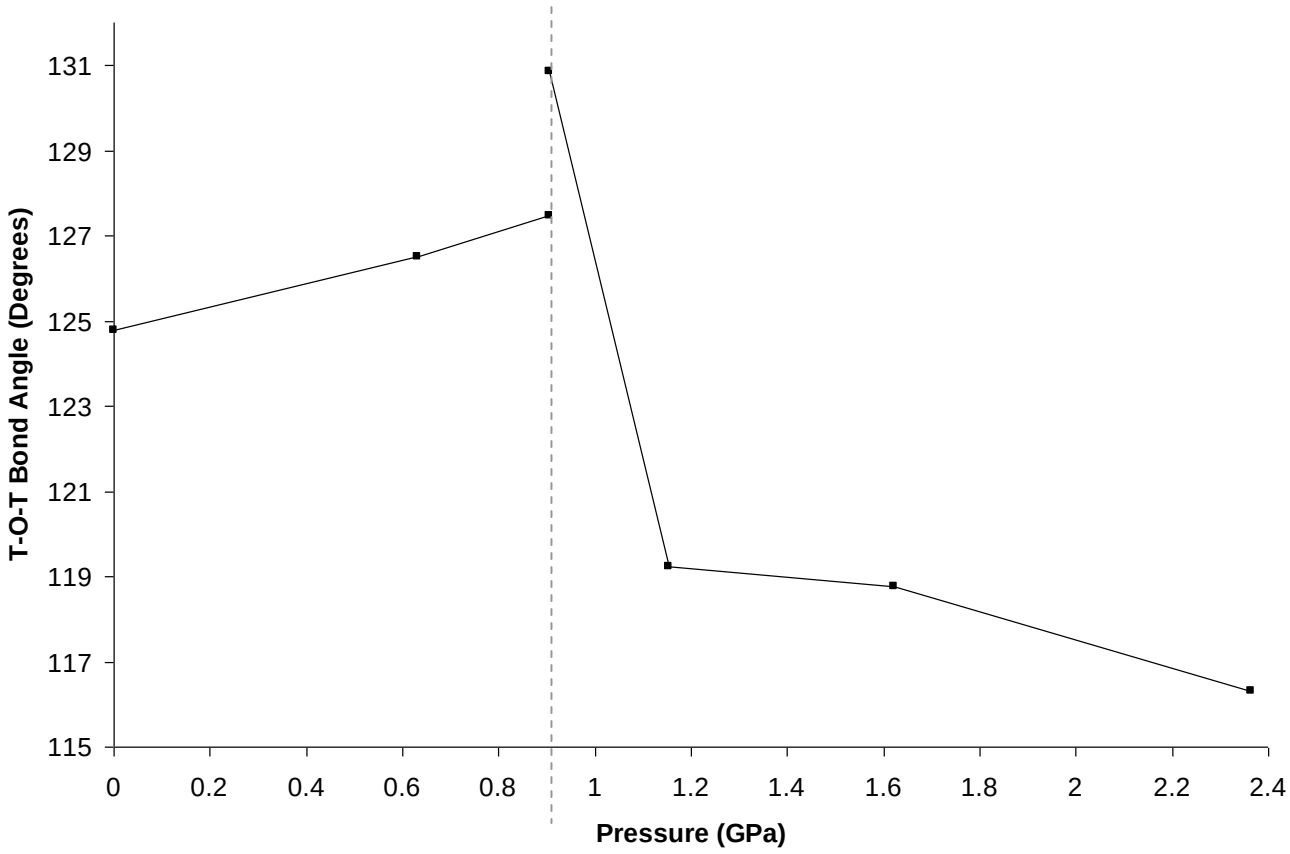

Figure 15: Changes in the T-O-T (Si2-O2-Ga) bond angle as a function of pressure. The grey dotted line indicates the pressure at which the phase transition to the superhydrated form occurs.

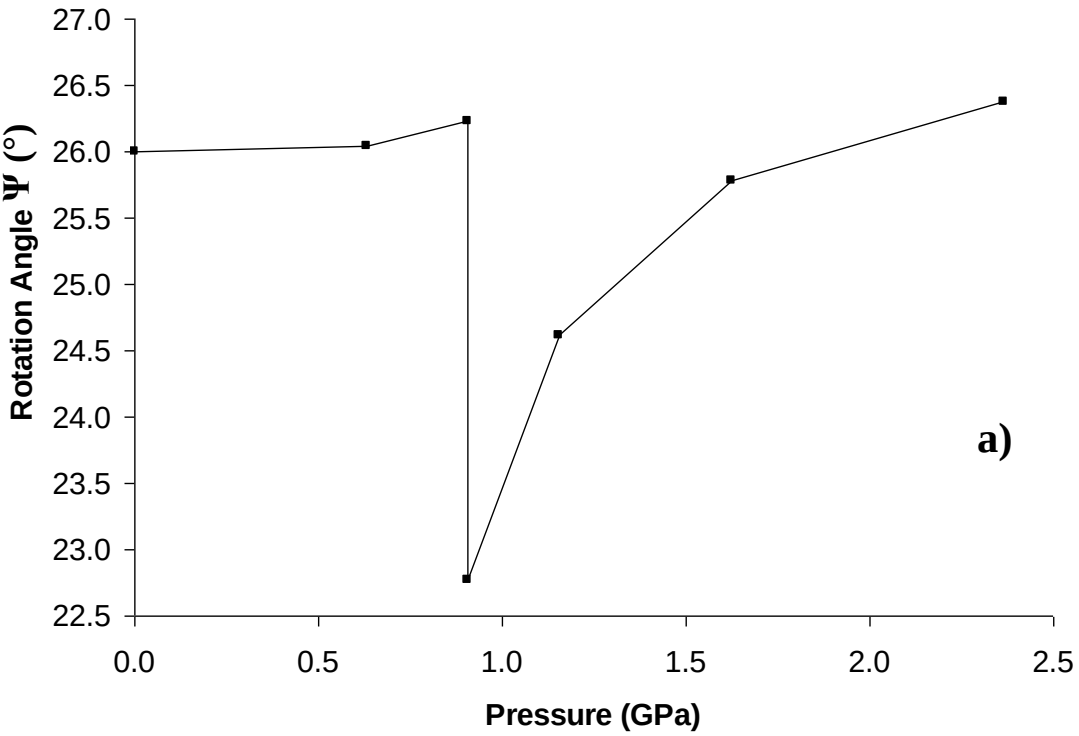
27.0
26.5
26.0
25.5
25.0
24.5
24.0
23.5
23.0
22.5
Rotation Angle Ψ (°)
0.0
0.5
1.0
1.5
2.0
2.5
Pressure (GPa)
a)

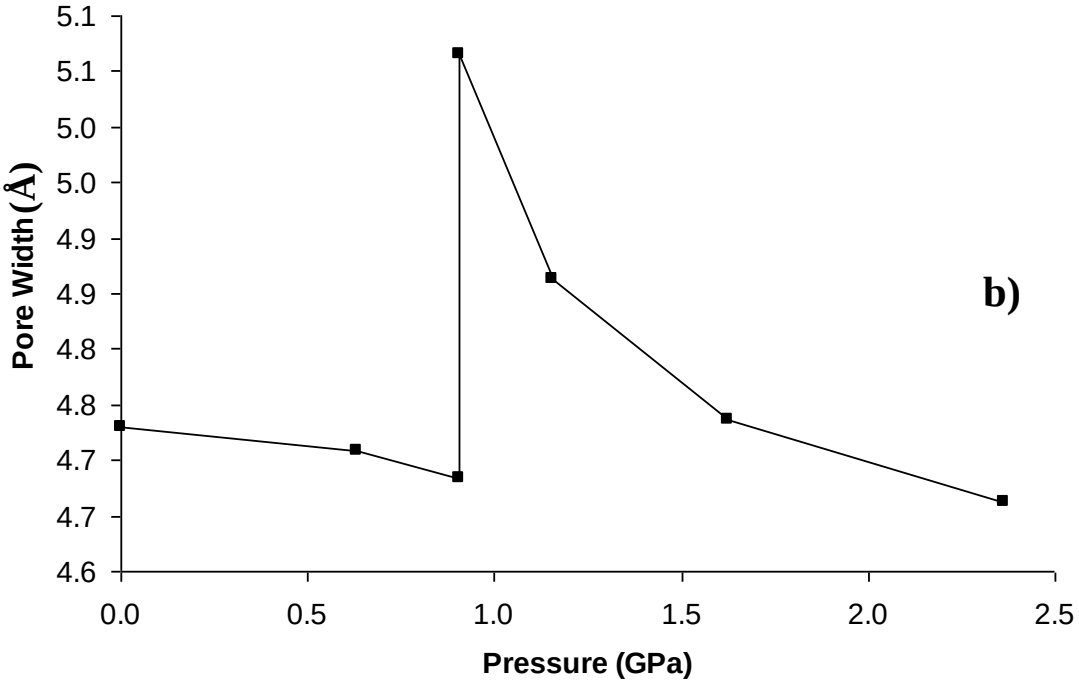
5.1
5.1
5.0
5.0
4.9
4.9
4.8
4.8
4.7
4.7
4.6
Pore Width (Å)
0.0
0.5
1.0
1.5
2.0
2.5
Pressure (GPa)
b)

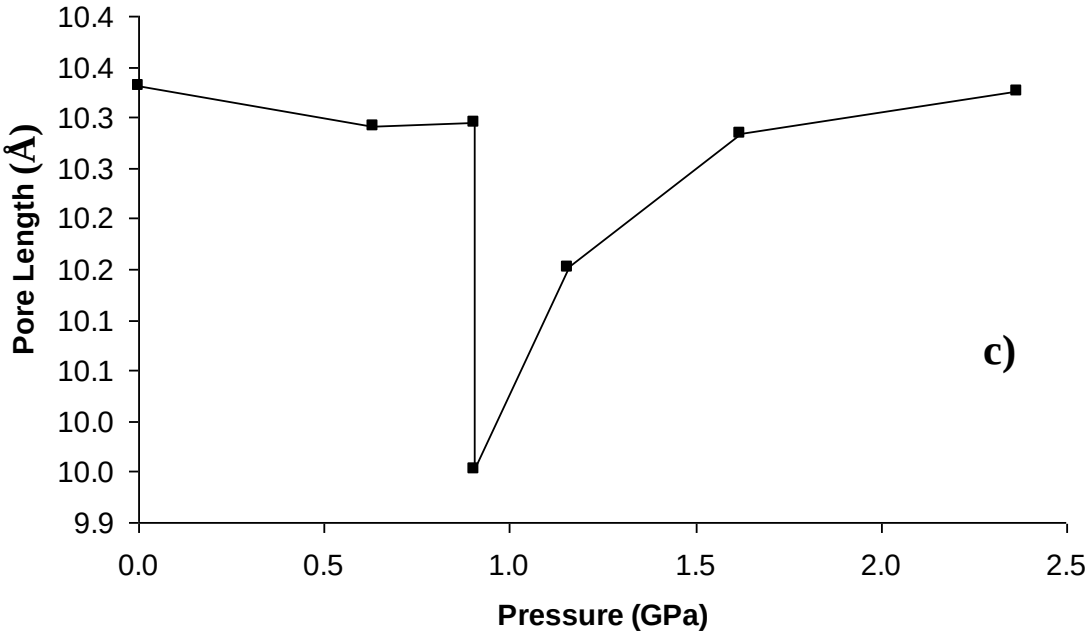

Figure 16: Changes in the pore dimensions and chain rotation angle (Ψ), of orthorhombic Na-GaSi-NAT, as a function of pressure: a) chain rotation angle (Ψ), b) pore width and c) pore length.

Superhydration 0.906 GPa

The most profound effect throughout the whole of the pressure series within this particular study occurs at 0.906 GPa. At this pressure point there is a two phase system, the transition from compressed Na-GaSi-NAT (phase 1), to expanded superhydrated Na-GaSi-NAT (phase 2). From phase 1 to phase 2 there is a sudden increase in cell volume of 2.42% from 2297.2(4) $Å^3$ up to 2311.4(7) $Å^3$, which is greater than the ambient pressure volume (V_0) by 0.619%. As discussed throughout this thesis, pressure-induced cell expansion is always accompanied by a similar change in cell parameters *a* and *b*, along with a pressure-induced hydration by way of OW2 site occupancy increasing to a maximum of 1. These effects were mentioned in an earlier section of this chapter and become particularly import here, when examining the structural changes that accompany this profound change.

During this superhydration step, we see a large and sudden increase in pore width of 8.132% (4.684 Å to 5.065 Å) with a concomitant decrease in pore length of 3.333%, (10.295 Å to 9.952 Å); shown in Figure 16. Cell expansion has caused an increase in pore size by way of a large reduction in elipticity, so that pore width: pore length ratio increases from 0.4549 to 0.5089 (where 1 would be a completely circular pore).

Opening of the pore to a more circular shape is facilitated by rotation of the fibrous chains. It comes as no surprise that we observe a large decrease in chain rotation angle (Ψ), which reduces by 12.858%. Similarly an increase in the T-O-T angle would indicate rotation of the fibrous chains and opening of the pores, this is what we observe here. Figure 15 shows the increase in the T-O-T angle (3.392°, 2.660%) upon superhydration.

Compression of the Superhydrated Phase 0.906-2.365 GPa

Following formation of the superhydrated phase at 0.906 GPa, further pressure increase compresses the newly formed phase. The unit cell volume and cell parameters *a* and *b* are reduced as a function of this pressure increase.

Within this pressure region the OW2 site remains fully occupied, as the superhydrated phase is compressed. With compression comes a decrease in pore width and an increase in pore length as the pore becomes more elliptical. Figure 16 shows smooth (post PIH) curves, demonstrating these trends. In the region 0.906 to 2.365 GPa, pore length increases by 3.757% (9.952 Å to 10.326 Å). Over the same pressure region, pore width decreases by 7.955% (5.065 Å to 4.662 Å).

As described earlier, we would expect compression to involve an increase in chain rotation angle (Ψ), causing the aperture to close down into a more elliptical shape. Facilitating this rotation is a decrease in the T-O-T angle. Figure 15 and Figure 16 show an 11.114% (14.545°) decrease in T-O-T angle as well as a 16.066% increase in Ψ (22.500 Å to 26.115 Å).

Bonding Changes during High Pressure Studies of Orthorhombic Na-GaSi-NAT.

Structural changes within the zeotype framework elucidate details of the mechanism of PIH and PIE. Equally important is understanding what is happening inside the apertures during these framework deformations. As discussed in chapter 4, coordination within the pores could explain the reversibility of the PIH phenomenon.

At ambient pressure there is one crystallographically unique sodium and one unique water oxygen (OW1), but each pore contains two of each related by symmetry. At this pressure, for this particular sample, no OW2 water molecules occupy the pore. Figure 17a shows the bonding within the pore at ambient pressure. Over all pressures, the sodium atoms coordinate with framework oxygens (O2 × 2, O3 and O4) and two water oxygens, OW1. Bridging between Na atoms is via bonding to O2 and OW1, in an alternating zigzag formation.

The OW2 site occupancy is evident at low pressures (0.44 at 0.35 GPa); this occupancy steadily increases up to a maximum of 1 at superhydration. Within this range, the OW2 molecules are held within the pores by hydrogen bonding networks (as discussed in chapter 4). Only when the occupancy of OW2 reaches values close to 1 does any bonding with Na occur, a weak Na-OW2 bond forms (2.73487(22) Å at 0.714 GPa). Addition of the Na-OW2 bond increases the coordination of the Na atom from 6 to 7. This acts to weaken one of the bridging O2 bonds (from 2.36917(13) Å to 2.71498(21) Å) and to weaken the Na coordination to O4 (from 2.54469(20) Å to 2.74849(27) Å). All other Na coordinations remain relatively unaffected at this point.

Upon superhydration the Na atoms become slightly staggered, so that the Na-O4 and Na-O3 are no longer similar in value. Figure 17 shows bonding in the Na environment at ambient pressure and at superhydration. At superhydration the Na-OW2 bond strengthens significantly (2.46415(29) Å). The weakened Na-O2 coordination remains longer than at

ambient pressure, The other Na-O2 coordination that makes up the oxygen bridge between Na atoms, is also weakened at superhydration, so that the two Na-O2 bonds become more evenly coordinated across the bridge. (2.62100(35) Å and 2.57496(28) Å). This is expected, as the pore has undergone dramatic opening. An increase in pore width means that Na and framework O2 are physically distanced. However, at superhydration, OW1 remains relatively static, and so Na-OW1 bridging bonds are not weakened by dimensional changes in the pore (when comparing superhydration bonding to that at 0.714 GPa).

The differences between Na-OW1 and Na-OW2 bonding can be used to explain why superhydration is a reversible process. At superhydration OW2 sites are at full occupancy and are bound by hydrogen bonding networks and a single Na-OW2 bond. The sum of this bonding energy is not enough to stabilise the strained high pressure, expanded state, as upon pressure release the OW2 molecule is ejected from the pore.

At all of the pressures studied here (including ambient), OW1 molecules remain at full site occupancy. OW1 has an advantage over the OW2 position due to Na bonding. Both positions produce various hydrogen bonding networks over a range of pressures (as discussed in chapter 4), but at all pressures including ambient, there are always two Na-OW1 bonds (2.6265(4) Å and 2.24548(25) Å at superhydration). When OW2 is introduced via pressure, only one Na-OW2 bond is made (2.46415(29) Å at superhydration). Energetically the extra Na bond to OW1 far outweighs any extra hydrogen bonding contribution to OW2, so OW1 is energetically much more stable and strongly bound over all pressures including ambient. The weaker bonded OW2 molecule is therefore lost upon pressure release.

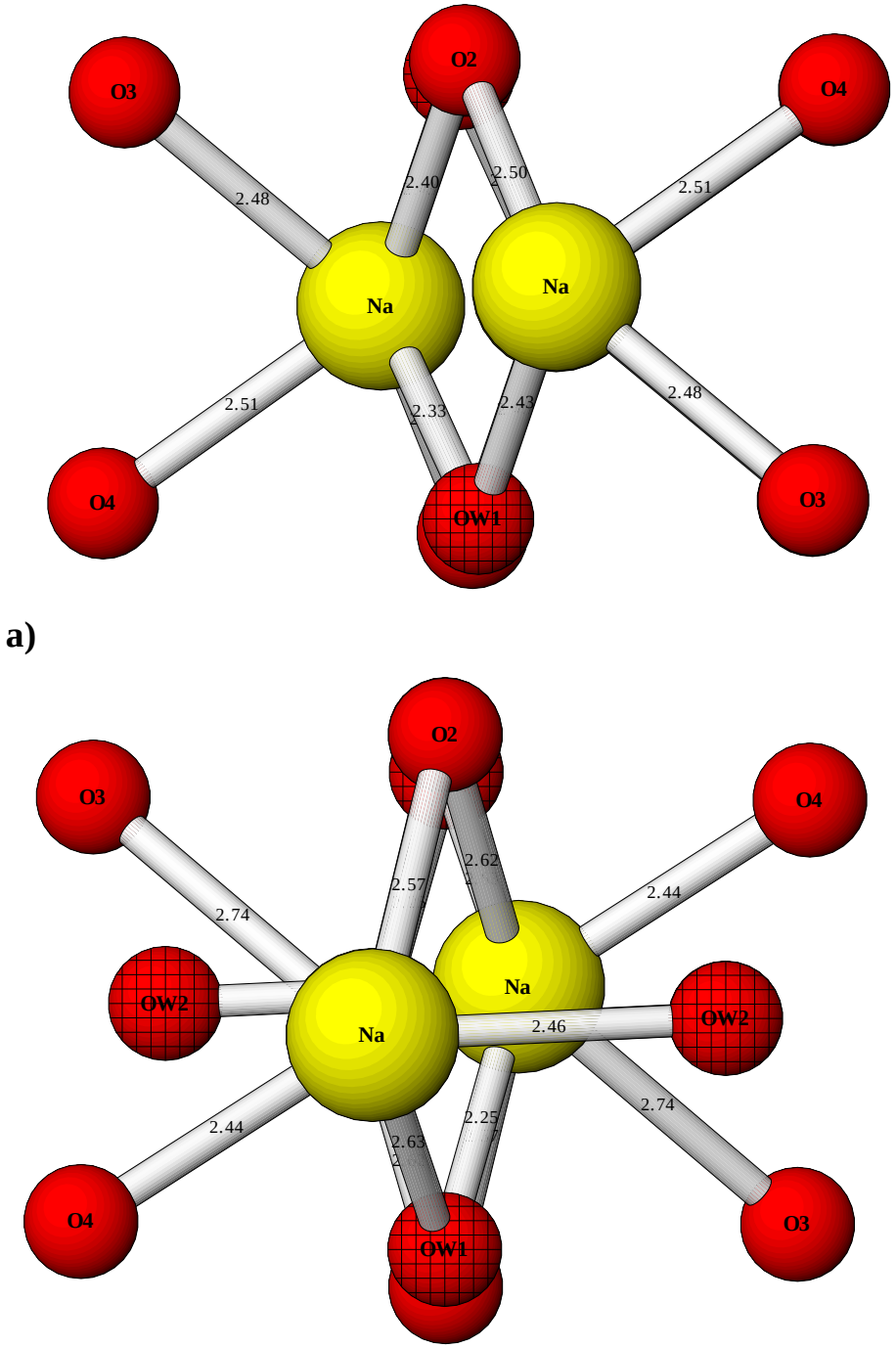

Figure 17: Structural representation of the sodium coordination environment in the *a-b* plane within orthorhombic Na-GaSi-NAT pores: a) ambient pressure model b) superhydrated model. Hatched red spheres are water oxygens and plain red spheres are framework oxygens.

Fitting Equations of State to High Pressure Data

As mentioned earlier in this chapter, the pressure and volume data obtained from the compression of both Na-GaSi-NAT and superhydrated Na-GaSi-NAT can be used to fit equations of state. From this the bulk modulus (K), bulk modulus pressure derivative (K') and an extrapolated zero volume (V_0) can be obtained for each phase. This is particularly valuable for the superhydrated phase, as a value for V_0 cannot experimentally measured due to the reversibility of the pressure-induced hydration step.

The equations of state were calculated using EoSFIT version 5.2.[3] A Murnaghan equation of state was used to fit the data where V_0, K_0 and K' were treated as variables. Other fitting methods, including fixing K' at 4 in a Murnaghan equation or applying a 2nd order Birch-Murnaghan equation gave similar, but poorer fits.

Fortunately, as a good quantity of data points were collected at low pressure for orthorhombic Na-GaSi-NAT, the bulk modulus for the standard phase could also be determined. Similar to the high pressure EoS formulation, a Murnaghan equation of state was used. In this case, refinement of K' gave little variation and so was fixed at 4 (the simplest form of the Murnaghan equation).

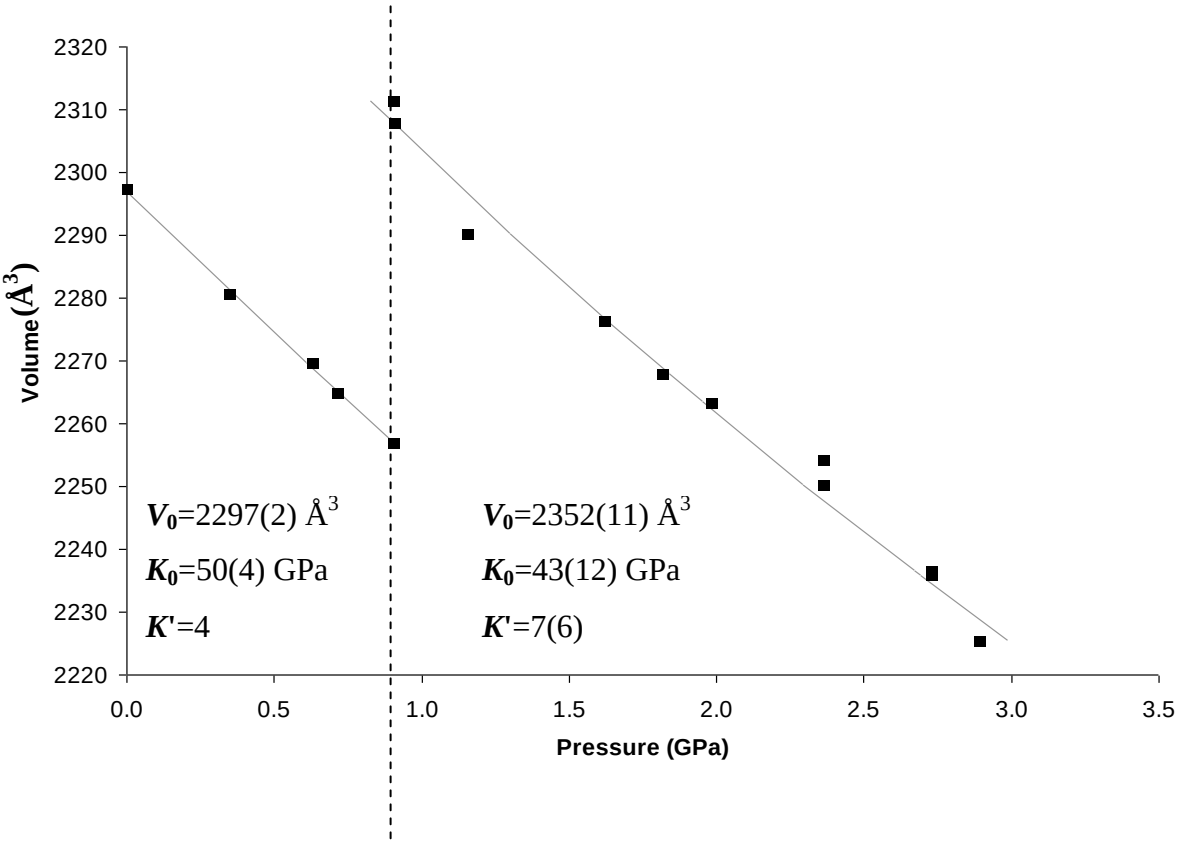

Figure 18: Pressure dependence of the unit cell volume of orthorhombic Na-GaSi-NAT and equation of state fits (solid grey line) for both the low pressure state and the high pressure, superhydrated form. The dashed black line indicates the transition to the expanded/superhydrated form.

The equations of state fitted to the two compression curves are shown in Figure 18. The V_0 calculated by fitting (2297(2) Å^3) is in excellent agreement with the experimental value (2297.2(4) Å^3). The bulk modulus for this fit was calculated as 54(4) GPa. For the superhydrated Na-GaSi-NAT, the refined V_0 value was 2352(11) Å^3. This is a difference of 54.8 Å^3, 2.4% larger than that of the normal, ambient condition phase. This is very similar to the refined value given in the report by Lee *et. al.*[6], 2365(4) Å^3, 58 Å^3 larger than the normal state. The difference in V_0 values calculated for the two phases acts to estimate the extra space required to incorporate OW2 water into the pores. The bulk modulus for the superhydrated phase was refined to 50(18) GPa. This value is identical to that calculated from the X7A data (earlier in this chapter), which gave a bulk modulus for superhydrated orthorhombic Na-GaSi-NAT of 50(12) GPa. Similar values were refined

during the neutron diffraction study of orthorhombic Na-GaSi-NAT, discussed in chapter 4 (V_0= 2389(4) and K_0=49(3)).

The transition between orthorhombic Na-GaSi-NAT and its superhydrated version alters the bulk modulus (54(4) GPa to 50(18) GPa), which indicates that the superhydrated phase has a high compressibility than the ambient pressure form. This trend has been reported in the aluminosilicate analogue, Al-NAT.[5,6] Values before and after PIH are 57(1) GPa and 53(1) GPa, respectively. The similarity in bulk modulus values between the two analogues is expected due to the structural similarities. However, orthorhombic Na-GaSi-NAT shows a slightly lower bulk modulus in each phase. This reflects the more open, flexible framework of orthorhombic Na-GaSi-NAT when compared to Al-NAT due to Al/Ga substitution.

5.3.3.2 Tetragonal Na-GaSi-NAT

High pressure data were collected using a diamond anvil cell from 0-5.10 GPa, inclusive. The experimental set up and specifications are discussed in chapter two. The pressure was increased at small increments for each data collection. At about 5GPa the pressure was released at increments so that pressure release steps were also collected. Raw diffraction patterns are shown in Figure 19. Rietveld refinement of diffraction data was performed using the GSAS suite (EXPGUI). Table 5 gives full listings of atomic coordinates and Table 6 shows selected bond distances and angles for each pressure step. Rietveld refinement profile plots, along with atoms structural schematics at each pressure step can be found in the appendices 1.2.2.2. and 1.3.2.

Upon application of pressure, the changes in cell volume and cell parameters follow the expected pattern, based upon the evolution of a superhydrated/expanded phase. In this experiment, within the pressure range 0-0.727 GPa, cell expansion rather than compression, is observed (Figure 21). This same early expansion pattern was observed in the neutron diffraction study discussed in chapter 4. As with all high pressure, natrolite studies, volume expansion is accompanied by an increase in the *a*- and *b*-axes (Figure 20). This pressure response differs from that of orthorhombic Na-GaSi-NAT, as no initial compression step is observed. The tetragonal framework begins expansion immediately upon pressure application. It is postulated that this early expansion is due to the increased flexibility of the tetragonal framework, when compared to the orthorhombic analogue. Framework flexibility will be discussed in later sections within this chapter.

In contrast to the orthorhombic analogue, tetragonal Na-GaSi-NAT shows OW2 site occupancy at ambient pressures (OW2 occupancy is not observed in orthorhombic Na-GaSi-NAT until 0.35 GPa). Again, this could be to the increased flexibility and larger pore framework of the tetragonal framework. The water site (OW2) is partially filled at ambient pressure (0.323). Occupancy increases regularly, up to a maximum of 1 (0.727 GPa), when full superhydration occurs. At every pressure step, including ambient, we see a Na-OW2 bond. This is very different to the trend observed for orthorhombic Na-GaSi-NAT; where Na-OW2 bonding is not established until the pressure approaches superhydrating values. This agrees well with the neutron diffraction studies

discussed in chapter 4; in which ambient pressure samples contained 0.168 OW2 site occupancy, with superhydration observed at 0.88 GPa. The differences in ambient pressure OW2 content, between that recorded by neutron studies and that recorded in these synchrotron X-ray studies, is due to sample source difference and/or humidity differences at the time of experiment.

At 0.727 GPa the characteristic unit cell volume expansion associated with the formation of a superhydrated phase is at a maximum of 1171.3(14) $Å^3$, (0.873% larger than V_0). There is a concomitant change in the *a*- and *b*-axes which have increased by 0.977% (from ambient values). See Figure 20 and Figure 21 for the pressure dependence of the unit cell volume and parameters. The diffraction pattern (Figure 19) shows clear evidence of significant peak broadening. This particular data set was recorded as one of the pressure release steps, so it is possible that slow kinetics of water release are playing a factor so caution will be used in the interpretation of data from this pressure point.

Following the formation of the superhydrated phase, the unit cell (whilst maintaining full OW2 occupancy), progresses down a compression curve as pressure is increased (from 0.727 to 5.108 GPa). The pressure and volume data obtained from this compression curve can be used to fit an equation of state to the superhydrated phase. In doing so, both the bulk modulus and an extrapolated 'V_0' were obtained as discussed in later sections within this chapter.

The PIH and volume expansion seen in this series of patterns differs somewhat from that observed during neutron diffraction studies upon tetragonal Na-GaSi-NAT. Both experiments show gradual OW2 water filling from low pressure, up to a maximum of 1 where superhydration occurs (at similar pressures in each case). However, the volume expansion due to superhydration, recorded in this study (0.873%), is significantly different from that recorded in the neutron diffraction study (3.757%). There could be many reasons why we observe such a difference. Possibilities include: differences in sample source; slow kinetics of the transition; differences in pressure step values i.e. maximum expansion may only be visible within a very narrow pressure margin; false cell volume data given from an unreliable pattern due to peak broadening.

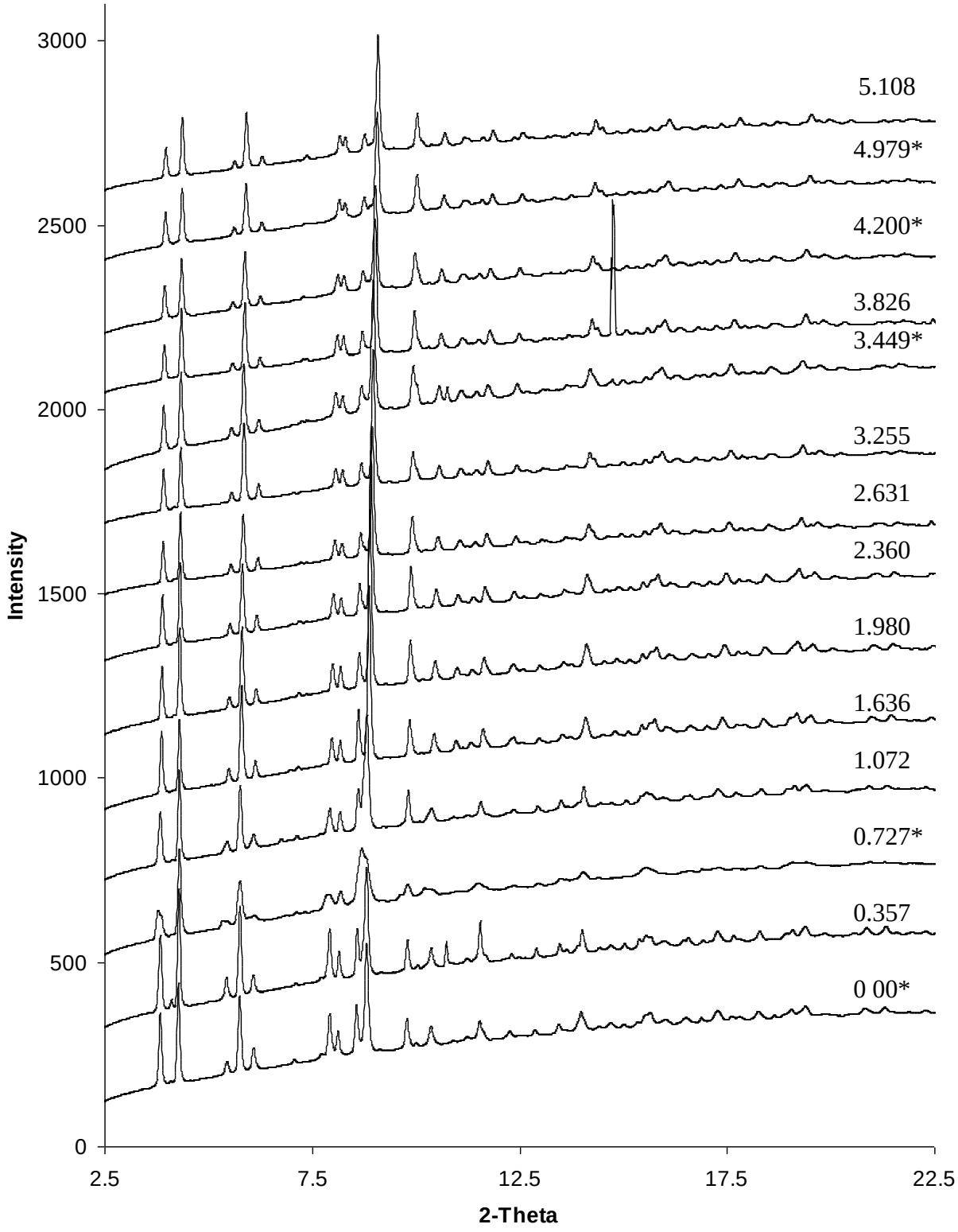

Figure 19: Synchrotron X-ray diffraction patterns collected for tetragonal Na-GaSi-NAT in sequential steps from ambient to 6.210 GPa and back again, data collected during release steps are noted with a *.

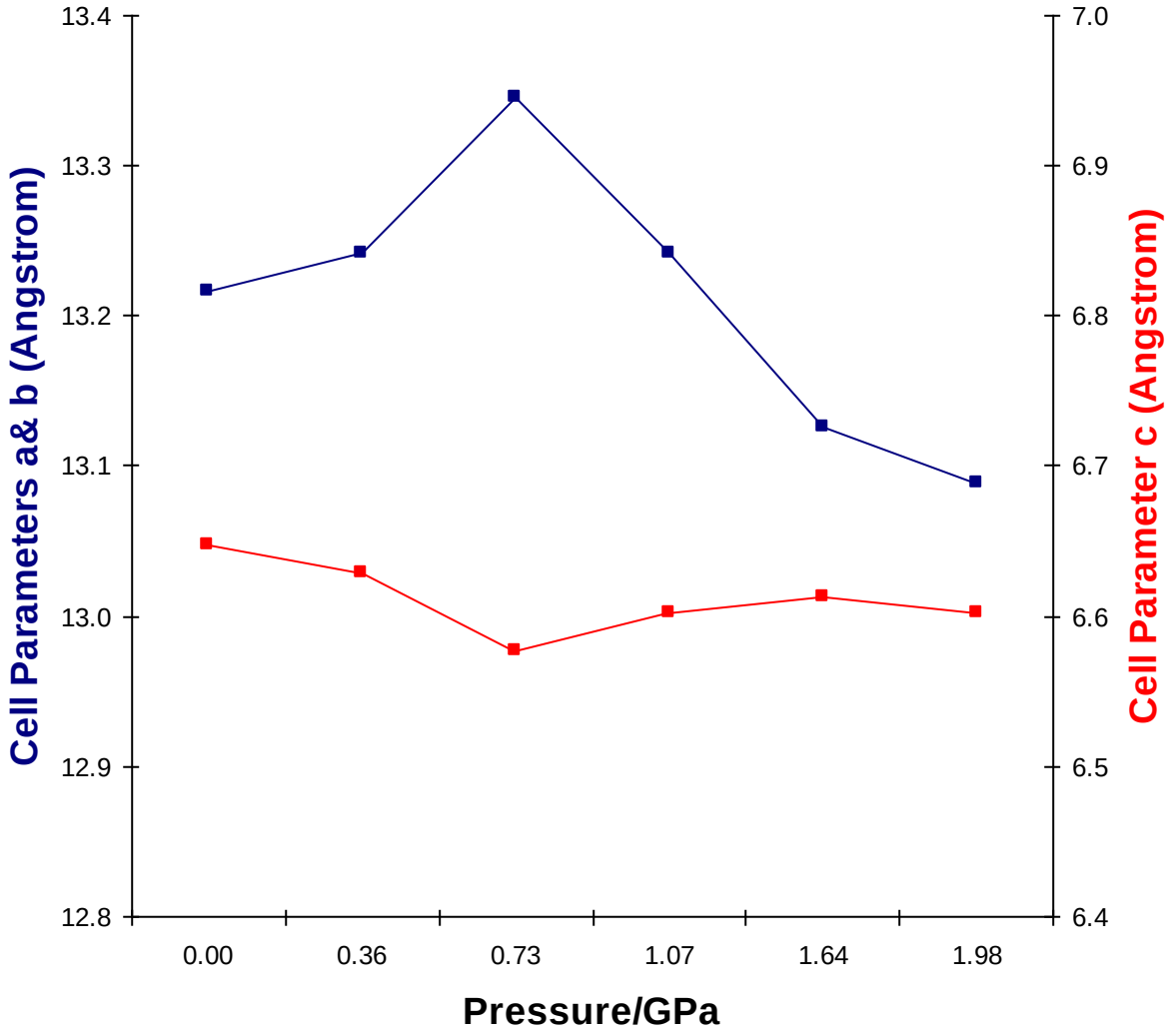

Figure 20: Changes in the unit cell parameters of tetragonal Na-GaSi-NAT as a function of pressure. For clarity, values >2 GPa are not included. Axes *a* and *b* are shown in blue (left scale) and *c* shown in red (right scale).

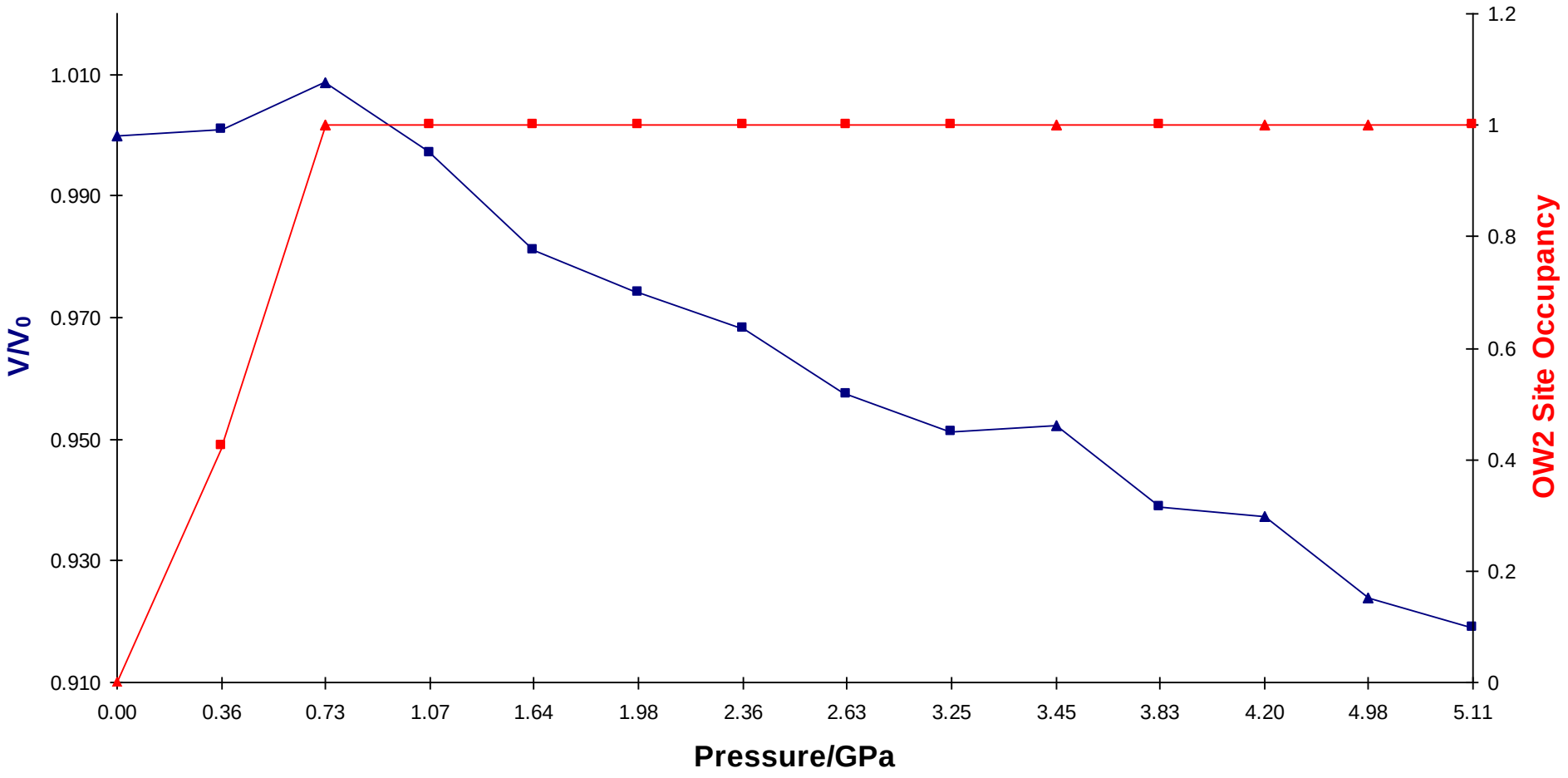

Figure 21: High pressure superhydration and volume expansion of tetragonal Na-GaSi-NAT. Where the blue points are the normalised unit cell volume, V/V_0, and the red points are the OW2 site occupancy. Triangular data points are those collected during pressure release steps.

Table 5: Rietveld refinement atomic coordinates for tetragonal Na-GaSi-NAT (I-42d) over a series of pressures from ambient to 5.10 GPa inclusive.[†] Part A) 0-1.98 GPa, inclusive. Part B) 2.36-5.10 GPa, inclusive

Part A

Reference		tape-4[‡] (gll52 not 58)	17g[§]	2d	16e[§]	3e	4e	5e
Pressure		0.0000	0.0000	0.3567	0.7270	1.0717	1.6360	1.9800
R_{wp}		0.0349	0.0135	0.0222	0.0285	0.0163	0.0200	0.0156
R_p		0.0241	0.0090	0.0134	0.0134	0.0102	0.0158	0.0114
Cell parameters	*a*	13.2422(19)	13.2159(17)	13.2416(21)	13.345(8)	13.242(4)	13.1254(17)	13.0884(15)
	b	13.2422(19)	13.2159(17)	13.2416(21)	13.345(8)	13.242(4)	13.1254(17)	13.0884(15)
	c	6.6574(14)	6.6481(12)	6.6288(15)	6.577(5)	6.6025(27)	6.6126(13)	6.6026(12)
volume		1167.40(33)	1161.16(30)	1162.3(4)	1171.3(14)	1157.7(7)	1139.20(31)	1131.06(27)
T1 (60% Si, 40% Ga) *4a*	*x*	0	0	0	0	0	0	0
	y	0	0	0	0	0	0	0
	z	0	0	0	0	0	0	0
	U_{iso} *100	2.5	2.5	2.5	2.5	2.5	2.5	2.5
T2 (60% Si, 40% Ga) *16e*	*x*	0.0575(10)	0.0599(9)	0.0626(10)	0.0566(20)	0.0509(14)	0.059257	0.0572(7)
	y	0.1331(6)	0.1357(5)	0.1347(6)	0.1348(15)	0.1328(10)	0.136484	0.1341(5)
	z	0.6179(10)	0.6184(8)	0.6200(9)	0.6385(18)	0.6421(15)	0.623912	0.6203(8)
	U_{iso} *100	2.5	2.5	2.5	2.5	2.5	2.5	2.5
O1 *8d*	*x*	0.3902(19)	0.3827(13)	0.3847(17)	0.395(4)	0.4027(29)	0.376461	0.3849(13)
	y	0.25	0.25	0.25	0.25	0.25	0.25	0.25
	z	0.125	0.125	0.125	0.125	0.125	0.125	0.125
	U_{iso} *100	2.5	2.5	2.5	2.5	2.5	2.5	2.5
O2 *16e*	*x*	0.1361(14)	0.1376(11)	0.1312(15)	0.116(4)	0.1201(27)	0.142888	0.1421(11)
	y	0.0532(7)	0.0536(5)	0.0456(6)	0.0311(13)	0.0386(12)	0.055414	0.0550(6)
	z	0.4920(36)	0.4947(31)	0.4892(38)	0.5361(58)	0.5282(48)	0.505579	0.5039(29)
	U_{iso} *100	2.5	2.5	2.5	2.5	2.5	2.5	2.5
O3 *16e*	*x*	0.0523(17)	0.0549(13)	0.0557(17)	0.049(4)	0.0358(27)	0.015743	0.0181(14)
	y	0.0976(10)	0.0958(8)	0.0968(10)	0.1244(18)	0.1338(9)	0.111307	0.1140(4)
	z	0.8651(10)	0.8644(7)	0.8665(10)	0.9167(19)	0.9213(17)	0.863497	0.8677(8)
	U_{iso} *100	2.5	2.5	2.5	2.5	2.5	2.5	2.5
Na *8d*	*x*	0.6913(22)	0.6887(17)	0.6704(20)	0.6624(32)	0.6837(31)	0.696239	0.6967(16)
	y	0.25	0.25	0.25	0.25	0.25	0.25	0.25
	z	0.125	0.125	0.125	0.125	0.125	0.125	0.125
	U_{iso} *100	2.5	2.5	2.5	2.5	2.5	2.5	2.5
OW1 *8d*	*x*	0.1387(29)	0.1253(22)	0.1431(29)	0.197(5)	0.1896(39)	0.13054	0.1370(22)
	y	0.25	0.25	0.25	0.25	0.25	0.25	0.25
	z	0.125	0.125	0.125	0.125	0.125	0.125	0.125
	U_{iso} *100	2.5	2.5	2.5	2.5	2.5	2.5	2.5
OW2 *8d*	*x*	0.8964(83)	0.9118(74)	0.8763(50)	0.897(5)	0.9003(32)	0.892501	0.8917(17)
	y	0.25	0.25	0.25	0.25	0.25	0.25	0.25
	z	0.125	0.125	0.125	0.125	0.125	0.125	0.125
	U_{iso} *100	2.5	2.5	2.5	2.5	2.5	2.5	2.5
	Occ	0.323(43)	0.337(25)	0.4255(39)	1	1	1	1

Part B

Reference		6h	7e	8e	14e§	9d	13e§	12e§	10e
Pressure		2.3600	2.6310	3.2549	3.4490	3.8260	4.1996	4.9790	5.1080
R_{wp}		0.0159	0.0149	0.0150	0.0125	0.0137	0.0109	0.0120	0.0137
R_p		0.0106	0.0108	0.0108	0.0075	0.0095	0.0076	0.0081	0.0095
Cell parameters	*a*	13.0566(17)	12.9986(17)	12.9660(16)	12.9726(20)	12.8967(16)	12.8927(20)	12.8219(20)	12.7927(18)
	b	13.0566(17)	12.9986(17)	12.9660(16)	12.9726(20)	12.8967(16)	12.8927(20)	12.8219(20)	12.7927(18)
	c	6.5952(13)	6.5800(13)	6.5703(13)	6.5705(16)	6.5536(12)	6.5479(16)	6.5262(16)	6.5215(14)
volume		1124.33(30)	1111.78(30)	1104.59(29)	1105.7(4)	1090.02(28)	1088.39(35)	1072.92(35)	1067.27(32)
T1 (60% Si, 40% Ga) *4a*	*x*	0	0	0	0	0	0	0	0
	y	0	0	0	0	0	0	0	0
	z	0	0	0	0	0	0	0	0
	U_{iso} *100	2.5	2.5	2.5	2.5	2.5	2.5	2.5	2.5
T2 (60% Si, 40% Ga) *16e*	*x*	0.0565(9)	0.0558(8)	0.0593(7)	0.0549(9)	0.0564(7)	0.0559(8)	0.0559(9)	0.0550(8)
	y	0.1336(6)	0.1337(5)	0.1365(5)	0.1350(5)	0.1340(5)	0.1349(5)	0.1336(6)	0.1332(5)
	z	0.6201(9)	0.6208(8)	0.6239(8)	0.6212(9)	0.6185(8)	0.6179(9)	0.6180(9)	0.6185(9)
	U_{iso} *100	2.5	2.5	2.5	2.5	2.5	2.5	2.5	2.5
O1 *8d*	*x*	0.3862(17)	0.3839(13)	0.3765(12)	0.3823(13)	0.3813(12)	0.3798(13)	0.3809(13)	0.3809(13)
	y	0.25	0.25	0.25	0.25	0.25	0.25	0.25	0.25
	z	0.125	0.125	0.125	0.125	0.125	0.125	0.125	0.125
	U_{iso} *100	2.5	2.5	2.5	2.5	2.5	2.5	2.5	2.5
O2 *16e*	*x*	0.1399(14)	0.1437(11)	0.1429(11)	0.1424(12)	0.1511(10)	0.1492(11)	0.1503(12)	0.1535(11)
	y	0.0517(7)	0.05342(62)	0.05541(57)	0.0517(6)	0.06061(59)	0.05633(64)	0.05483(67)	0.06350(65)
	z	0.5062(35)	0.5134(32)	0.5056(29)	0.5196(34)	0.5121(30)	0.5198(35)	0.5223(37)	0.5122(35)
	U_{iso} *100	2.5	2.5	2.5	2.5	2.5	2.5	2.5	2.5
O3 *16e*	*x*	0.0158(16)	0.0127(15)	0.0157(14)	0.0165(15)	0.0110(13)	0.0136(15)	0.0099(15)	0.0096(15)
	y	0.1132(4)	0.11445(33)	0.11131(34)	0.1155(4)	0.11444(31)	0.11297(33)	0.11316(31)	0.11563(31)
	z	0.8650(10)	0.8659(8)	0.8635(7)	0.8702(8)	0.8634(8)	0.8631(7)	0.8612(8)	0.8648(8)
	U_{iso} *100	2.5	2.5	2.5	2.5	2.5	2.5	2.5	2.5
Na *8d*	*x*	0.6998(19)	0.6995(17)	0.6962(16)	0.6966(17)	0.6979(16)	0.6994(18)	0.7039(20)	0.7043(19)
	y	0.25	0.25	0.25	0.25	0.25	0.25	0.25	0.25
	z	0.125	0.125	0.125	0.125	0.125	0.125	0.125	0.125
	U_{iso} *100	2.5	2.5	2.5	2.5	2.5	2.5	2.5	2.5
OW1 *8d*	*x*	0.1358(26)	0.1343(24)	0.1305(22)	0.1295(24)	0.1305(22)	0.1267(25)	0.1234(26)	0.1308(25)
	y	0.25	0.25	0.25	0.25	0.25	0.25	0.25	0.25
	z	0.125	0.125	0.125	0.125	0.125	0.125	0.125	0.125
	U_{iso} *100	2.5	2.5	2.5	2.5	2.5	2.5	2.5	2.5
OW2 *8d*	*x*	0.8874(20)	0.8860(19)	0.8925(19)	0.8762(19)	0.8844(19)	0.8833(20)	0.8822(21)	0.8879(22)
	y	0.25	0.25	0.25	0.25	0.25	0.25	0.25	0.25
	z	0.125	0.125	0.125	0.125	0.125	0.125	0.125	0.125
	U_{iso} *100	2.5	2.5	2.5	2.5	2.5	2.5	2.5	2.5
	Occ	1	1	1	1	1	1	1	1

† Weights in parenthesis. Isotropic displacement factors (U_{iso} * 100) were fixed at 2.5 for all models (excluding ambient pressure data collected using mounting tape).

‡ Data collected at ambient pressure, using mounting tape rather than a DAC.

§ Data points collected during pressure release steps.

Table 6: A summary of selected bond distances and angles.

	Pressure (GPa)														
	0	0	0.3567	0.727	1.0717	1.636	1.98	2.36	2.631	3.254	3.449	3.826	4.19	4.979	5.108
T-O Tetrahedra															
Bond Length (Å)															
T1-O3 x4	1.719(5)	1.715(4)	1.723(5)	1.867(7)	1.736(4)	1.72969(19)	1.745(4)	1.738(5)	1.737(4)	1.711(4)	1.737(4)	1.732(4)	1.719(4)	1.715(4)	1.727(4)
T2-O1	1.696(8)	1.691(6)	1.679(8)	1.671(11)	1.682(7)	1.71227(22)	1.696(6)	1.694(7)	1.703(6)	1.691(6)	1.699(6)	1.698(6)	1.701(6)	1.699(6)	1.705(6)
T2-O2	1.705(8)	1.706(6)	1.723(8)	1.733(11)	1.716(7)	1.71741(19)	1.703(7)	1.701(8)	1.701(6)	1.699(6)	1.703(6)	1.695(6)	1.699(6)	1.696(6)	1.692(6)
	1.639(14)	1.678(10)	1.607(11)	1.658(20)	1.578(11)	1.73367(19)	1.684(11)	1.642(13)	1.677(13)	1.715(11)	1.667(12)	1.749(12)	1.715(14)	1.702(15)	1.759(14)
T2-O3	1.713(7)	1.720(5)	1.712(7)	1.838(10)	1.724(6)	1.71620(29)	1.732(6)	1.721(6)	1.726(6)	1.704(5)	1.729(6)	1.727(5)	1.719(5)	1.713(5)	1.722(5)
Bond Angles (°)															
T2-O2-T2	139.5(14)	140.9(12)	148.6(16)	154.(4)	145.0(16)	137.050(2)	135.2(11)	137.1(16)	133.3(13)	137.1(12)	134.9(14)	126.3(11)	128.7(13)	127.2(13)	122.9(11)
T1-O3-T2	136.5(5)	138.0(4)	137.0(5)	112.2(8)	136.5(5)	133.167(4)	129.9(5)	130.4(6)	129.0(5)	133.3(5)	128.8(5)	129.3(5)	131.2(5)	130.1(5)	127.7(5)
T2-O1-T2	131.8(16)	126.6(12)	130.9(16)	134.(4)	133.9(16)	120.956(0)	126.9(11)	127.7(14)	125.2(12)	121.0(11)	122.7(12)	123.6(11)	121.6(11)	123.0(12)	122.5(12)
Na Environment															
Na-O1 × 2	2.612(17)	2.548(11)	2.653(16)	2.794(32)	2.578(15)	2.44662(28)	2.516(12)	2.513(15)	2.483(12)	2.423(11)	2.474(12)	2.450(11)	2.430(12)	2.415(12)	2.410(12)
Na-O2 × 2	2.495(25)	2.455(19)	2.404(22)	2.72(4)	2.576(25)	2.47763(28)	2.482(19)	2.560(22)	2.518(21)	2.449(19)	2.527(21)	2.360(19)	2.447(22)	2.492(23)	2.359(22)
Na-OW1 × 2	2.355(25)	2.477(20)	2.421(24)	2.136(34)	2.378(25)	2.38523(28)	2.323(19)	2.318(22)	2.323(20)	2.363(20)	2.371(21)	2.347(19)	2.373(22)	2.376(23)	2.308(22)
Na-OW2 × 2	2.72(11)	2.95(10)	2.73(7)	3.13(8)	2.73(4)	2.57603(33)	2.552(31)	2.45(4)	2.425(32)	2.545(32)	2.329(31)	2.404(31)	2.372(34)	2.29(4)	2.35(4)
Na-Na	3.673(25)	3.698(20)	3.927(29)	4.03(5)	3.661(26)	3.5949(6)	3.584(16)	3.549(18)	3.543(17)	3.569(16)	3.565(17)	3.541(16)	3.525(18)	3.471(17)	3.464(17)
OW1-Na-OW1	141.5(14)	141.8(11)	128.4(13)	113.7(21)	141.1(15)	145.585(4)	145.1(10)	147.1(12)	147.2(11)	145.7(10)	146.0(11)	146.8(10)	148.1(12)	151.2(12)	150.6(12)
OW1-Na-OW2	70.7(7)	70.9(5)	64.2(7)	56.8(10)	70.6(7)	72.792(2)	72.5(5)	73.6(6)	73.(6)	72.8(5)	73.0(5)	73.4(5)	74.0(6)	75.6(6)	75.3(6)

As discussed earlier, the contraction and expansion of the Na-GaSi-NAT framework as a function of pressure is facilitated by the flexibility of the T-O-T bond which connects neighbouring fibrous chains. The angle of this flexible bond varies with pressure, according to the respective contraction or expansion response of the system. Changes in this T-O-T angle accompany the pore opening mechanism. With this mechanism in mind, examination of the changes in T-O-T bond angle, pore dimensions and chain rotation (Ψ) as a function of pressure are important.

Expansion 0-0.727 GPa

From ambient pressure up to 0.727 GPa, we see a progressive expansion of the unit cell so that the volume and cell parameters *a* and *b* increase with pressure as shown in Figure 20 and Figure 21. During this period the pore width progressively increases by a total of 5.072% and the pore length decreases by a total of 2.248%, so that the pore becomes more open and less elliptical. The ratio of pore width : pore length increases from 0.471 Å to 0.506 Å (where 1 is fully circular). At the point of superhydration (0.727 GPa), the pore length reaches a minimum of 10.032 Å and pore width reaches a maximum of 5.077 Å. Figure 23 shows the pressure dependence of pore width and length. The percentage changes in pore dimension are approximately half of that observed for neutron diffraction studies. This makes sense, as in this study, we only see approximately one quarter of the total volume expansion compared to that observed in the neutron diffraction data.

If the pore dimensions have changed with pressure, then we can assume with some certainty that the chain rotation angle (Ψ) as well as the T-O-T bond angle (which links the fibrous chains in the *a*,*b*-plane), have also changed in a similarly progressive format. This is exactly what we observe. Figure 23 shows the gradual decrease in Ψ, representing the increasing chain rotation as the pore/unit cell expands with pressure. From ambient pressure up to the superhydrating pressure point (0.727GPa), Ψ decreases by 9.387% to a minimum of 22.78° (~½ the percentage change seen in the neutron study). Similarly, the T-O-T angle shows an increase which reflects the expansion and opening of the pores,

leading up to a maximum (134.(4) °, 5.845%), at full PIH. Figure 22 shows the pressure dependence of the bridging T-O-T bond angles.

The increase in the T-O-T angle and the decrease in the chain rotation angle prior to the superhydration point means that filling of the OW2 site is particularly favourable for the tetragonal form of Na-GaSi-NAT. Hence, OW2 water is present even under ambient conditions. At ambient pressure, the pores are more open/much less elliptical than that seen in the orthorhombic form; the width/length ratio is 0.471 versus 0.457. This becomes exaggerated with pressure application, so that expansion and increased OW2 intake is established immediately, reaching full PIH and maximum expansion at very low pressures. Since the only structural difference between the two forms is the ordering of the T sites (ordered in the orthorhombic form and disordered in the tetragonal form), we can assume that disordering across the T sites yields a more flexible, open framework. This difference is most likely due to the effects of T atom disordering upon the flexibility in the T-O-T bridging bond angle.

To summarise, the application of pressures between 0 and 0.727 GPa induces a cell volume increase and an expansion in the *a*,*b*-plane (where a contraction is seen in orthorhombic Na-GaSi-NAT within this range). The pores increase in size with the application of pressure; there is an increase in the T-O-T angle with a simultaneous decrease in Ψ. The OW2 site filling begins from ambient pressure, with immediate onset of expansion upon pressure application. This response is due to the increased flexibility seen in the tetragonal, compared with orthorhombic, gallosilicate framework.

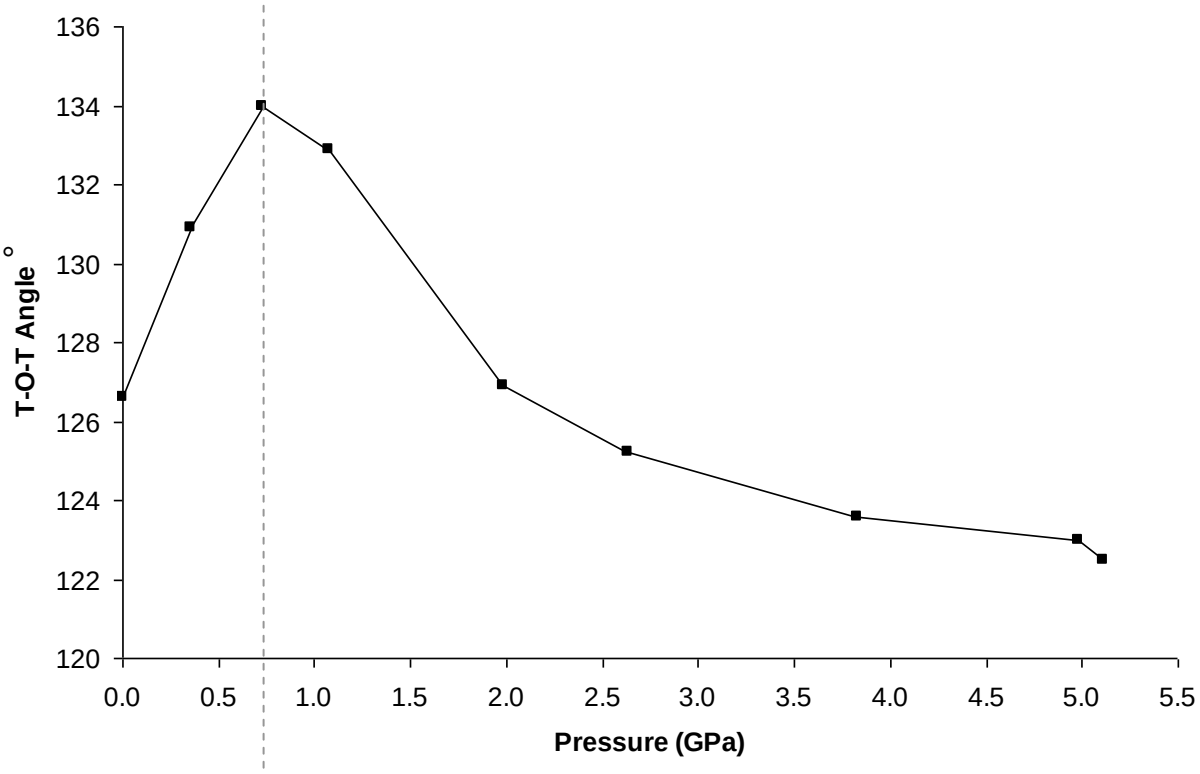

Figure 22: Changes in the T-O-T (T2-O1-T2), bond angle as a function of pressure. The grey dotted line indicates the pressure at which phase transition to the superhydrated form occurs.

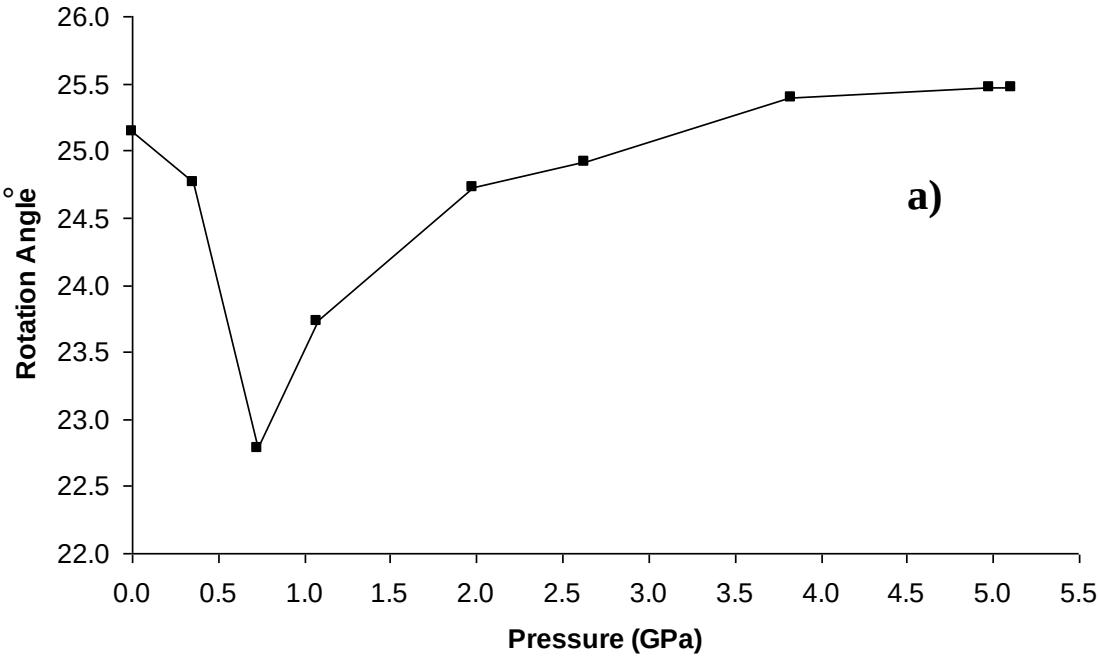
26.0
25.5
25.0
24.5
24.0
23.5
23.0
22.5
22.0
Rotation Angle°
a)
0.0 0.5 1.0 1.5 2.0 2.5 3.0 3.5 4.0 4.5 5.0 5.5
Pressure (GPa)

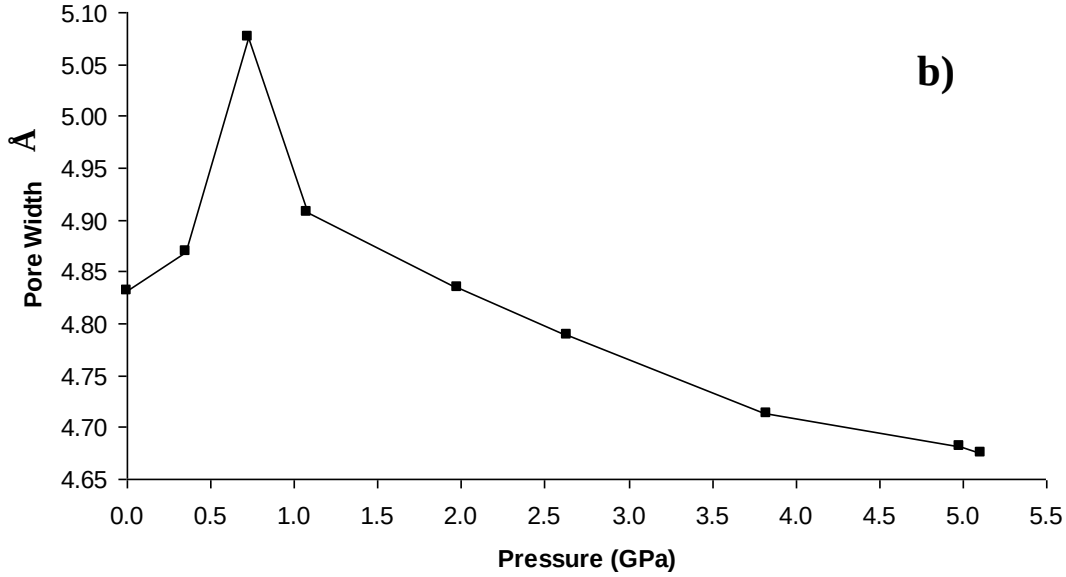
5.10
5.05
5.00
4.95
4.90
4.85
4.80
4.75
4.70
4.65
Pore Width Å
b)
0.0 0.5 1.0 1.5 2.0 2.5 3.0 3.5 4.0 4.5 5.0 5.5
Pressure (GPa)

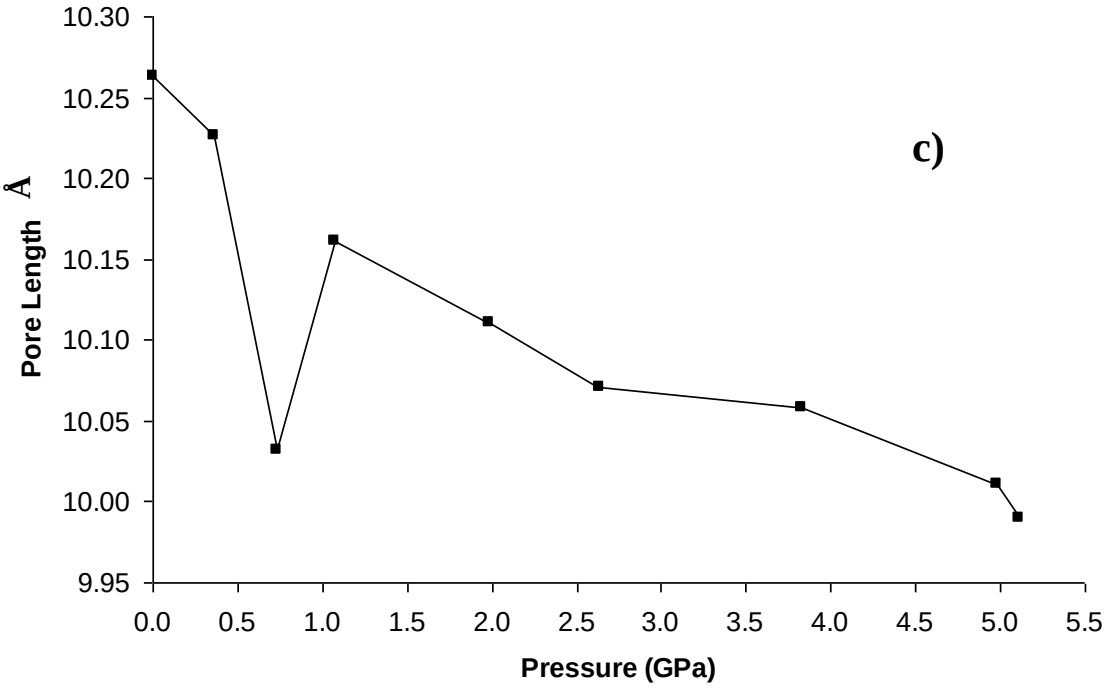

Figure 23: Changes in the pore dimensions and chain rotation angle (Ψ) of tetragonal Na-GaSi-NAT as a function of pressure: a) chain rotation angle (Ψ), b) pore width and c) pore length.

Compression of the Superhydrated Phase from 0.727-5.108 GPa

Following formation of the superhydrated phase at 0.727 GPa, further pressure increase compresses the newly formed phase. The unit cell volume and *a* and *b* parameters are reduced as a function of this pressure increase. Within this pressure region the OW2 site remains fully occupied, as the superhydrated phase is compressed.

With compression comes a decrease in pore width and an increase in pore length as the pore becomes more elliptical (Figure 23). The pore width shows a relatively smooth (post PIH) decrease; from 0.727 to 5.108 GPa it decreases from 5.077 Å to 4.675 Å, a total of 7.909%. The changes in pore length (post PIH) deviate slightly from that expected, initially it increases by 1.289% in the step immediately after PIH followed by a slight, but continuous, decrease in pore length towards higher pressures as values plateau.

As described earlier, we would expect compression to involve an increase in chain rotation angle (Ψ). Facilitating this rotation is a decrease in the T-O-T angle. Figure 22 shows a smooth, steady decrease of 8.582% in T-O-T angle (post PIH). Figure 23 shows an increase in Ψ of 11.809% (post PIH), which plateaus at high pressures.

Bonding Changes during High Pressure Studies of Tetragonal Na-GaSi-NAT.

Structural changes within the framework can elucidate details of the mechanism of expansion and superhydration. Equally important is understanding what is happening inside the apertures during these framework deformations. As discussed in chapter 4 and earlier in this chapter, coordination within the pores could explain the reversibility of the PIH phenomenon.

At ambient pressure each pore contains two sodium atoms, two water molecules at full occupancy (OW1), and two water molecules at partial occupancy (OW2 at 0.337(25)). At all pressures, including ambient, tetragonal Na-GaSi-NAT contains OW2 water molecules, unlike the orthorhombic analogue which only contains OW2 once pressure is applied. Figure 24 shows the bonding within the pore at ambient pressure. Over all pressures, the two sodium atoms coordinate with framework oxygens (O1 and O2) and the oxygens in both water molecules, OW1 and OW2. The ambient pressure model contains strong Na-OW1 bonds (2.477(20) Å), with weaker Na-OW2 bonds (2.95(10) Å). Bridging between the Na atoms is via bonding to O1 and OW1, in an alternating zigzag formation. This format is very similar to the bonding observed in the orthorhombic analogue. A key difference between the two is Na-OW2 bonding under ambient conditions. Over all pressure including ambient, tetragonal Na-GaSi-NAT has a Na-OW2 bond, where orthorhombic does not establish Na-OW2 bonding until pressures approach the point of superhydration. The increased symmetry in the tetragonal form forces eight coordinations around each sodium, compared to seven coordinations in the orthorhombic form. The site occupancy of sodium-bound OW2 increases with pressure up to a maximum of one at superhydration (0.727 GPa). After superhydration, bonding between Na and framework oxygen O2 weakens slightly by increasing in length from 2.455(19) Å (ambient) to 2.576(25) Å (1.0717GPa). As the pore opens Na and O2 become further apart. Similarly, Na and O1 become distanced as the pore opens. This is reflected in the bridging bond distances increasing slightly from 2.548(11) Å to 2.578(15) Å.

Water molecules remain relatively static within the pore during expansion of the unit cell, as they are not part of the framework. Bonding from Na to OW1 strengthens (when other Na-O are weakened), as pore expansion does not cause an increased distance between the Na and the OW1 water molecule. Bonding between these two strengthens from 2.477(20) Å to 2.378(25) Å (from ambient to 1.0717 GPa). Similarly, the OW2 water molecule, which is not part of the framework, is not distanced from Na following superhydration. When other Na to framework oxygen bonds are lengthened, Na-OW bonds strengthen. In this case Na-OW2 shortens from 2.95(10) Å to 2.73(4) Å.

As discussed earlier, differences between Na-OW1 and Na-OW2 bonding can be used to explain why superhydration is a reversible process. At superhydration OW2 sites are at full occupancy and are bound by hydrogen bonding networks and a single Na-OW2 bond (2.73(4) Å). The sum of this bonding energy is not enough to stabilise the strained high pressure, expanded state, and upon pressure release the OW2 molecule in ejected from the pore. Conversely, the OW1 molecule remains over all pressures. The presence of OW1 is energetically favourable due to the two bridging Na-O bonds formed. The sum of these two strong bonds (2.378(25) Å) exceed any of the bonding energy contribution from OW2 and is therefore always stable inside the pore.

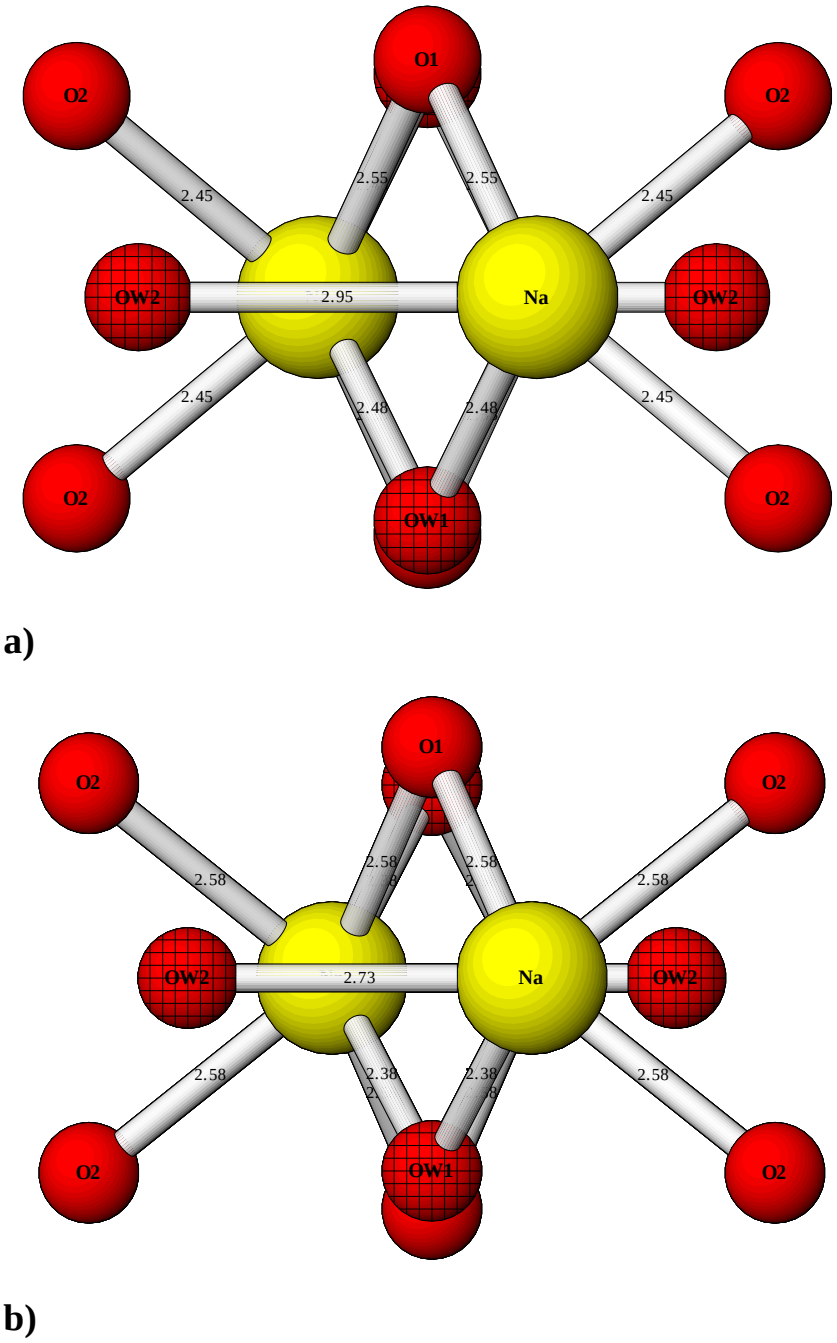

Figure 24: Structural representation of the sodium coordination environment in the *a-b* plane within tetragonal Na-GaSi-NAT pores: a) ambient pressure model and b) superhydrated model.[*] The hatched red spheres are water oxygens and plain red spheres are framework oxygens.

[*] Model used is for the pressure point 1.0717 GPa rather than 0.727 GPa (as this data is more reliable).

Fitting Equations of State to High Pressure Data

As mentioned earlier in this chapter, the pressure and volume data obtained from the compression of Na-GaSi-NAT (tetragonal) and superhydrated Na-GaSi-NAT (tetragonal), can be used to fit equations of state. From this the bulk modulus (K_0), pressure derivative (K') and an extrapolated 'V_0' can be obtained. This is particularly valuable for the superhydrated phase, as a value for V_0 would not be possible to collect experimentally (due to the reversibility of the pressure-induced hydration step).

The equations of state were calculated using EoSFIT version 5.2.[3] A Murnaghan equation of state was used to fit the data where V_0, K_0 and K' were treated as variables. Other methods, including fixing K' at 4 in a Murnaghan equation or applying a 2nd order Birch-Murnaghan equation gave similar, but poorer fits.

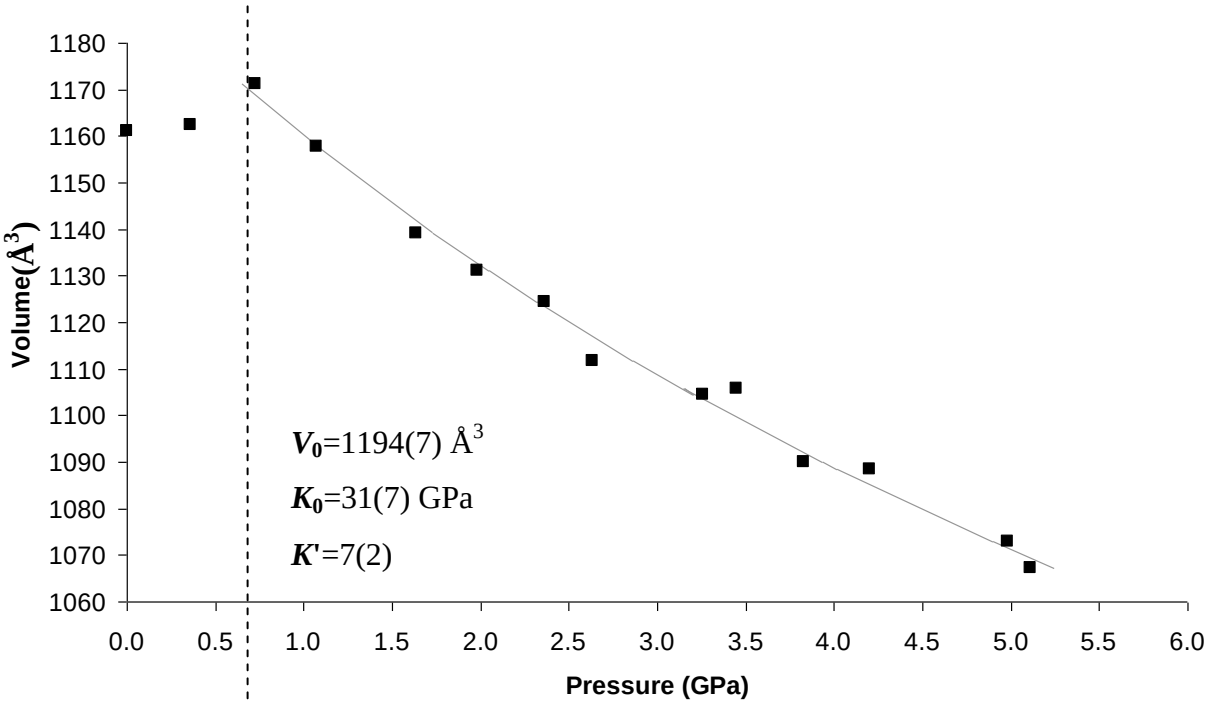

Figure 25: Pressure dependence of the unit cell volume of tetragonal Na-GaSi-NAT and the equation of state fit (solid grey line), for the high pressure, superhydrated form. The dashed black line indicates the transition to the expanded/superhydrated form.

The fit to the data (Figure 25) produced a refined V_0 value for the superhydrated phase of 1194(7) Å^3. This is a difference of 32.8 Å^3, 2.8% larger than that of the normal, ambient condition phase (as measured experimentally). The bulk modulus, 38(9) GPa, is larger than the values calculated in neutron diffraction work (23(3) GPa). This is unsurprising as we did not see as great a cell expansion in this study compared to the neutron diffraction study, so the compression gradient is not as steep.

The difference in V_0 values between the two phases gives an estimate of the extra space required to incorporate OW2 water into the pores. However, we must remember that this particular study did not yield the full high pressure expansion expected for the tetragonal phase (for reasons discussed earlier in this chapter), and so data interpretation is with caution. For example, the V_0 increase is expected to be much greater than that observed for the orthorhombic gallosilicate analogue, as the tetragonal framework is more open

and flexible. In this case only a very small difference in the change in V_0 is seen between the two analogues, as full expansion was not achieved. Conversely, the neutron diffraction study of tetragonal Na-GaSi-NAT shows the expected trend, where the difference in V_0 between phases (8.1%), is significantly larger than that recorded for the orthorhombic version.

5.3.3.3 Quality of Data

Experiments performed at the 9.5 HPT beamline, Daresbury, gave data of sufficient quality to refine the crystal structure, including inner-pore water positions and occupancy. In the previous, Le Bail refined data (collected from X7a, Brookhaven); no structural information was obtained other than cell parameters and volume. In theory the ambient pressure run performed on X7a should have given better quality data as collection was from a rotating capillary rather than mounting tape. Data collection from a rotating capillary gives excellent orientational averaging. However, the ambient data from 9.5 HPT, Daresbury is clearly much better. This is due a 360 degree/2 dimensional data collection from a Mar345 image plate as well as the advantages that come with the FIT2d software. Data collection at X7a was via a psd detector, which gives a '1 dimensional slice' from the diffraction rings, rather than the full 360 degree image. As we saw in the diffraction image shown in Figure 9, gallosilicates (despite intense grinding), give a very spotted pattern due to the glass-like texture of the sample. When using a psd detector, a slice of this spotted data will give poor structure averaging. During the high pressure runs, it may also include any spots or reflections produced from ruby chips or the diamond within the anvil. The differences in the data detection methods means that the X7a data was unrefinable (even at ambient pressure where we benefit from rotary capillary collection), whereas the 9.5HPT data gave full structural resolution via a good Reitveld refinement fit.

5.4 Conclusions

Synchrotron X-ray diffraction experiments from this chapter compare well to the neutron diffraction experiments in chapter 4. Both show superhydration and pressure-induced expansion in both gallosilicate natrolites. Synchrotron X-ray experiments allowed a greater number of pressure points in the high pressure series, with smaller pressure increments. This allowed for a more detailed picture of the superhydration process in orthorhombic and tetragonal gallosilicate which occurs at 0.909 and 0.727 GPa respectively. These superhydration pressure values reflect the nature of the framework. Lower pressure onset values are seen in the tetragonal compared to the orthorhombic form. This is due to an increase in framework flexibility as a result of disordering of the T atom sites. Other measurements including pore dimensions, T-O-T bond flex, and bulk modulus support this (larger pores, more flexible T-O-T bridging bonds and a lower bulk modulus).

Data quality was improved when using the 9.5HPT compared to X7a beamline. Improved data was via use of an improved sample preparation technique, use of a MAR345 image plate (compared to a psd detector) and use of Fit2d software.

[1] Evans Jr. H. T.; Konnert J. A.; Ross M. 'The crystal structure of tetranatrolite from Mont Saint-Hilaire, Quebec, and its chemical and structural relationship to paranatrololite and gonnardite' **2000**. *American Mineralogist. 85.* 1808-1815.

[2] Lee Y.; Hriljac J. A.; Parise J. B.; Vogt T. 'Pressure-induced stabilisation of ordered paranatrolite: a possible solution to the paranatrolite controversy' **2005**. *American Mineralogist. 90(1).* 252-257.

[3] Angel R. J., 'Equations of State, High-Pressure, High-Temperature Crystal Chemistry' **2000**. *Reviews in Minerology and Geochemistry*. 41.

[4] Lee Y.; Hriljac J. A.; Kim S. J.; Vogt T.; Hanson, J. C. 'Pressure-induced hydration at 0.6 GPa in a synthetic gallosilicate zeolite' **2003**. *J. Am. Chem. Soc. 125*. 6036-6037.

[5] Lee Y.; Hriljac J. A.; Kim S. J.; Vogt T.; Parise J. B.; Artioli G. 'Pressure-induced volume expansion of zeolites in the Natrolite family' **2002.** *J. Am. Chem. Soc. 124.* 5466-5475.

[6] Lee Y.; Hriljac J. A.; Parise J. B.; Artioli G.; Vogt T. 'First structural investigation of a super-hydrated zeolite' **2001**. *J. Am. Chem. Soc. 123*: 12732-12733.

CHAPTER SIX

Hydrothermal Ion Exchange in Natrolite and Gallosilicate Natrolite

6.1 Introduction

In this part of the thesis work we wish to exploit the pressure-induced expansion seen in aluminosilicate and gallosilicate natrolite for ion exchange purposes.[1,2,3,4] Whilst under pressure, in the expanded state, it may be possible to insert cations into the pores, which at ambient pressures would not exchange into the structure. Since this pressure-induced expansion is reversible, we expect to trap any exchanged material in the structure upon pressure release. Any high pressure ion exchanged cations can only be described as 'trapped' if they remain within the framework after the sample is exposed to a back-exchange sequence (e.g. conc. NaCl(aq) solution, reflux, 24 hours). In order to find cations appropriate to this kind of high pressure exchange, a series of ambient/hydrothermal ion exchanges were performed. Any cations which can be exchanged and then back-exchanged in this manner will not be suitable for high pressure ion exchange experiments. Cations of interest include: Rb^{+}, Sr^{2+}, Cs^{+}, Ba^{2+} and Cd^{2+}. In particular the strontium, cesium and cadmium ions are of interest. Successful high pressure trapping of these cations could offer a relevant form of nuclear waste immobilisation. Full experimental details for these experiments are given in chapter 2.

A small number of reports have been published which document cation ion exchange of natrolite, none of which include the use of high pressure trapping. [5,6,7,8,9,10,11] These reports include low, partial exchange of Li^{+}, K^{+}, Ti^{+}, NH_4^{+}, Hg^{2+}, Cd^{2+}, Zn^{2+}, Ba^{2+}, Ni^{2+} and Co^{2+}. All of the reported exchange methods require forcing conditions. To date, ion exchange of cesium, rubidium or strontium into any natrolite form has not been reported. A report in the Indian Chemistry Society Journal describes ambient pressure, mild temperature ion exchange with Cd(II). Samples of aluminosilicate natrolite were heated at 60°C with shaking in a saturated cadmium(II) sulfate solution for 50 days.[5] Analysis of the exchanged samples included TGA and PXRD evaluation. In thermal studies, weight loss from each exchanged sample was recorded. This weight loss could be attributed to surface cation loss and or some decomposition. Although these results definitely suggest possible surface absorption, it is unclear whether pore ion exchange has occurred in this

instance. In order to investigate these reports a repeat of this work was performed using Cd(II). The two gallosilicate forms, as well as the reported Al-NAT, were used in these experiments. Results showed no evidence of exchange, by means of PXRD and SEM EDX analysis.

There are a few reports of successful exchange of Na-NAT using smaller cation species including Li, K and NH_4. Use of a NH_4NO_3 melt (16 days at 463K) by Stuckenschmidt *et. al.* shows NH_4 exchanged Na-Aluminosilicate natrolite.[12] A comprehensive structural refinement and comparison of unit cell parameters of the reported exchange and the standard Na-NAT, show strong evidence of successful pore cation exchange (Table 1). A K-NAT form can be produced by using KCl solution at 60 °C for 60 days. Extensive structural, thermal and kinetic studies have been performed by Yamazaki *et. al.*[7,8,9,10] This K^+ exchanged form was first reported by Baur in 1990, along with a Li-exchanged form.[6] Table 1 shows a summary of the refined cell parameters and volumes of exchanged natrolite for comparison with Na-NAT. For larger species, particularly divalent cations, exchange is partial, with exchange levels as high as 35% (Ag^+) and as low as 2% (Co^{2+}). Reports of ion exchange in Na-NAT with larger species include: Ti^+, Ag^+, Hg^{2+}, Cd^{2+}, Zn^{2+}, Ba^{2+}, Ni^{2+} and Co^{2+}.[11]

Summary of ion exchange reports

- Ambient pressure, 60°C with shaking for 50 days. Reports show exchange in Na-Al-NAT with Cd(II).[5]
- NH_4 exchanged Na-Al-NAT using a NH_4NO_3.[12]
- Potassium exchanged Na-Al-NAT using KCl solution at 60 °C for 60 days.[7]
- Lithium exchanged Na-Al-NAT using LiCl solution at 60 °C for 60 days.[7]
- Ti^+, Ag^+, Hg^{2+}, Zn^{2+}, Ba^{2+}, Ni^{2+} and Co^{2+} solution at 60 °C for 7 days.[11]

By exploitation of the cell volume expansion seen in Natrolite and Ga-NAT under pressure it should be possible to show exchange with some larger cation species. In this

chapter we investigate potential cations for use in high pressure ion exchange experiments.

Table 1: Cell parameters a, b & c (Å) and cell volume (Å^3) of cation varied aluminosilicate natrolites.

	a (Å)	b (Å)	c (Å)	V(Å^3)	Space group
Li-NAT [6]	17.678	18.509	6.488	2123	*Fdd2*
K-NAT [6]	19.274	19.664	6.469	2451	*Fdd2*
NH_4-NAT[12]	17.899	18.390	6.529	2149	$C112_1$
Na-NAT[13]	18.272	18.613	6.593	2242	*Fdd2*

6.2 Na/Cs hydrothermal Ion Exchange

Experiments were performed using a Paar Teflon^{TM} lined autoclave. Samples of Al-NAT and Ga-NAT (tetragonal and orthorhombic), were treated with a CsCl solution at 100°C for 24 hours. Samples were analysed using PXRD and SEM EDX. Following hydrothermal exposure to CsCl solution, any samples which showed evidence of Na/Cs exchange were heated in a NaCl(aq) reflux for 24 hours (back-exchange) and PXRD and SEM EDX analysis was repeated. For a more detailed explanation of the experimental set-up see chapter 2.

Powder X-ray diffraction patterns for Al-NAT, Orthorhombic Ga-NAT and tetragonal Ga-NAT are given in Figure 1 to Figure 3, respectively. A summary of the SEM EDX analysis of each sample is shown in Table 2.

For Al-NAT, there was little evidence of ion exchange. SEM EDX analysis shows zero exchanged Cs, so it is not surprising that the powder X-ray diffraction patterns also show no change (Figure 1).

Similarly, we do not observe any clear evidence of Na/Cs exchange for orthorhombic Ga-NAT. This is unsurprising, as this structure is very similar to that of the aluminosilicate natrolite. As shown in Table 2 there is some evidence of Cs presence, with a calculated composition of $Na_{15.30}Cs_{0.45}Si_{24}Ga_{16.91}O_{81.82}$, based upon SEM EDX analysis. However this amount is very small (~3%) and is therefore most likely due to the presence of surface Cs; this is supported by the cell volume values which remain unchanged following ion exchange. When using SEM EDX analysis it is not possible to determine whether a given atom/cation is present within the natrolite framework, on the surface or is part of a Cs-based impurity. Matrix effects can also cause some discrepancies in the qualitative analysis of the calculated unit cell composition. As a consequence SEM EDX results should be interpreted with moderate caution by using PXRD results to compare and correlated any SEM EDX results obtained.

The powder pattern of orthorhombic Ga-NAT, post CsCl(aq) hydrothermal treatment, shows no change and therefore no evidence of Na/Cs inner framework exchange (Figure 2).

When using tetragonal Ga-NAT some definite changes in the PXRD relative peak intensity is seen following treatment (Figure 3). Following hydrothermal treatment there is a clearly visible shift in relative intensities in the 2-theta region 18-22°. Figure 3 shows an enlargement of this region to highlight the change. SEM EDX analysis of this sample shows that a good proportion of Na has been replaced by exchanged Cs (28%), to give an approximate composition of $Na_{5.53}Cs_{2.03}Si_{12}Ga_{7.87}O_{39.73.}$ These two measurements give strong evidence of Na/Cs framework exchange for the tetragonal form of Ga-NAT. As established in chapters 4 and 5, tetragonal Ga-NAT has the more open, flexible framework of all the natrolites studied here. This flexibility facilitates ion exchange, even with large cations like Cs. The nature of the framework accounts for the evidence of ion exchange, which is not seen in the other two natrolite forms.

Back-exchange experiments were performed in order to investigate whether or not the newly exchanged Cs could be leached out using a simple NaCl(aq) reflux. The sample was heated in a NaCl solution at 80°C and 100°C. Following back-exchange experiments Cs is leached out of the framework at temperatures as low as 80°C. PXRD patterns show that the previously seen shift in relative intensity, upon Cs exposure, has returned back to that of Na-GaNAT (Figure 3). This suggests that possible Na/Cs exchange was achieved but that back exchange easily causes leaching of these exchanged cations. The SEM EDX results concur. According to EDX, as little as 3.73% and 1.90% Cs remains after treatment at 80°C and 100°C respectively. This low amount, together with the strong evidence from PXRD means that we should assume that any remaining Cs is due to surface cation presence, this is supported by the cell volume values which, after a slight increase from 1166.22(6) to 1170.62(3) after ion exchange, reverts back to a value similar to that of untreated tetragonal gallosilicate natrolite (1167.38(6)). As described earlier, the open flexible framework of tetragonal Ga-NAT can be used to explain ion exchange

behaviour. The large open pores, which showed a large initial Na/Cs ion- exchange, also allows easy cation exit under mild conditions (80°C).

If Cs were used in later high pressure studies, it is predicted that Al-NAT and orthorhombic Ga-NAT, should offer the greatest chance of cation trapping upon pressure release. Since no Na/Cs exchange was observed in these mild condition experiments we don't expect that exchanged Cs would leach upon back-exchange; should high pressure exchange occur. Therefore, high pressure Na/Cs experiments will be investigated in chapter 6b.

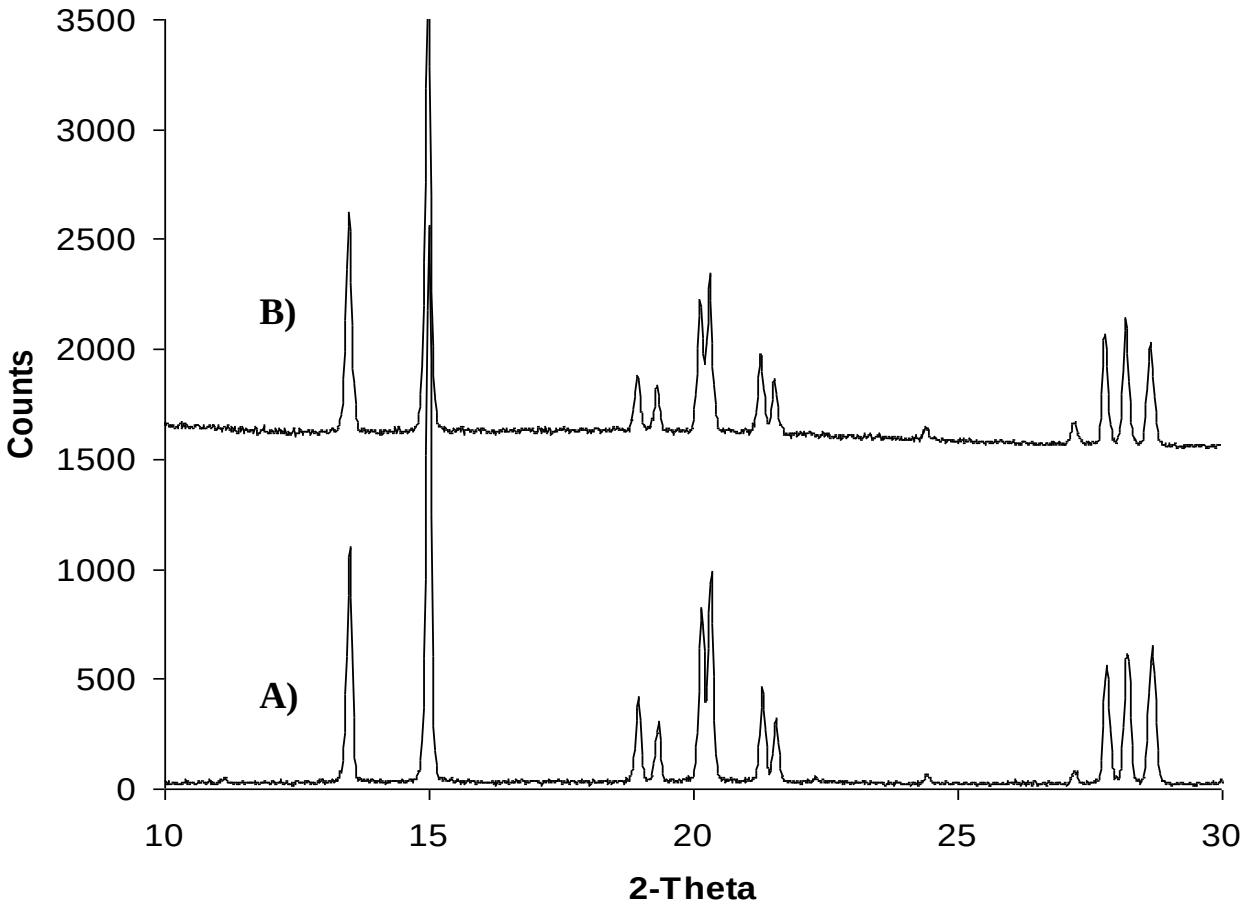

Figure 1: PXRD pattern of a) Na-Al-NAT and b) Na-Al-NAT hydrothermally treated with a CsCl solution (GLL69).

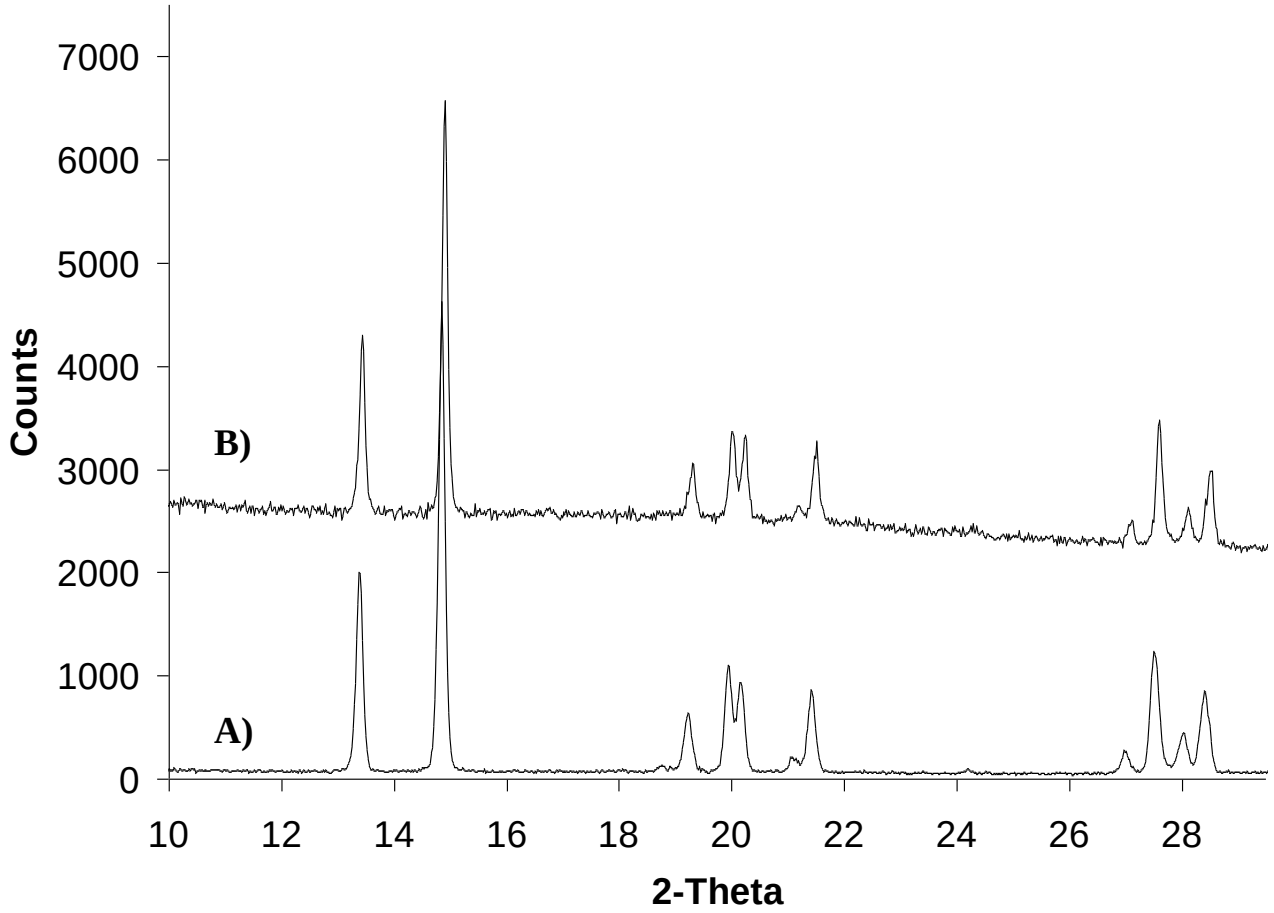

Figure 2: Powder X-ray diffraction patterns of a) Orthorhombic Na-Ga-NAT b) Orthorhombic Na-Ga-NAT hydrothermally treated with CsCl solution.

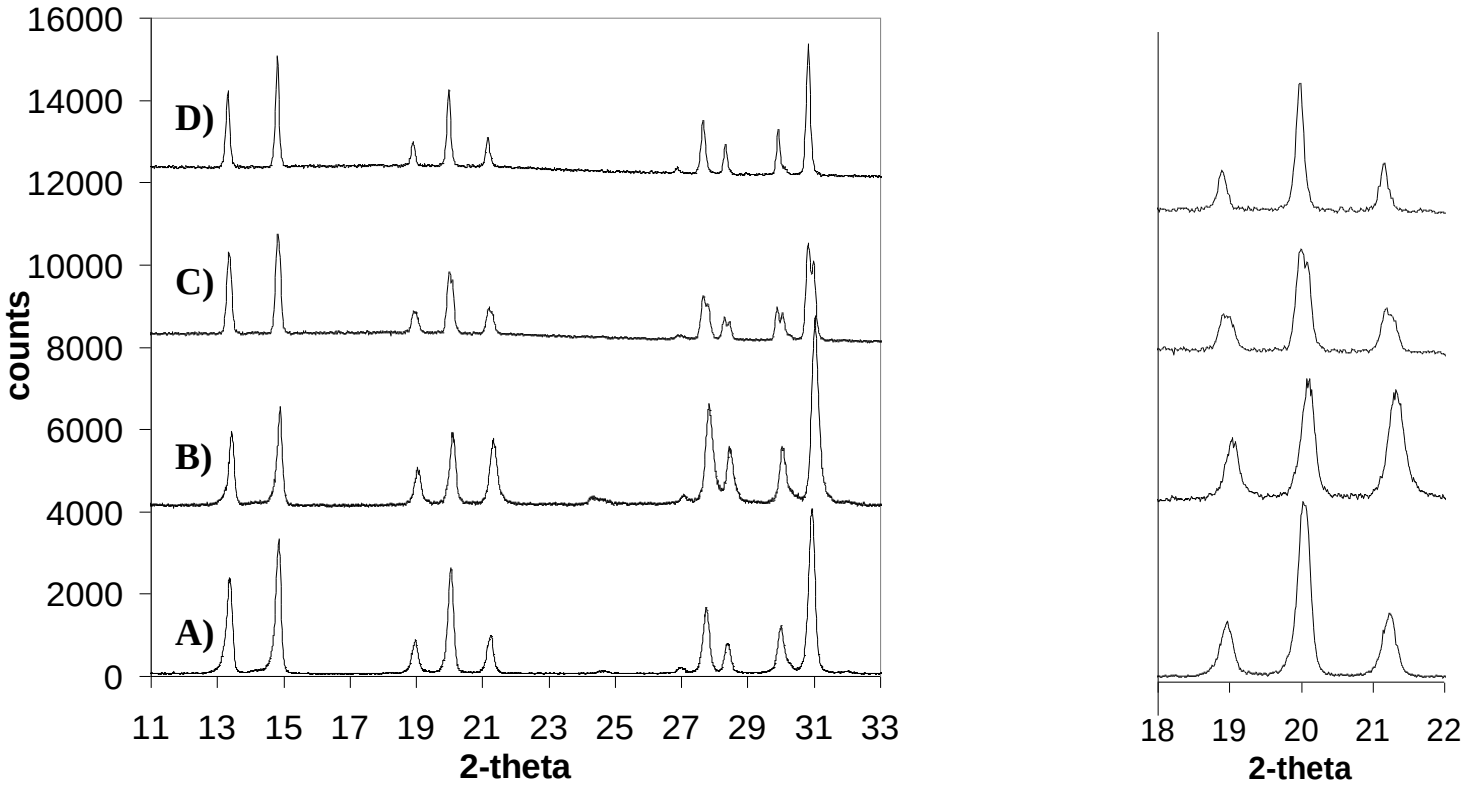

Figure 3: PXRD patterns of a) tetragonal Na-Ga-NAT, b) tetragonal Na-Ga-NAT hydrothermally treated with CsCl solution, c) 80 °C back-exchange of hydrothermally treated tetragonal Na-Ga-NAT and d) 100 °C back-exchange of hydrothermally treated tetragonal Na-Ga-NAT. A zoom-in of selected peaks shows a change in relative peak intensities.

Table 2: Summary of the results of SEM EDX analysis of samples following hydrothermal exposure to a CsCl(aq) ion exchange solution, with back-exchange results where appropriate.

		Sample	Treatment	Calculated Unit Cell Composition *,†	T atom ratio ‡	Na^+ replacement (%) §	Cs/Na	Cell Volume ($Å^3$)
Ideal Stoichiometery	**Al-Si-NAT** $Na_{16}Al_{16}Si_{24}O_{80}$	NAT	None	**$Na_{14.37}Si_{24}Al_{14.97}O_{77.95}$**	1.60	-	-	2244.30(6)
		GLL69	Hydrothermal treatment with $CsCl_{(aq)}$	**$Na_{12}Si_{24}Al_{14.68}O_{77.36}$**	1.64	0.00	0.00	2243.91(3)
	Ga-Si-NAT (orth) $Na_{16}Ga_{16}Si_{24}O_{80}$	GLL68	None	**$Na_{16.16}Si_{24}Ga_{16.02}O_{80.04}$**	1.51	-	-	2310.07(8)
		GLL68i	Hydrothermal treatment with $CsCl_{(aq)}$	**$Na_{15.30}Cs_{0.45}Si_{24}Ga_{16.91}O_{81.82}$**	1.42	2.97	0.03	2307.77(6)
	Ga-Si-NAT (tet) $Na_8Ga_8Si_{12}O_{40}$	GLL63	None	**$Na_{7.70}Si_{12}Ga_{7.68}O_{39.36}$**	1.58	-	-	1166.22(6)
		GLL63i	Hydrothermal treatment with $CsCl_{(aq)}$	**$Na_{5.53}Cs_{2.03}Si_{12}Ga_{7.87}O_{39.73}$**	1.53	27.99	0.39	1170.62(3)
		GLL63i80R	Back-exchange of GLL63i via $NaCl_{(aq)}$ reflux at 80°C	**$Na_{6.46}Cs_{0.25}Si_{12}Ga_{8.42}O_{40.84}$**	1.43	3.73	0.04	1168.42(4)
		GLL63i100R	Back-exchange of GLL63i via $NaCl_{(aq)}$ reflux at 100°C	**$Na_{7.46}Cs_{0.14}Si_{12}Ga_{7.69}O_{39.39}$**	1.56	1.90	0.02	1167.38(6)

* Calculated from SEM EDX compositional analysis. Composition averaged over ≥ 3 EDX scans, each over a $2mm^2$ sample area. Compositions should not be regarded as absolute. Interpretation of SEM EDX compositional results should account for matrix effects and should always be used in conjunction with supporting PXRD results.

† Oxygen content estimated based upon T atom content.

‡ T=Si/Al or Ga.

§ Calculated as a percentage of the total cation content after treatment.

6.3 Na/Sr Hydrothermal Ion Exchange

As described in the hydrothermal Na/Cs ion exchange, experiments were performed using a Parr Teflon^{TM} lined autoclave. Samples of Al-NAT and Ga-NAT (tetragonal and orthorhombic), were hydrothermally treated with a $SrCl_2$ solution at 100°C for 24 hours. Samples were analysed using PXRD and SEM EDX. Following hydrothermal exposure to $SrCl_2$ solution, any samples which showed evidence of Na/Sr exchange were heated in a NaCl(aq) reflux for 24 hours (back-exchange) and PXRD and SEM EDX analyses were repeated. A more detailed explanation of the experimental set-up is given in chapter 2.

Powder X-ray diffraction patterns for Al-NAT, Orthorhombic Ga-NAT and tetragonal Ga-NAT are given in Figure 4 to Figure 6, respectively. A summary of the SEM EDX analysis of each sample is shown in Table 3.

When analysing the extent of ion exchange or back-exchange, it is important to remember that Sr(II) has twice the charge of Na(I). Therefore, one Sr(II) cation will replace two Na(I) ions upon exchange. The total cation charge should be +16 for all except tetragonal Ga-NAT, which has a total of +8. In order to gain a good comparison the amount of Sr present is doubled when considering contribution to total cation content. Also, in the figures given in Table 3, the stoichiometric amount of Na replaced is twice that of the Sr stoichiometery shown by SEM EDX.

For Al-NAT, there was little evidence of Na/Sr ion exchange. The powder X-ray diffraction patterns shown in Figure 4 show no strong evidence of ion-exchange, although SEM EDX analysis shows a small amount of Sr present, (6.72% of the total cation content). This amount is small and could be attributed to surface Sr, this is supported by cell volume values which remain unchanged following Na/Sr ion exchange. Back-exchange experiments were performed and the Sr content monitored by SEM EDX. Powder patterns still remain relatively unchanged throughout, as do cell volumes, but

SEM results show that back-exchange has resulted in a Sr decrease from 6.72% to 4.07% of the total cation content). Again this small amount can be attributed to surface Sr.

Na/Sr ion-exchange investigation gave somewhat inconclusive results for orthorhombic gallosilicate. Powder XRD shows no obvious evidence of ion exchange (Figure 5), but SEM EDX results show that 37.34% of Na has been replaced by Sr. Cell volume values show a very slight increase upon Na/Sr exchange from 2310.07(8) to 2313.98(2), suggesting that some successful ion exchange occurred. However, upon examination of the unit cell composition it is clear that there is something amiss. The total cation charge should be +16 as shown in Table 3 for the untreated orthorhombic Ga-NAT. After hydrothermal treatment with $SrCl_2$(aq) the total cation charge is +4.41 (2.77+(0.82x2)), to give $Na_{2.77}Sr_{0.82}Si_{24}Ga_{16.83}O_{81.66,}$ approximately 1/3 of the cation total that should be present. There is no evidence of loss of gallium, similar to the dealumination common in zeolites undergoing steam treatment.[14] PXRD does not show any framework decomposition products, so to date this result is unexplained and requires further investigation to resolve. Based upon these results, it is quite possible that some Na/H ion exchange occurred during hydrothermal treatment. If this is the case, it could account for the low recorded cation content as any exchanged H^+ ions would not be detected during SEM EDX analysis. Conformation of this requires further investigations. Alternatively, these discrepancies could be (at least in part) explained by matrix effects. These effects alter the quality of quantitative results from SEM EDX analysis. These effects are discussed in more detail in Chapter 2.

When tetragonal Ga-NAT is hydrothermally treated with $SrCl_2$(aq) we see evidence of a large Sr presence without the large cation loss observed in the previous Sr study. However, the results throughout this experiment should be treated with caution as the total cation content of untreated tetragonal Ga-NAT was much lower than expected, 5.24 per unit cell. After hydrothermal treatment SEM results give a very significant 42.53% Na replacement. The total cation charge is +6.35 (3.65+ (1.35x2)) approximately 1/5 less than the expected but still within range of the untreated value. PXRD patterns of this result show no change, none of the relative intensity shifts (as seen in Na/Cs exchange)

are observed in this case. For PXRD there is no evidence of structure decomposition or of the presence of decomposition products (Figure 6). Back-exchange of this sample gives a reduction in Sr from 42.53% to 10.30%. The total cation charge remains stable at +6.25 (5.61+ (2x0.32)).

From these results, an assumption that some significant Na/Sr occurs with hydrothermal treatment is not unrealistic. SEM EDX results show strong evidence of Na/Sr exchange, with some leaching upon back-exchange treatment. Cell volume values support this by increasing from 1165.19(5) to 1169.42(2) upon exchange and reverting back to 1166.10(2) following back exchange. From this evidence, strontium is not suitable for use in high pressure ion exchange experiments.

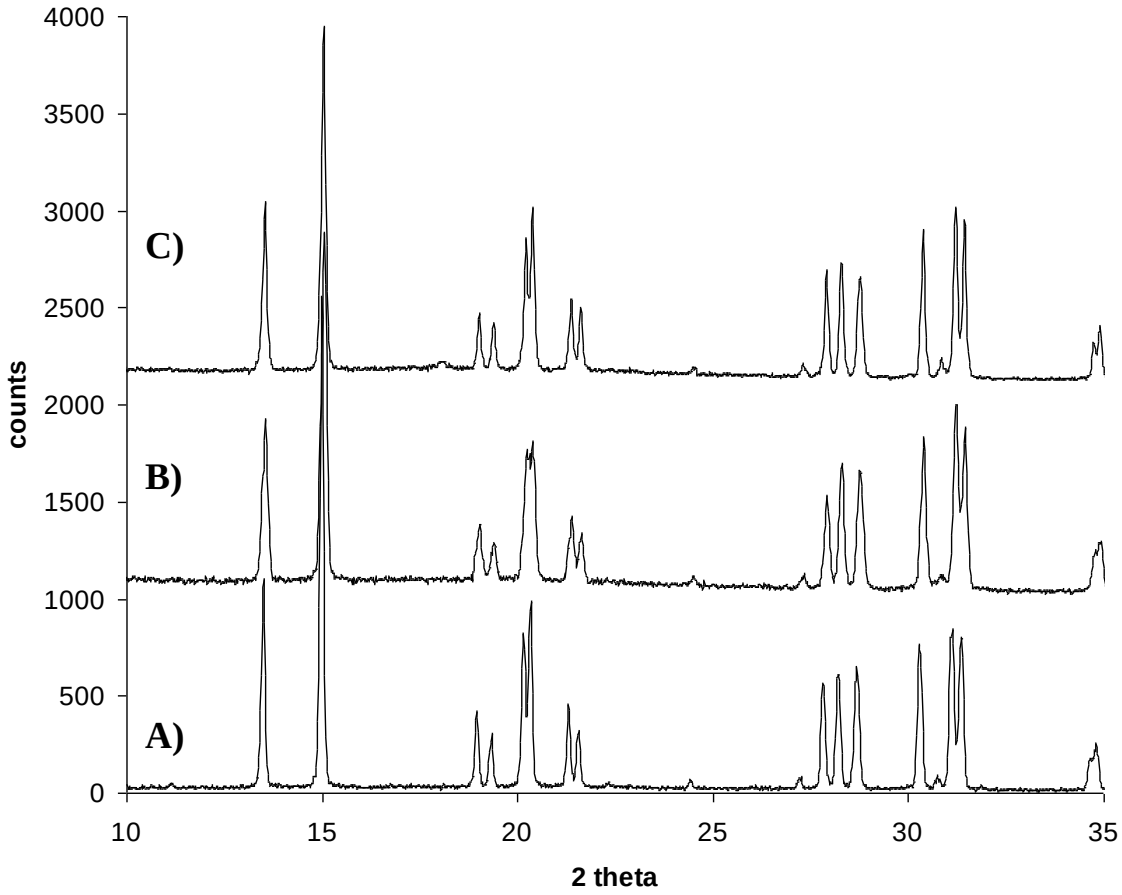

Figure 4: PXRD pattern of a) Na-Al-NAT, b) Na-Al-NAT hydrothermally treated with a $SrCl_2$ solution, c) 100°C back-exchange of b.

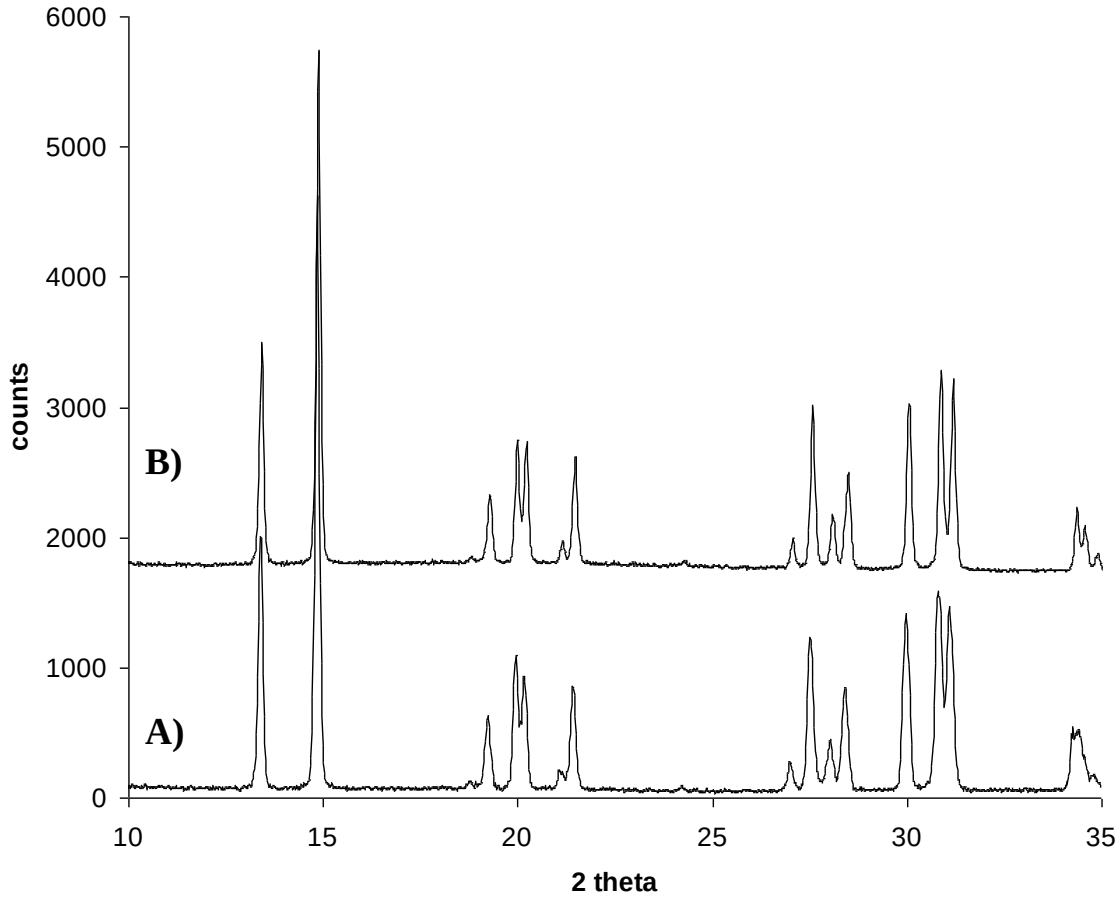

Figure 5: PXRD pattern of a) orthorhombic Na-Ga-NAT (GLL68), b) orthorhombic Na-Ga-NAT hydrothermally treated with a $SrCl_2$ solution.

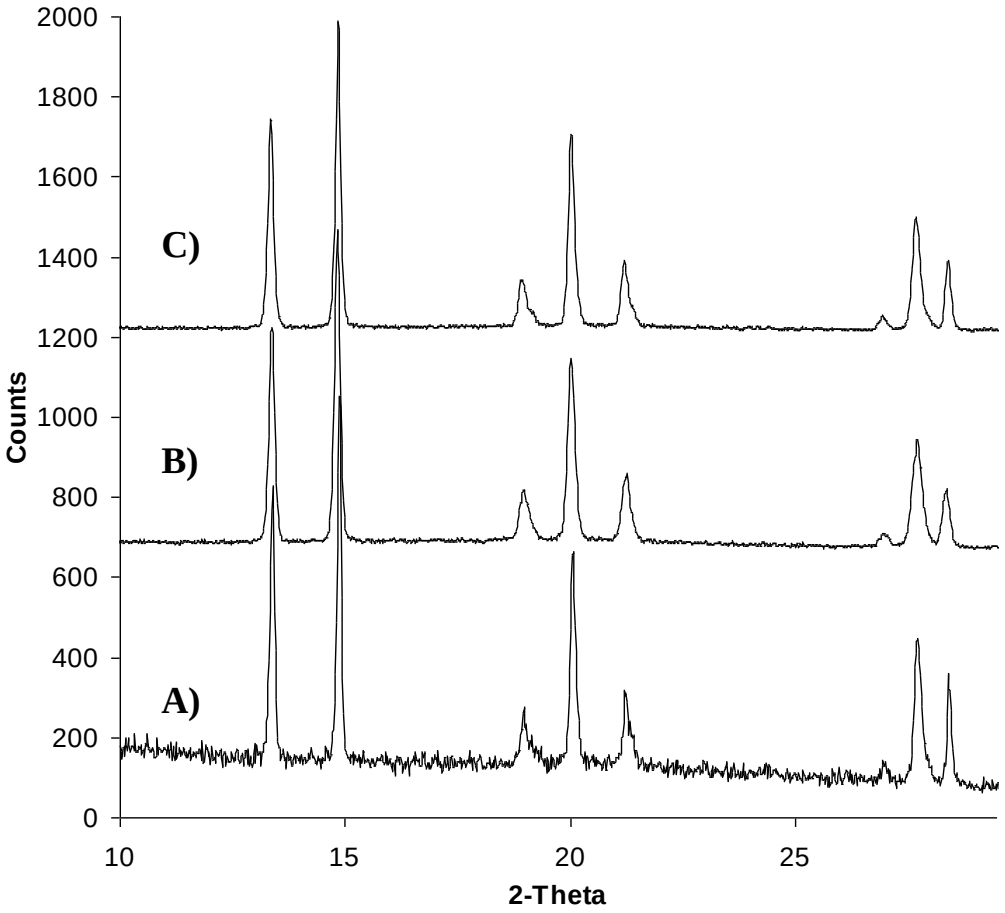

Figure 6: PXRD pattern of a) tetragonal Na-Ga-NAT (GLL56), b) tetragonal Na-Ga-NAT hydrothermally treated with a $SrCl_2$ solution, c) 100°C back-exchange of b.

Table 3: Summary of the results of SEM EDX analysis of samples following hydrothermal exposure to a $SrCl_2$ (aq) ion exchange solution, with back-exchange results where appropriate.

		Sample	Treatment	Calculated Unit Cell Composition *,†	T atom ratio ‡	Na^+ replacement (%) §	Sr/Na	Cell volume ($Å^3$)
Ideal Stoichiometery	**Al-Si-NAT** $Na_{16}Al_{16}Si_{24}O_{80}$	NAT	None	**$Na_{14.37}Si_{24}Al_{14.97}O_{77.95}$**	1.60	-	-	2244.30(6)
		NATiSr	Hydrothermal treatment with $SrCl_{2(aq)}$	**$Na_{11.28}Sr_{0.40}Si_{24}Al_{13.67}O_{75.34}$**	1.76	6.72	0.04	2244.18(3)
		NATiSr100R	Back-exchange of NATiSr via $NaCl_{(aq)}$ reflux at 100°C	**$Na_{13.39}Sr_{0.30}Si_{24}Al_{14.39}O_{76.77}$**	1.67	4.07	0.02	2246.13(3)
	Ga-Si-NAT (orth) $Na_{16}Ga_{16}Si_{24}O_{80}$	GLL68	None	**$Na_{16.16}Si_{24}Ga_{16.02}O_{80.04}$**	1.51	-	-	2310.07(8)
		GLL68iSr	Hydrothermal treatment with $SrCl_{2(aq)}$	**$Na_{2.77}Sr_{0.82}Si_{24}Ga_{16.83}O_{81.66}$**	1.43	37.34	0.30	2313.98(2)
	Ga-Si-NAT (tet) $Na_8Ga_8Si_{12}O_{40}$	GLL56	None	**$Na_{5.24}Si_{12}Ga_{9.33}O_{42.67}$**	1.29	-	-	1165.19(5)
		GLL56iSr	Hydrothermal treatment with $SrCl_{2(aq)}$	**$Na_{3.65}Sr_{1.35}Si_{12}Ga_{9.54}O_{43.08}$**	1.26	42.53	0.37	1169.42(2)
		GLL56iSr100R	Back-exchange of GLL56iSr via $NaCl_{(aq)}$ reflux at 100°C	**$Na_{5.61}Sr_{0.32}Si_{12}Ga_{9.72}O_{43.43}$**	1.24	10.30	0.06	1166.10(2)

* Calculated from SEM EDX compositional analysis. Composition averaged over ≥ 3 EDX scans, each over a $2mm^2$ sample area. Compositions should not be regarded as absolute. Interpretation of SEM EDX compositional results should account for matrix effects and should always be used in conjunction with supporting PXRD results.

† Oxygen content estimated based upon T atom content.

‡ T=Si/Al or Ga.

§ Calculated as a percentage of the total cation content after treatment when Sr is considered as a 2^+ cation. $2Na^+=1Sr^{2+}$

6.4 Na/Rb Hydrothermal Ion Exchange

Experiments were performed as described in the previous sections, using a Parr Teflon™ lined autoclave. Samples of Al-NAT and Ga-NAT (tetragonal and orthorhombic), were hydrothermally treated with a RbCl solution at 100°C for 24 hours. Samples were analysed using PXRD and SEM EDX. Following hydrothermal exposure to RbCl solution, any samples which showed evidence of Na/Rb exchange were heated in a NaCl(aq) reflux for 24 hours (back-exchange) and PXRD and SEM EDX analysis was repeated.

Powder X-ray diffraction patterns for Al-NAT, Orthorhombic Ga-NAT and tetragonal Ga-NAT are given in Figure 7 to Figure 9 respectively. A summary of the SEM EDX analysis of each sample is shown in Table 4. Ion exchange experiments using RbCl show dramatic changes in PXRD patterns and high levels of Rb (post hydrothermal treatment), for all three of the natrolite samples.

Al-NAT shows a phase transition following Na/Rb exchange, so that no Na-Al-NAT peaks remain within the pattern (Figure 7). This transition is assumed to be the formation of Rb-Al-NAT and not due to framework decomposition or the presence of decomposition products; since the transition appears to be reversible by back-exchange. Hydrothermal Na/Rb exchange alters the unit cell composition quite significantly from $Na_{14.37}Si_{24}Al_{14.97}O_{77.95}$ to $Na_{0.17}Rb_{11.04}Si_{24}Ga_{12.38}O_{72.75,}$ so that 98.48% Na is replaced by Rb, almost total ion exchange. Back-exchange removes all presence of Rb. The structure returns essentially back to normal, so that Na-Al-NAT peaks are evident in the PXRD pattern, with no visible Rb-Al-NAT. Upon back-exchange the powder pattern does show significant peak broadening and some unresolved peak splitting, in comparison with the original untreated sample pattern. Results from SEM EDX analysis of this back-exchanged sample suggest that it is unlikely that this broadening and amorphous nature is due to framework decomposition; since the T atom ratio remains exactly that of the untreated sample.

Al-NAT has shown almost complete ion-exchange to Rb-Al-NAT. To date, this new ion-exchanged NAT has not been reported. Since complete ion exchange and back-exchange is seen, Rb is deemed unsuitable for further high pressure ion-exchange studies. In the interests of time and resource management, this new Rb-Al-NAT form remains uncharacterised as it is not applicable to the focus of this work; high pressure cation trapping.

Both the orthorhombic and the tetragonal gallosilicates show a dramatic Na/Rb ion exchange (60.03% and 87.74% Na replacement respectively). Upon back-exchange, all the previously exchanged Rb is leached out. Cell volume values reflect this level of exchange increasing from 2310.07(8) to 2314.67(3) (orthorhombic) and from 1165.19(5) to 1169.78(2) (tetragonal) following exchange. Cell volumes decrease upon back exchange so that similar values to that of untreated samples are recorded. Powder XRD patterns before treatment and after back-exchange are well matched, so Na/Rb ion exchange and any associated structural change must be completely reversible. The powder patterns of the hydrothermally treated forms show definite change. Orthorhombic Ga-NAT shows a visible emergence of broad peaks, most apparent at the 2-theta values 22.5° and 29°. Similarly the hydrothermally exchanged tetragonal Ga-NAT pattern shows new and broad peaks, the most prominent at 2-theta values of 14°, 22.5°, and 32°. As well as new peaks there is reduction in crystallinity (particularly in tetragonal Ga-NAT). All powder XRD's were collected in transmission mode with Cu radiation. Consequently, samples which contain heavy atoms (Cs, Rb, Sr and Ba), will give a poor signal to noise ratio due to high X-ray adsorption. Reduced crystallinity and high X-ray adsorption can be used to explain the powder patterns of Na/Rb ion exchanged samples.

Neither of the gallosilicate forms show the dramatic change in pattern as seen in the Al-NAT form. Since the only difference between Al-NAT and the orthorhombic Ga-NAT is Al/Ga substitution, the effect of Al in the natrolite framework must in some way allow for this dramatic change. The nature of the T atom can affect pore shape and size as well as framework flexibility, this ultimately effects ion exchange. However, it is

unreasonable to speculate at this point until the structures of all Na/Rb exchanged samples have been resolved.

The successful exchange observed in this series means that rubidium is not suitable for use in the high pressure exchange experiments.

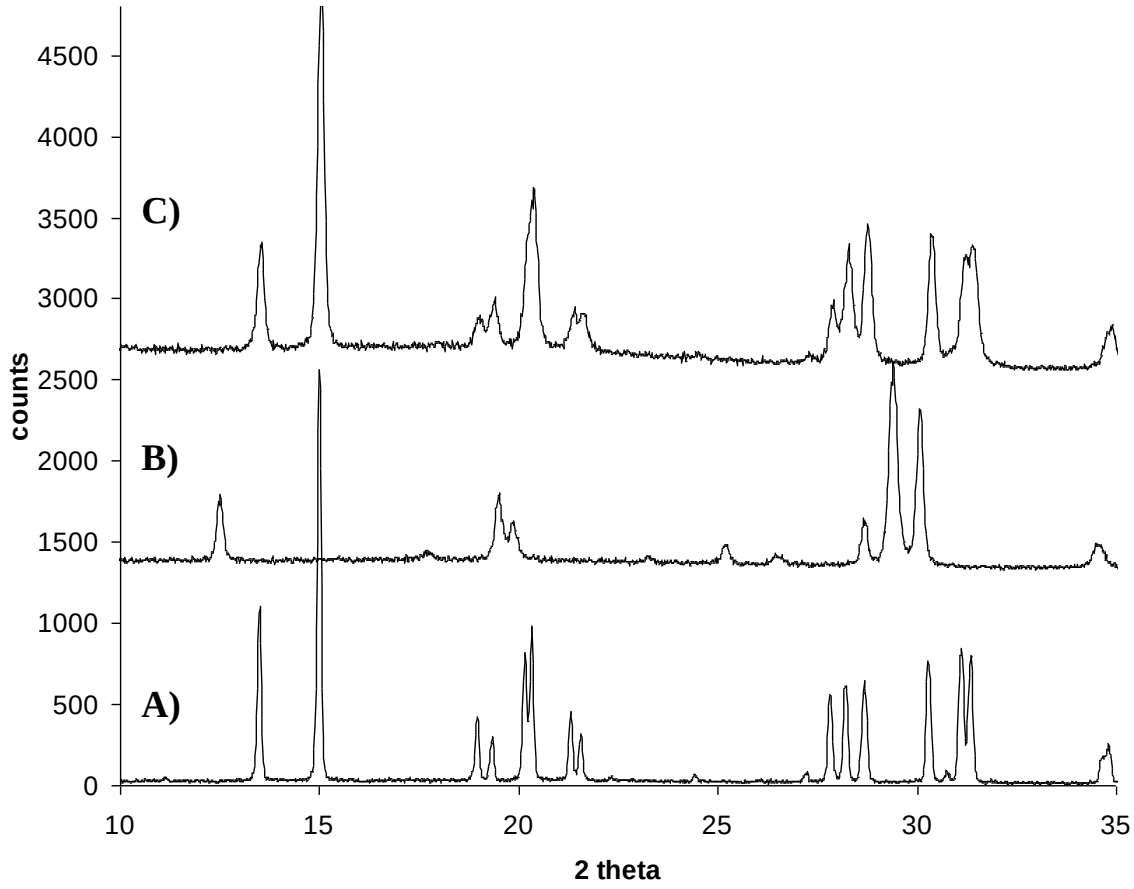

Figure 7: PXRD pattern of a) Na-Al-NAT, b) Na-Al-NAT hydrothermally treated with a RbCl solution, c) 100°C back-exchange of b.

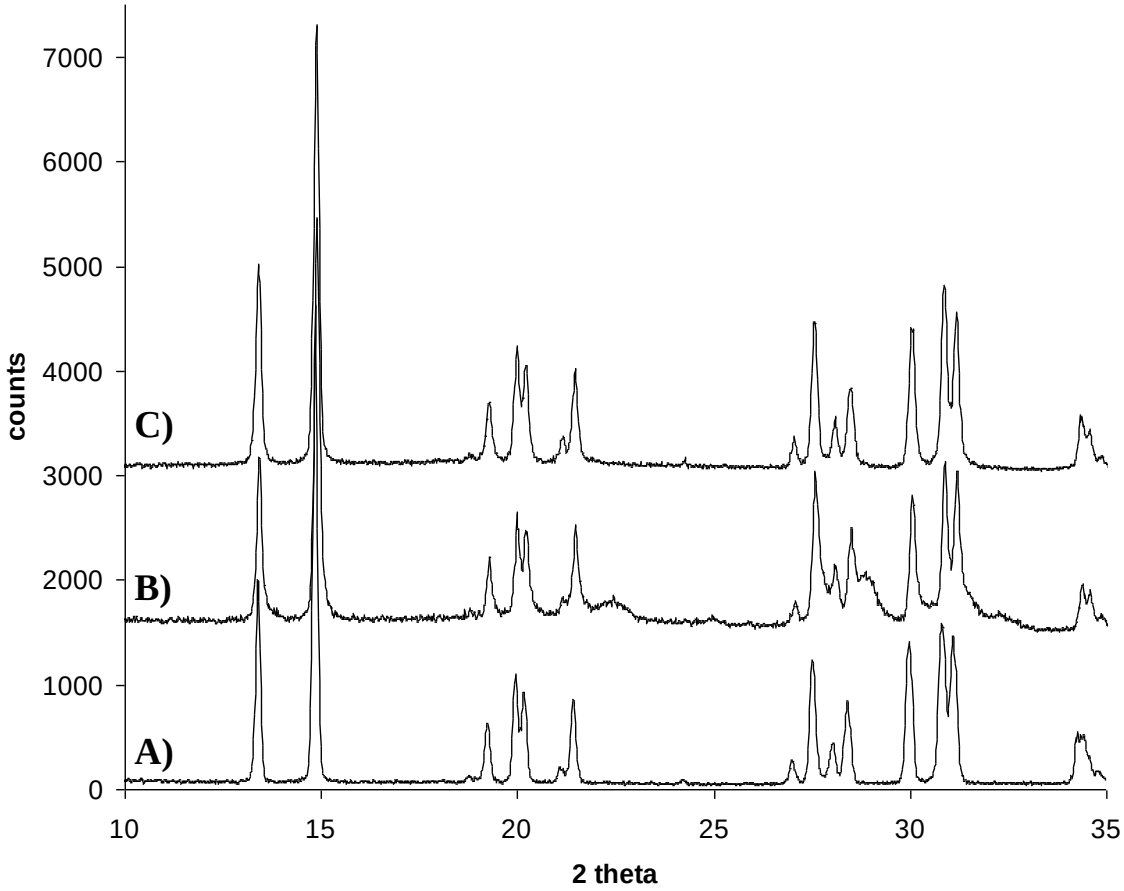

Figure 8: PXRD pattern of a) orthorhombic Na-Ga-NAT (GLL68), b) orthorhombic Na-Ga-NAT hydrothermally treated with a RbCl solution, c) 100°C back-exchange of b.

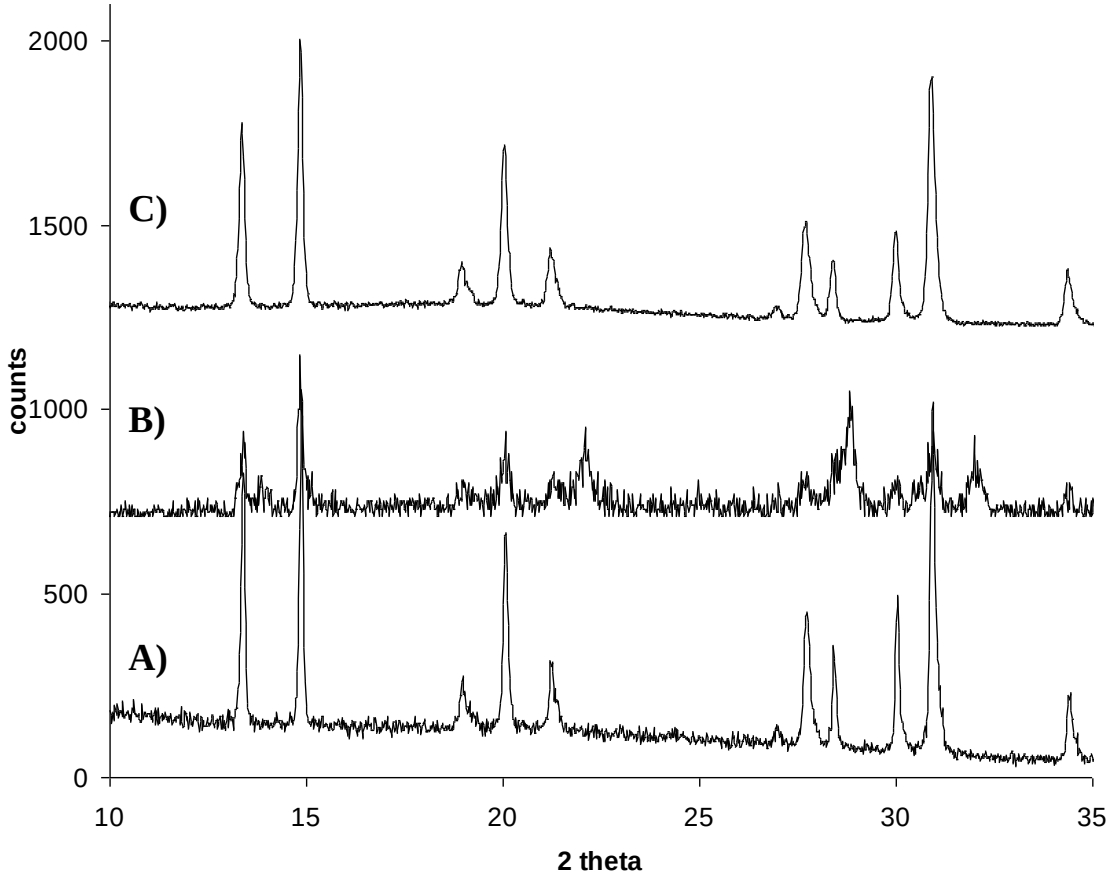

Figure 9: PXRD pattern of a) tetragonal Na-Ga-NAT (GLL56), b) tetragonal Na-Ga-NAT hydrothermally treated with a RbCl solution, c) 100°C back-exchange of b.

Table 4: Summary of the results of SEM EDX analysis of samples following hydrothermal exposure to a RbCl (aq) ion exchange solution, with back-exchange results where appropriate.

		Sample	Treatment	Calculated Unit Cell Composition *,†	T atom ratio ‡	Na^+ replacement (%) §	Rb/Na	Cell volume ($Å^3$)
Ideal Stoichiometery	**Al-Si-NAT** $Na_{16}Al_{16}Si_{24}O_{80}$	NAT	None	**$Na_{14.37}Si_{24}Al_{14.97}O_{77.95}$**	1.60	-	-	2244.30(6)
		NATiRb	Hydrothermal treatment with $RbCl_{(aq)}$	**$Na_{0.17}Rb_{11.04}Si_{24}Al_{12.38}O_{72.75}$**	1.94	98.48	64.68	-
		NATiRb100R	Back-exchange of GLL68iRb via $NaCl_{(aq)}$ reflux at 100°C	**$Na_{13.62}Si_{24}Al_{14.98}O_{77.97}$**	1.60	0	0	2247.50(3)
	Ga-Si-NAT (orth) $Na_{16}Ga_{16}Si_{24}O_{80}$	GLL68	None	**$Na_{16.16}Si_{24}Ga_{16.02}O_{80.04}$**	1.51	-	-	2310.07(8)
		GLL68iRb	Hydrothermal treatment with $RbCl_{(aq)}$	**$Na_{3.49}Rb_{5.25}Si_{24}Ga_{14.98}O_{77.97}$**	1.60	60.03	1.50	2314.67(3)
		GLL68iRb100R	Back-exchange of GLL68iRb via $NaCl_{(aq)}$ reflux at 100°C	**$Na_{10.72}Si_{24}Ga_{17.76}O_{83.52}$**	1.35	0	0	2311.74(3)
	Ga-Si-NAT (tet) $Na_8Ga_8Si_{12}O_{40}$	GLL56	None	**$Na_{5.24}Si_{12}Ga_{9.33}O_{42.67}$**	1.29	-	-	1165.19(5)
		GLL56iRb	Hydrothermal treatment with $RbCl_{(aq)}$	**$Na_{0.65}Rb_{4.63}Si_{12}Ga_{7.12}O_{38.24}$**	1.69	87.74	7.16	1169.78(2)
		GLL56iRb100R	Back-exchange of GLL56iRb via $NaCl_{(aq)}$ reflux at 100°C	**$Na_{5.76}Si_{12}Ga_{8.49}O_{40.99}$**	1.42	0	0	1166.10(6)

* Calculated from SEM EDX compositional analysis. Composition averaged over ≥ 3 EDX scans, each over a $2mm^2$ sample area. Compositions should not be regarded as absolute. Interpretation of SEM EDX compositional results should account for matrix effects and should always be used in conjunction with supporting PXRD results.

† Oxygen content estimated based upon T atom content.

‡ T=Si/Al or Ga.

§ Calculated as a percentage of the total cation content after treatment.

6.5 Na/Ba Hydrothermal Ion Exchange

Experiments were performed in a Parr Teflon^{TM} lined autoclave. Samples of Al-NAT and Ga-NAT (tetragonal and orthorhombic) were hydrothermally treated with a $BaCl_2$ solution at 100°C for 24 hours. Samples were analysed using PXRD and SEM EDX. Following hydrothermal exposure to $BaCl_2$ solution, samples were heated in a NaCl(aq) reflux for 24 hours (back-exchange) and PXRD and SEM EDX analysis was repeated.

Powder X-ray diffraction patterns for Al-NAT, Orthorhombic Ga-NAT and tetragonal Ga-NAT are given in Figure 10 to Figure 12, respectively. A summary of the SEM EDX analysis of each sample is shown in Table 5.

When analysing the extent of ion exchange or back-exchange, it is important to remember that, just like the Sr(II) used in prior experiments; Ba(II) has twice the charge of Na(I). Therefore, one Ba(II) cation will replace two Na(I) ions upon exchange. The total unit cell cation charge should be +16 for all except tetragonal Ga-NAT, which has a total of +8. In order to gain a good comparison the amount of Ba present is doubled when considering contribution to total cation content. In the figure given in Table 5, the stoichiometric amount of Na replaced is twice that of the Ba stoichiometery shown by SEM EDX.

The PXRD patterns from samples which were hydrothermally treated with $BaCl_2$(aq) show some newly emerging broad peaks which indicate the formation of some amorphous materials in the hydrothermally treated samples. The least affected pattern is that of Al-NAT. The new broad peaks are most prominent at the 2-theta values 18° and 30° (Figure 10). Orthorhombic Ga-NAT also shows broad peaks at 22° and 29° and tetragonal Ga-NAT shows prominent peaks at 18° and 24°. As seen in Na/Rb ion exchange from the previous section, there is some reduced crystallinity and a poor signal to noise ratio in the powder patterns of ion exchanged samples. SEM EDX results from these samples show an increasing degree of Na/Ba exchange from Al-NAT through to Tetragonal Ga-NAT, with Na replacement values of 37.81%, 64.04%

and 81.05% respectively. This is reflected in the cell volume values given in Table 5. This trend of increasing exchange reflects the increase in framework flexibility across the series. So it is unsurprising that cation exchange within the framework is facilitated by flexible, open pores. Back-exchange of these samples causes almost total Ba leaching, so that PXRD patterns return to normal and SEM results show very low Ba content. From these results, Barium is deemed unsuitable for use in high pressure ion exchange experiments.

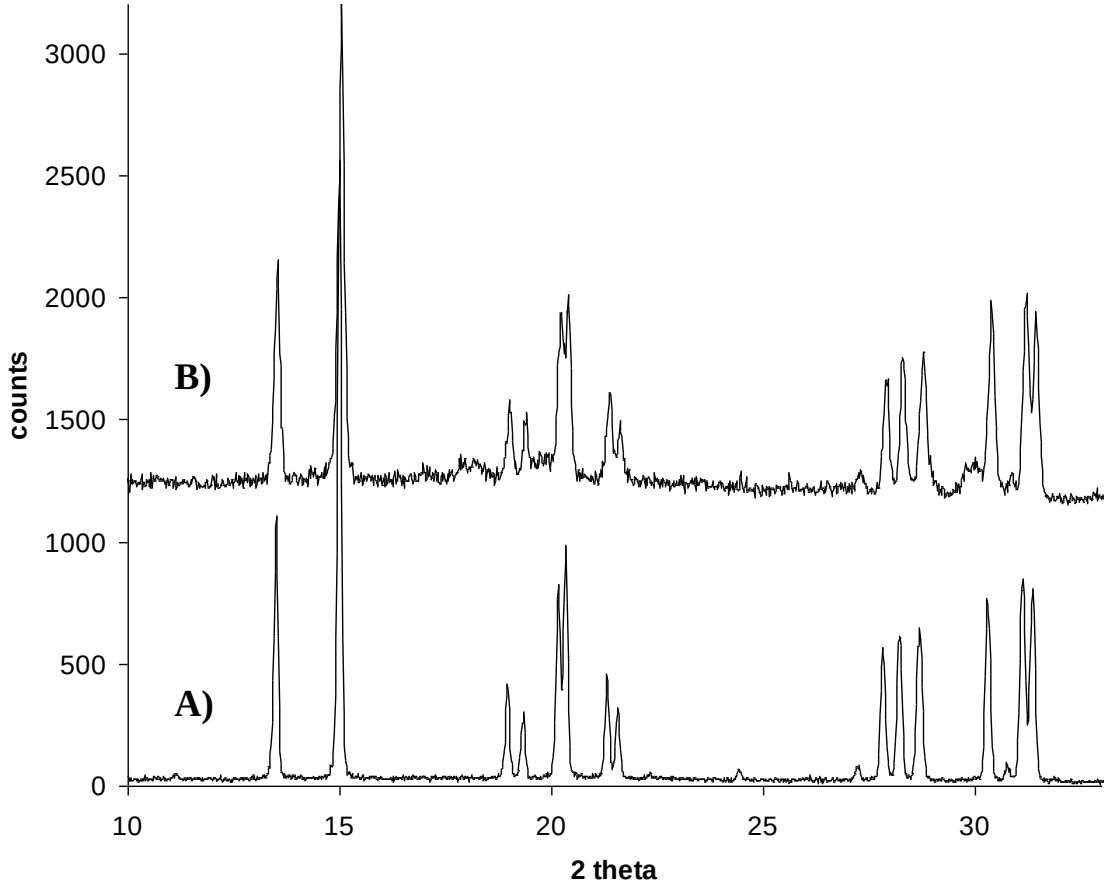

Figure 10: PXRD pattern of a) Na-Al-NAT, b) Na-Al-NAT hydrothermally treated with a $BaCl_2$ solution.

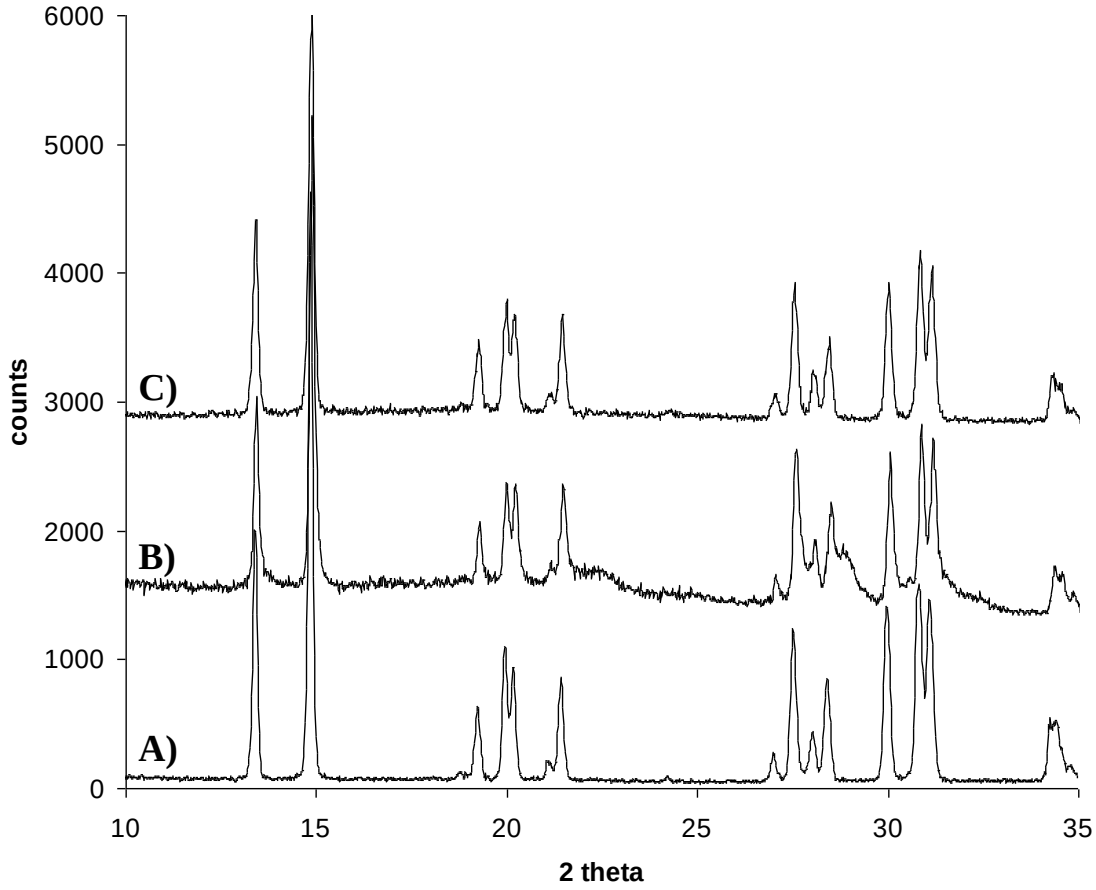

Figure 11: PXRD pattern of a) orthorhombic Na-Ga-NAT (GLL68), b) orthorhombic Na-Ga-NAT hydrothermally treated with a $BaCl_2$ solution, c) 100°C back-exchange of b.

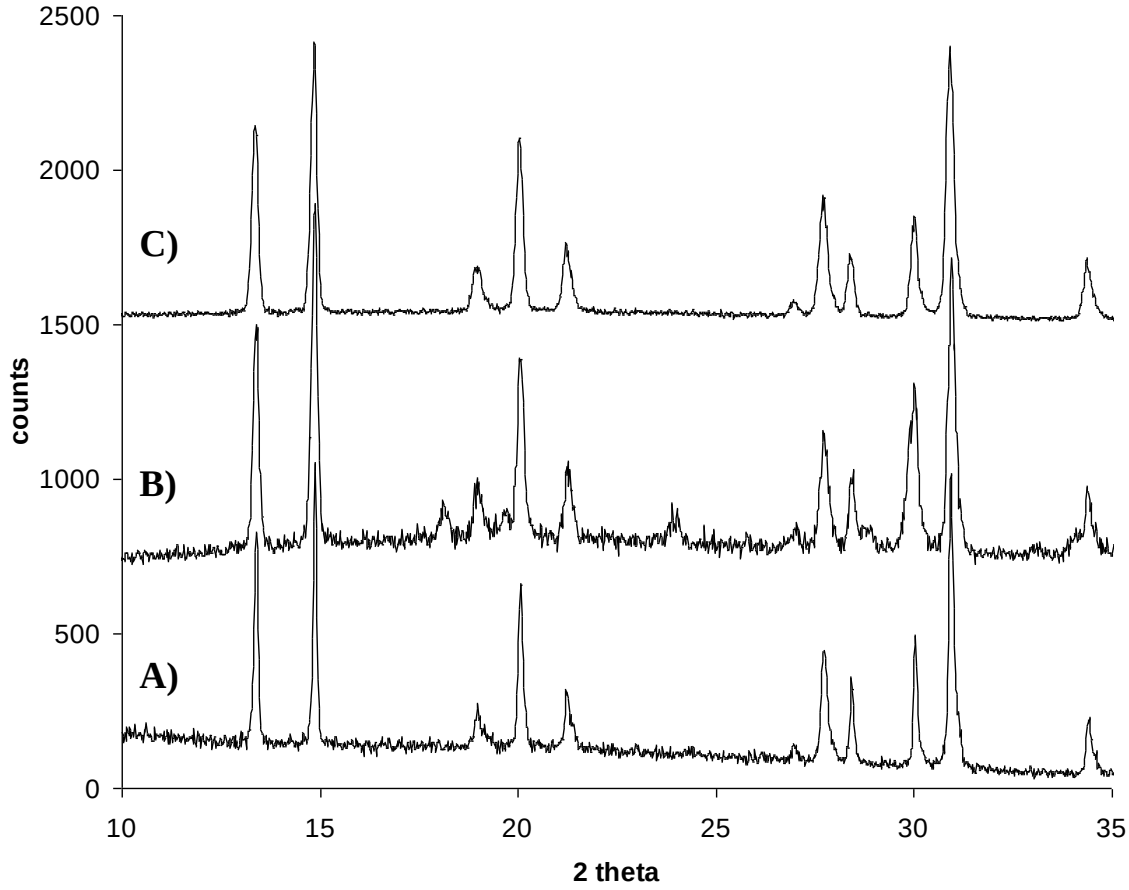

Figure 12: PXRD pattern of a) tetragonal Na-Ga-NAT (GLL56), b) tetragonal Na-Ga-NAT hydrothermally treated with a $BaCl_2$ solution, c) 100°C back-exchange of b.

Table 5: Summary of the results of SEM EDX analysis of samples following hydrothermal exposure to a $BaCl_2$(aq) ion exchange solution, with back-exchange results where appropriate.

		Sample	Treatment	Calculated Unit Cell Composition *,†	T atom ratio ‡	Na^+ replacement (%) §	Ba/Na	Cell volume ($Å^3$)
Ideal Stoichiometery	**Al-Si-NAT** $Na_{16}Al_{16}Si_{24}O_{80}$	NAT	None	**$Na_{14.37}Si_{24}Al_{14.97}O_{77.95}$**	1.60	-	-	2244.30(6)
		NATiBa	Hydrothermal treatment with $BaCl_{2(aq)}$	**$Na_{9.17}Ba_{2.78}Si_{24}Al_{14.06}O_{76.12}$**	1.71	37.81	0.30	2248.12(4)
	Ga-Si-NAT (orth) $Na_{16}Ga_{16}Si_{24}O_{80}$	GLL68	None	**$Na_{16.16}Si_{24}Ga_{16.02}O_{80.04}$**	1.51	-	-	2310.07(8)
		GLL68iBa	Hydrothermal treatment with $BaCl_{2(aq)}$	**$Na_{5.23}Ba_{4.65}Si_{24}Ga_{21.73}O_{91.46}$**	1.10	64.04	0.89	2313.35(3)
		GLL68iBa100R	Back-exchange of GLL68iBa via $NaCl_{(aq)}$ reflux at 100°C	**$Na_{12.35}Ba_{0.26}Si_{24}Ga_{17.51}O_{83.03}$**	1.37	4.05	0.02	2311.12(3)
	Ga-Si-NAT (tet) $Na_8Ga_8Si_{12}O_{40}$	GLL56	None	**$Na_{5.24}Si_{12}Ga_{9.33}O_{42.67}$**	1.29	-	-	1165.19(5)
		GLL56iBa	Hydrothermal treatment with $BaCl_{2(aq)}$	**$Na_{1.89}Ba_{4.01}Si_{12}Ga_{8.21}O_{40.42}$**	1.47	81.05	2.14	1171.24(6)
		GLL56iBa100R	Back-exchange of GLL56iBa via $NaCl_{(aq)}$ reflux at 100°C	**$Na_{5.19}Ba_{0.09}Si_{12}Ga_{8.68}O_{41.36}$**	1.38	3.50	0.02	1168.26(7)

* Calculated from SEM EDX compositional analysis. Composition averaged over ≥ 3 EDX scans, each over a $2mm^2$ sample area. Compositions should not be regarded as absolute. Interpretation of SEM EDX compositional results should account for matrix effects and should always be used in conjunction with supporting PXRD results.

† Oxygen content estimated based upon T atom content.

‡ T=Si/Al or Ga.

§ Calculated as a percentage of the total cation content after treatment when Ba is considered as a 2^+ cation. $2Na^+=1Ba^{2+}$

6.6 Summary

Hydrothermal ion exchange experiments were performed in order to identify a suitable cation for use in the high pressure experiments (discussed in the next chapter). Ion exchange was observed using Sr(II), Rb(I) and Ba(II). In each case, partial ion exchange was observed, with one exception (98.48 % Na/Rb exchange in Al-NAT). In all cases ion exchange was completely reversible, as evidenced by SEM EDX and PXRD results post back-exchange. For the 2^+ cations the trend in amount of ion exchange followed the trend in framework flexibility. Ion exchange experiments performed using rubidium showed dramatic and unexpected results for Al-NAT. PXRD shows a phase transition to Rb-Al-NAT, with very different symmetry to Na-Al-NAT. Formation of Rb-Al-NAT was completely reversible via back-exchange experiments.

Experiments performed upon Al-NAT and orthorhombic Ga-NAT using cesium showed no evidence of Na/Cs ion exchange. Powder XRD patterns and SEM EDX results show no obvious signs of exchange. For tetragonal Ga-NAT, some definite evidence of Na/Cs exchange is seen. PXRD patterns show a shift in relative intensities and SEM results show a 28% Na/Cs exchange. This exchange is completely reversible upon back-exchange treatment.

Based upon the ion exchange results from this chapter, we have discarded Sr(II), Rb and Ba(II) as potential cations for use in high pressure cation trapping experiments. The only cation which does not show ion exchange under these mild conditions is cesium. For Al-NAT and orthorhombic Ga-NAT, cesium did not show any ion exchange. Therefore, if Cs were to be successfully exchanged into the pores, whilst under pressure, hopefully no cation leaching should occur upon back-exchange testing i.e. we hope that Cs offers the best chance of high pressure cation trapping. The following chapter will discuss the results from these high pressure works.

[1] Colligan M.; Lee Y.; Vogt T.; Celestian A. J.; Parise J. B.; Marshall W. B.; Hriljac J. A. 'High-pressure neutron diffraction study of superhydrated natrolite' 2005. J. Phys. Chem. B. 109. 18223-18225.

[2] Lee Y.; Hriljac J. A.; Kim S. J.; Vogt T.; Hanson, J. C. 'Pressure-induced hydration at 0.6 GPa in a synthetic gallosilicate zeolite' **2003**. *J. Am. Chem. Soc. 125*. 6036-6037.

[3] Lee Y.; Hriljac J. A.; Kim S. J.; Vogt T.; Parise J. B.; Artioli G. 'Pressure-induced volume expansion of zeolites in the Natrolite family' **2002**. *J. Am. Chem. Soc. 124*. 5466-5475.

[4] Lee Y.; Hriljac J. A.; Parise J. B.; Artioli G.; Vogt T. 'First structural investigation of a super-hydrated zeolite' **2001**. *J. Am. Chem. Soc. 123*: 12732-12733.

[5] Choudhary A.; Banerjee S. 'Studies of natrolite type natural zeolite and its cation-exchanged and adsorbed derivatives with cadmium(II) and NH_3 and H_2S' **2002**. *J. Indian. Chem. Soc. 79*. 580-582.

[6] Baur W. H., Kassner D., Kim C. H., Sieber N. H. W. **1990.** *European Journal of Mineralogy. 2* (6): 761-769.

[7] Otsuka R., Yamazaki A., Kato K. **1991**. *Thermochimica Acta. 181*. 45-46.

[8] Yamazaki A., Kamioka K., Matsumoto H. , Otsuka R. **1987**. *School Sci Eng., Waseda University. 118.* 40.

[9] Yamazaki A., Otsuka R.,**1986.** *Thermochimica Acta. 109.* 237.

[10] Yamazaki A., Kamioka K., Matsumoto H., Otsuka R., Nendo Kagaku. **1988**. *J. Clay Sci. Soc. Jpn. 28.* 143.

[11] Dyer A.; Faghihian H. 'Diffusion in heteroionic zeloites: part 1. Diffusion of water in heteroionic natrolites' **1998**. Microporous and Mesoporous Materials. 21: 27-38.

[12] Stuckenschmidt E., Kassner D. **1992**. *Eur. J. Mineral. 4.* 1229-1240.

[13] Artioli, G.; Smith, J. V.; Kvick, Å. 'Neutron diffraction study of natrolite, $Na_2Al_2Si_3O_{10}.2H_2O$, at 20 K' **1984.** *Acta Cryst. C40.* 1658-1662.

[14] Breck. 'Zeolite Molecular Sieves' **1984.** *Krieger Publishing Company.*

CHAPTER SEVEN

High Pressure Ion Exchange

High pressure diffraction experiments have been performed on orthorhombic [1] and tetragonal[2,3,4] gallosilicate forms of natrolite ($Na_{16}Ga_{16}Si_{24}O_{80}.XH_2O$ and $M_8Ga_8Si_{12}O_{40}.XH_2O$, respectively, where *M*=Na or K). In these reports, the gallosilicate natrolites show pressure-induced expansion and superhydration, as seen in the aluminosilicate counterparts. Lower pressures are required to expand the gallosilicates due to their increased flexibility when compared to aluminosilicate natrolite.

In this report we wish to exploit the pressure-induced expansion seen in alumino- and gallosilicate natrolite for ion exchange purposes. Whilst under pressure, in the expanded state, it may be possible to insert cations into the pores which at ambient pressures would not exchange into the structure. Since this pressure-induced expansion is reversible, we expect to trap any exchanged material in the structure upon pressure release.

A small number of reports have been published in which aluminosilicate natrolite undergoes ion exchange. [5,6,7,8,9,10] . These reports are under forcing conditions and have shown no evidence of pressure trapping. To date, ion exchange of cesium into any natrolite form has not been reported, and the use of pressure to trap cations is also novel and unreported to date.

Two high pressure devices were used in this work: a diamond anvil cell and piston cylinder (Quickpress) press. Each has its advantages and disadvantages, as we will see later in this section.

7.1 In-Situ X-ray Diffraction High Pressure Exchange (DAC)

Ion exchange at pressure can be performed using a diamond anvil cell. Use of a DAC means only very little sample quantities are needed. Synchrotron X-ray data can be collected in-situ, yielding high quality structural information. The diffraction data is used to gauge the extent of ion exchange occurring at pressure. The quality of the synchrotron diffraction data means that this method would be first choice to gain detailed crystallographic evidence of high pressure exchange.

In experiments performed at NSLS Brookhaven (beamline X7a), initial tests were performed at pressure upon aluminosilicate natrolite (in the superhydrated phase), in an aqueous cesium solution. Further experimental details can be seen in chapter 2. The data recorded in this test run showed phase transitions of aluminosilicate natrolite through paranatrolite to super hydrated-natrolite but no evidence of ion exchange. See Figure 1 for a summary of the diffraction patterns gathered during these experiments.

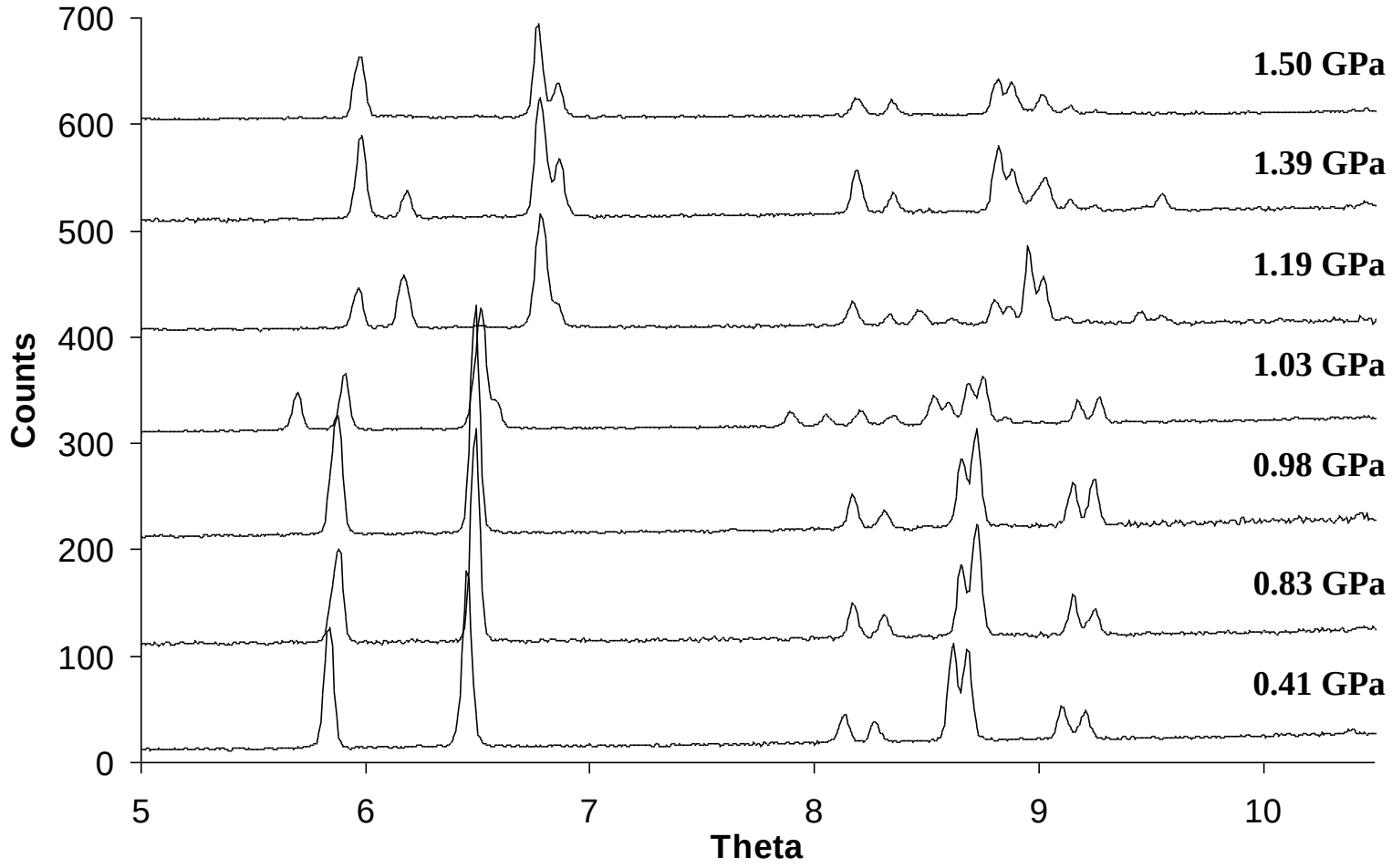

Figure 1: High pressure synchrotron X-Ray diffraction patterns of natrolite in a DAC loaded with CsCl solution.

The experimental set-up for in-situ high pressure ion exchange using a DAC is such that, in order to get to high pore-swelling pressures we must work with a very small volume since we are restricted by practical diamond size and the pressure=force/area dependence. With very small sample size, only 1-2 drops of exchange solution can be added (most of which is washed away when closing the DAC). Therefore, even when using a saturated solution we may not generate high enough cation concentrations to drive exchange. Another issue with this particular method is the washing and handling of the very small sample following high pressure experiments. Should ion exchange occur using this method, it is very difficult to collect any further data on the sample, as washing and recovery of samples as small as $3x10^{-6}$ cm^3 is extremely difficult. This does not allow for further tests, for example SEM EDX confirmation of ion content.

7.2 Quickpress Ion Exchange Experiments

In-order to negate some of the difficulties seen in the previous high pressure exchange experiments using diamond anvil cells, a different piece of pressure generating equipment, the Quickpress (a piston cylinder device), was used in a novel manner for ion exchange purposes. Details of the equipment and the experimental setup can be seen in chapter 2.

7.2.1 Quickpress Vs. Diamond Anvil

There are some significant advantages of using the Quickpress method, these are summarised below:

1) The sample chamber is larger, ~0.5 cm^3 vs. $3x10^{-6}$ cm^3 for a diamond anvil cell.

This means that more exchangeable material can be used (30-50 mg of sample with 2-3 drops of saturated ion exchange solution). The larger chamber size means enough ion exchange solution can be locked in the chamber, giving an excess of cations which drive the exchange. The larger sample size also means that recovery, washing and further testing is made much more manageable. In these runs, sample size was sufficient (in most cases) to allow for PXRD patterns and SEM EDX of the sample. For samples showing successful high pressure ion exchange, enough sample remains for a back-exchange reflux and corresponding SEM EDX analysis. However, in some cases, the remaining sample, post reflux is insufficient for PXRD data collection. This is due to variation in the volume capacity of the Teflon™ capsules and product loss during the many sequential processing steps. In some cases these experiments were repeated to gain a full collection of analytical results, but with time and equipment access limited, this was not possible in all cases.

2) Experiment parameter control

With this equipment pressure values can be maintained over time. A digital pressure gauge indicates when top-ups (generated via oil hydraulic piston pumping), are required to maintain the hydrostatic pressure.

The sample can be both heated and pressurised simultaneously (via use of a miniature thermocouple graphite furnace). The heating facility should provide further drive to cation exchange under pressure.

7.2.2 Results and Discussion

From the results discussed in chapters 4 and 5, we can compare the pressures at which we begin to see high pressure cell expansion effects and then relate these data to predictions about the ability of each natrolite form to exchange and trap particular cations. In chapters 4 and 5 we showed how both Na-GaSi-NAT samples superhydrate (with an associated cell volume expansion) at much lower pressures than the aluminosilicate analogue (~0.8 compared to 1.5 GPa). In particular, the tetragonal form shows signs of slight cell expansion at pressures as low as 0.14 GPa, whereas the earliest signs of expansion in the aluminosilicate are not seen until ~1 GPa. From this we can conclude that Na-GaSi-NAT has a more open, flexible framework than that of the aluminosilicate. This is reflected in pore dimension measurements (Table 1). We can make predictions about the success of each natrolite form, in high pressure Na/Cs exchange, based upon this pore size and framework flexibility. With a more flexible, large pore framework, we expect a greater degree of ion exchange to occur (as large Cs ions are easily inserted into pores). Conversely, the larger pores may not offer the desired effect of 'trapping' the cations post pressure release i.e. the pores are still large enough at ambient pressure to allow for ion leaching. A marriage between the two ideals should give optimum exchange and 'trapping' results.

Table 1: Pore dimensions of alumino- and gallosilicate natrolites over a number of hydrostatic pressures.

	Pressure (GPa)	Pore Length (Å)	Pore width (Å)
Aluminosilicate Natrolite[11]	0	10.007	4.882
	1	9.740	5.300
	1.5	10.020	4.940
Orthorhombic Ga-NAT[2]	0	10.1946	4.8578
	0.22	10.2844	4.7846
	0.74	9.8572	5.2252
	1.83	10.0400	4.9732
	2.26	10.0665	4.9126
Tetragonal Ga-NAT[2]	0	10.1654	4.9123
	0.14	10.1890	4.9788
	0.88	9.7331	5.4883
	1.88	9.9837	5.0278
	2.30	10.0083	4.9693

Although we do not have the pore dimensions for exactly 1 GPa for all three materials, extrapolation from the data shown in Table 1 suggests pore size is as follows:

Tet Ga-NAT> Al-NAT[a] > Orth Ga-NAT

It is this pattern we expect to see in ion exchange results. Ion leaching results should depend also upon pore size, with larger pores showing more ion leaching.

[a] Al-NAT is in the paranatrolite form (phase with the largest cell/pore expansion) at 1 GPa rather than the superhydrated form.

Each sample was treated in the Quickpress in independent, not successive reactions. Interpretation of results is in the form of observation of cation and T-atom ratios via SEM EDX, and decomposition detection and approximate cell parameters via PXRD.

Only a relatively small number of Quickpress experiments were able to be performed, due to high cost and equipment access. Therefore, a small range of parameters were selected for investigation. Pressures during all experiments were kept at 1 GPa. Please note that at these pressures the aluminosilicate natrolite is in the paranatrolite phase, whereas both gallosilicates are in the superhydrated phase. So, although not directly phase comparable, we aim here to investigate the effects of reaction time and of reaction temperature in an effort to assess the usefulness of each sample as a cation trapper; and not to directly compare the superhydrated phases of all three natrolite samples. At 1 GPa the cell parameters and pore dimensions are known for each sample, and so results can be rationalised against these points. Future work should be extended to include experiments performed on aluminosilicate natrolite at 1.5 GPa (superhydration phase).

In initial experiments, temperature variation was investigated. To date, there have been no reports of this kind of equipment being used for high pressure exchange. Initial investigation was to establish an appropriate temperature to drive exchange whilst at high pressure. Temperatures should not be so low that reaction times are unreasonable but not so high to cause any kind of thermal decomposition to the framework. Temperatures of 60, 100 and 150°C were selected. Temperatures were increased from room temperature, only when the sample was at pressure; this prevents evaporation loss of the ion exchange liquor from the unpressurised Teflon^{TM} sample holder.

7.2.2.1 Temperature Dependence

In these initial investigations we will assess the viability of this exchange method and the optimum temperature for further experimental investigation. Assessment of samples will be via:

- PXRD

We will be looking for signs of framework decomposition which should be avoided. Also, shifts in the relative intensities of some diffraction peaks (indicating possible change in the nature of the ions present i.e. exchange) and the 2-theta values of the peaks within the pattern, indicating possible cell volume change (i.e. different ions are different sizes. Changes to composition due to ion exchange will affect the cell volume of the natrolite framework).

- SEM EDX elemental analysis

Elemental analysis should indicate and/or confirm that the nature of the intrapore cations has changed. This method should give an indication of the relative proportion of exchanged material to that of other atoms within the natrolite framework or natrolite pores. This method will not distinguish between intrapore cations and surface adsorbed cations, so correlation to PXRD data is important here. More significantly SEM EDX analysis will give a reasonably accurate T atom ratio (when calibrated). Deviation from an ideal T atom ratio will indicate some framework decomposition or dealumination/degalliation which might not otherwise be detectable in PXRD peaks.

A summary of the temperature dependant Quickpress treatments and SEM results are given in Table 2 with a discussion and presentation of PXRD patterns to follow.

Table 2: High pressure (Quickpress) Na/Cs ion exchange. SEM EDX compositional results and experimental treatment with variation of temperature.

		Sample	Treatment	Pressure (GPa)	Temp (°C)	Time (hours)	Calculated Unit Cell Composition *,†	T atom ratio ‡	Cs+ (%) §	Cs/Na
Ideal Stoichiometery	**Al-Si-NAT** $Na_{16}Al_{16}Si_{24}O_{80}$	NAT	None	-	-	-	$\mathbf{Na_{14.37}Si_{24}Al_{14.97}O_{77.95}}$	1.60	-	-
		NATQP60-60	QP	1	60	1	$\mathbf{Na_{11.97}Cs_{1.63}Si_{24}Al_{14.04}O_{76.00}}$	1.71	11.98	0.14
		NATQP100-60	QP	1	100	1	$\mathbf{Na_{11.45}Cs_{2.49}Si_{24}Al_{14.41}O_{76.82}}$	1.67	17.86	0.22
		NATQP100-60R	Back-exchange of NATQP100-60**	ambient	100	24	$\mathbf{Na_{11.28}Cs_{1.52}Si_{24}Al_{13.03}O_{74.07}}$	1.84	11.88	0.14
		NATQP150-60	QP	1	150	1	$\mathbf{Na_{8.28}Cs_{9.04}Si_{24}Al_{14.87}O_{77.75}}$	1.61	52.19	1.12
	Ga-Si-NAT (orth) $Na_{16}Ga_{16}Si_{24}O_{80}$	GLL68	None	-	-	-	$\mathbf{Na_{16.16}Si_{24}Ga_{16.02}O_{80.04}}$	1.51	-	-
		GLL68QP60-60	QP	1	60	1	$\mathbf{Na_{10.44}Cs_{0.59}Si_{24}Ga_{19.35}O_{86.71}}$	1.24	5.35	0.06
		GLL68QP100-60	QP	1	100	1	$\mathbf{Na_{9.19}Cs_{3.50}Si_{24}Ga_{19.23}O_{86.46}}$	1.25	27.58	0.38
		GLL68QP100-60R	Back-exchange of GLL68QP100-60**	ambient	100	24	$\mathbf{Na_{13.57}Cs_{0.68}Si_{24}Ga_{6.41}O_{60.83}}$	3.75	4.77	0.05
		GLL68QP150-60	QP	1	150	1	$\mathbf{Na_{0.11}Cs_{15.09}Si_{24}Ga_{18.31}O_{84.31}}$	1.32	99.27	137.18
	Ga-Si-NAT (tet) $Na_8Ga_8Si_{12}O_{40}$	GLL56	None	-	-		$\mathbf{Na_{5.24}Si_{12}Ga_{9.33}O_{42.67}}$	1.29	-	-
		GLL56QP60-60	QP	1	60	1	$\mathbf{Na_{4.56}Cs_{1.63}Si_{12}Ga_{9.57}O_{43.15}}$	1.25	26.38	0.36
		GLL56QP100-60	QP	1	100	1	$\mathbf{Na_{4.46}Cs_{2.08}Si_{12}Ga_{8.34}O_{40.69}}$	1.44	31.73	0.46
		GLL56QP100-60R	Back-exchange of GLL56QP100-60**	ambient	100	24	$\mathbf{Na_{5.48}Cs_{0.01}Si_{12}Ga_{8.56}O_{41.12}}$	1.40	0.13	0.00
		GLL56QP150-60	QP	1	150	1	$\mathbf{Na_{3.78}Cs_{4.05}Si_{12}Ga_{10.30}O_{44.61}}$	1.17	51.69	1.07

QP=High pressure Quickpress treatment with $CsCl_{(aq)}$

* Calculated from SEM EDX compositional analysis. Composition averaged over ≥ 3 EDX scans, each over a $2mm^2$ sample area. Compositions should not be regarded as absolute. Interpretation of SEM EDX compositional results should account for matrix effects and should always be used in conjunction with supporting PXRD results.

** Back exchange via $NaCl_{(aq)}$ reflux at 100°C

† Oxygen content estimated based upon T atom content.

‡ T=Si/Al or Ga.

§ Calculated as a percentage of the total cation content after treatment.

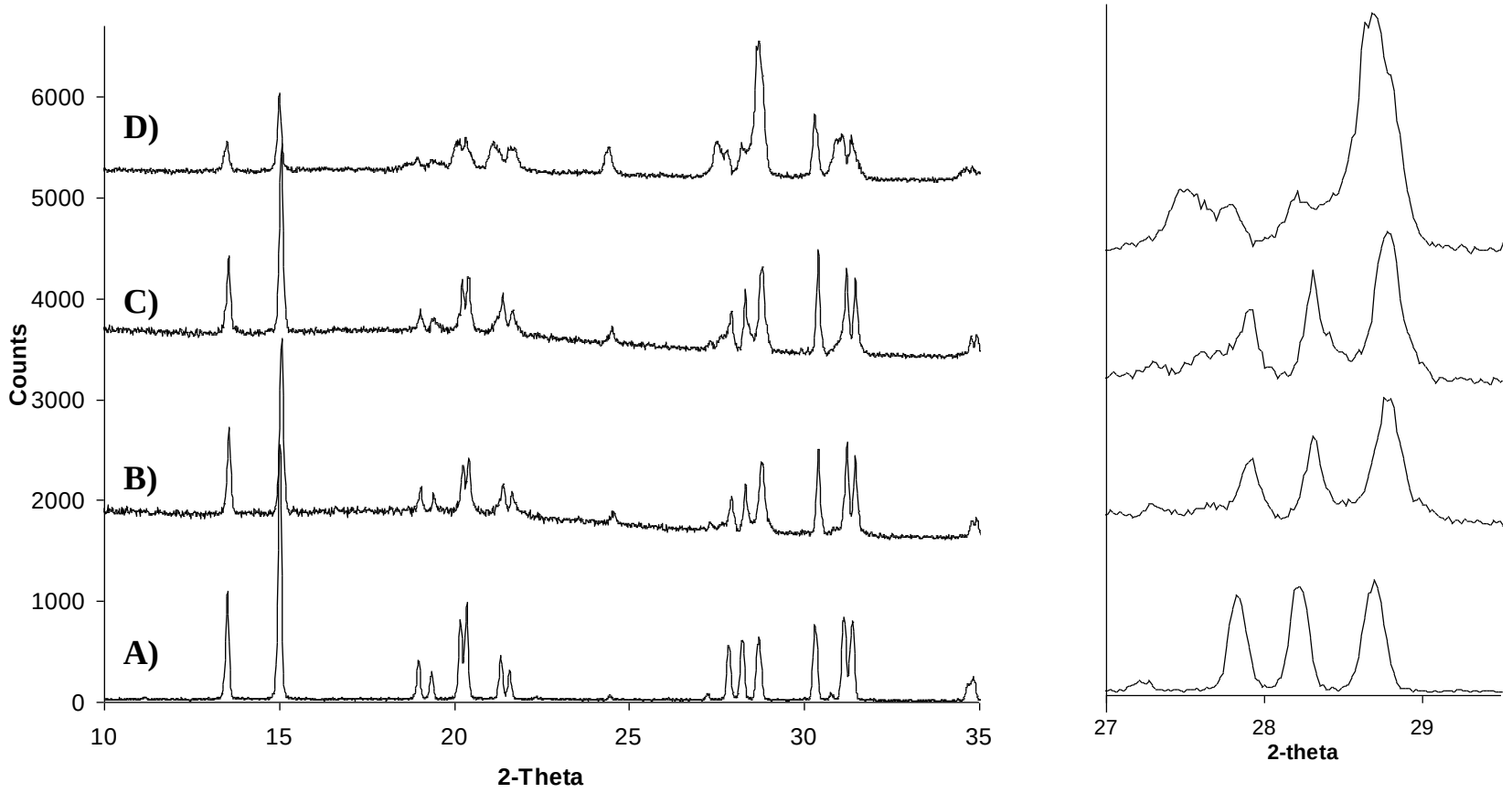

Figure 2: PXRD patterns of a) Na-Al-NAT and b-d) Na-Al-NAT exposed to a saturated solution of CsCl at temperatures of 60, 100 and 150 °C respectively. Runs b-d were performed under hydrostatic pressure (1 GPa), maintained over 60 minutes. A zoom-in of selected peaks shows a change in relative peak intensities and some decomposition at 150°C.

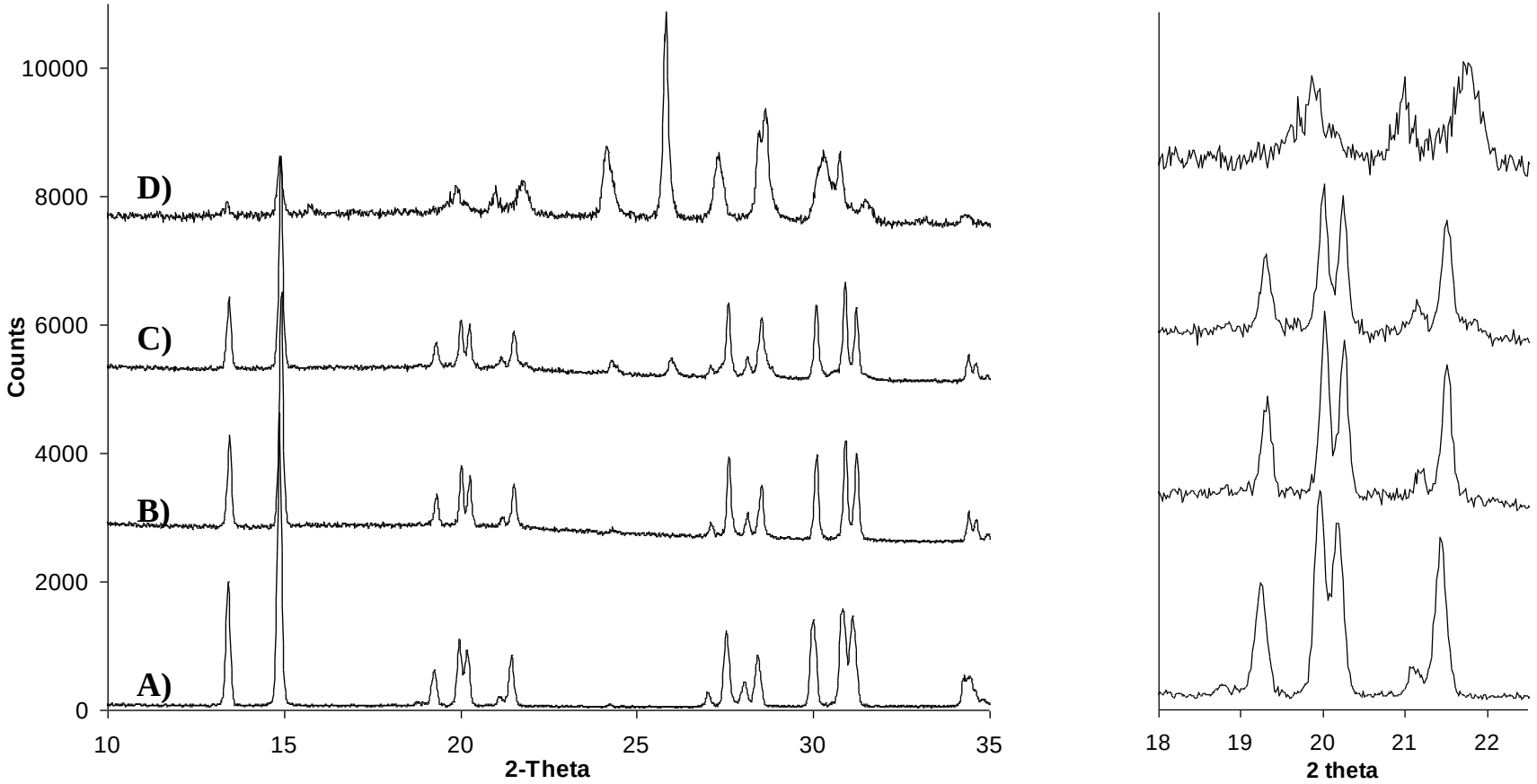

Figure 3: PXRD patterns of a) orthorhombic Na-GaSi-NAT and b-d) orthorhombic Na-GaSi-NAT exposed to a saturated solution of CsCl at temperatures of 60, 100 and 150 °C respectively. Runs b-d were performed under hydrostatic pressure (1 GPa), maintained over 60 minutes. A zoom-in of selected peaks shows a change in relative peak intensities and some decomposition at 150°C.

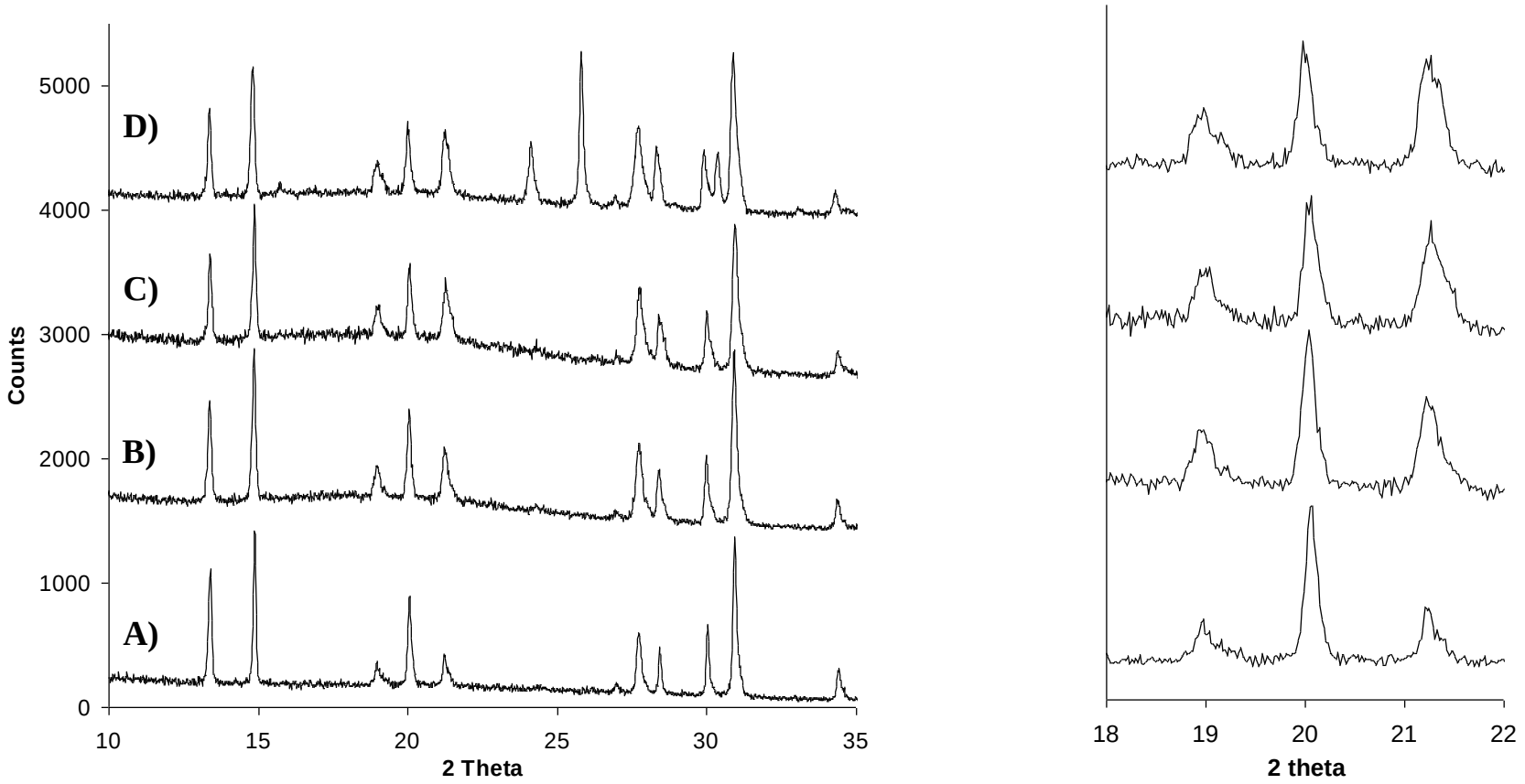

Figure 4: PXRD patterns of a) tetragonal Na-GaSi-NAT and b-d) tetragonal Na-GaSi-NAT exposed to a saturated solution of CsCl at temperatures of 60, 100 and 150 °C respectively. Runs b-d were performed under hydrostatic pressure (1 GPa), maintained over 60 minutes. A zoom-in of selected peaks shows a change in relative peak intensities and some decomposition at 150°C.

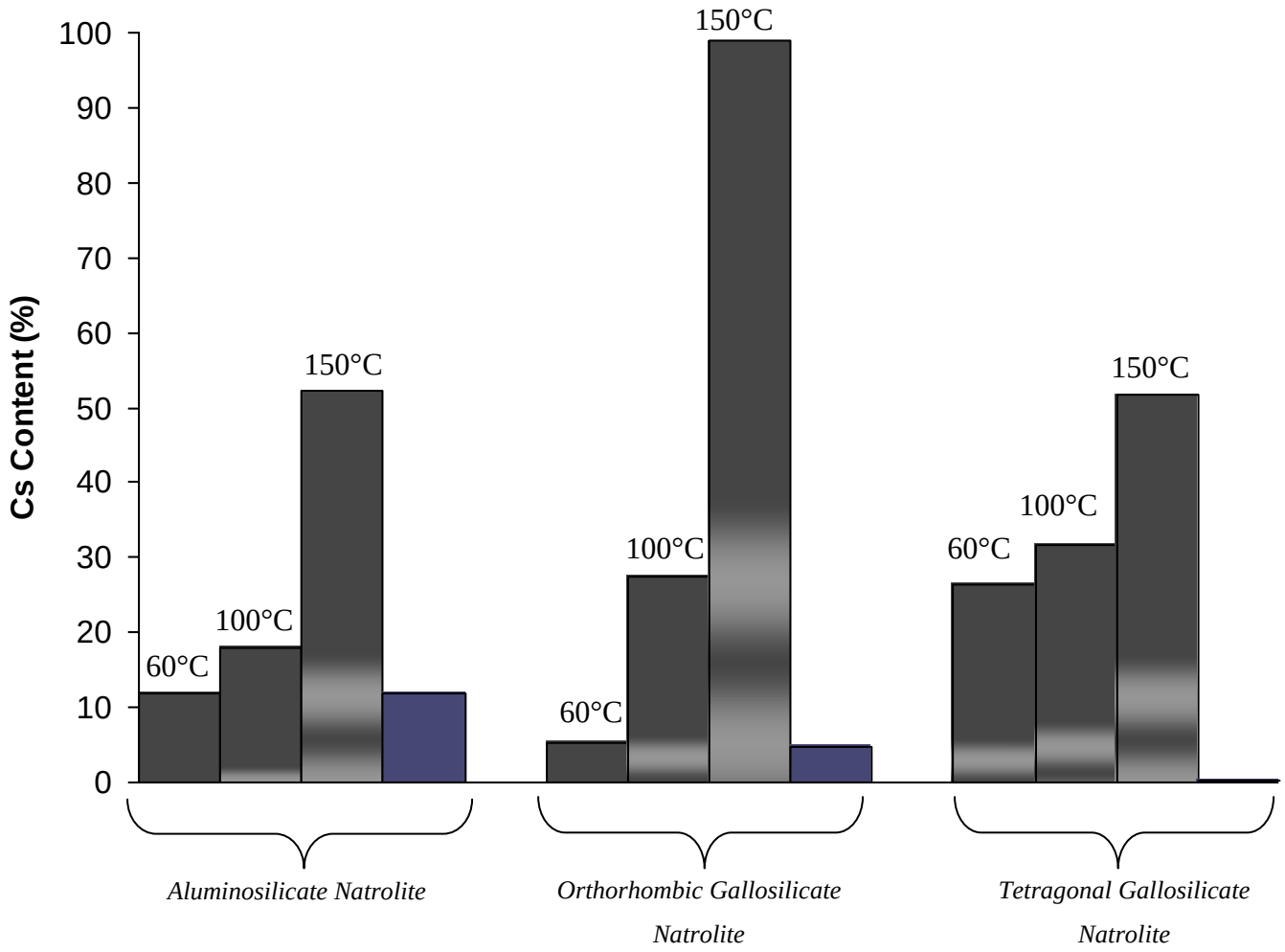

Figure 5: Graphical representation of the percentage of Na^+ replaced with Cs^+ in Quickpress ion exchange experiments using both alumino- and gallosilicate natrolite. *Grey columns* = experiments performed at 1 GPa over temperatures 60-150°C inclusive, *Blue columns* = *b*ack-exchange of the sample from the optimum run of 100°C/1 GPa.

Table 3: Summarised cell volume data for Quickpress, high pressure temperature dependence tests performed on three forms of natrolite. These data are calculated using ChekCell software from PXRD (Bruker D5000).[b]

	Sample I.D.	Treatment*	V	esd's (x100)	V_0	V/V_0*	Increase from V_0 (%)
AlSi-NAT	NAT	none	2244.30	0.566	2244.30	1.0000	0.00
	NATQP60-60	60°C	α				
	NATQP100-60	100°C	2250.82	0.401	2244.30	1.0029	0.29
	NATQP100-60R	§	2250.26	0.203	2244.30	1.0027	0.27
	NATQP150-60	150°C	†				
Orthorhombic Na-GaSi-NAT	GLL68	none	2310.07	0.756	2310.07	1.0000	0.00
	GLL68QP60-60	60°C	α				
	GLL68QP100-60	100°C	2317.92	0.645	2310.07	1.0034	0.34
	GLL68QP100-60R	§	‡				
	GLL68QP150-60	150°C	†				
Tetragonal Na-GaSi-NAT	GLL56	none	1165.19	0.876	1165.19	1.0000	0.00
	GLL56QP60-60	60°C	α				
	GLL56QP100-60	100°C	1165.30	0.823	1165.19	1.0001	0.01
	GLL56QP100-60R	§	‡				
	GLL56QP150-60	150°C	†				

* Unless otherwise stated, experiments were performed using saturated CsCl solution at a pressure of 1GPa, for 60 min.

† Sample shows framework decomposition so assessment of accurate cell parameter information in not possible.

§ Ambient pressure back-exchange experiment, performed in a NaCl(aq) reflux over 24 hours.

‡ Sample size following PXRD, SEM EDX, NaCl(aq) reflux was too small to recover for PXRD of the back-exchanged portion of the sample.

α Low level ion exchange values from SEM EDX.

[b] Samples for PXRD are very small, sometimes a few grains, so diffraction pattern collection (even with long run, short step size collection), gave some patterns with poor signal to noise ratios; so chekcell volume calculations should be considered with some error parameters.

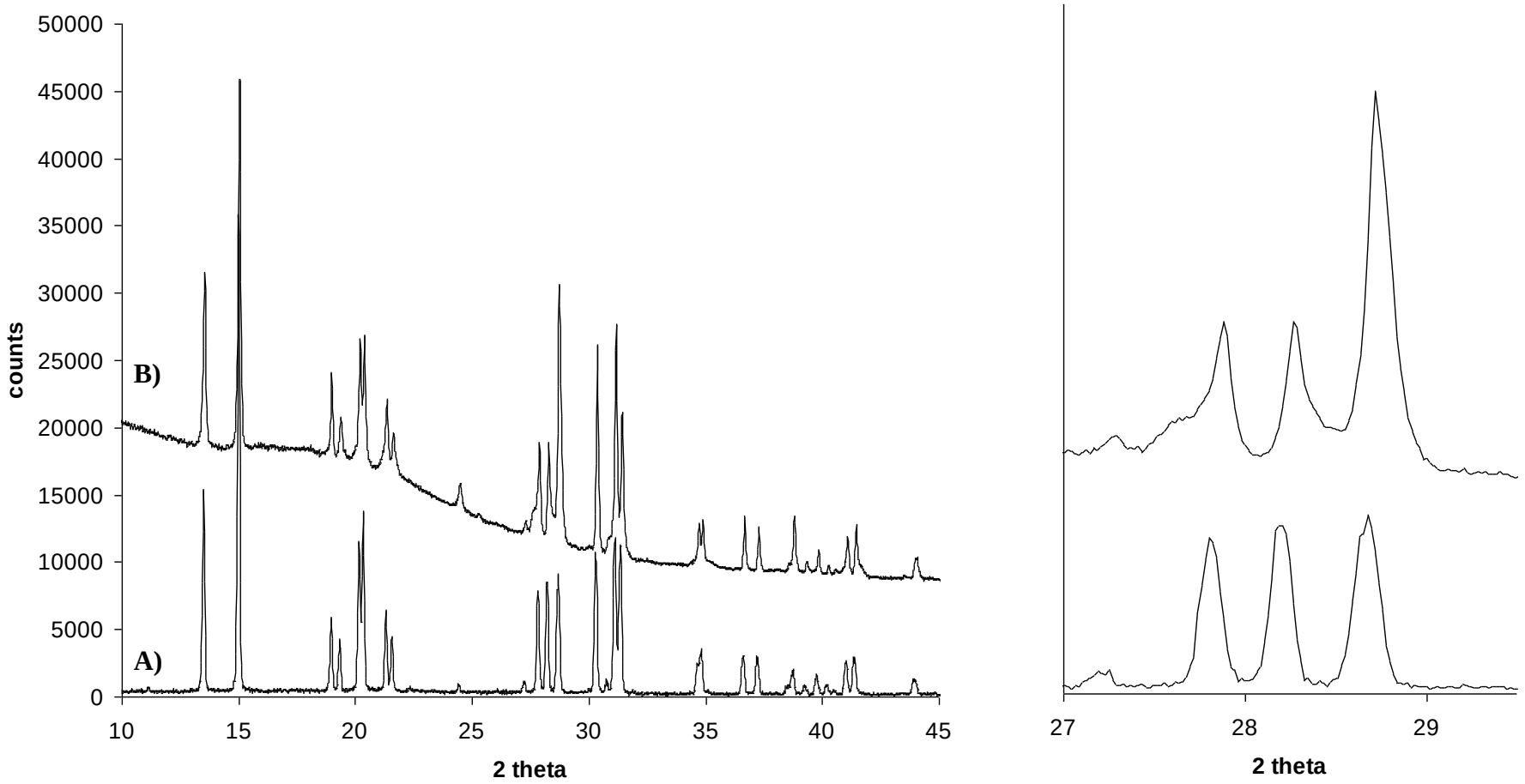

Figure 6: PXRD patterns of a) Untreated Na-Al-NAT and b) Na-Al-NAT post Cs leaching reflux experiments. Back-exchanged sample from that initially exposed to a saturated solution of CsCl for 60minutes, under hydrostatic pressure (1 GPa), at 100°C (NATQP100-60R).

Discussion of Temperature Dependence Results

Aluminosilicate Natrolite

From a starting sample of aluminosilicate natrolite, with reasonably ideal composition (Table 2 and Figure 2), experiments performed at 60 and 100°C show little deviation from ideal stoichiometery other than variation in the cation character. Minimal dealumination/decomposition of the framework has occurred during high pressure exchange, this is supported by the T atom ratio (which remains relatively stable), and by comparison of the respective PXRD patterns (Figure 2). By closer examination of the PXRD pattern we can see some definite shifts in relative intensity in the 2θ region of 27-29° (Figure 2). These shifts support the SEM EDX results which indicate partial replacement of Na cations with Cs cation.

In Quickpress experiments performed at 150°C we see high exchange levels (Figure 5), and a T atom ratio very similar to the starting sample. This initially suggests structural integrity of the aluminosilicate framework and a very successful high pressure exchange. However, when examining the PXRD pattern of this sample we see some possible decomposition phase peaks emerging along with slight loss of crystallinity. Although, as expected, the higher temperature yields a greater % Na replacement, we cannot assume that this is by means of the natrolite pores, as we see some decomposition of the framework. Based upon these findings, this temperature will not be used in further, optimisation experiments.

Of the two temperatures (60 and 100°C) which show little/no framework decomposition, those at 100°C show the greatest amount of exchange. This temperature seems the obvious choice for further investigation in the pursuit of process optimisation. To test cation trapping success, ambient pressure leaching in the form of a NaCl(aq) reflux, was performed on this sample. The SEM EDX results obtained for this back-exchange indicated only a very small deviation in T atom ratio and slight reduction in Cs content (Table 2 and Figure 5). This could be the first evidence of high pressure cation trapping.

After Quickpress treatment at 100°C, 1 GPa, over 60 min, aluminosilicate natrolite shows a cesium exchange of 18 % and a definite cell volume increase from 2244.30(6) to 2250.82(4) (see Table 3). After Ion leaching studies, Cs content drops down to 12%, but the cell volume remains relatively constant at 2250.26. Therefore we can conclude that Cs was successfully introduced into the aluminosilicate framework, with the loss of 6% Cs during reflux; an amount which could be attributed to loss of surface cations as there is no change to the cell volume. There is a definite shift in the relative peak intensities post high pressure exchange and sequential reflux leaching, compared to untreated aluminosilicate natrolite (Figure 6). This adds further weight to the idea that the exchanged Cs content has remained in the structure and is effectively 'trapped' because of the novel method of high pressure insertion.

Gallosilicate Natrolite

From the values shown in Table 2 and the graphical representation in Figure 5, we can compare the amount of Na replacement in alumino- and gallosilicate natrolite with temperature.

At 60°C the amount of exchange at 1GPa follows expectations of tet Ga-NAT> Al-NAT>orth Ga-NAT. This trend (based upon pore dimensions at 1 GPa) was discussed earlier within this chapter. The amount of high pressure exchange occurring at this temperature is still very low and so 60°C will not be used in further high pressure exchange optimisation experiments.

As assumed, a temperature increase to 100°C thermally drives an increase in the amount of exchange seen. More specifically, we see a slight increase in the amount of exchange seen in the orthorhombic gallosilicate from compared to the aluminosilicate from. This is contrary to the predicted pattern of exchange at 1 GPa, based upon pore dimensions. The slight differences from the predicted pattern can be accounted for by the emergence of some decomposition peaks in the PXRD pattern of the orthorhombic gallosilicate sample

run at 100°C (Figure 3). Tetragonal Na-GaSi-NAT shows the highest amount of exchange, as expected (32% at 100°C). However, back-exchange experiments performed upon samples treated at 100°C/1 GPa, showed that almost all high pressure ion exchange was leachable at ambient pressures for both forms of Na-GaSi-NAT.

In Quickpress experiments performed at 150°C, SEM EDX results would lead us to believe that almost total exchange had occurred in both gallosilicate samples at this temperature. However, we also see in the PXRD pattern some new peaks (as yet unassigned) which could be a new phase or simply decomposition product. So although, as expected, the higher temperature yields a greater % Na replacement, we cannot assume that this is by means of the gallosilicate-natrolite structure since a significant portion of "decomposition product" maybe partly or wholly responsible for these results.

In a compromise between degree of decomposition and percentage Na exchange, the samples used at 100°C were deemed suitable for a back-exchange study in which Cs exchanged Na-GaSi-NAT was refluxed in a NaCl solution for 24 hours. For the orthorhombic form, the SEM EDX results obtained for this back-exchange indicates significant degradation of the framework, shown in a divergence of the T atom ratio to 3.75. Little to no framework degradation upon back exchange is seen in the SEM EDX results for the tetragonal form; as the T atom ratio remains relatively stable (Table 2). However, almost total loss of exchanged ions was seen during these back-exchange tests, i.e. no pressure trapping occurs.

7.2.2.2 Time Dependence

From the previous results, the optimum high pressure exchange temperature was established as 100°C. Generally higher temperatures showed structural decomposition and lower gave very little exchange at all. In this section, further tests were performed at 100°C with the aim of maximising the amount of exchange/ion trapping by exploring the effect of high pressure exchange time. As in previous tests, PXRD and SEM EDX results will be used to determine the extent of exchange. Tests were performed at / 1 GPa, 100°C, in a saturated CsCl solution for 30, 60, 150 or 270 minutes with Al-NAT, orthorhombic Na-GaSi-NAT and tetragonal Na-GaSi-NAT. Post high pressure exchange, ion-leaching test (via reflux with NaCl(aq) solution), were performed on all samples.

Table 4: High pressure (Quickpress) Na/Cs ion exchange for Na-Al-NAT. SEM EDX compositional results and experimental treatment with variation of exchange time.

		Sample	Treatment	Pressure (GPa)	Time (hours)	Calculated Unit Cell Composition *,†	T atom ratio ‡	Cs+ (%) §	Cs/Na
Ideal Stoichiometery	**Al-Si-NAT** $Na_{16}Al_{16}Si_{24}O_{80}$	NAT	None	-	-	$\mathbf{Na_{14.37}Si_{24}Al_{14.97}O_{77.95}}$	1.60	-	-
		NATQP100-30	QP	1	0.5	$\mathbf{Na_{11.57}Cs_{3.65}Si_{24}Al_{14.31}O_{76.62}}$	1.68	23.98	0.32
		NATQP100-30R	Back-exchange of NATQP100-30**	ambient	24	$\mathbf{Na_{10.98}Cs_{3.33}Si_{24}Al_{14.01}O_{76.01}}$	1.71	23.29	0.30
		NATQP100-60	QP	1	1	$\mathbf{Na_{11.45}Cs_{2.49}Si_{24}Al_{14.41}O_{76.82}}$	1.67	17.86	0.22
		NATQP100-60R	Back-exchange of NATQP100-60**	ambient	24	$\mathbf{Na_{11.28}Cs_{1.52}Si_{24}Al_{13.03}O_{74.07}}$	1.84	11.86	0.14
		NATQP100-150	QP	1	2.5	$\mathbf{Na_{12.19}Cs_{3.85}Si_{24}Al_{15.02}O_{78.04}}$	1.60	23.99	0.32
		NATQP100-150R	Back-exchange of NATQP100-150**	ambient	24	$\mathbf{Na_{11.32}Cs_{3.36}Si_{24}Al_{14.47}O_{77.55}}$	1.63	22.90	0.30
		NATQP100-270	QP	1	4.5	$\mathbf{Na_{9.39}Cs_{6.98}Si_{24}Al_{14.69}O_{77.37}}$	1.64	42.69	0.75
		NATQP100-270R	Back-exchange of NATQP100-270**	ambient	24	$\mathbf{Na_{11.04}Cs_{5.41}Si_{24}Al_{15.27}O_{78.53}}$	1.58	32.90	0.49

QP=High pressure Quickpress treatment with $CsCl_{(aq)}$

* Calculated from SEM EDX compositional analysis. Composition averaged over ≥ 3 EDX scans, each over a $2mm^2$ sample area. Compositions should not be regarded as absolute. Interpretation of SEM EDX compositional results should account for matrix effects and should always be used in conjunction with supporting PXRD results.

** Back exchange via $NaCl_{(aq)}$ reflux at 100°C

† Oxygen content estimated based upon T atom content.

‡ T=Si/Al or Ga.

§ Calculated as a percentage of the total cation content after treatment.

Table 5: High pressure (Quickpress) Na/Cs ion exchange for orthorhombic Na-GaSi-NAT. SEM EDX compositional results and experimental treatment with variation of exchange time.

		Sample	Treatment	Pressure (GPa)	Time (hours)	Calculated Unit Cell Composition *,†	T atom ratio ‡	Cs+ (%) §	Cs/Na
Ideal Stoichiometery	**Ga-Si-NAT (orth)** $Na_{16}Ga_{16}Si_{24}O_{80}$	GLL68	None	-	-	$\mathbf{Na_{16.16}Si_{24}Ga_{16.02}O_{80.04}}$	1.51	-	-
		GLL68QP100-30	QP	1	0.5	$\mathbf{Na_{11.32}Cs_{1.59}Si_{24}Ga_{13.07}O_{74.14}}$	1.84	12.34	0.14
		GLL68QP100-30R	Back-exchange of GLL68QP100-30**	ambient	24	$\mathbf{Na_{13.13}Cs_{0.17}Si_{24}Ga_{14.33}O_{76.66}}$	1.68	1.27	0.01
		GLL68QP100-60	QP	1	1	$\mathbf{Na_{9.19}Cs_{3.50}Si_{24}Ga_{19.23}O_{86.46}}$	1.25	27.58	0.38
		GLL68QP100-60R	Back-exchange of GLL68QP100-60**	ambient	24	$\mathbf{Na_{13.57}Cs_{0.68}Si_{24}Ga_{6.41}O_{60.83}}$	3.75	4.77	0.05
		GLL68QP100-150	QP	1	2.5	$\mathbf{Na_{10.91}Cs_{3.01}Si_{24}Ga_{13.85}O_{75.69}}$	1.73	21.65	0.28
		GLL68QP100-150R	Back-exchange of GLL68100-150**	ambient	24	$\mathbf{Na_{10.86}Cs_{1.16}Si_{24}Ga_{12.62}O_{73.25}}$	1.90	9.63	0.11
		GLL68QP100-270	QP	1	4.5	$\mathbf{Na_{10.32}Cs_{2.71}Si_{24}Ga_{19.57}O_{87.14}}$	1.23	20.94	0.26
		GLL68QP100-270R	Back-exchange of GLL68P100-270**	ambient	24	$\mathbf{Na_{11.14}Cs_{1.69}Si_{24}Ga_{16.88}O_{81.76}}$	1.42	13.15	0.15

QP=High pressure Quickpress treatment with $CsCl_{(aq)}$

* Calculated from SEM EDX compositional analysis. Composition averaged over ≥ 3 EDX scans, each over a $2mm^2$ sample area. Compositions should not be regarded as absolute. Interpretation of SEM EDX compositional results should account for matrix effects and should always be used in conjunction with supporting PXRD results.

** Back exchange via $NaCl_{(aq)}$ reflux at 100°C

† Oxygen content estimated based upon T atom content.

‡ T=Si/Al or Ga.

§ Calculated as a percentage of the total cation content after treatment.

Table 6: High pressure (Quickpress) Na/Cs ion exchange for tetragonal Na-GaSi-NAT. SEM EDX compositional results and experimental treatment with variation of exchange time.

		Sample	Treatment	Pressure (GPa)	Time (hours)	Calculated Unit Cell Composition *,†	T atom ratio ‡	Cs+ (%) §	Cs/Na
Ideal Stoichiometery	**Ga-Si-NAT (tet)** $Na_8Ga_8Si_{12}O_{40}$	GLL56	None	-	-	$\mathbf{Na_{5.24}Si_{12}Ga_{9.33}O_{42.67}}$	1.29	-	-
		GLL56QP100-30	QP	1	0.5	$\mathbf{Na_{5.79}Cs_{0.81}Si_{12}Ga_{6.42}O_{36.85}}$	1.87	12.34	0.14
		GLL56QP100-30R	Back-exchange of GLL56QP100-30**	ambient	24	$\mathbf{Na_{5.90}Cs_{0.16}Si_{12}Ga_{6.41}O_{36.81}}$	1.88	2.58	0.03
		GLL56QP100-60	QP	1	1	$\mathbf{Na_{4.46}Cs_{2.08}Si_{12}Ga_{8.34}O_{40.69}}$	1.44	31.73	0.46
		GLL56QP100-60R	Back-exchange of GLL56QP100-60**	ambient	24	$\mathbf{Na_{5.48}Cs_{0.01}Si_{12}Ga_{8.56}O_{41.12}}$	1.40	0.13	0.00
		GLL56QP100-150	QP	1	2.5	$\mathbf{Na_{5.31}Cs_{1.95}Si_{12}Ga_{6.53}O_{37.05}}$	1.84	26.81	0.37
		GLL56QP100-150R	Back-exchange of GLL56QP100-150**	ambient	24	$\mathbf{Na_{5.92}Cs_{0.34}Si_{12}Ga_{6.51}O_{37.03}}$	1.84	5.46	0.06
		GLL56QP100-270	QP	1	4.5	$\mathbf{Na_{5.98}Cs_{1.40}Si_{12}Ga_{8.13}O_{40.25}}$	1.48	19.02	0.24
		GLL56QP100-270R	Back-exchange of GLL56QP100-270**	ambient	24	$\mathbf{Na_{5.12}Cs_{0.28}Si_{12}Ga_{8.77}O_{41.54}}$	1.37	5.18	0.05

QP=High pressure Quickpress treatment with $CsCl_{(aq)}$

* Calculated from SEM EDX compositional analysis. Composition averaged over ≥ 3 EDX scans, each over a $2mm^2$ sample area. Compositions should not be regarded as absolute. Interpretation of SEM EDX compositional results should account for matrix effects and should always be used in conjunction with supporting PXRD results.

** Back exchange via $NaCl_{(aq)}$ reflux at 100°C.

† Oxygen content estimated based upon T atom content.

‡ T=Si/Al or Ga.

§ Calculated as a percentage of the total cation content after treatment.

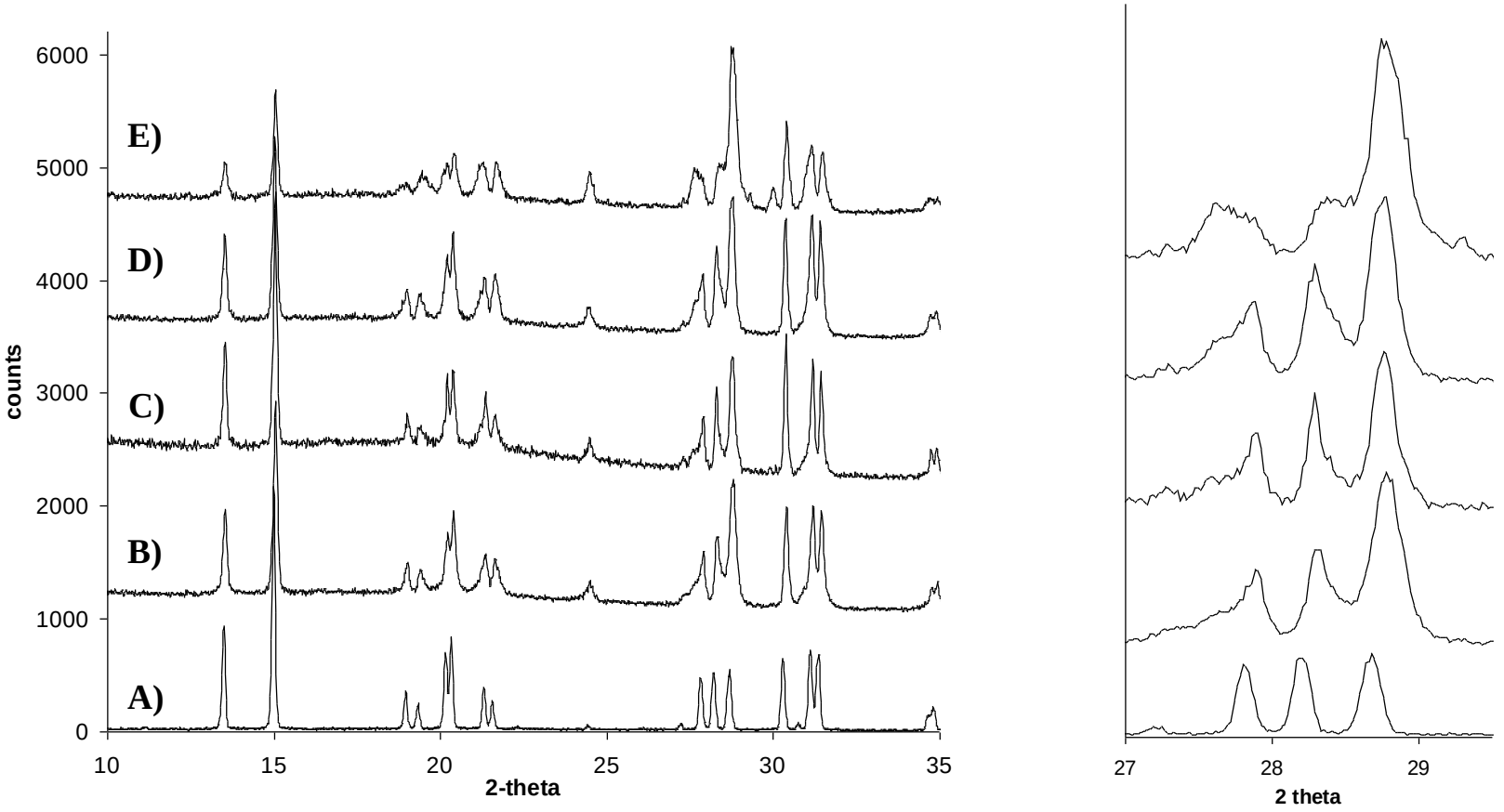

Figure 7: PXRD patterns of a) Na-Al-NAT and b-e) Na-Al-NAT exposed to a saturated solution of CsCl for 30, 60, 150 or 270 minutes respectively. Runs b-e were performed under hydrostatic pressure (1 GPa), at a temperature of 100°C. A zoom-in of selected peaks shows a change in relative peak intensities.

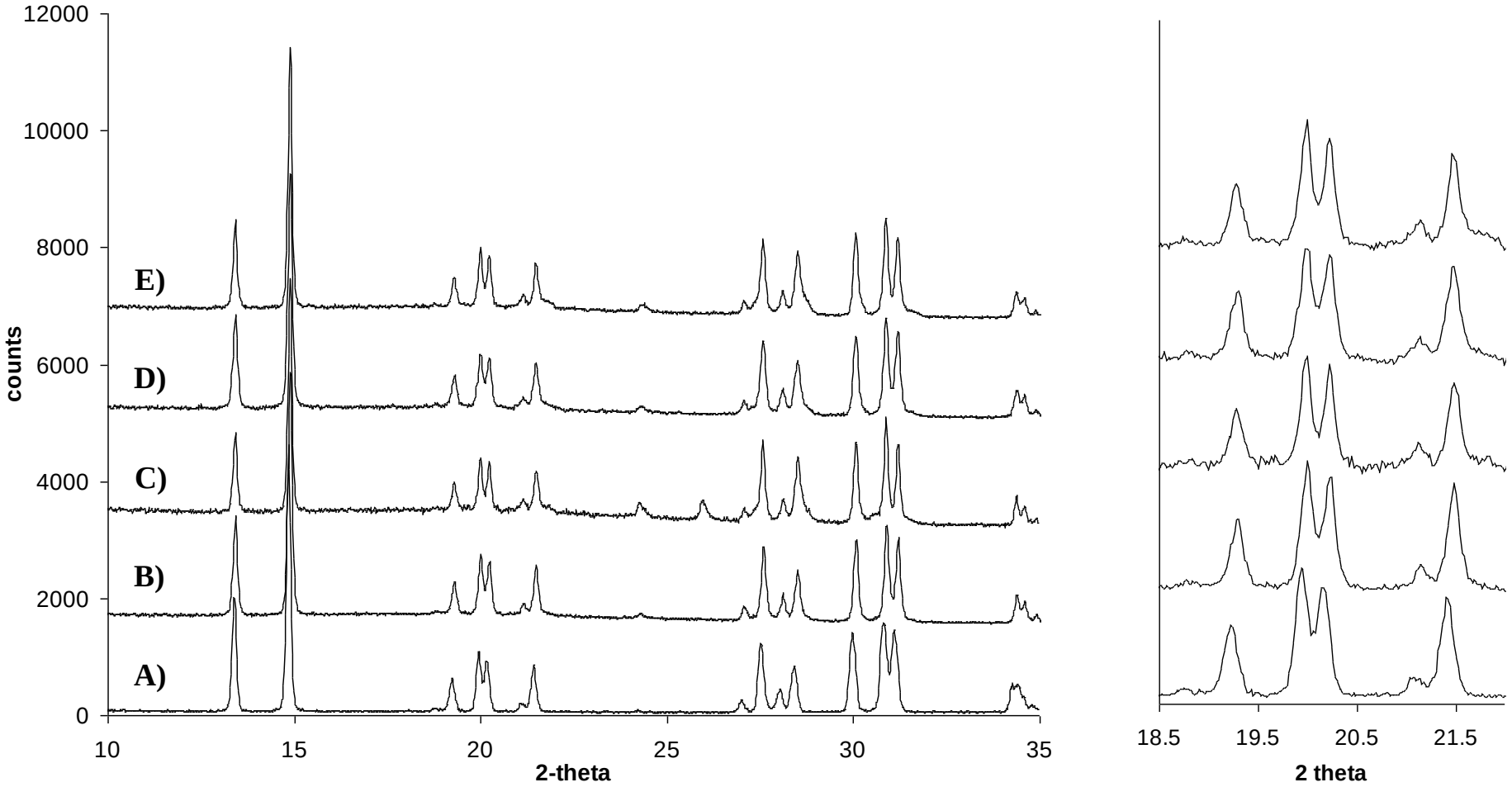

Figure 8: PXRD patterns of a) orthorhombic Na-GaSi-NAT and b-e) orthorhombic Na-GaSi-NAT exposed to a saturated solution of CsCl for 30, 60, 150 or 270 minutes respectively. Runs b-e were performed under hydrostatic pressure (1 GPa), at a temperature of 100°C.

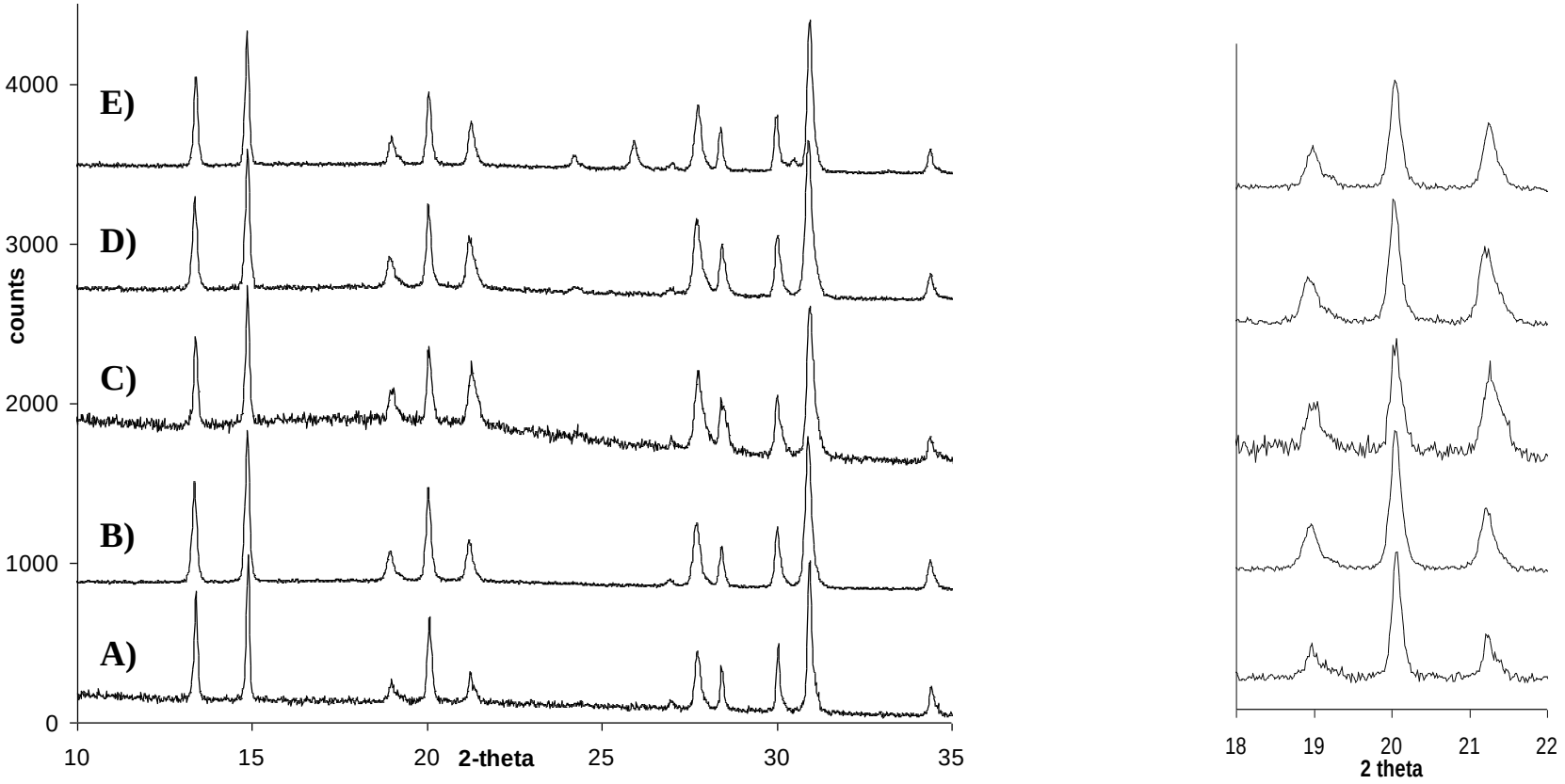

Figure 9: PXRD patterns of a) tetragonal Na-GaSi-NAT and b-e) tetragonal Na-GaSi-NAT exposed to a saturated solution of CsCl for 30, 60, 150 or 270 minutes respectively. Runs b-e were performed under hydrostatic pressure (1 GPa), at a temperature of 100°C. A zoom-in of selected peaks shows a slight change in relative peak intensities.

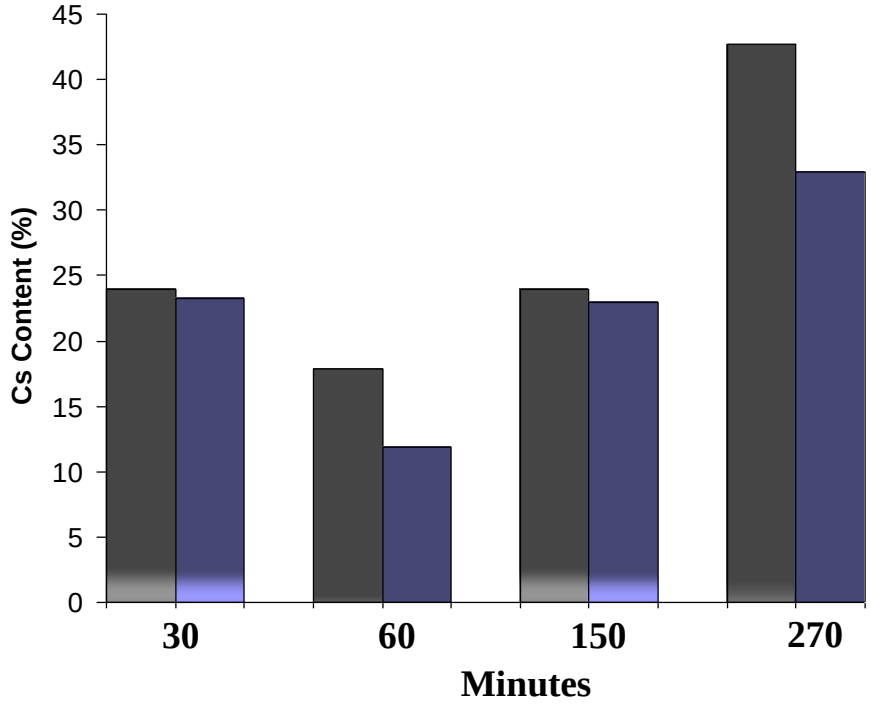
45
40
35
30
25
20
15
10
5
0
Cs Content (%)
30
60
150
270
Minutes

A)

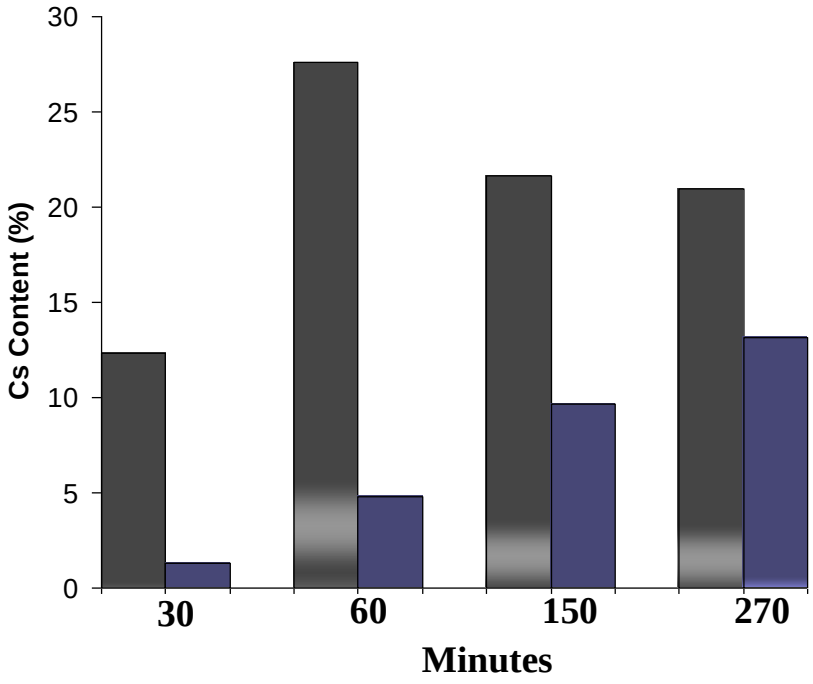
30
25
20
15
10
5
0
Cs Content (%)
30
60
150
270
Minutes

B)

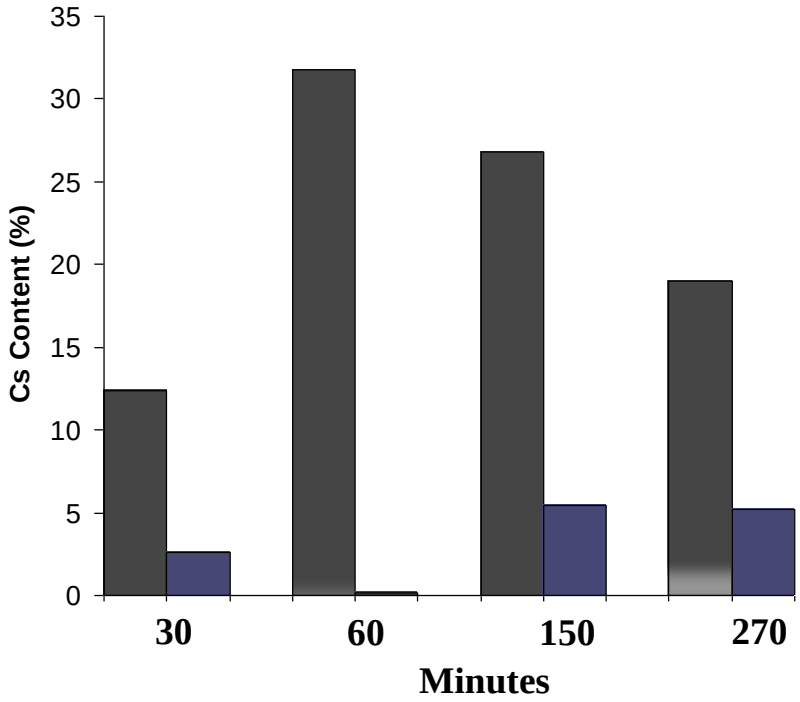

C)

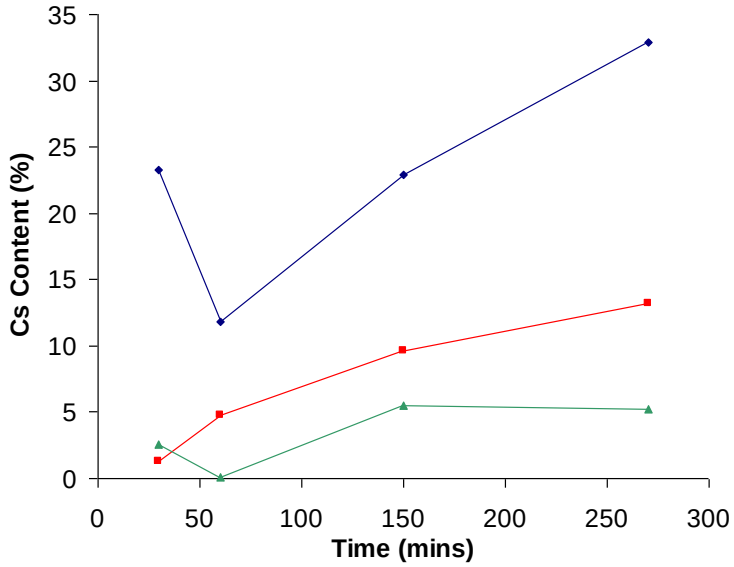

D)

Figure 10: The percentage cesium content of Quickpress ion exchange samples A) Al-NAT, B) orthorhombic Na-GaSi-NAT and C) tetragonal Na-GaSi-NAT. Samples treated at 10Kbar/1GPa, 100°C for 30-270 minutes (grey columns). Ambient pressure back-exchange samples (blue columns). D) A comparison of the percentage cesium content remaining after back-exchange experiments for Al-NAT (blue), orthorhombic Na-GaSi-NAT (red) and tetragonal Na-GaSi-NAT (green).

Table 7: Summarised cell volume data for Quickpress, high pressure time dependence tests performed on three forms of natrolite. These data are calculated using ChekCell software from PXRD (Bruker D5000).[c]

	Sample I.D.	Treatment series	V	esd's (x100)	V_0	V/V_0*	Increase from V_0 (%)
Al-Si-NAT	NAT	time Cs/Na	2244.30	0.566	2244.30	1.0000	0.00
	NATQP100-30	time Cs/Na	2256.10	0.435	2244.30	1.0053	0.53
	NATQP100-30R	time Cs/Na	2252.63	0.807	2244.30	1.0067	0.37
	NATQP100-60	time Cs/Na	2250.82	0.401	2244.30	1.0029	0.29
	NATQP100-60R	time Cs/Na	2250.26	0.203	2244.30	1.0027	0.27
	NATQP100-150	time Cs/Na	2256.36	0.566	2244.30	1.0054	0.54
	NATQP100-150R	time Cs/Na	2255.99	0.392	2244.30	1.0052	0.52
	NATQP100-270	time Cs/Na	2254.37	1.087	2244.30	1.0045	0.45
	NATQP100-270R	time Cs/Na	2256.39	1.08	2244.30	1.0054	0.54
Orthorhombic Na-GaSi-NAT	GLL68	time Cs/Na	2310.07	0.76	2310.07	1.0000	0.00
	GLL68QP100-30	time Cs/Na	2314.12	0.356	2310.07	1.0018	0.18
	GLL68QP100-30R	time Cs/Na	2316.96	0.384	2310.07	1.0030	0.30
	GLL68QP100-60	time Cs/Na	2317.92	0.645	2310.07	1.0034	0.34
	GLL68QP100-60R	time Cs/Na	*		2310.07		
	GLL68QP100-150	time Cs/Na	2316.46	0.375	2310.07	1.0028	0.28
	GLL68QP100-150R	time Cs/Na	2317.31	0.322	2310.07	1.0031	0.31
	GLL68QP100-270	time Cs/Na	2316.09	0.547	2310.07	1.0026	0.26
	GLL68QP100-270R	time Cs/Na	2318.30	0.794	2310.07	1.0036	0.36

[c]Samples for PXRD are very small, sometimes a few grains, so diffraction pattern collection (even with long run, short step size collection), gave some patterns with poor signal to noise ratios; so chekcell volume calculations should be considered with some error parameters.

Tetragonal Na-GaSi-NAT	GLL56	time Cs/Na	1165.19	0.566	1165.19	1.0000	0.00
	GLL56QP100-30	time Cs/Na	1172.70	0.435	1165.19	1.0064	0.64
	GLL56QP100-30R	time Cs/Na	1170.38	0.807	1165.19	1.0045	0.45
	GLL56QP100-60	time Cs/Na	1165.30	0.401	1165.19	1.0001	0.01
	GLL56QP100-60R	time Cs/Na	*	0.203			
	GLL56QP100-150	time Cs/Na	1170.28	0.566	1165.19	1.0044	0.44
	GLL56QP100-150R	time Cs/Na	1172.28	0.392	1165.19	1.0061	0.61
	GLL56QP100-270	time Cs/Na	1168.72	1.087	1165.19	1.0030	0.30
	GLL56QP100-270R	time Cs/Na	1169.79	1.08	1165.19	1.0039	0.39

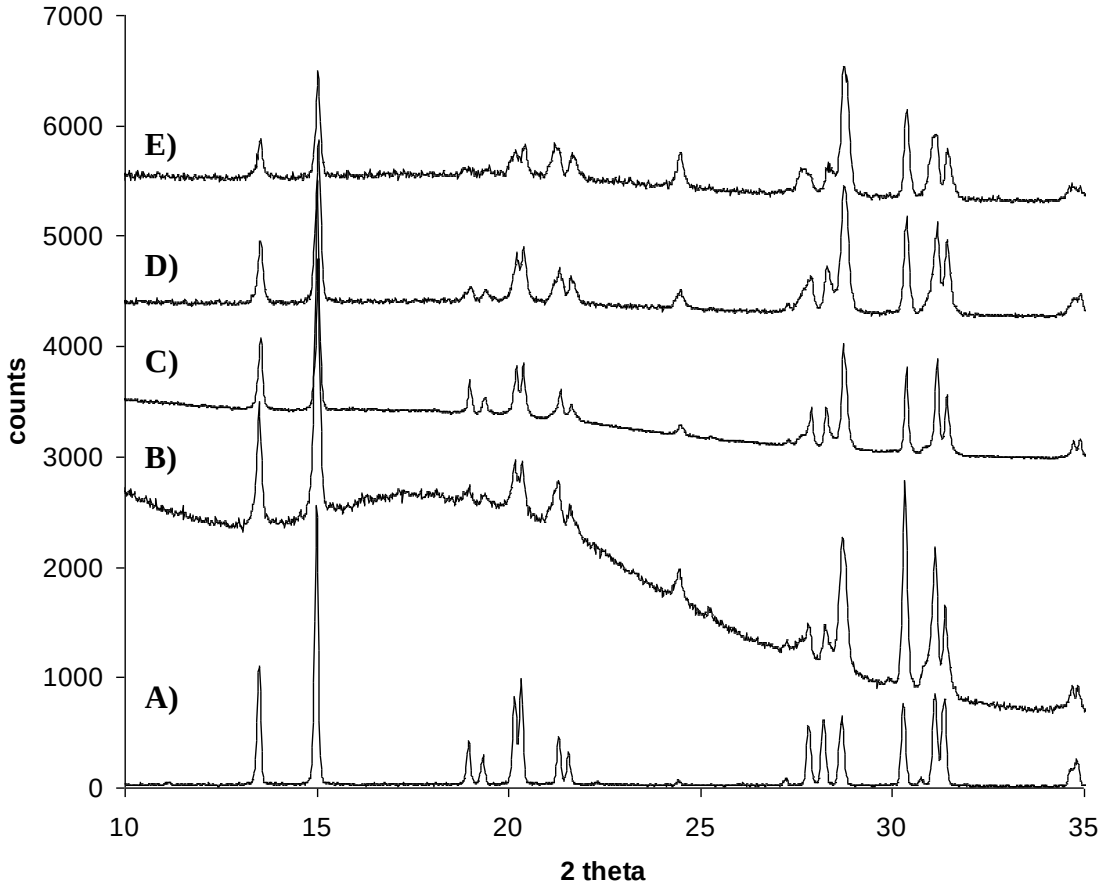

Figure 11: PXRD patterns of a) Untreated Na-Al-NAT and b-d) Na-Al-NAT post Cs leaching reflux experiments. Back-exchanged samples from those initially exposed to a saturated solution of CsCl for 30, 60, 150 or 270 minutes, under hydrostatic pressure (1 GPa), at a temperature of 100°C. b-d) NATQP100-30R, NATQP100-60R, NATQP100-150R and NATQP100-270R respectively.

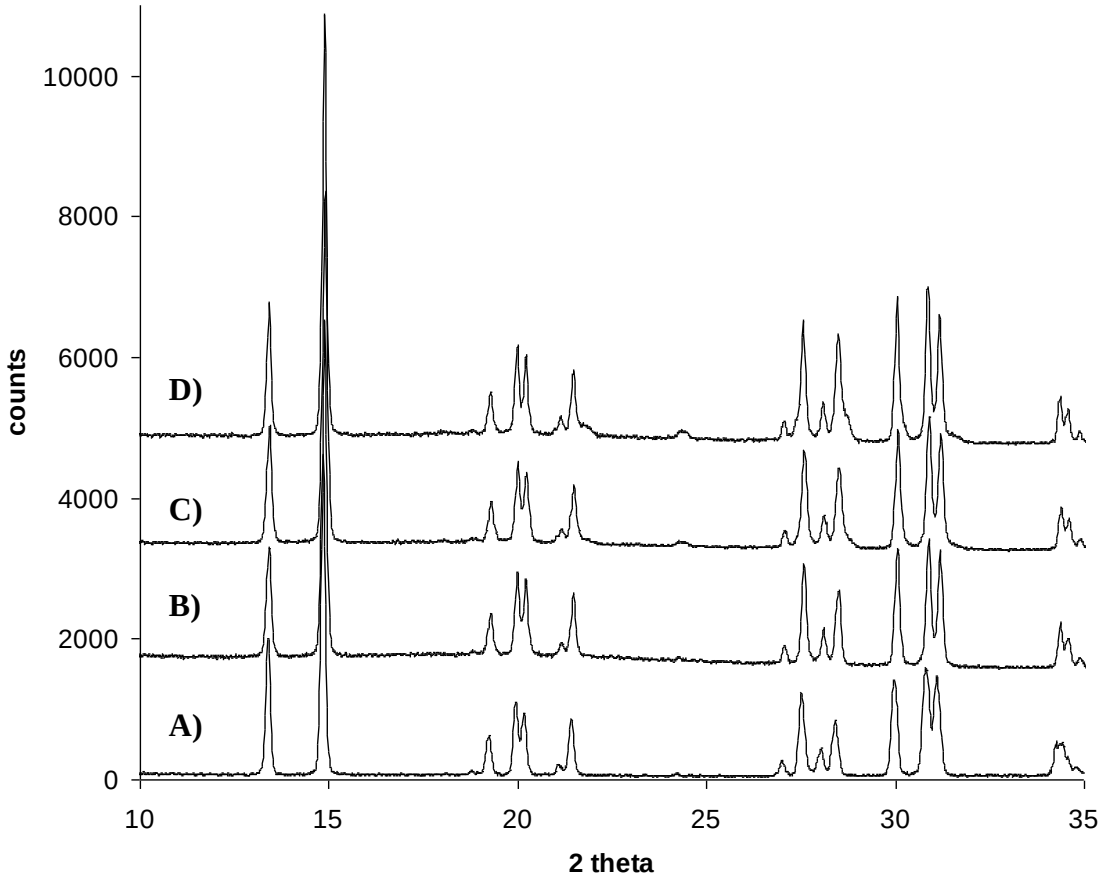

Figure 12: PXRD patterns of a) Untreated orthorhombic Na-GaSi-NAT and b-d) orthorhombic Na-GaSi-NAT post Cs leaching reflux experiments. Back-exchanged samples from those initially exposed to a saturated solution of CsCl for 30, 150 or 270 minutes, under hydrostatic pressure (1 GPa), at a temperature of 100°C. b-d) GLL68QP100-30R, GLL68QP100-150R and GLL68QP100-270R respectively.

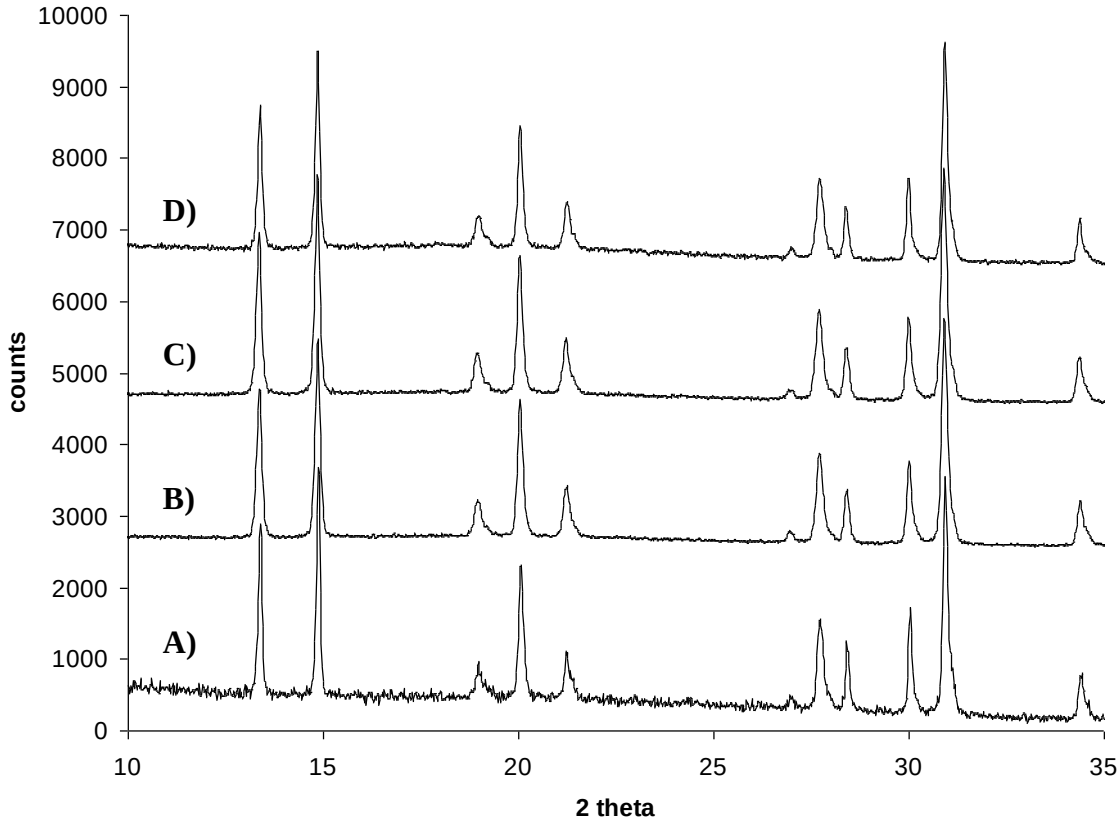

Figure 13: PXRD patterns of a) Untreated tetragonal Na-GaSi-NAT and b-d) tetragonal Na-GaSi-NAT post Cs leaching reflux experiments. Back-exchanged samples from those initially exposed to a saturated solution of CsCl for 30, 150 or 270 minutes, under hydrostatic pressure (1 GPa), at a temperature of 100°C. b-d) GLL56QP100-30R, GLL56QP100-150R and GLL56QP100-270R respectively.

Discussion of Time Dependence Results

Al-NAT

In previous high pressure exchange tests performed at 100°C, Al-NAT showed measurable high pressure exchange and ion-trapping character. Changing the amount of time the sample is exposed to the exchange fluid at high pressure and temperature has been shown to make a difference in both the amount of Cs exchange and the amount of Cs trapped in the framework (post back-exchange tests). In Table 4 the SEM EDX results are given as the time is changed from 30, 60, 150 to 270 minutes; with corresponding SEM EDX results post back-exchange testing. A maximum exchange of 43%, which drops to 33% after reflux back-exchange, was achieved. The difference is likely due in part to the loss of surface adsorbed cations with little if any back-exchange. This is reflected in the cell volume values (Table 7). The cell volume of untreated Al-NAT rises from 2244.30(6) to 2254.37(11). After leach testing of this sample the cell volume stays the same (within reasonable errors), at 2256.39(11). This gives a cell volume increase of approximately 0.45%, due to the insertion and trapping of 33% Cs. The SEM EDX results showing ion loss post-leaching are likely explained by washing off of surface adsorbed Cs as the cell volume is unaffected.

This maximum exchange was achieved after high pressure exposure to CsCl solution for 270 minutes. For Al-NAT there is a general trend in the amount of cation trapping with exposure time (Figure 10 a and d). This trend (within errors), shows an increase in trapping with exposure time. The results obtained for the run performed with a 30 minute exposure time does not fit with the general trend and should be repeated. However, results for this point are not unreasonable with a slight discrepancy probably due to inconsistency in the preparation or performance of experiments (as experiments were performed with large time intervals between each batch and new equipment pieces were used in each batch run).

Supporting this conclusion of successful, time dependant cation trapping character is evidence from PXRD patterns, which show definite and significant relative peak

intensity shifts post-exchange (Figure 7). These relative peak intensity shifts remained after the back exchange experiments (Figure 11).

Orthorhombic Na-GaSi-NAT

Orthorhombic Na-GaSi-NAT showed a very similar pattern to that of Al-NAT (see Figure 10 b and d). The amount of Cs remaining in the framework after back-exchange tests shows a general increase with increased exposure time.

From 30 min to 270 min the amount of exchanged Cs trapped within the framework increases. This is evident from the SEM EDX values reported in Table 5, which show an increase from 1.3% to 13% Cs trapping from 30 to 270 min. This is supported by Cell volume calculation (Table 7). At the maximum Cs trapping (270 min) the cell volume changes from 2310.07(8) (untreated), to 2316.09(5). After ion leaching tests, by exposure to a NaCl(aq) reflux, the cell volume remains the same (within reasonable errors) at 2318.30(8). This gives a cell volume increase of approximately 0.36%, due to the insertion and trapping of 13% Cs.

PXRD patterns of the high pressure treated and the back exchange treated samples (Figure 8 and Figure 12 respectively), show no evidence of decomposition (previously a problem at higher temperatures); with the only exception seen as an isolated result for the 60 min run (where some very small decomposition peaks can be seen emerging). It is difficult to decipher any shift in relative intensity in these series of PXRD patterns, but a slight shift in 2-theta values from the untreated sample values is evident in both the high pressure sequence and the back exchange sequence of PXRD patterns. This indicates a change in cell volume i.e. large Cs ion insertion has increased the cell volume parameter.

Tetragonal Na-GaSi-NAT

As with the other two natrolite forms, we see a general pattern of increase in the amount of ion trapping (i.e. Cs content post back-exchange), as exposure time is increased (Figure 10 c and d, Table 6). From 30 to 270 min the amount of Cs trapped within the tetragonal framework increases from 2.6% to 5.2%. At maximum exposure time, SEM EDX results show the highest ion trapping level of 5.2%. The cell volume changes associated with this maximum are 1165.19(9) (untreated), rising to 1168.72(5) after 270 min exposure at high pressure. After ion leaching tests, by exposure to a NaCl(aq) reflux, the cell volume remains the same (within reasonable errors) at 1169.79(6). This gives a cell volume increase of approximately 0.39%, due to the insertion and trapping of 0.52% Cs.

PXRD patterns of high pressure exchange tests are of some value here, as they show a slight shift in the relative intensities of certain peaks i.e. ion exchange has occurred to some extent. This is also evident in the PXRD patterns of back-exchanged samples. So the high level ion leaching upon back-exchange; as evidenced in SEM EDX data (Table 6), must be due to surface ion loss.

Cell volume calculations for this series of tests should be considered to have very high error values. The ChekCell method is a quick, rough refinement. It is assumed that the inconsistencies seen here are due to poor quality PXRD patterns.

7.3 Summary

In this report we have shown the first evidence of high pressure ion exchange and ion trapping upon pressure release. All natrolite samples show a general pattern of increase in ion trapping with increased exposure times (Figure 10). All samples show the highest amount of trapping character at 270 min exposure. When comparing the trapping ability of the three natrolite forms we see that:

Al-NAT>Orth Ga-NAT> Tet Ga-NAT

This follows the trend in framework flexibility and pore size at ambient pressure (discussed in chapter 4 and 5).

PXRD and SEM EDX results provide good evidence for high pressure ion exchange and ion-trapping. Results show that optimum Cs ion trapping occurs when using Al-NAT at 100°C at 1 GPa for 270 min. Further investigation should include extensions of exposure times, re-runs of results to confirm successes and to investigate erratic data (tetragonal cell volume values). Experiments should be performed upon Al-NAT at 1.5 GPa (known optimum pressure for isolation of the superhydrated phase), in order to produce data which is directly comparable to that achieved for the gallosilicate analogues. Of, course investigation into the exchange and trapping of other ions of different sizes should be considered.

[1] Lee Y.; Hriljac J. A.; Kim S. J.; Hanson J. C.; Vogt T. **2003.** *J. Am. Chem. Soc. 125.* 6036-6037.

[2] Unpublished results: Hriljac J. A.; Little G. L.; 'A high pressure neutron study of gallosilicate natrolite'.

[3] Unpublished results: Hriljac J. A.; Little G. L.; 'A high pressure synchrotron X-ray study of gallosilicate natrolite'.

[4] Lee Y.; Vogt T.; Hriljac J. A.; Parise J. B.; Hanson J. C.; Kim S. 'Non-framework cation migration and irreversible pressure-induced hydration in a zeolite' **2002.** *Letters to Nature. 420.* 485-489.

[5] Choudhary A.; Banerjee S. 'Studies of natrolite type natural zeolite and its cation-exchanged and adsorbed derivatives with cadmium (II) and NH_3 and H_2S' **2002**. *J. Indian. Chem. Soc. 79.* 580-582.

[6] Baur W. H.; Kassner D.; Kim C. H.; Sieber N. H. W. **1990.** *European Journal of Mineralogy. 2 (6).* 761-769.

[7] Otsuka R.; Yamazaki A.; Kato K. **1991.** *Thermochimica. Acta. 181*. 45-46.

[8] Yamazaki A.; Kamioka K.; Matsumoto H.; Otsuka R. **1987.** *School Sci. Eng., Waseda University. 118.* 40.

[9] Yamazaki A.; Otsuka R. **1986.** *Thermochimica. Acta. 109*. 237.

[10]Yamazaki A.; Kamioka K.; Matsumoto H.; Otsuka R.; Nendo Kagaku. **1988.** *J. Clay Sci. Soc. Jpn. 28*. 143.

[11] Colligan; M.; Lee; Y.; Vogt; T.; Celestian; A. J.; Parise; J. B.; Marshall; W. B.; Hriljac; J. A. 'High-pressure neutron diffraction study of superhydrated natrolite.' **2005.** *J. Phys. Chem. B. 109*, 18223-18225.

CHAPTER EIGHT

Summary

The aims of this thesis, as indicated in the first chapter, were based upon the structural study of two forms of gallosilicate natrolite; the orthorhombic and the tetragonal forms. These forms differ by the ordering of the T atom sites, Si (two sites) and Ga (one site) order in the orthorhombic form and disorder in the tetragonal form (2 sites of equal occupation). Each is a zeotype and isostructural analogue of the naturally occurring zeolite, aluminosilicate natrolite ($Na_{16}Al_{16}Si_{24}O_{80}.16H_2O$) which exists in the orthorhombic ordered form. There have been some previous reports detailing partial structure studies of these gallosilicates, but not at the level of detail in this thesis.

The orthorhombic form is reasonably well investigated, with inclusion in the ICSD (Inorganic Crystal Structure Database).[1] A previous report of pressure-induced hydration and cell volume expansion (as seen in aluminosilicate natrolite), gave details at a limited number of pressures of Rietveld refined structures including atomic coordinates and bond distances and angles.[2] The work carried out in this thesis includes a similar high pressure synchrotron X-ray diffraction study, but with emphasis on a good number of data points in the pressure region at which superhydration occurs. This has allowed for a more detailed picture of the superhydration transition in the orthorhombic form. This study was discussed in chapter 5, where high pressure experiments were carried out at the 9.5HPT station, Daresbury Laboratory. To date, there are no reports of resolution of the hydrogen positions (associated with inner pore water OW1 and OW2). Chapter 4 gave details of a high pressure neutron diffraction study which elucidated the hydrogen positioning over a number of pressures. This study (never before reported), included 5 pressure increments. Most importantly, this series of high pressure structure resolutions included the ambient pressure phase and the superhydrated phase. As a result of this study the hydrogen bonding network was resolved. This network revealed a very different pattern to that expected. The report mentioned earlier measured the distances between the water oxygens and postulated that the intrapore waters were hydrogen bonded to each other forming water nanotubes which extend through the pore along the *c* axis.[2] The neutron diffraction study carried out in this thesis shows that the water molecules form extensive hydrogen bonds with framework oxygens and some direct hydrogen bonds between water molecules. However, these direct hydrogen bonds occur only across the channels and not within them, and so do not show the proposed

water nanotube formation postulated by Lee *et. al.*[3] At pressures above the superhydration point there is no direct hydrogen bond between water molecules, but a hydrogen bonded link via a framework oxygen. This study disproves the possibility of an intrapore hydrogen bonding network. Structural representations of ambient pressure orthorhombic Na-GaSi-NAT and superhydrated Na-GaSi-NAT are shown in Figure 1, which displays the unit cell with details of hydrogen positioning and hydrogen bonding.

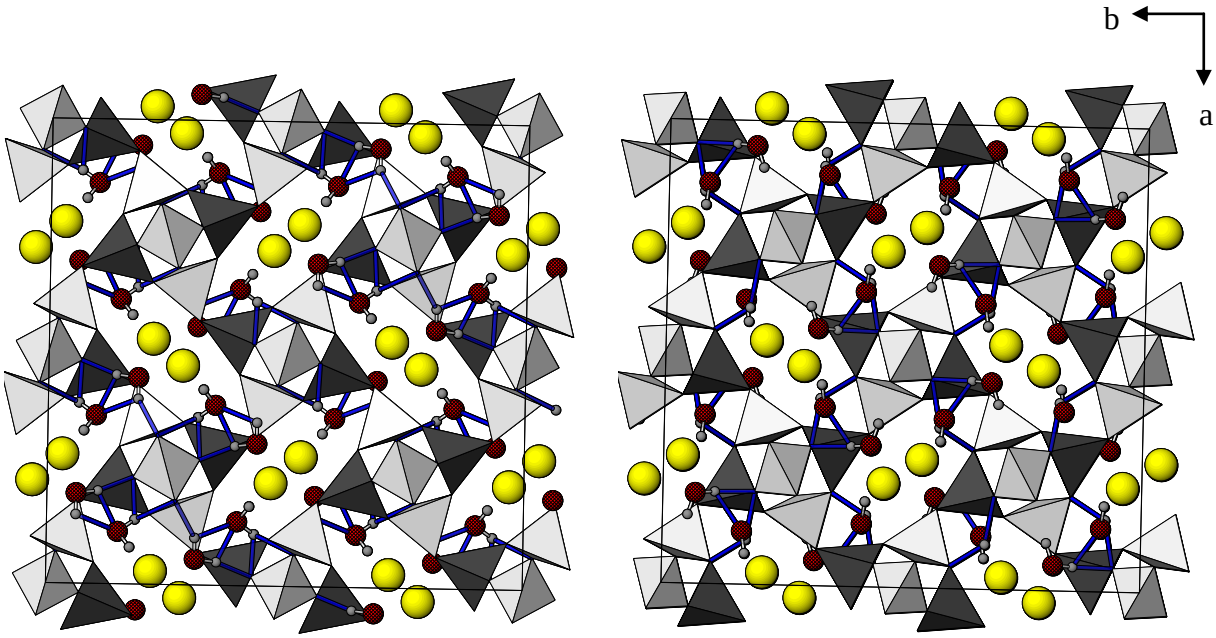

Figure 1: Structural representation of orthorhombic Na-GaSi-NAT from refined high pressure neutron diffraction data at a) ambient pressure and b) 0.74 GPa. Silicon tetrahedra (white), gallium tetrahedra (Grey), Na^+ (yellow), framework and water oxygen (red and hatched red), deuterium (grey) and hydrogen bonds (blue).

Hong et. al. gave the first and only report of tetragonal Na-GaSi-NAT synthesis, along with a space group and cell parameters (gained from whole pattern fitting).[4,5] Other than these reports by Hong no other structural information was available for the tetragonal form. In this thesis the structure was fully resolved with well fitting Rietveld refinements of both neutron and synchrotron X-ray diffraction data. For the first time the tetragonal structure was resolved. These studies also revealed the hydrogen position/ordering of the ambient pressure model.

Studies of the tetragonal form also extended to high-pressures. For the first time, evidence of pressure-induced hydration and cell volume expansion was shown. A series of high pressure neutron diffraction experiments reveal the changing hydrogen bonding network. Through this, we have provided evidence that hydrogen bonded water nanotubes (as discussed earlier), are not present in the tetragonal form. In fact, over all pressures there is no direct hydrogen bonding between water molecules. Unlike the orthorhombic form, there is no cross-channel hydrogen bonding. Figure 2 shows structural representations of ambient pressure tetragonal Na-GaSi-NAT and superhydrated tetragonal Na-GaSi-NAT.

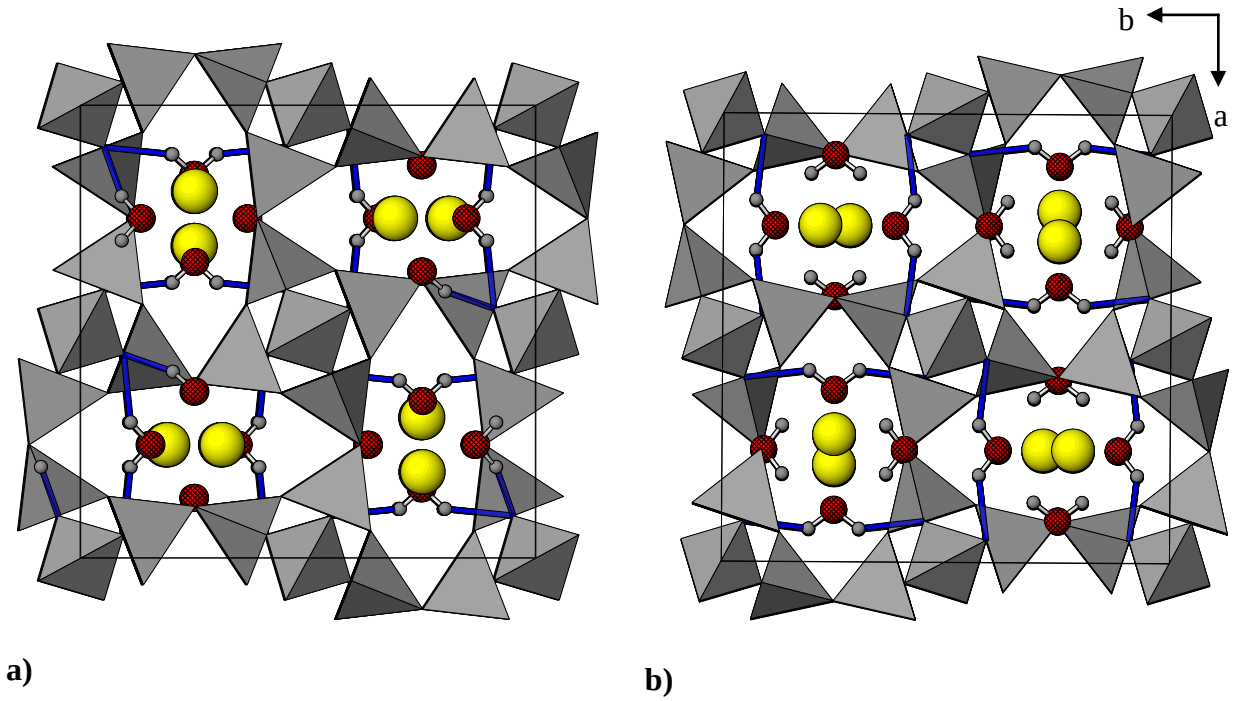

Figure 2: Structural representation of tetragonal Na-GaSi-NAT from refined high pressure neutron diffraction data at a) ambient pressure and b) 0.88 GPa. Silicon/gallium tetrahedra (Grey), Na^+ (yellow), framework and water oxygen (red and hatched red), deuterium (grey) and hydrogen bonds (blue).

8.1 High Pressure Data Evaluation and Comparison

From the structural information gained for both gallosilicate forms, structural trends and comparisons were assessed. These included water occupancy and cell volume as a function of pressure, pore measurements, fibrous chain rotation angles, T-O-T bond angles and equation of state fitting (which gave V_0 and bulk moduli). Evaluation of the secondary measurements made from each experiment affords a comparison between the two gallosilicate forms and also between the different diffraction techniques. This elucidates the nature of the superhydration mechanism in each gallosilicate form.

The name ‘superhydration’ suggests an increase in hydration, compared to the normal ambient state. The superhydration, which occurs in both gallosilicate forms, shows an increase (of almost double) from the ambient phase water content up to the superhydrated phase water content. This occurs by filling a second water site, the OW2 site, up to a maximum occupancy of 1. At this maximum occupancy superhydration has occurred and a cell volume expansion is observed. In each case there is a gradual filling of the OW2 site before we see the sudden increase in cell volume. When comparing the refined occupancies of the OW2 sites as a function of pressure, for both the neutron diffraction and the synchrotron X-ray experiments, there is a strong correlation in results. Both the tetragonal and the orthorhombic form show good correlation between the two complimentary diffraction techniques. When merging data from the two methods we see a well formed pattern in hydration as a function of pressure, for each of the gallosilicates (Figure 3 and Figure 4).

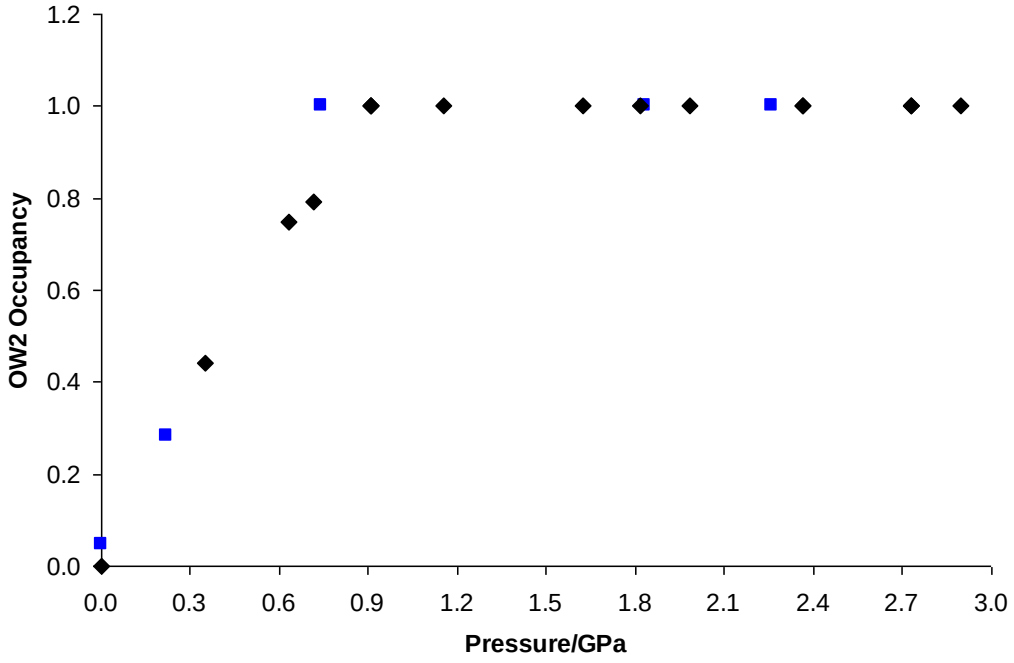

Figure 3: The hydration of the orthorhombic unit cell as a function of pressure expressed in terms of OW2 occupancy, where 1=full occupancy and superhydration. Neutron diffraction results (blue), Synchrotron X-ray diffraction results from 9.5HPT (black).

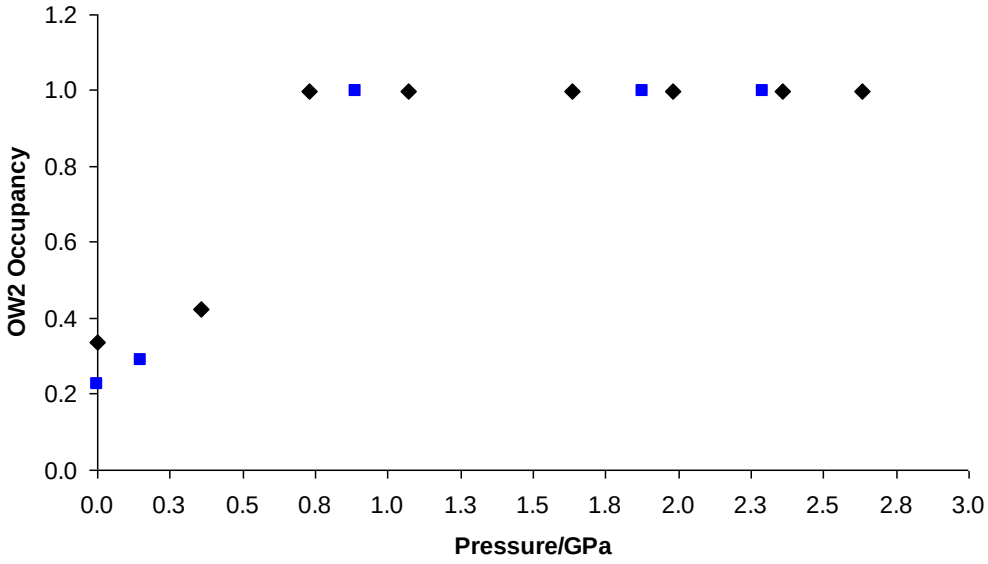

Figure 4: The hydration of the tetragonal unit cell as a function of pressure expressed in terms of OW2 occupancy, where 1=full occupancy and superhydration. Neutron diffraction results (blue), Synchrotron X-ray diffraction results from 9.5HPT (black).

Another characteristic of superhydration, other than an increase in water content, is a sudden and significant increase in cell volume. To continue the comparison of the results from the two diffraction techniques we must look at the changes in cell volume as a function of pressure. Figure 5 and Figure 6 show a plot of the normalised cell volume as a function of pressure for the orthorhombic and the tetragonal forms. As well as the neutron diffraction and the synchrotron X-ray (9.5HPT) diffraction, there is also Le Bail refined synchrotron X-ray diffraction results from experiments performed at the X7a station, Brookhaven National Laboratory. The X7a experiment only included orthorhombic Na-GaSi-NAT and gave only cell parameters i.e. no OW2 occupancies.

From the orthorhombic results shown in Figure 5 the characteristic expansion is observed in each case. For each, the superhydration point is slightly different, but within a narrow pressure region. Each technique used an orthorhombic sample from a different synthetic batch, so there will have been slight differences in starting composition and hydration which could have affected the high-pressure behaviour. Taking this and reasonable errors into account, all three methods show good agreement. From these data we can define the point of superhydration transition (for the orthorhombic gallosilicate) as a cell volume expansion from 1.43% to 2.42% occurring in the pressure region 0.74 GPa to 0.906 GPa, with full OW2 occupancy occurring at the point of transition.

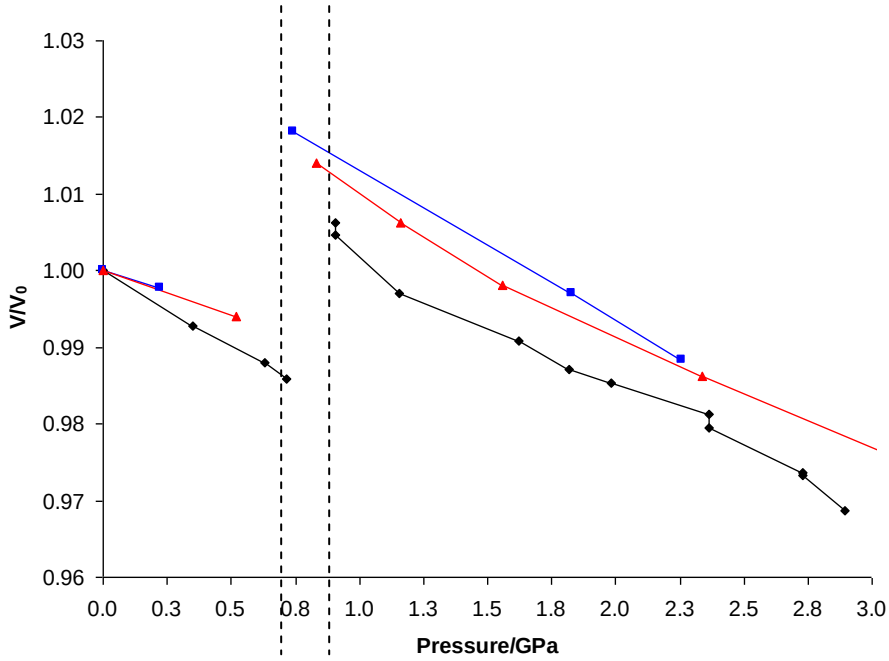

Figure 5: Comparison of the normalised volume as a function of pressure for orthorhombic Na-GaSi-NAT. Neutron diffraction results (blue) and synchrotron X-ray diffraction results from X7a (red) and 9.5HPT (black). The pressure region in which superhydration and cell expansion occurs is indicated by dashed lines.

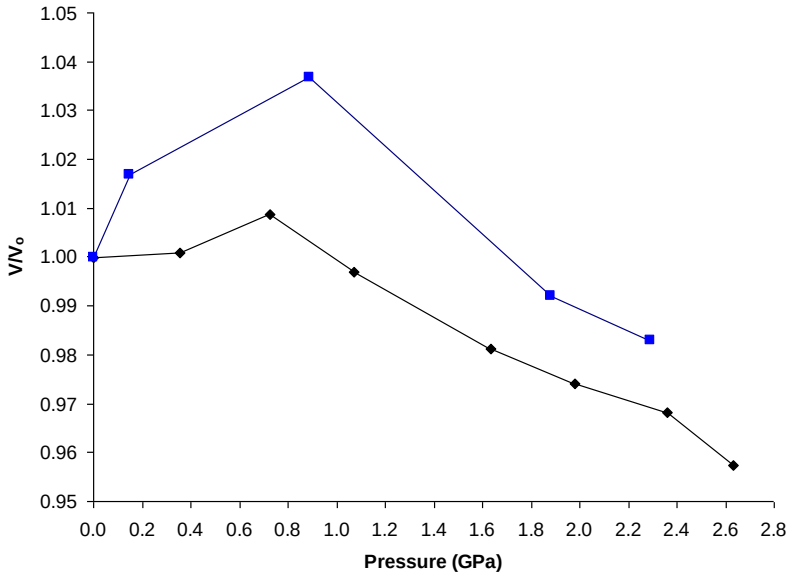

Figure 6: Comparison of the normalised volume as a function of pressure for tetragonal Na-GaSi-NAT. Neutron diffraction results (blue) and synchrotron X-ray diffraction results 9.5HPT (black). The pressure region in which superhydration and cell expansion occurs is indicated by dashed lines.

For the tetragonal gallosilicate it is not as easy to compare the two diffraction techniques. It is clear from Figure 6 that there is a slight discrepancy in the extent of cell expansion observed in each experiment data set. The neutron diffraction experiment shows a 3.75 % volume expansion verses a 0.87% expansion for the synchrotron X-ray diffraction experiment (9.5HPT). In fact, over all pressure points the X-ray diffraction data set has cell volume values lower than expected. In Chapter 5 the validity of this data set was discussed, with the conclusion that full cell expansion was not observed due to experimental factors and possible sample composition differences. This is confirmed when comparing the changes in cell parameter, pore dimensions and chain rotation angle; all of which are lower than expected. For example cell parameter *a*, pore width, and chain rotation angle are 13.345(8) Å, 5.077 Å and 22.78° respectively (at 0.727 GPa). This compares to 13.5606(11) Å, 5.488 Å and 19.36° for the neutron diffraction experiment (at 0.880 GPa). For the neutron diffraction data set there is an increased chain rotation (giving a smaller angle), causing a greater pore width, which in turn causes an increased cell expansion in the *a*,*b*-plane.

From the comparison of the two data sets the superhydration point of tetragonal Na-GaSi-NAT can be defined by the pressure region 0.73 GPa to 0.89 GPa with a maximum observed net cell expansion of 3.75%, with full OW2 occupancy occurring at the point of transition.

8.1.1 Framework Flexibility-The Mechanism by Which PIH Occurs

The volume expansion response which occurs at the point of superhydration can be described in terms of the framework flexibility as this facilitates the cell volume expansion characteristic of the superhydration step. The greater the flexibility, the larger the expansion and the earlier it occurs (in terms of pressure). The flexibility of the framework in the natrolite family comes specifically from the flex within the T-O-T bond that connects the tetrahedra of the fibrous chains in the *a*,*b*-plane. For further information and a graphical representation of the T-O-T bridging bond refer back to chapter 5. The T-O-T bond shows considerable flex and it is this which allows the fibrous chains to rotate, giving a more open rounded pore and an expanded unit cell.

Using these measurements we can surmise that tetragonal is the more flexible of the two gallosilicate natrolites. Tetragonal Na-GaSi-NAT shows a greater cell expansion, lower rotation angle, wider less elliptical pores and a greater change in the T-O-T bond angle; when compare with the orthorhombic form. In turn these parameters can be used to compare the orthorhombic gallosilicate with the isostructural analogue aluminosilicate natrolite. In this case the orthorhombic gallosilicate shows an increased flexibility when compared to the aluminosilicate; this is evidenced by comparison of the aforementioned parameters. This comparison, along with a more detailed discussion of these parameters is included in chapters 4 and 5.

The difference between the aluminosilicate and the gallosilicates is the substitution of a T atom, Al for Ga. Substitution of a larger Ga for Al atom increases the openness and flexibility of the framework. The difference between the two gallosilicate forms is the T atom ordering, ordered in the orthorhombic form and disordered in the tetragonal form. The ordering of the T-atom sites has an effect upon the nature of the T-O-T chain-bridging bond and consequently the flexibility of the framework. In this case disorder over the T sites causes an increase in flexibility. So, by considering the substitution and ordering across the three natrolites, the trend in flexibility (as

evidenced by T-O-T bond angles, cell parameters, pore dimensions, chain rotation, bulk moduli and V_0 values) at ambient and high pressure is:

Tet Na-GaSi-NAT>Orth Na-GaSi-NAT>Orth Al-NAT

8.1.2 Reversibility

The mechanism by which unit cell volume expansion is achieved during superhydration was discussed in the previous section. Equally important is consideration of the reversible nature of the superhydrated state.

The differences between Na-OW1 and Na-OW2 bonding can be used to explain why superhydration is a reversible process (chapters 4 and 5). At any of the pressures studied in these works (including ambient), OW1 molecules remain at full site occupancy. Why do OW1 molecules remain when OW2 molecules are only reversibly inserted at high pressure? OW1 has an advantage over the OW2 position due to Na bonding. Both positions produce various hydrogen bonding networks over a range of pressures (as discussed in chapter 4), but at all pressures including ambient, there are always two Na-OW1 bonds. When OW2 is introduced via pressure, only one Na-OW2 bond is made and in some cases this bond does not form until OW2 reaches full occupancy i.e. the point of superhydration. Energetically the extra Na-O bond seen for OW1, makes OW1 much more stable and strongly bound over all pressures including ambient. Therefore, the OW1 molecule is a permanent resident within the pore whilst the weaker bonded OW2 molecule is lost upon pressure release.

8.2 Ion Exchange Experiments

The pressure induced hydration and pore-swelling mechanism, extensively investigated throughout this thesis, have been applied to an original ion exchange mechanism. By exploitation of the pore swelling mechanism observed in the aluminosilicate and gallosilicate natrolites upon pressure application cations were exchanged into the pore. These cations would not normally exchange under ambient pressures, but the expanded state allows entry to the pores. Upon pressure release, pore-swelling and volume expansion is reversed. The reversibility of this mechanism has presented a pressure-trapping mechanism, locking the exchanged cation within the framework.

Initially, hydrothermal ion exchange experiments were performed upon 3 natrolite samples (aluminosilicate Al-NAT, orthorhombic Na-GaSi-NAT, tetragonal Na-GaSi-NAT). These experiments were used to assess the suitability of specific cations for use in high pressure ion exchange. Cations of interest included Cs, Rb, Sr, and Ba. From results cesium was selected and used in high pressure ion exchange. A Quickpress apparatus was used with a customised Teflon^{TM} capsule. This capsule modification allows a much larger sample size compared to ion exchange in a diamond anvil cell. Experiments performed include temperature and reaction time variation at a pressure of 1GPa. The first evidence of high pressure ion-exchange was gained from the results of these experiments. Evidence of significant Cs remaining within the pores after leaching treatment show that the cations are trapped within the framework due to reduced cell volume/pore size upon pressure release.

Optimum high pressure trapping occurred in aluminosilicate natrolite at 100°C, 1 GPa and over 270 minutes. Only surface cations were lost during back-exchange of this sample; leaving 33% exchanged cesium trapped within the pores. Cell volume measurements reflect this with an increased value of 0.54%.

8.3 Summary of New and Original Work Reported In This Thesis.

- The first detailed structural study of tetragonal gallosilicate natrolite, from the refinement of ambient pressure neutron diffraction and synchrotron X-ray diffraction data.

- The first details of hydrogen position and occupancy in both the gallosilicate forms. These details were gained from refinement of ambient pressure neutron diffraction data. These data gave the first resolution of the hydrogen bonding network within each gallosilicate form.

- The first observation of a superhydrated phase in the tetragonal form during high pressure diffraction experiments (both neutron and synchrotron X-ray).

- Detailed measurements of pore dimensions, chain rotation angles and T-O-T angles over a large number of pressure points for both gallosilicates. Chain rotation angles and T-O-T angles have been previously reported by Lee et al. in their high pressure study of the orthorhombic form.[2] In the work carried out in this thesis, the measurements for the orthorhombic form are given from data form both neutron and synchrotron X-ray diffraction experiments; giving a more detailed data set. In the tetragonal form, no reports (to date) give details of these measurements. Work in this thesis offers the first data set of its kind for tetragonal gallosilicate natrolite.

- Equations of state were fitted to the compression curve of the superhydrated phase in both gallosilicates. This gave a V_0 value for the superhydrated phase and a bulk modulus for the compression curve. To date, there are no reports of these data for the tetragonal form and only one for the orthorhombic form.[2]

- Hydrothermal ion-exchange experiments provide initial evidence of sodium ion exchange with strontium, barium and rubidium in gallosilicate natrolite. In each case of ion exchange the cations were leached and the exchange reversed by treatment $NaCl_{(aq)}$ reflux. Following Na/Rb exchange in aluminosilicate natrolite, a new Rb-Al-NAT phase (with very different symmetry to the sodium form), was isolated.

- A Quickpress apparatus was used in a new way, with the use of a customised Teflon^{TM} capsule. These high pressure, variable temperature experiments give the first evidence of high pressure cation trapping. Results show that optimum Cs ion trapping occurs when using Al-NAT at 100°C at 1GPa for 270 min. High pressure cation trapping is optimised with decreased framework flexibility i.e. the most successful trapping is observed in aluminosilicate natrolite, the least flexible of the 3 natrolites tested (Al-NAT, orthorhombic Na-GaSi-NAT and tetragonal Na-GaSi-NAT). The least amount of trapping occurred in the most flexible of the three natrolites, tetragonal Na-GaSi-NAT. Increased framework flexibility allows a large initial exchange which is easily leached during reflux i.e. not trapped.

8.4 Conclusions

From the results from experiments performed in this thesis it is clear that slight changes to the parent aluminosilicate natrolite material produces significant effects on the nature and properties of the resulting material. Substitution of Al for Ga produces orthorhombic gallosilicate natrolite. This material is very similar to the aluminosilicate parent, sharing space group, similar (but slightly larger) unit cell volumes and similar intrapore bonding networks. As expected substitution of Al for slightly larger Ga, produces an increase in cell volume (from 2244 $Å^3$ to 2310 $Å^3$). This increase allows for a more open flexible framework than that of the parent aluminosilicate natrolite. This is evidenced by a lower superhydration pressure value and an increase in the potential for ion exchange into the pores. Measurements of pore dimensions, T-O-T bond flex and bulk modulus support this.

Tetragonal gallosilicate differs from orthorhombic gallosilicate natrolite in the ordering of T atom sites (ordered in orthorhombic and disordered in tetragonal). Disorder of the T atom sites acts to further increase the framework flexibility and hence a lower superhydration pressure value and increase ion exchange is observed.

All three natrolite materials undergo superhydration and pressure-induced expansion. In this thesis the high pressure behaviour and the variation in framework flexibility of the three natrolite materials has been used to investigate the possibility of high pressure cation trapping. By exchange of a large cation under pressure and subsequent pressure release the cation is trapped within the framework. An increase in framework flexibility allows for more successful ion exchange whilst under pressure. However, high framework flexibility means that exchanged cations can be leached out at ambient pressure. All three natrolite materials show Na/Cs ion exchange under pressure, but the least flexible of the three (aluminosilicate natrolite) show little/no cation leaching, demonstrating successful cation trapping via this novel high pressure mechanism.

By altering the nature of the natrolite framework, superhydration and cell volume expansion is still observed, but the nature the framework shows significant differences. These differences can be used to design high pressure cation trapping experiments. By altering the framework and/or nature of the cation it is possible that this novel cation trapping mechanism could be tailored to specific uses e.g. in the immobilisation of cations from nuclear industry waste.

8.5 Further Work

8.5.1 High Pressure Behaviour in the Natrolite Family

Further work could include high pressure diffraction experiments (both neutron and synchrotron X-ray), upon other synthetic analogues of aluminosilicate natrolite e.g. the germanium analogue $Na_2Al_2Ge_3O_{10}.2H_2O$.[6,7] If superhydration is observed in other synthetic forms, high pressure studies could allow comparison of the high pressure behaviour to that of the aluminosilicate and gallosilicate natrolites. Using both methods of diffraction will allow structure resolution over a number of pressures steps as well as resolution of the hydrogen bonding network.

8.5.2 Ion Exchange

The high pressure ion exchange method used in this thesis has proved successful in providing evidence of high-pressure cation trapping. For a direct comparison to the work reported in this thesis, further studies could include investigation into the effect of CsCl(aq) concentration upon exchange (work in this thesis made use of a saturated solution to drive exchange). Also, treatment times above the 270 minutes used in this thesis could be investigated (as amount of exchange was shown to increase with treatment time). Further work could also explore the use of other cations and of other materials including other synthetic analogues of aluminosilicate natrolite.

Full characterisation of the Rb-Al-NAT phase, isolated during hydrothermal ion exchange, could also provide a starting point for a new branch of research. Also, further measurements to improve the accuracy of the level of ion exchange of samples exchanged both hydrothermally and using a Quickpress, could be obtained by employing methods such as X-ray fluorescence (XRF) and/or inductively coupled plasma mass spectroscopy (ICP-MS).

[1] International Crystal Structure Database. *Card number 79-1073*.

[2] Lee Y.; Hriljac J. A.; Kim S. J.; Vogt T.; Hanson J. C. 'Pressure-induced hydration at 0.6 GPa in a synthetic gallosilicate zeolite' **2003.** *J. Am. Chem. Soc. 125*. 6036-6037.

[3] Lee Y.; Hriljac J. A.; Kim S. J.; Vogt T.; Parise J. B.; Artioli G. 'Pressure-induced volume expansion of zeolites in the Natrolite family' **2002**. *J. Am. Chem. Soc. 124*. 5466-5475.

[4] Hong S. B.; Kim S. H.; Kim Y. G.; Kim Y. C.; Barrett P. A.; Camblor M. A. 'Synthesis of microporous gallosilicates with the CGS topology' **1999.** *J. Mater. Chem. 9.* 2287.

[5] Hong S. B.; Lee S.-H.; Shin C.-H.; Woo A. J.; Alvarez L. J.; Zicovich-Wilson C. M.; Camblor M. A. 'In Situ Disorder-Order Transformation in Synthetic Gallosilicate Zeolites with the NAT Topology' **2004.** *J. Am. Chem. Soc. 126(42).* 13742-13751.

[6] Tripathi A.; Johnson G. M.; Kim S. J.; Parise J. B. '$Na_2Al_2Ge_3O_{10}.2H_20$: An aluminogerminate with the tetranatrolite topology' **2000.** *J. Mat. Chem. 10.* 451-455.

[7] Lee Y. J.; Kim S. J.; Parise J. B. 'Synthesis and crystal structures of gallium- and germanium- variants of the fibrous zeolite with the NAT, EDI and THO structure types' **2000**. *Microporous and Mesoporous Mat. 34*. 255-271.

Appendix

1.1 Rietveld Refinement Profile Plots for High Pressure Neutron Diffraction Data

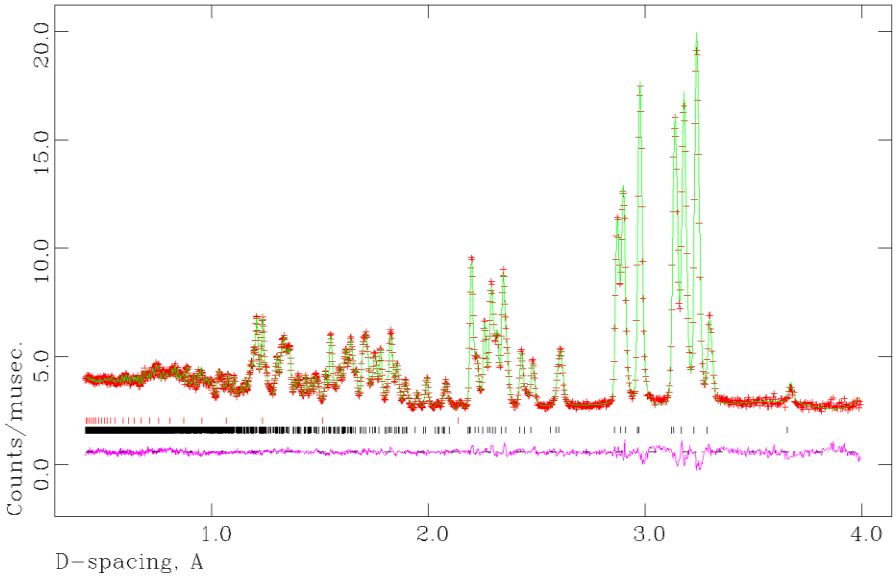

Figure 1: Rietveld refinement of orthorhombic Gallosilicate at ambient pressure. Vertical tick marks indicate allowed reflections for each phase: Na-GaSi-NAT (black); Vanadium (red).

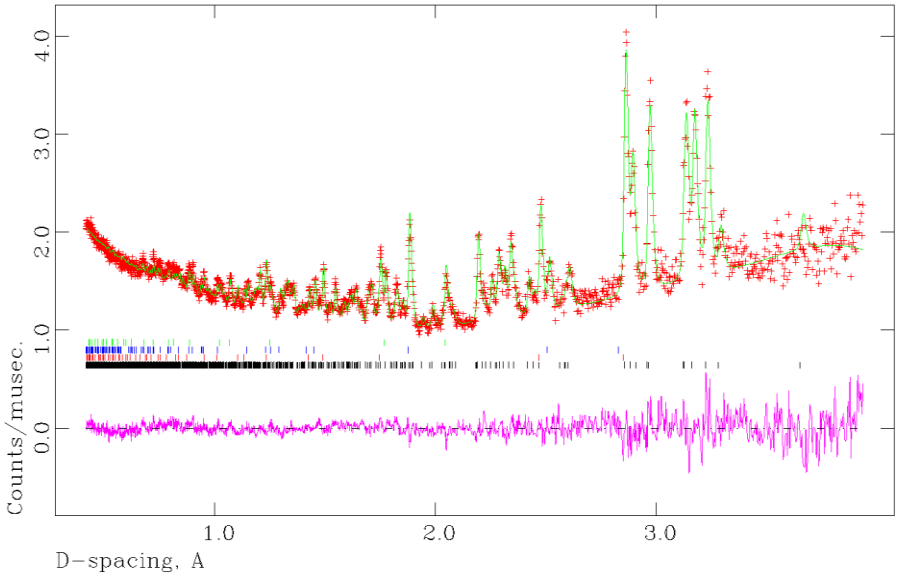

Figure 2: Rietveld refinement of orthorhombic Gallosilicate at 7tns. Vertical tick marks indicate allowed reflections for each phase: Na-GaSi-NAT (black); Pb (red); WC (blue); Ni (green).

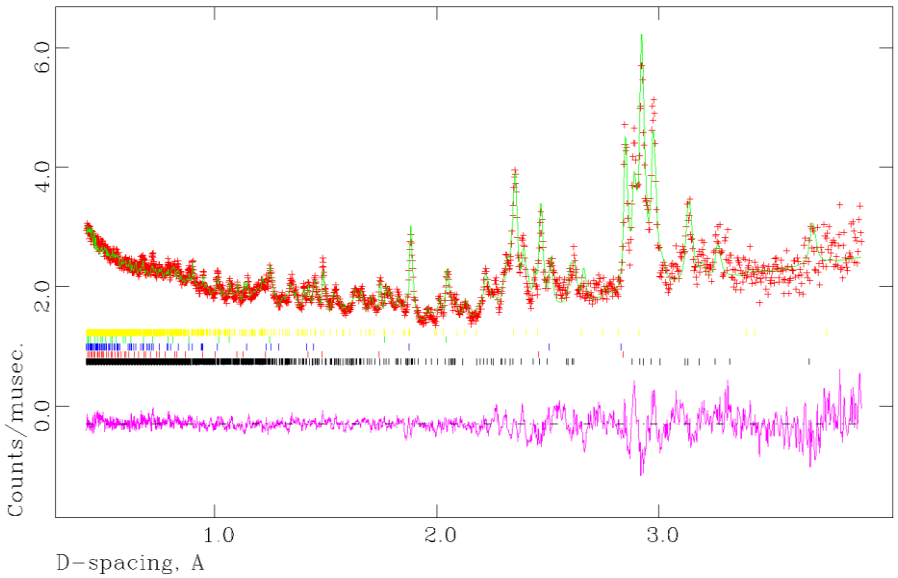

Figure 3: Rietveld refinement of orthorhombic Gallosilicate at 12tns. Vertical tick marks indicate allowed reflections for each phase: Na-GaSi-NAT (black); Pb (red); WC (blue); Ni (green); Ice IV (yellow).

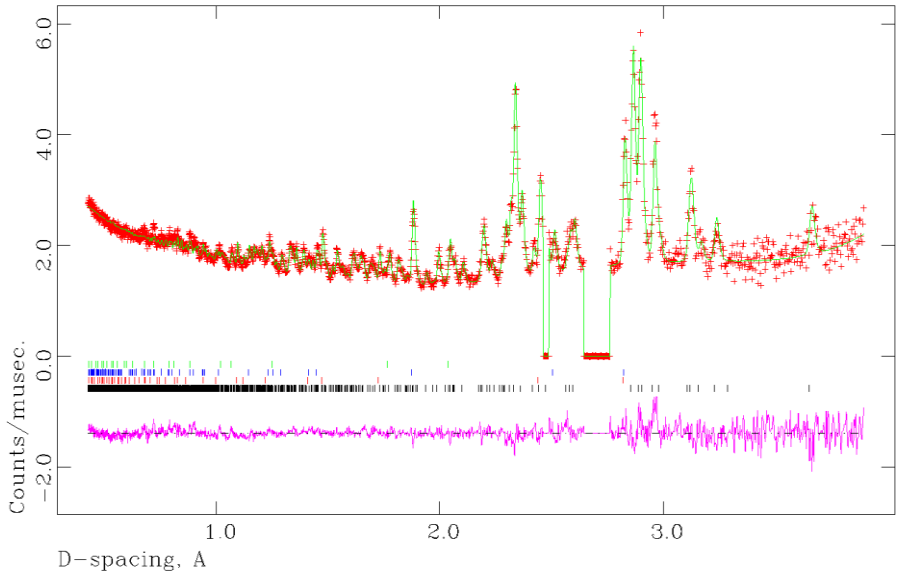

Figure 4: Rietveld refinement of orthorhombic Gallosilicate at 22tns. Vertical tick marks indicate allowed reflections for each phase: Na-GaSi-NAT (black); Pb (red); WC (blue); Ni (green).

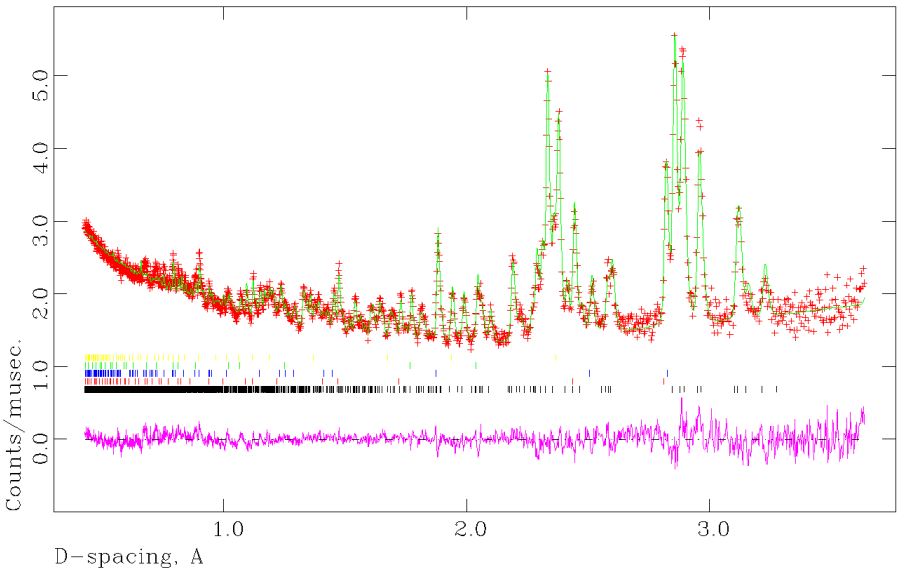

Figure 5: Rietveld refinement of orthorhombic Gallosilicate at 26tns. Vertical tick marks indicate allowed reflections for each phase: Na-GaSi-NAT (black); Pb (red); WC (blue); Ni (green); Ice VII (yellow).

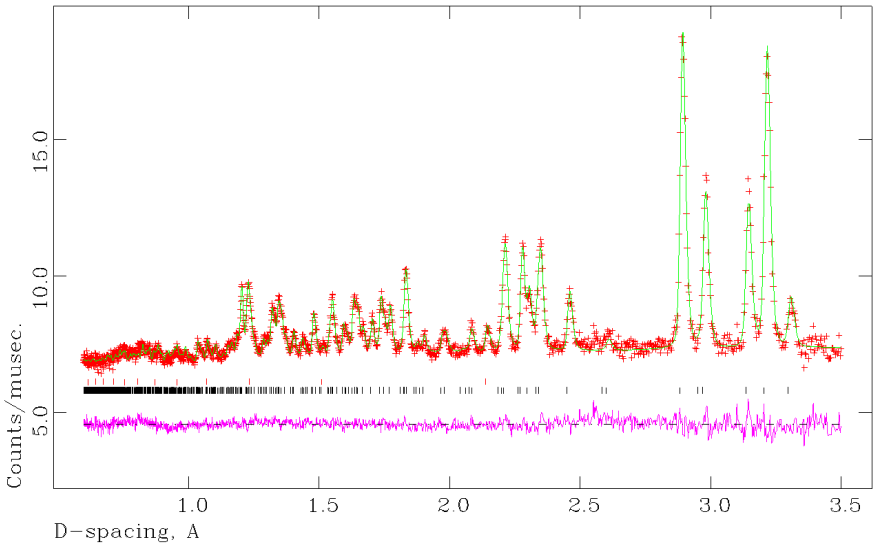

Figure 6: Rietveld refinement of tetragonal gallosilicate at ambient pressure. Vertical tick marks indicate allowed reflections for each phase: Na-GaSi-NAT (black); Vanadium (red).

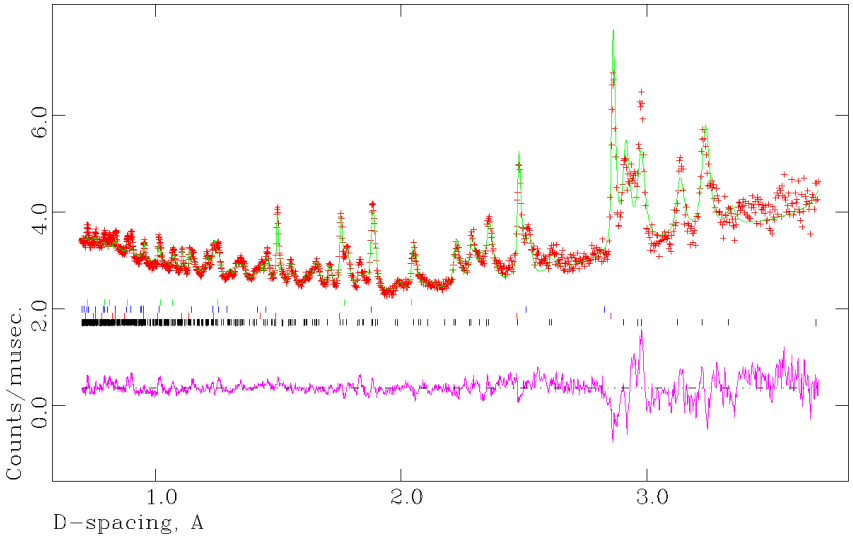

Figure 7: Rietveld refinement of tetragonal gallosilicate at 7tns. Vertical tick marks indicate allowed reflections for each phase: Na-GaSi-NAT (black); Pb (red); WC (blue); Ni (green).

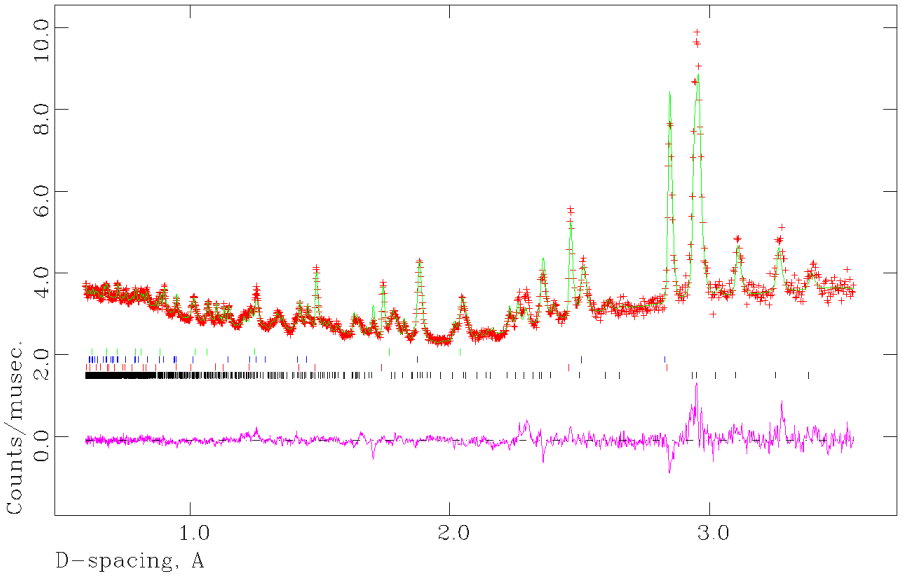

Figure 8: Rietveld refinement of tetragonal gallosilicate at 12tns. Vertical tick marks indicate allowed reflections for each phase: Na-GaSi-NAT (black); Pb (red); WC (blue); Ni (green).

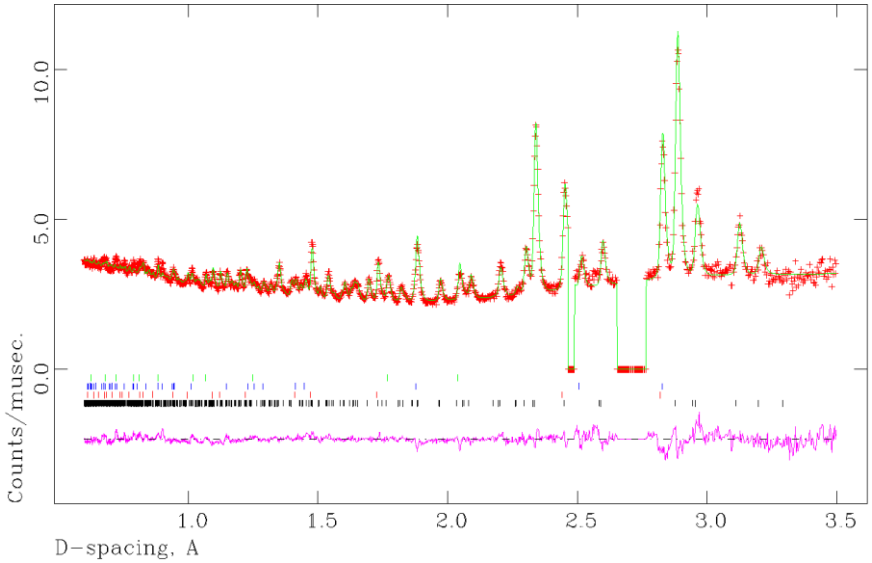

Figure 9: Rietveld refinement of tetragonal gallosilicate at 22tns. Vertical tick marks indicate allowed reflections for each phase: Na-GaSi-NAT (black); Pb (red); WC (blue); Ni (green).

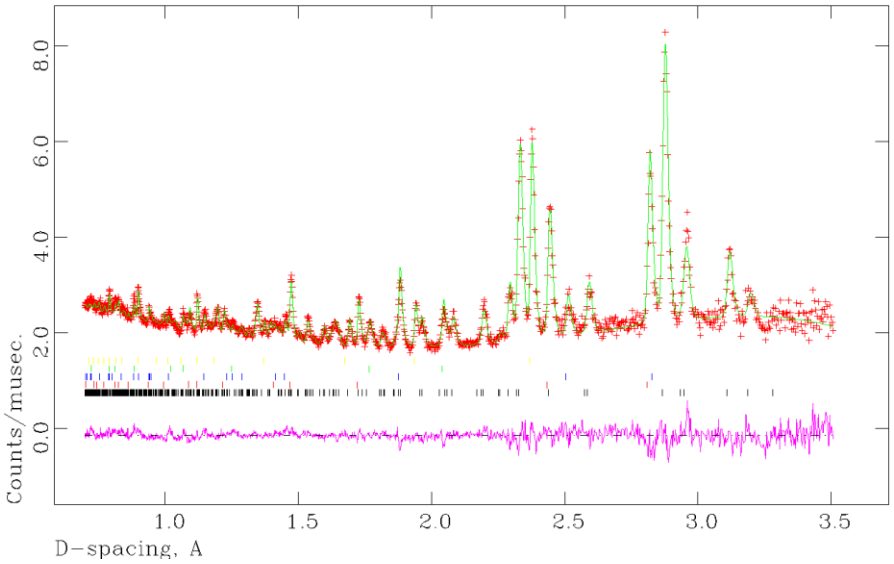

Figure 10: Rietveld refinement of tetragonal gallosilicate at 26tns. Vertical tick marks indicate allowed reflections for each phase: Na-GaSi-NAT (black); Pb (red); WC (blue); Ni (green).

1.2 Rietveld Refinement Profile Plots for High Pressure Synchrotron X-Ray Diffraction data

1.2.1 Synchrotron X-Ray Diffraction Data from X7a

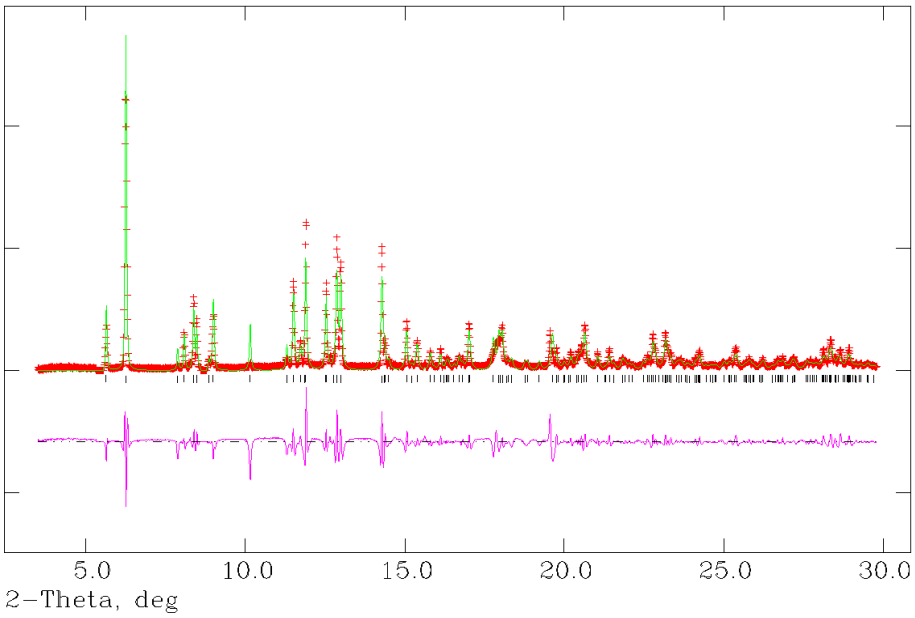

Figure 11: Le Bail refinement profile for orthorhombic Na-GaSi-NAT at 0.52 GPa. Vertical tick marks indicate allowed reflections for each phase: Na-GaSi-NAT (black).

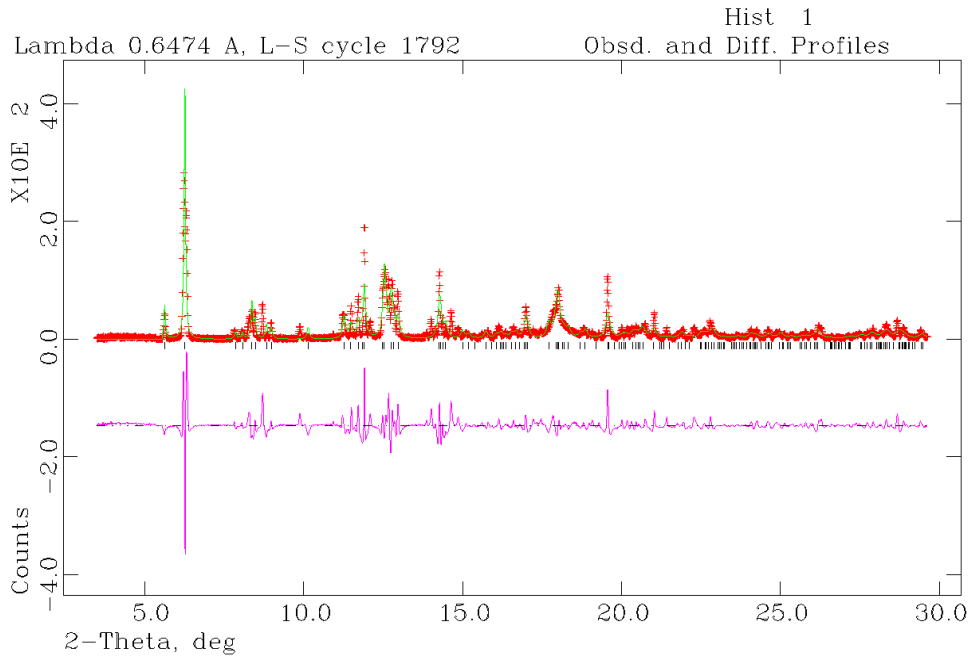

Figure 12: Le Bail refinement profile for orthorhombic Na-GaSi-NAT at 0.60 GPa. Vertical tick marks indicate allowed reflections for each phase: Na-GaSi-NAT (black).

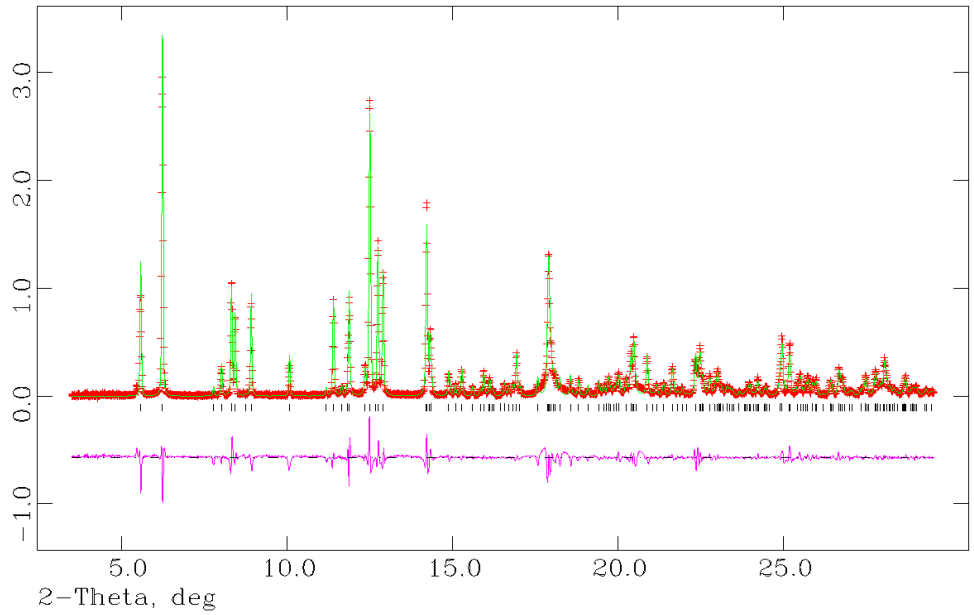

Figure 13: Le Bail refinement profile for orthorhombic Na-GaSi-NAT at 0.83 GPa. Vertical tick marks indicate allowed reflections for each phase: Na-GaSi-NAT (black).

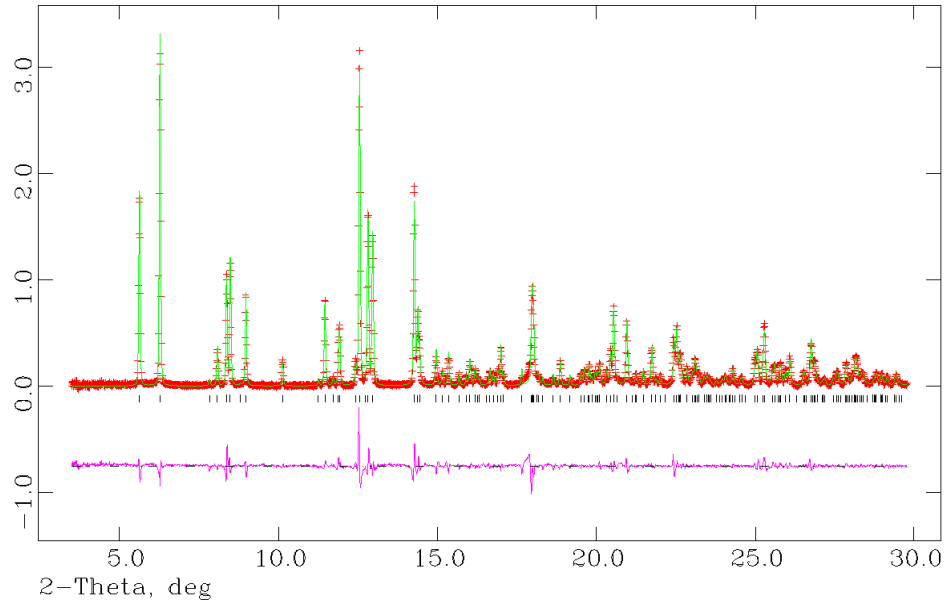

Figure 14: Le Bail refinement profile for orthorhombic Na-GaSi-NAT at 1.16 GPa. Vertical tick marks indicate allowed reflections for each phase: Na-GaSi-NAT (black).

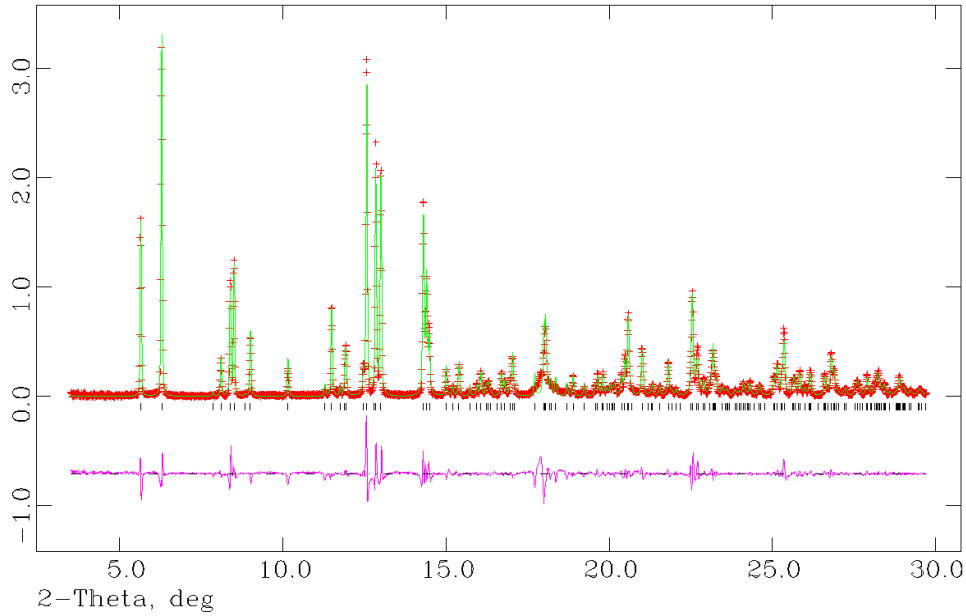

Figure 15: Le Bail refinement profile for orthorhombic Na-GaSi-NAT at 1.56 GPa. Vertical tick marks indicate allowed reflections for each phase: Na-GaSi-NAT (black).

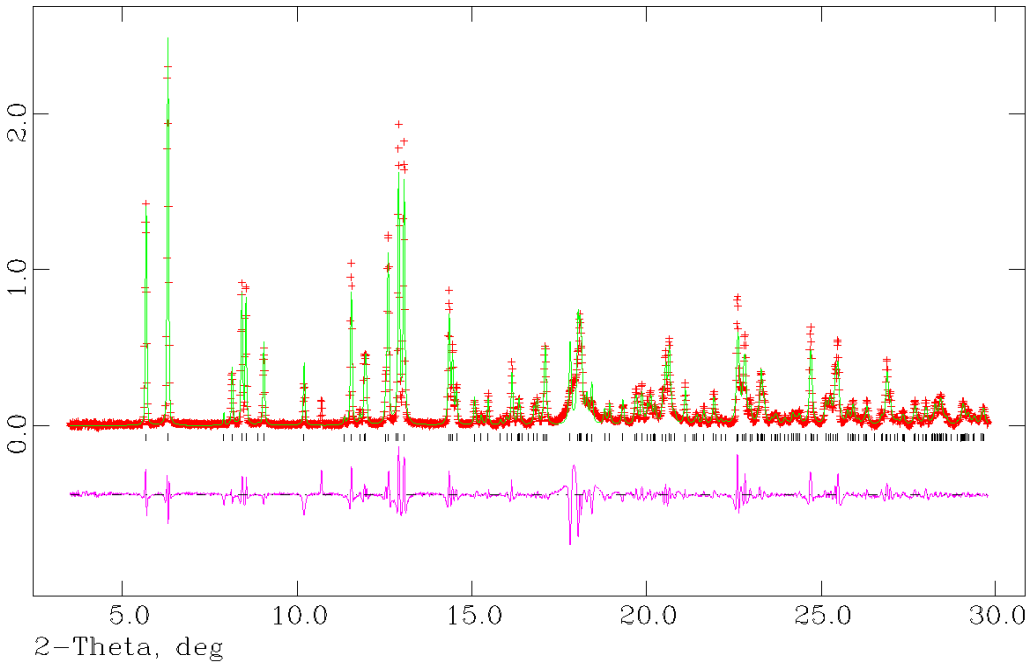

Figure 16: Le Bail refinement profile for orthorhombic Na-GaSi-NAT at 2.34 GPa. Vertical tick marks indicate allowed reflections for each phase: Na-GaSi-NAT (black).

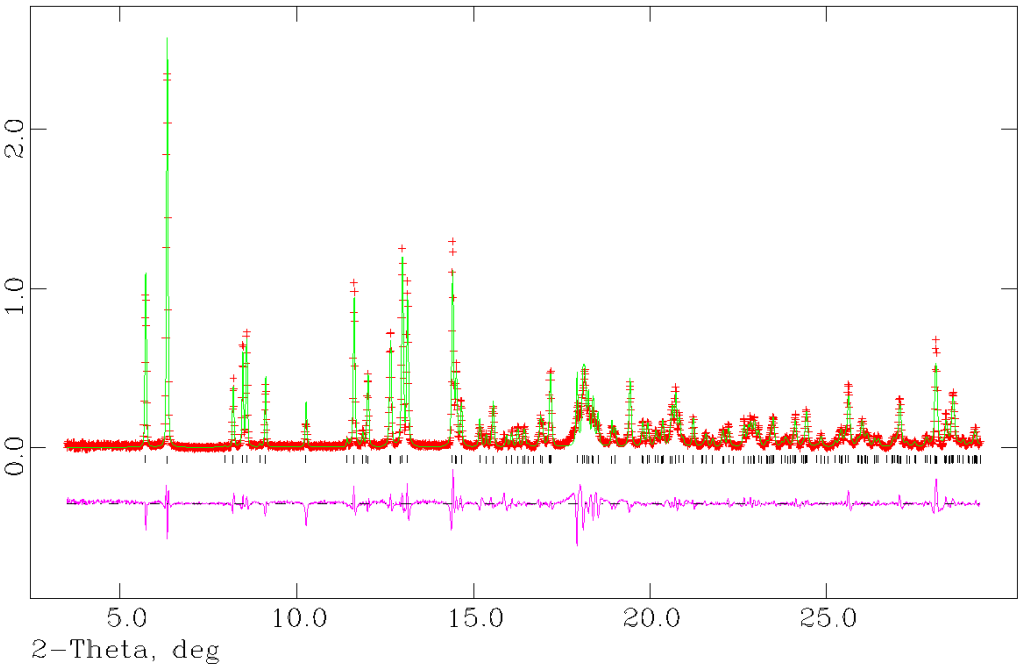

Figure 17: Le Bail refinement profile for orthorhombic Na-GaSi-NAT at 3.24 GPa. Vertical tick marks indicate allowed reflections for each phase: Na-GaSi-NAT (black).

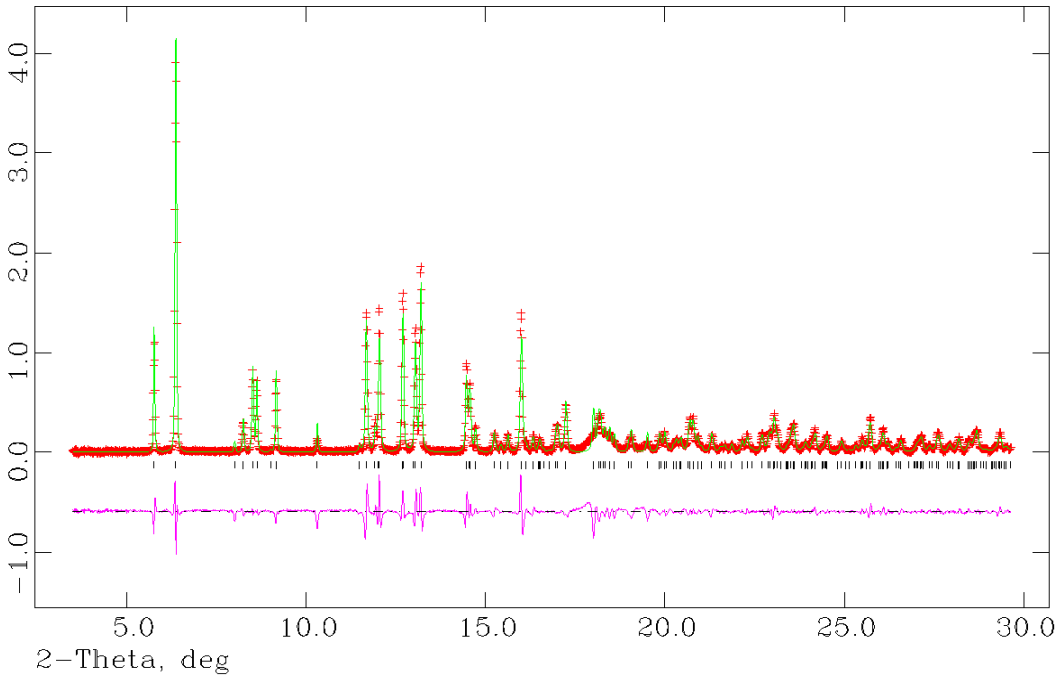

Figure 18: Le Bail refinement profile for orthorhombic Na-GaSi-NAT at 3.85 GPa. Vertical tick marks indicate allowed reflections for each phase: Na-GaSi-NAT (black).

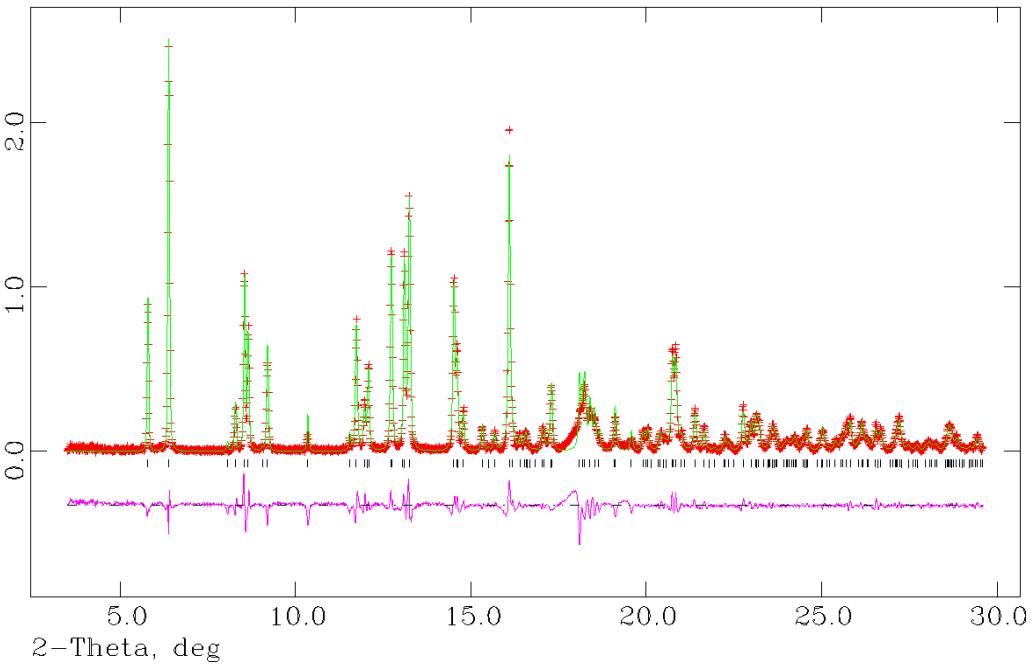

Figure 19: Le Bail refinement profile for orthorhombic Na-GaSi-NAT at 4.58 GPa. Vertical tick marks indicate allowed reflections for each phase: Na-GaSi-NAT (black).

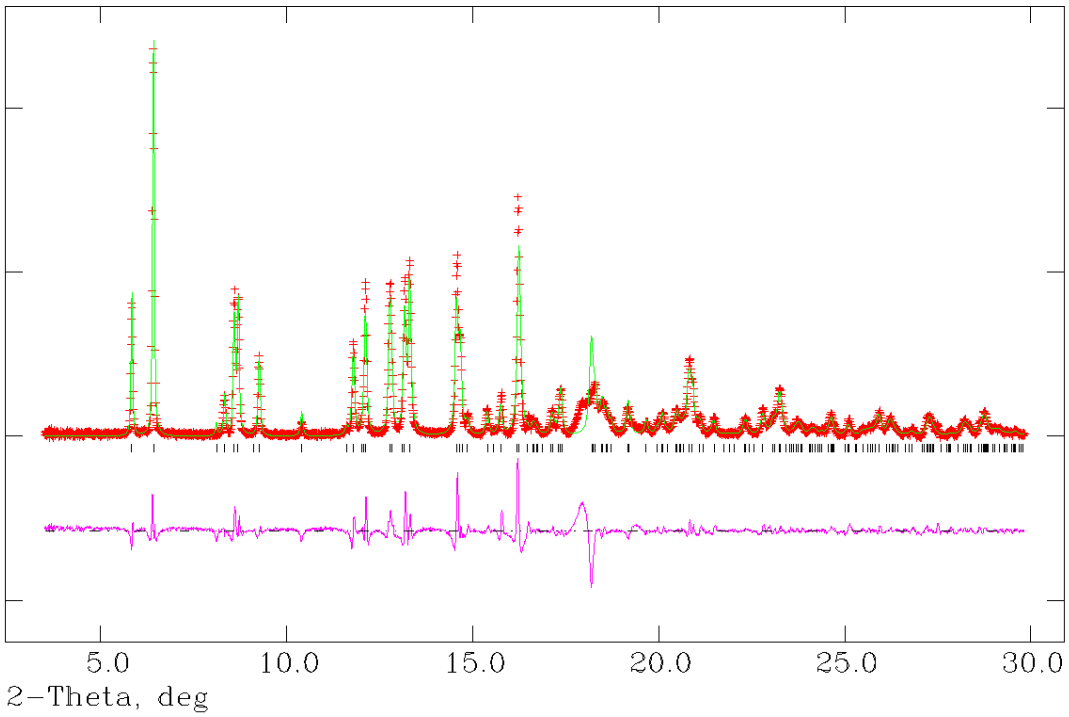

Figure 20: Le Bail refinement profile for orthorhombic Na-GaSi-NAT at 5.42 GPa. Vertical tick marks indicate allowed reflections for each phase: Na-GaSi-NAT (black).

1.2.2 Synchrotron X-Ray Diffraction Data from 9.5 HPT

1.2.2.1 Orthorhombic Na-GaSi-NAT

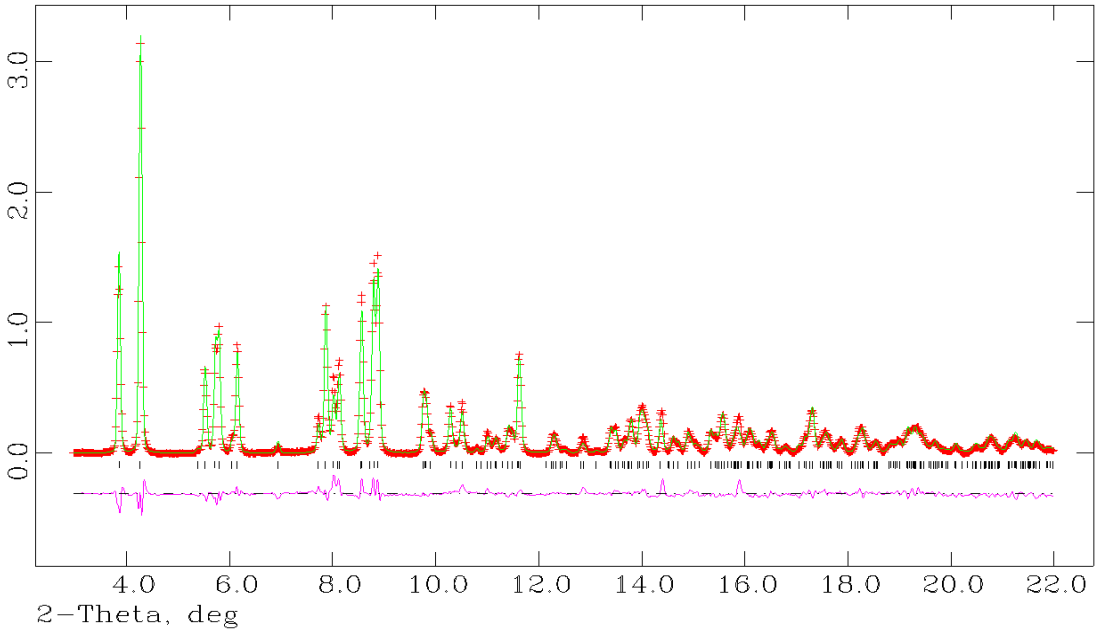

Figure 21: Refinement profile for orthorhombic Na-GaSi-NAT at ambient pressure performed using mounting tape. † Vertical tick marks indicate allowed reflections for each phase: Na-GaSi-NAT (black).

†Data series collected using mounting tape, rather than a diamond anvil cell.

*Data series collected during a pressure release step.

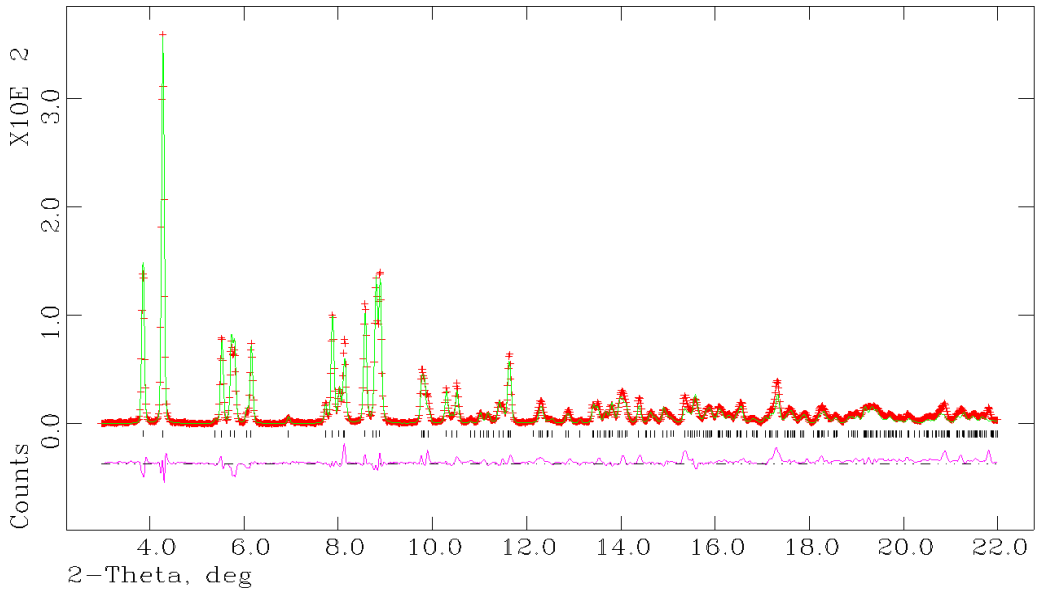

Figure 22: Refinement profile for orthorhombic Na-GaSi-NAT at ambient pressure.* Vertical tick marks indicate allowed reflections for each phase: Na-GaSi-NAT (black).

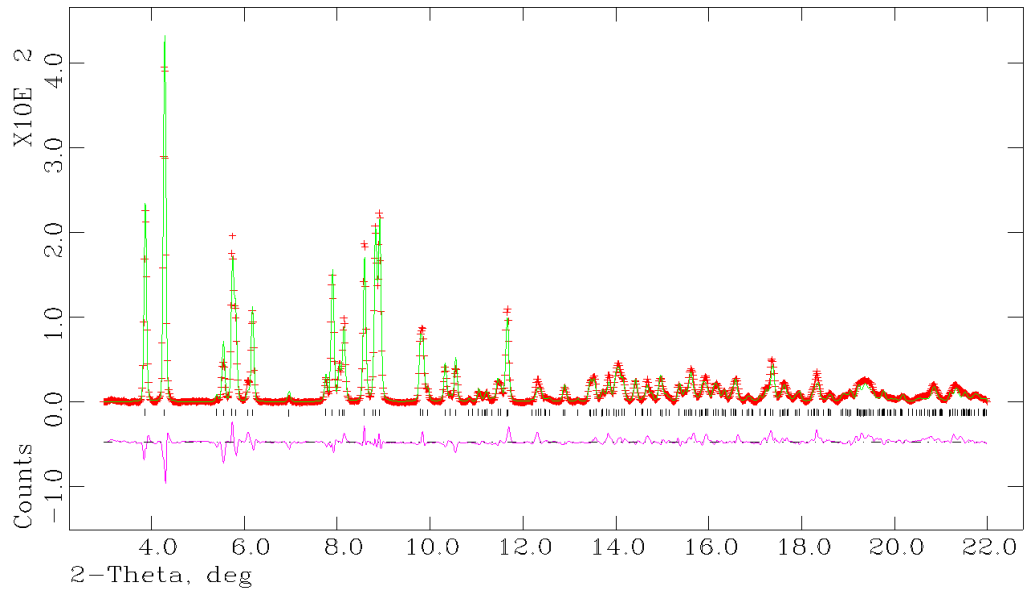

Figure 23: Refinement profile for orthorhombic Na-GaSi-NAT at 0.350 GPa. Vertical tick marks indicate allowed reflections for each phase: Na-GaSi-NAT (black).

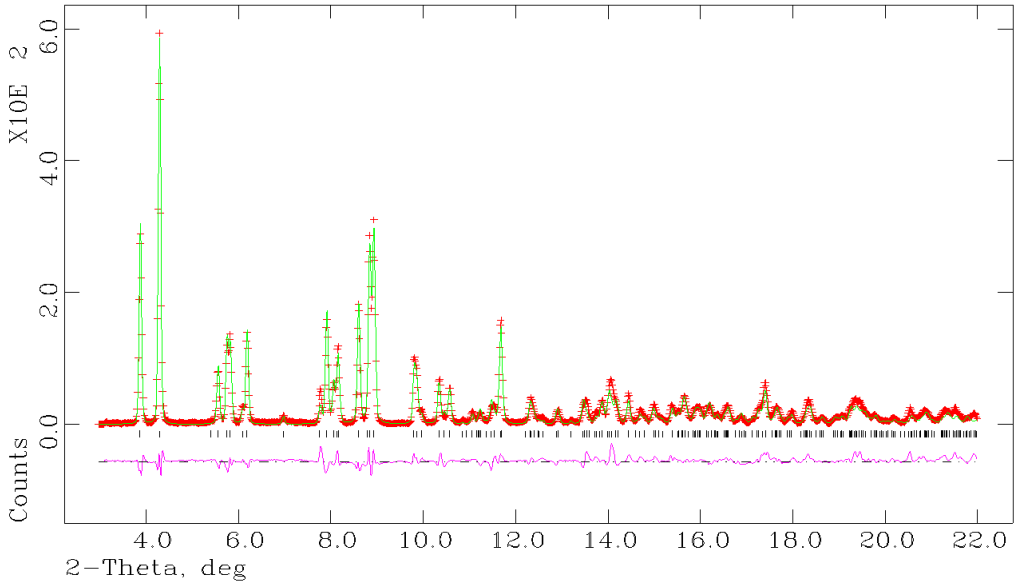

Figure 24: Refinement profile for orthorhombic Na-GaSi-NAT at 0.631 GPa. Vertical tick marks indicate allowed reflections for each phase: Na-GaSi-NAT (black).

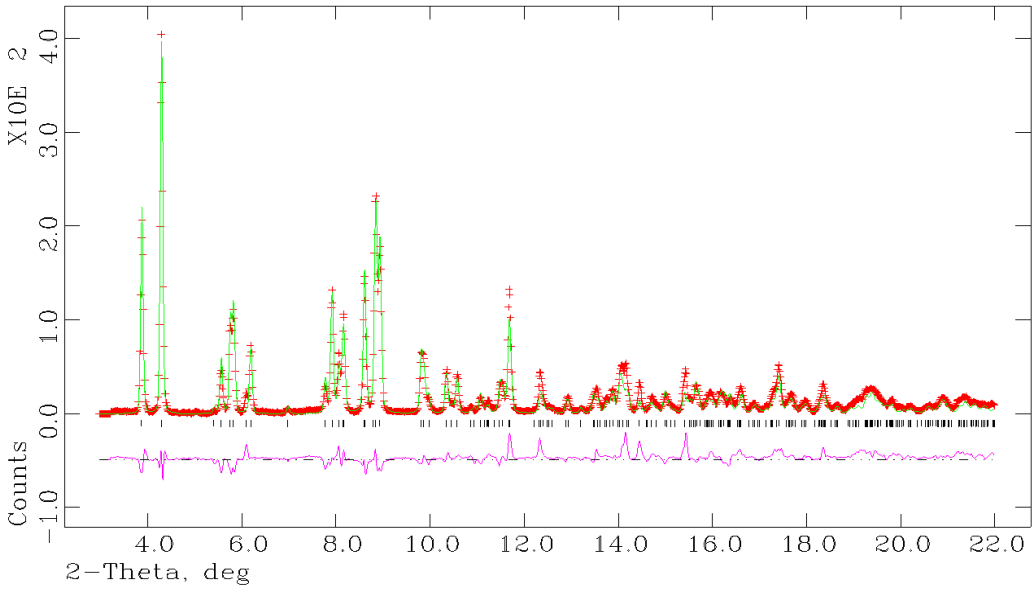

Figure 25: Refinement profile for orthorhombic Na-GaSi-NAT at 0.714 GPa. Vertical tick marks indicate allowed reflections for each phase: Na-GaSi-NAT (black).

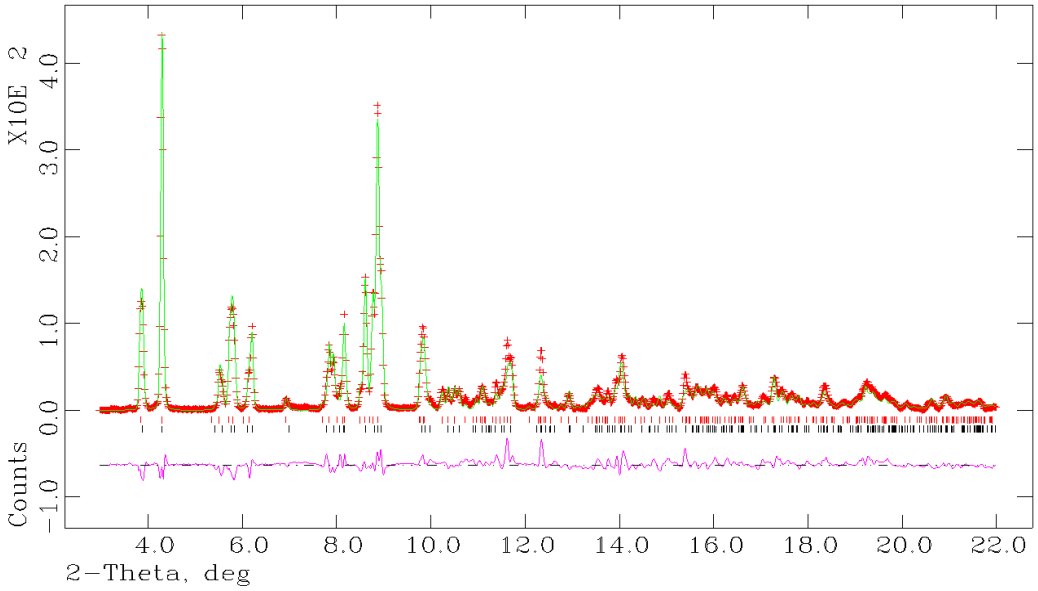

Figure 26: Refinement profile for orthorhombic Na-GaSi-NAT at 0.906 GPa. Vertical tick marks indicate allowed reflections for each phase: Na-GaSi-NAT phase 1 (black); Na-GaSi-NAT phase 2 (red).

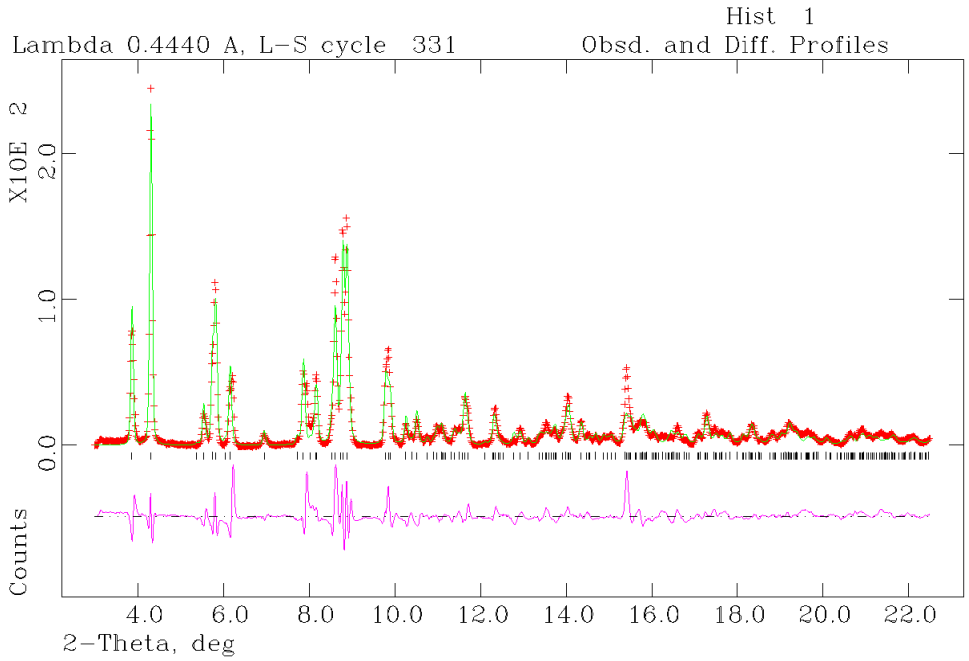

Figure 27: Refinement profile for orthorhombic Na-GaSi-NAT at 0.909 GPa.* Vertical tick marks indicate allowed reflections for each phase: Na-GaSi-NAT (black).

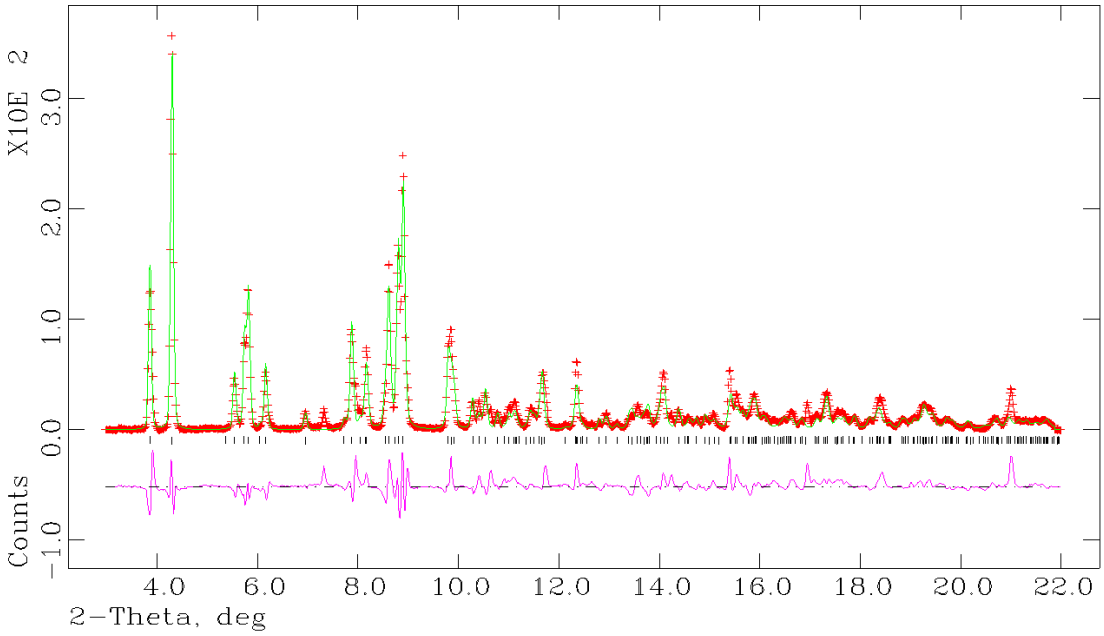

Figure 28: Refinement profile for orthorhombic Na-GaSi-NAT at 1.154 GPa. Vertical tick marks indicate allowed reflections for each phase: Na-GaSi-NAT (black).

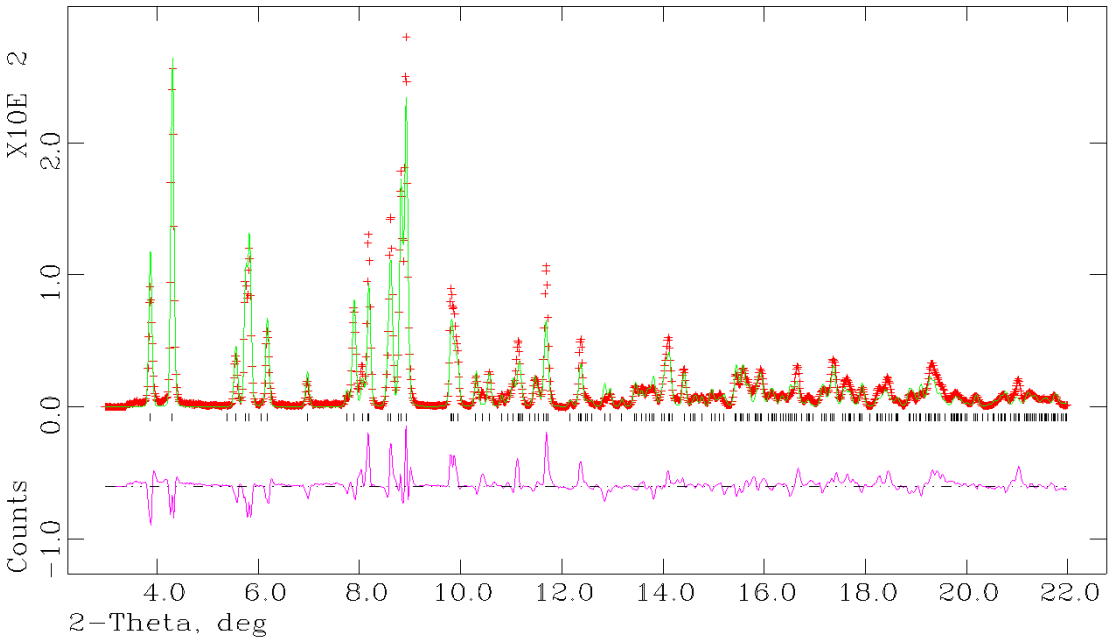

Figure 29: Refinement profile for orthorhombic Na-GaSi-NAT at 1.623 GPa. Vertical tick marks indicate allowed reflections for each phase: Na-GaSi-NAT (black).

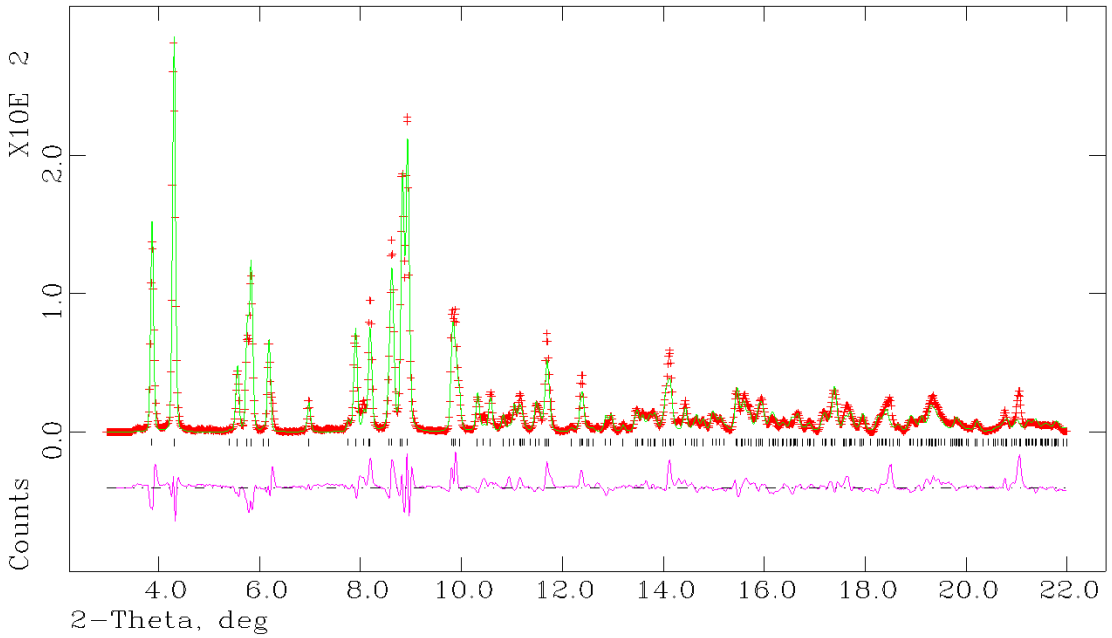

Figure 30: Refinement profile for orthorhombic Na-GaSi-NAT at 1.816 GPa. Vertical tick marks indicate allowed reflections for each phase: Na-GaSi-NAT (black).

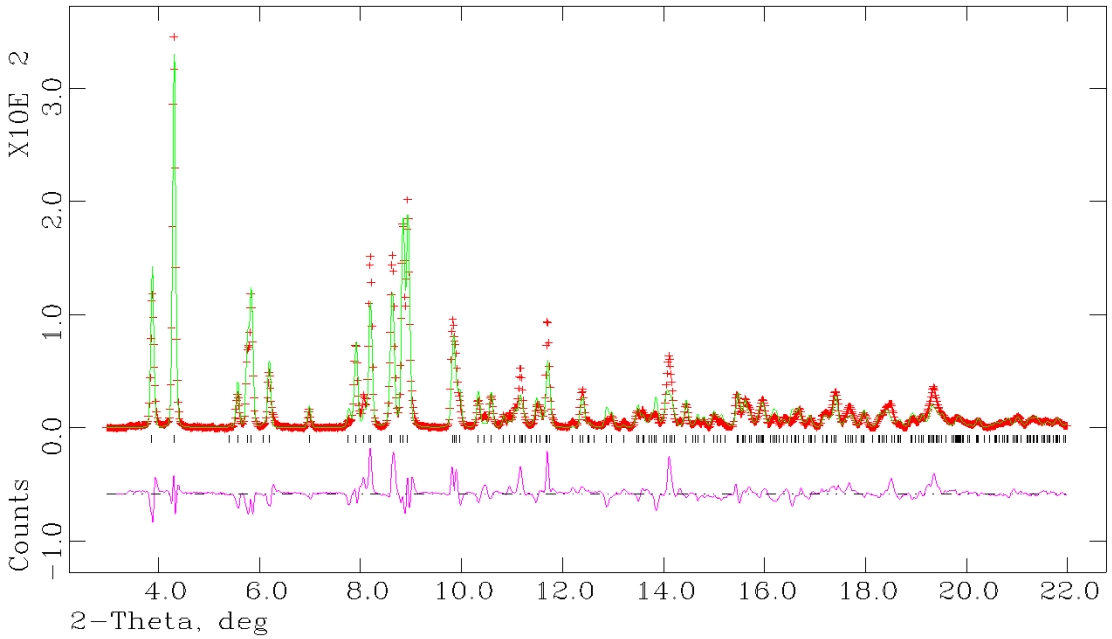

Figure 31: Refinement profile for orthorhombic Na-GaSi-NAT at 1.981 GPa. Vertical tick marks indicate allowed reflections for each phase: Na-GaSi-NAT (black).

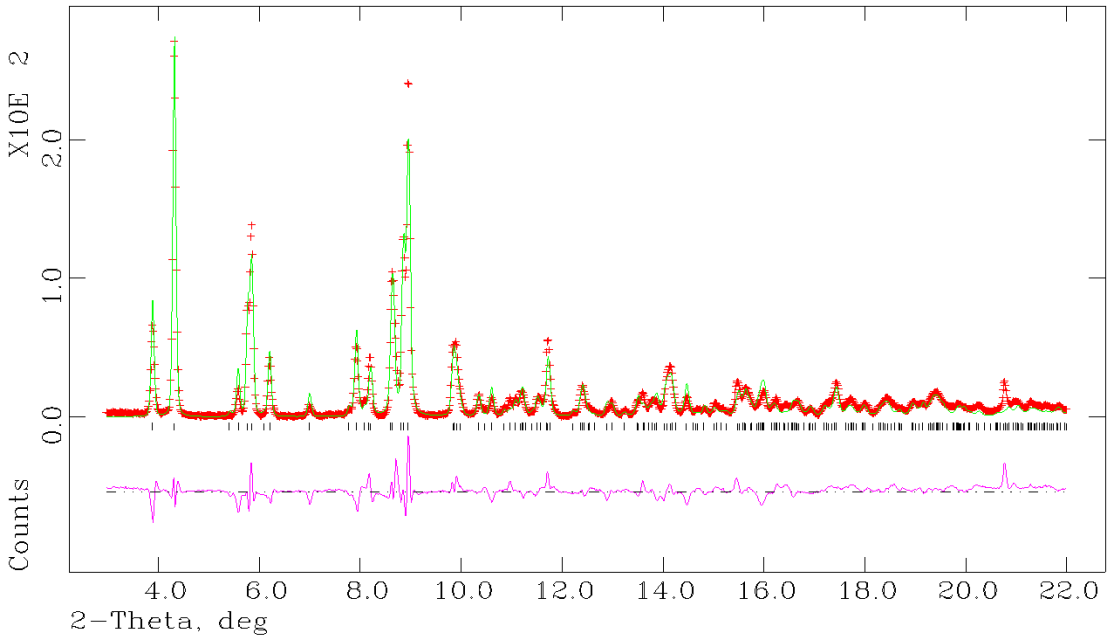

Figure 32: Refinement profile for orthorhombic Na-GaSi-NAT at 2.365 GPa.* Vertical tick marks indicate allowed reflections for each phase: Na-GaSi-NAT (black).

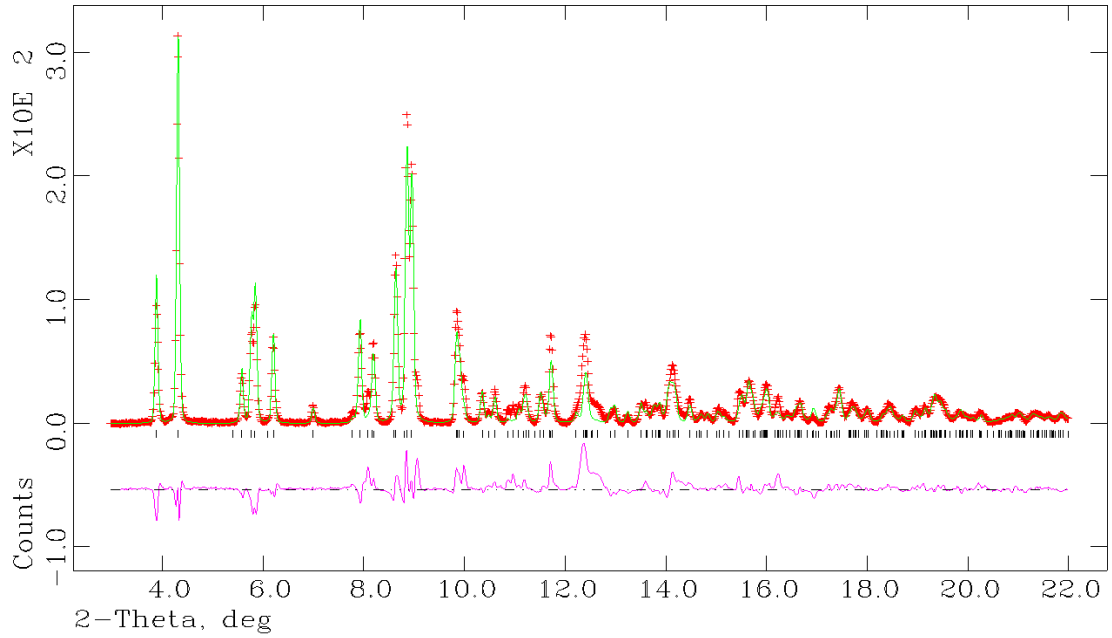

Figure 33: Refinement profile for orthorhombic Na-GaSi-NAT at 2.365 GPa. Vertical tick marks indicate allowed reflections for each phase: Na-GaSi-NAT (black).

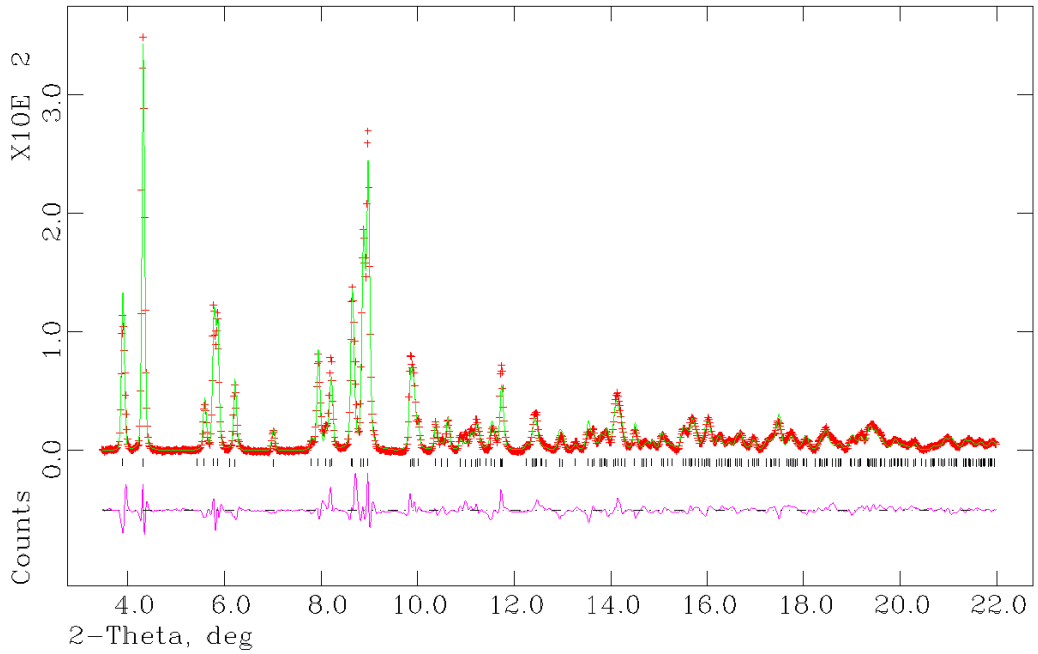

Figure 34: Refinement profile for orthorhombic Na-GaSi-NAT at 2.731 GPa. Vertical tick marks indicate allowed reflections for each phase: Na-GaSi-NAT (black).

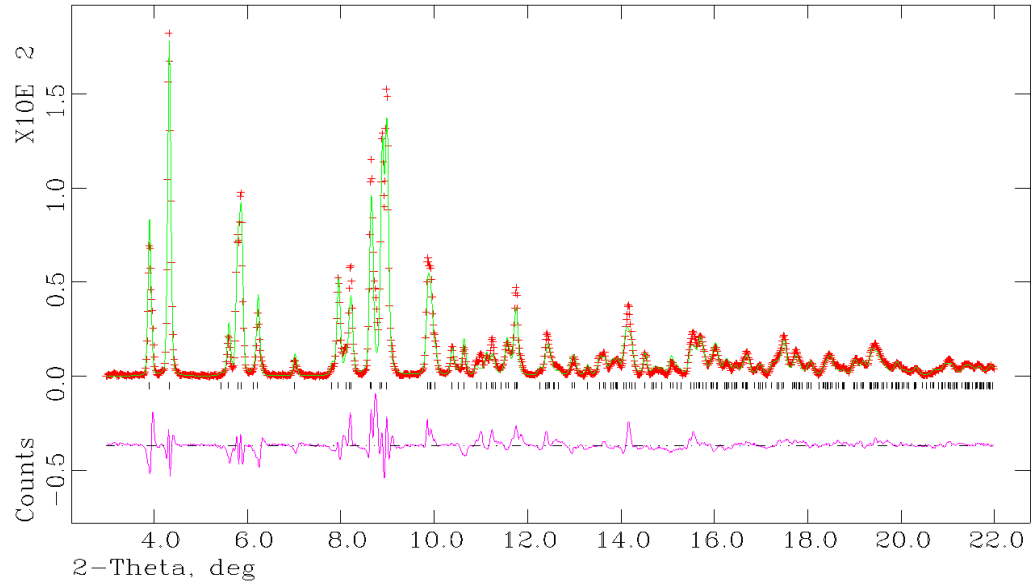

Figure 35: Refinement profile for orthorhombic Na-GaSi-NAT at 2.729 GPa.* Vertical tick marks indicate allowed reflections for each phase: Na-GaSi-NAT (black).

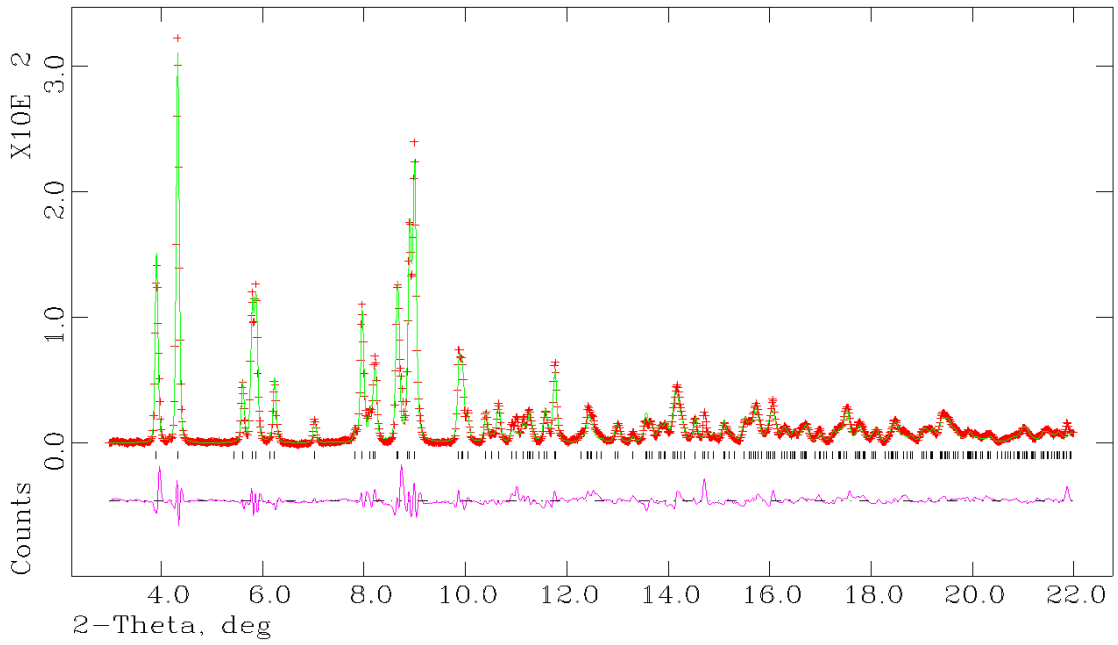

Figure 36: Refinement profile for orthorhombic Na-GaSi-NAT at 2.895 GPa. Vertical tick marks indicate allowed reflections for each phase: Na-GaSi-NAT (black).

1.2.2.2 Tetragonal Na-GaSi-NAT

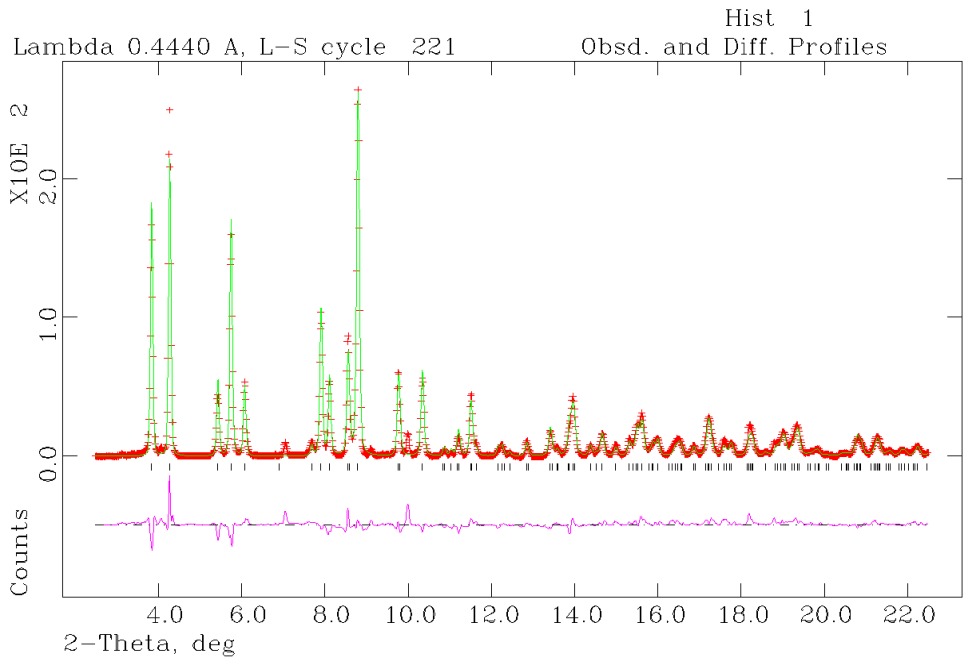

Figure 37: Refinement profile for tetragonal Na-GaSi-NAT at ambient pressure performed using mounting tape. † Vertical tick marks indicate allowed reflections for each phase: Na-GaSi-NAT (black).

†Data series collected using mounting tape, rather than a diamond anvil cell.

*Data series collected during a pressure release step.

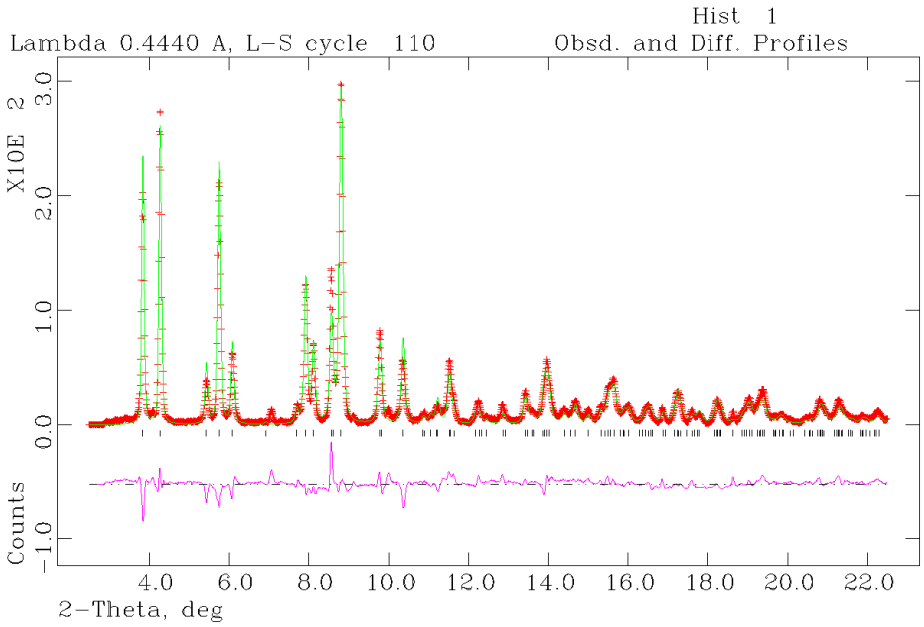

Figure 38: Refinement profile for tetragonal Na-GaSi-NAT at ambient pressure.* Vertical tick marks indicate allowed reflections for each phase: Na-GaSi-NAT (black).

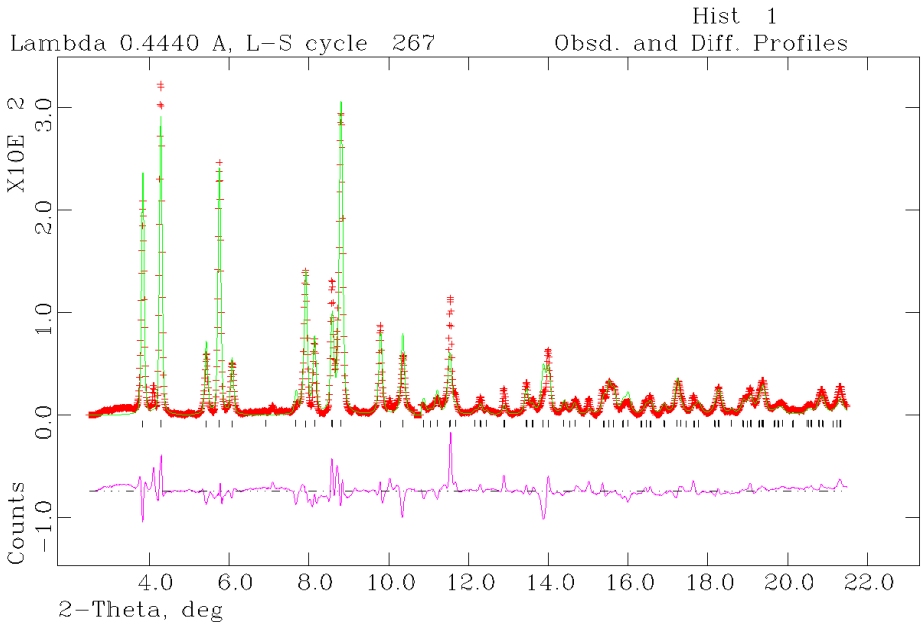

Figure 39: Refinement profile for tetragonal Na-GaSi-NAT at 3.567 GPa. Vertical tick marks indicate allowed reflections for each phase: Na-GaSi-NAT (black).

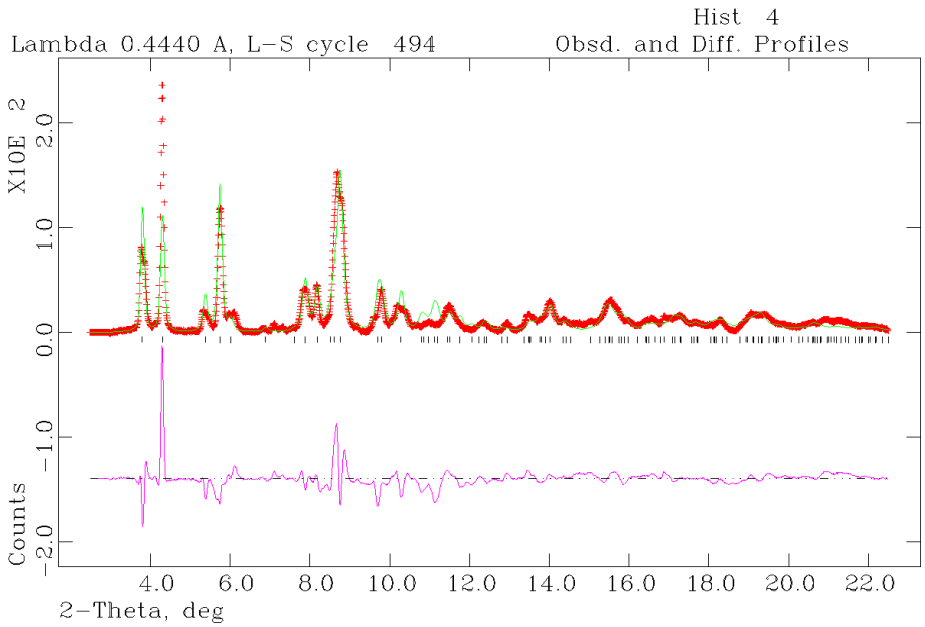

Figure 40: Refinement profile for tetragonal Na-GaSi-NAT at 0.727 GPa.* Vertical tick marks indicate allowed reflections for each phase: Na-GaSi-NAT (black).

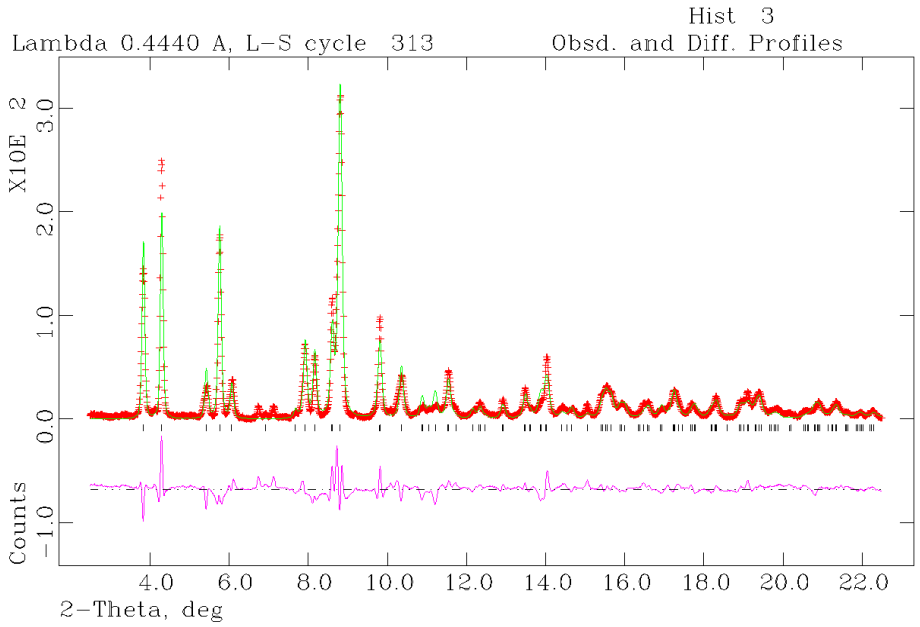

Figure 41: Refinement profile for tetragonal Na-GaSi-NAT at 1.0717 GPa. Vertical tick marks indicate allowed reflections for each phase: Na-GaSi-NAT (black).

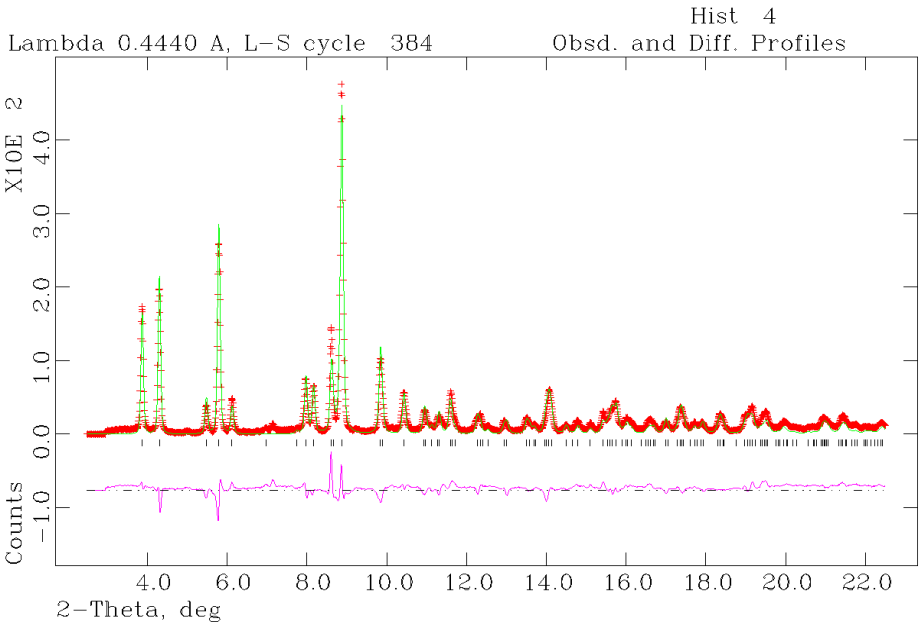

Figure 42: Refinement profile for tetragonal Na-GaSi-NAT at 1.636 GPa. Vertical tick marks indicate allowed reflections for each phase: Na-GaSi-NAT (black).

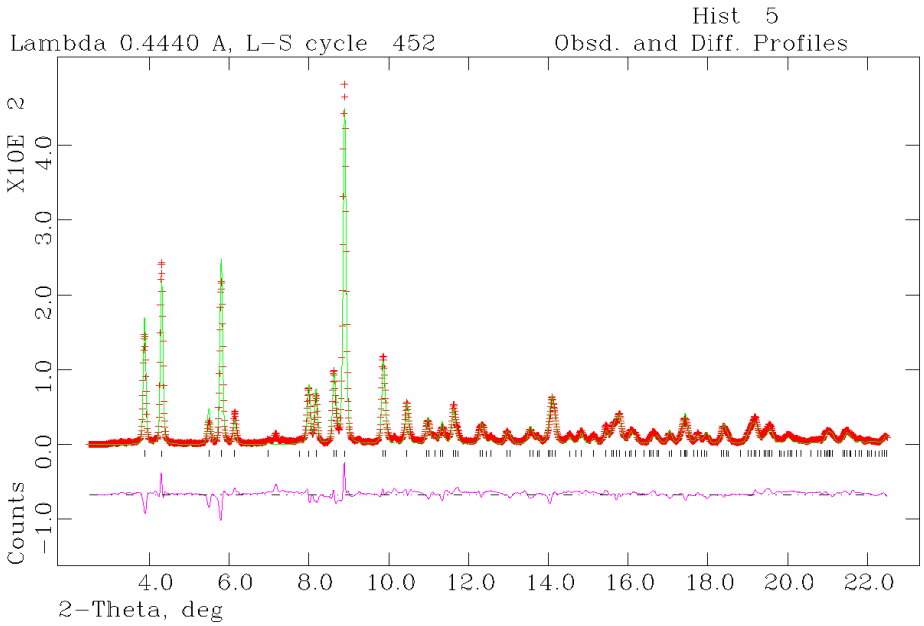

Figure 43: Refinement profile for tetragonal Na-GaSi-NAT at 1.98 GPa. Vertical tick marks indicate allowed reflections for each phase: Na-GaSi-NAT (black).

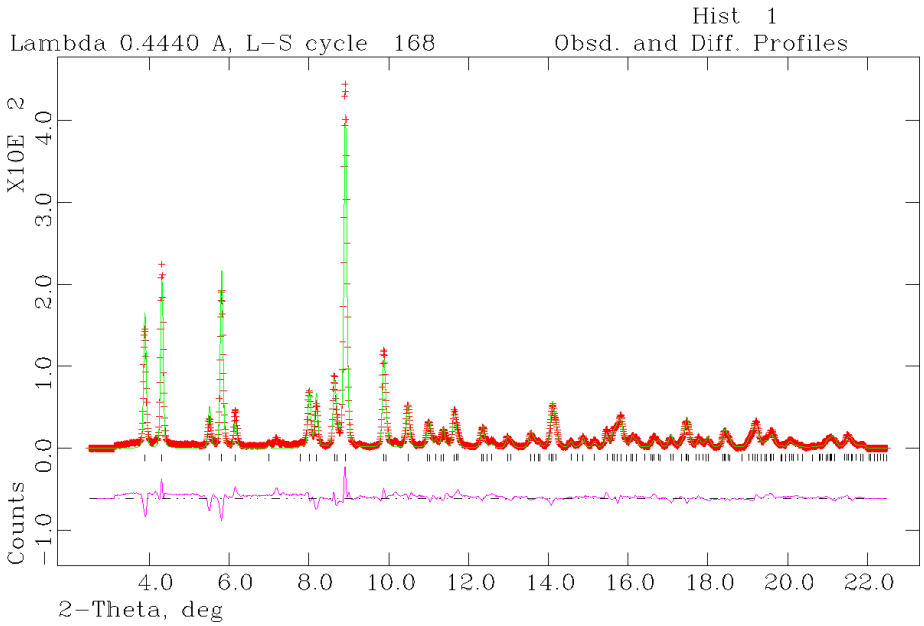

Figure 44: Refinement profile for tetragonal Na-GaSi-NAT at 2.36 GPa. Vertical tick marks indicate allowed reflections for each phase: Na-GaSi-NAT (black).

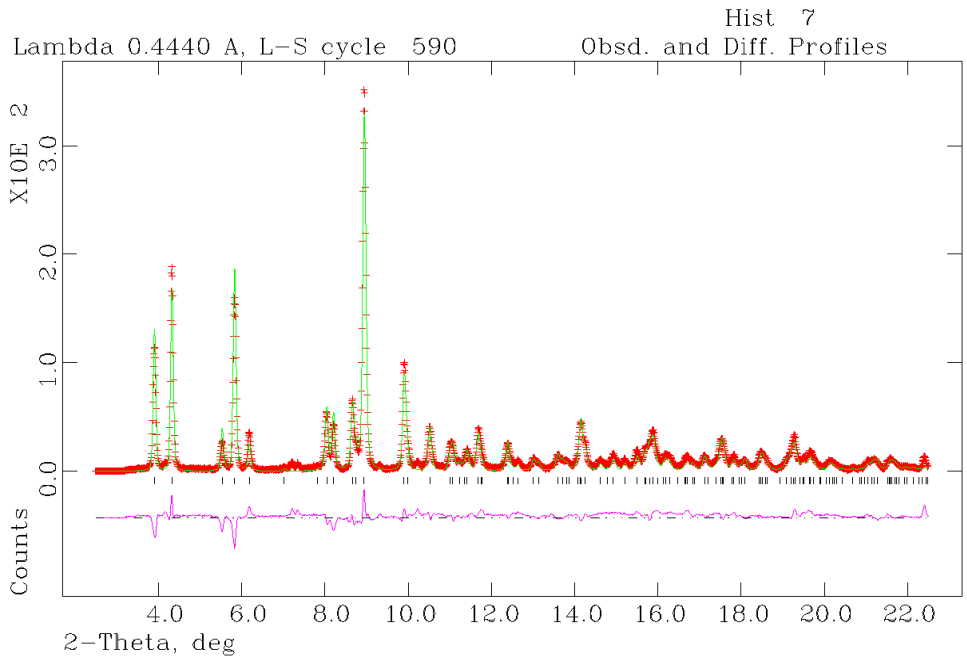

Figure 45: Refinement profile for tetragonal Na-GaSi-NAT at 2.636 GPa. Vertical tick marks indicate allowed reflections for each phase: Na-GaSi-NAT (black).

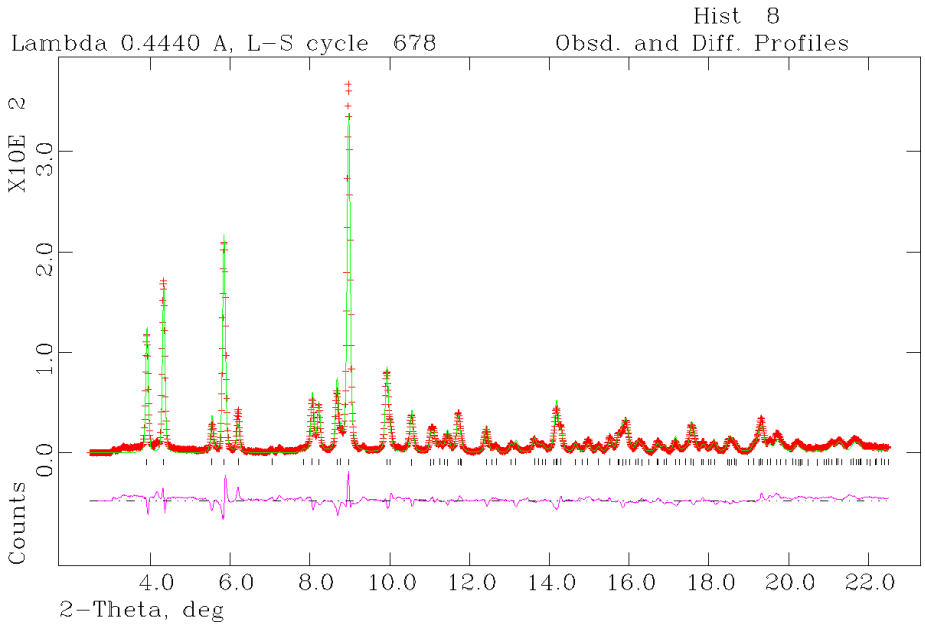

Figure 46: Refinement profile for tetragonal Na-GaSi-NAT at 3.255 GPa. Vertical tick marks indicate allowed reflections for each phase: Na-GaSi-NAT (black).

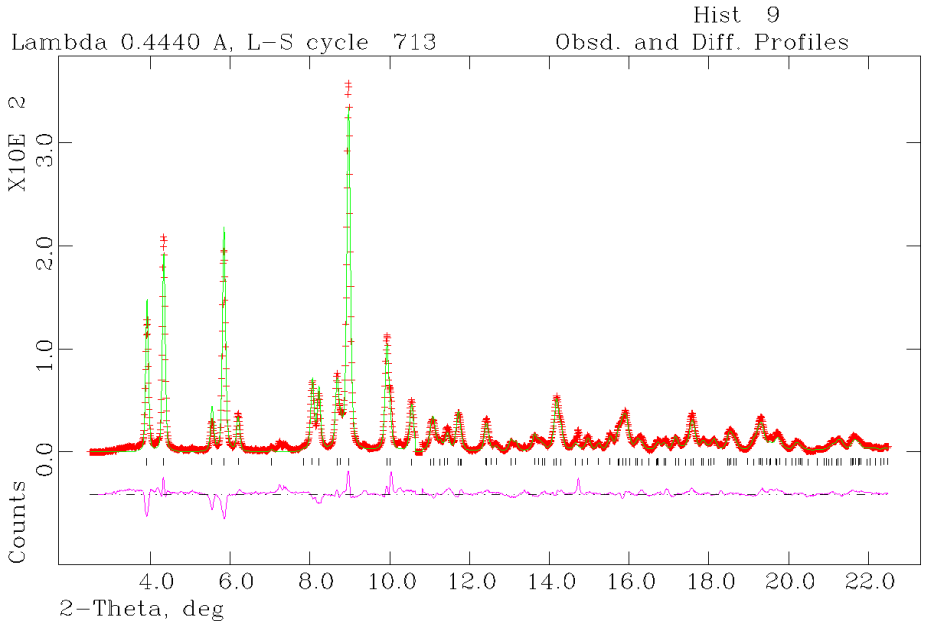

Figure 47: Refinement profile for tetragonal Na-GaSi-NAT at 3.449 GPa.* Vertical tick marks indicate allowed reflections for each phase: Na-GaSi-NAT (black).

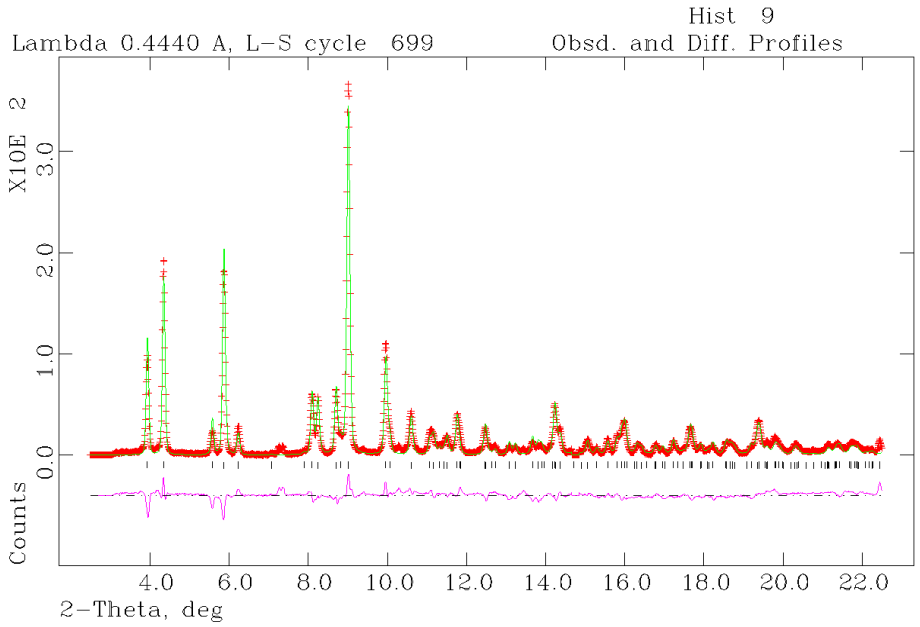

Figure 48: Refinement profile for tetragonal Na-GaSi-NAT at 3.826 GPa. Vertical tick marks indicate allowed reflections for each phase: Na-GaSi-NAT (black).

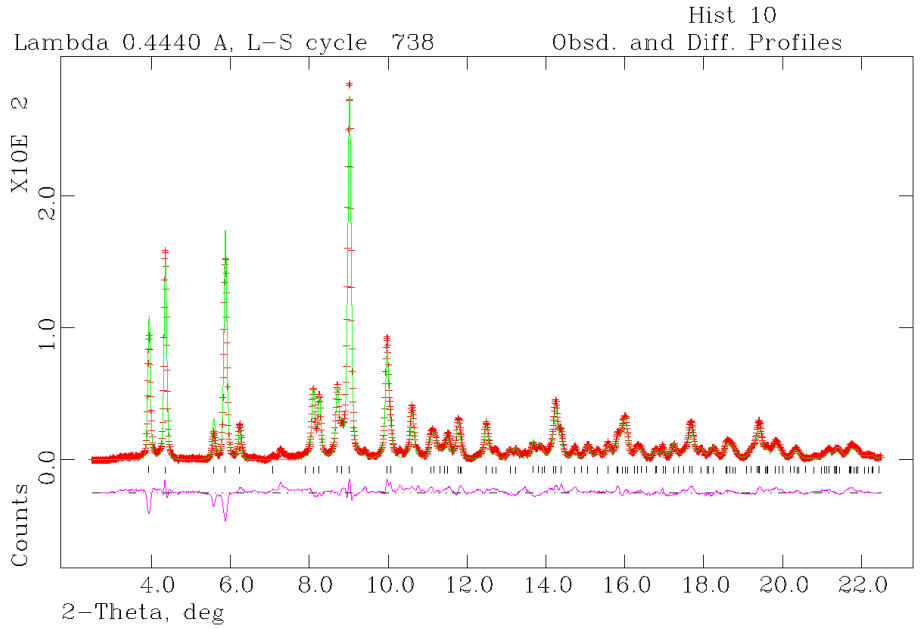

Figure 49: Refinement profile for tetragonal Na-GaSi-NAT at 4.199 GPa.* Vertical tick marks indicate allowed reflections for each phase: Na-GaSi-NAT (black).

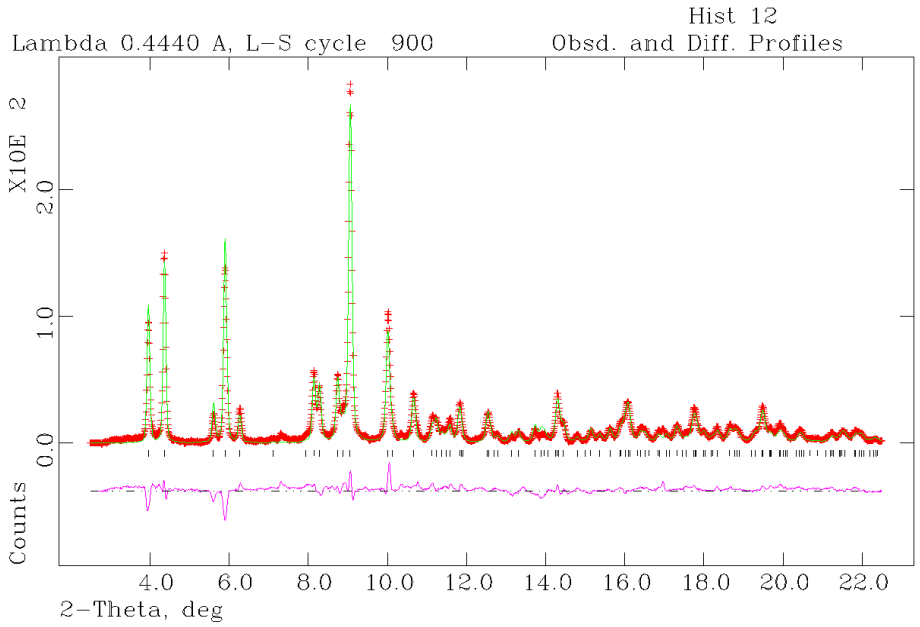

Figure 50: Refinement profile for tetragonal Na-GaSi-NAT at 4.979 GPa.* Vertical tick marks indicate allowed reflections for each phase: Na-GaSi-NAT (black).

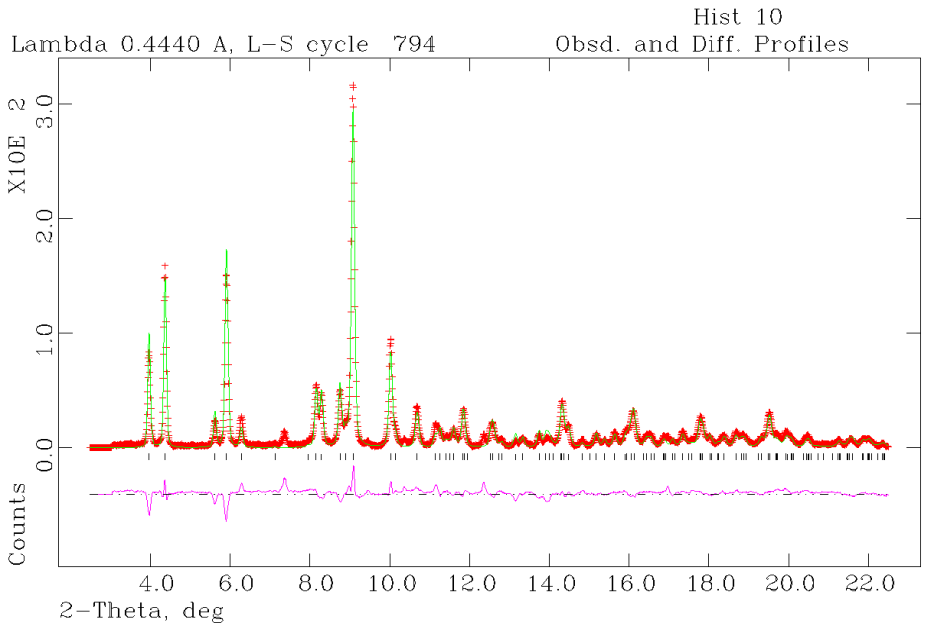

Figure 51: Refinement profile for tetragonal Na-GaSi-NAT at 5.108 GPa. Vertical tick marks indicate allowed reflections for each phase: Na-GaSi-NAT (black).

1.3 Atoms Drawings from Refined, High Pressure, Synchrotron X-Ray Diffraction Data

1.3.1 Orthorhombic Na-GaSi-NAT

Ga/Al/Si tetrahedra (grey), Sodium cations (yellow), Oxygen of water molecules (red).

†Data series collected using mounting tape, rather than a diamond anvil cell.

*Data series collected during a pressure release step.

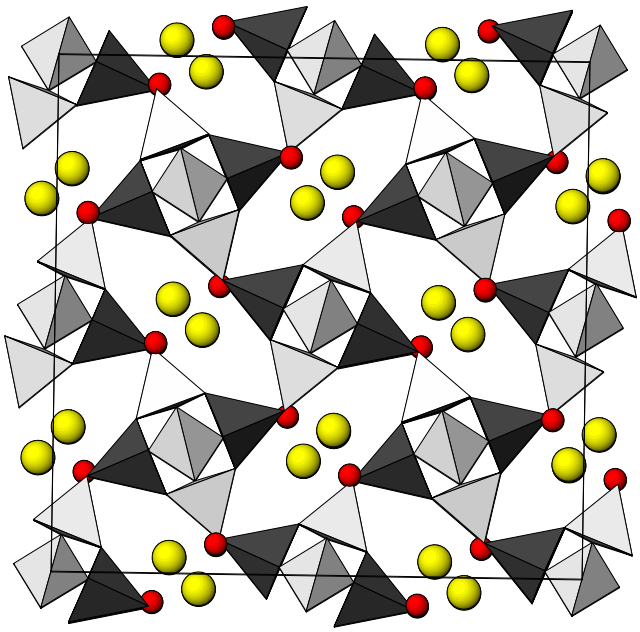

0 GPa†

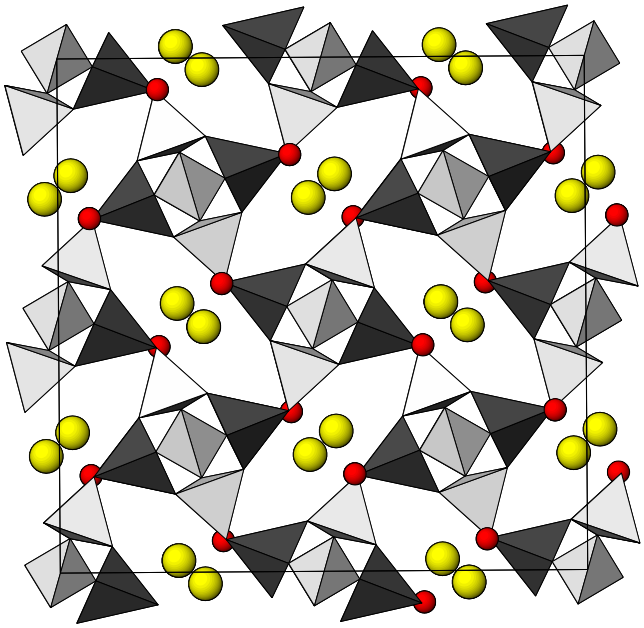

0 GPa*

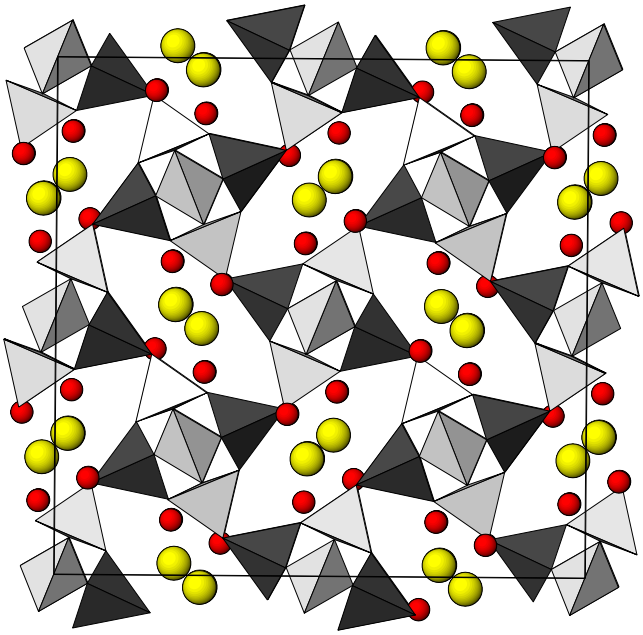

0.350 GPa

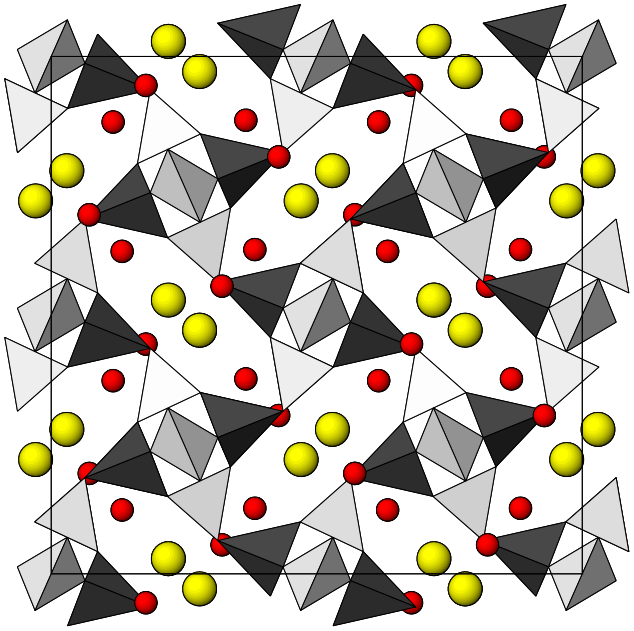

0.631 GPa

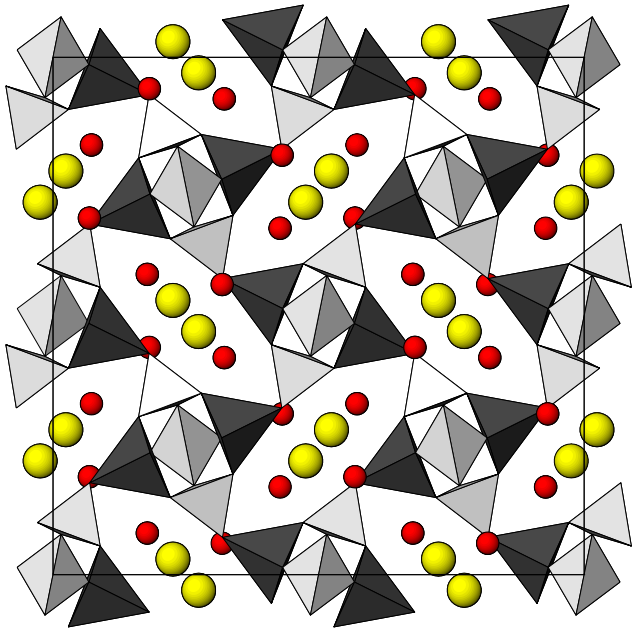

0.714 GPa

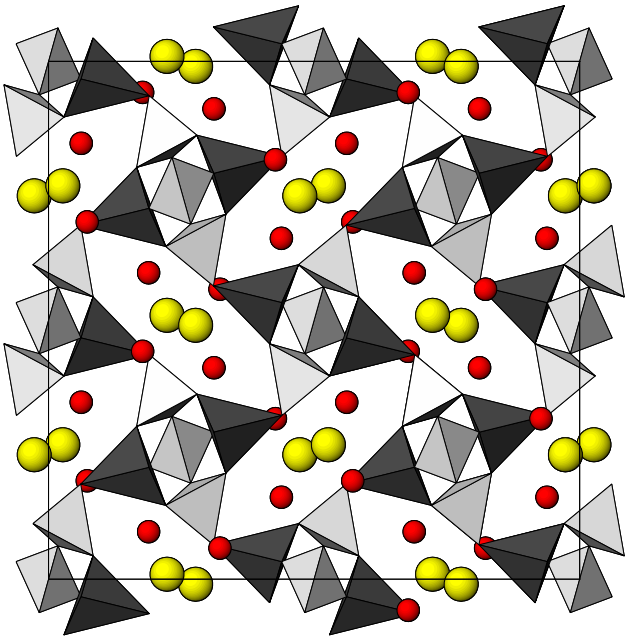

0.906 GPa (phase 1)

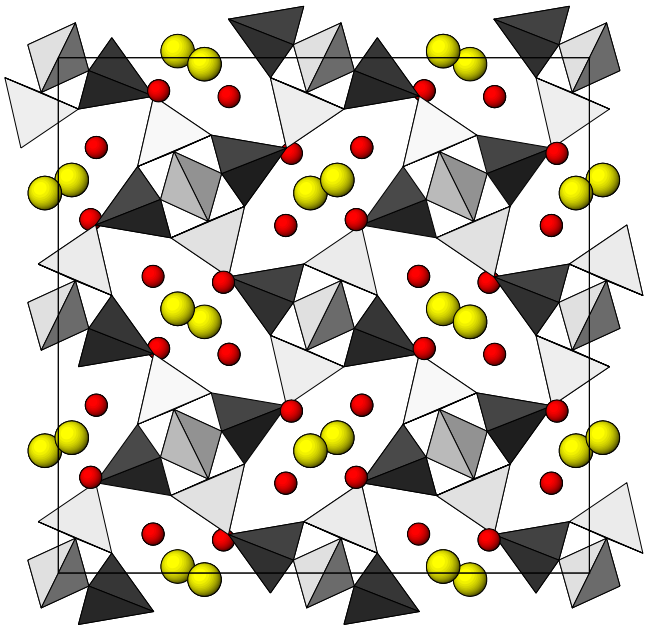

0.906 GPa (Phase 2)

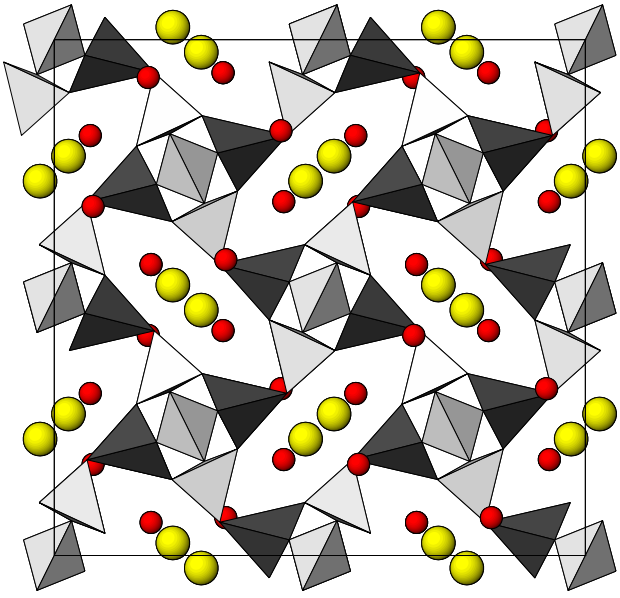

0.909 GPa*

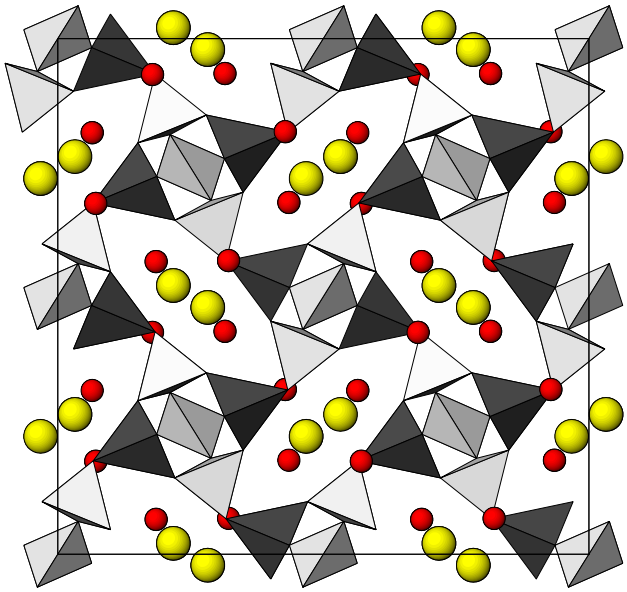

1.154 GPa

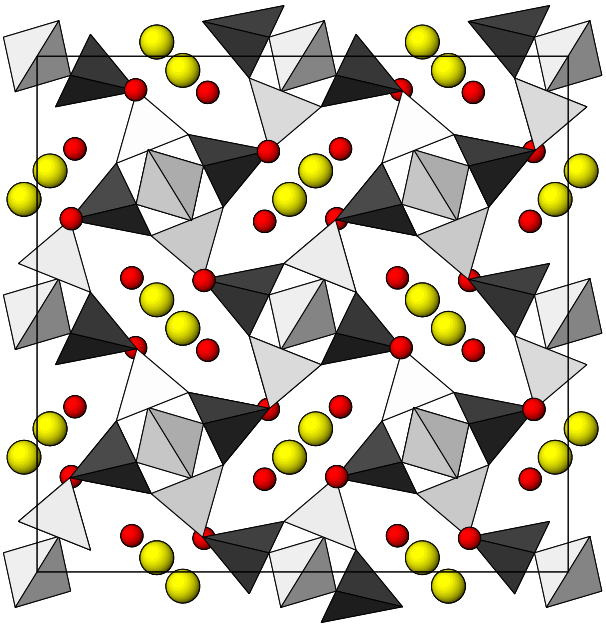

1.623 GPa

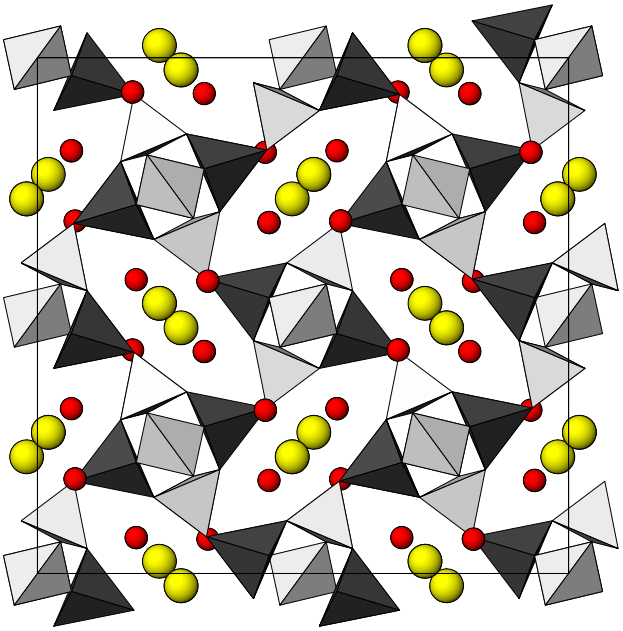

1.816 GPa

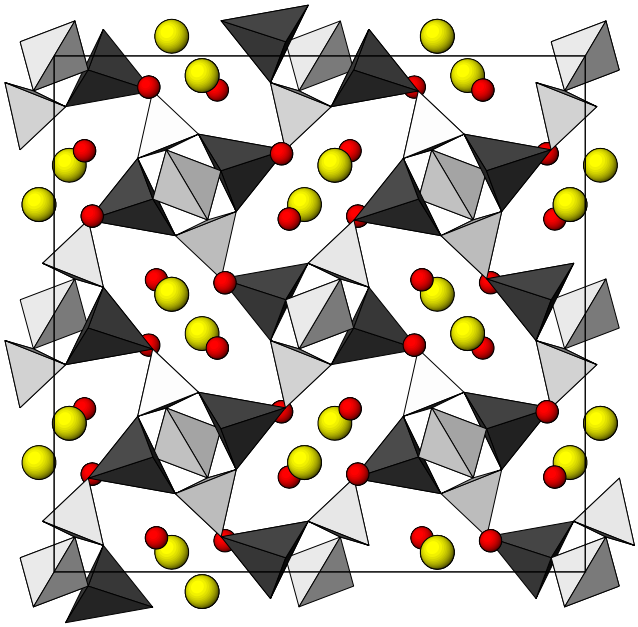

1.981 GPa

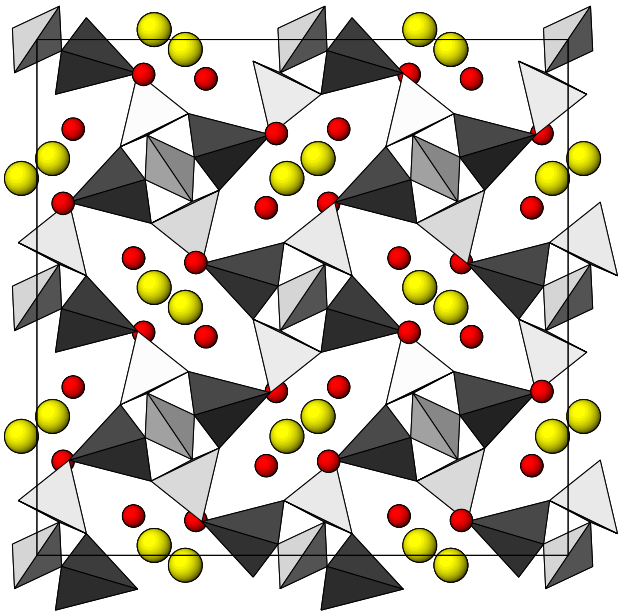

2.365 GPa*

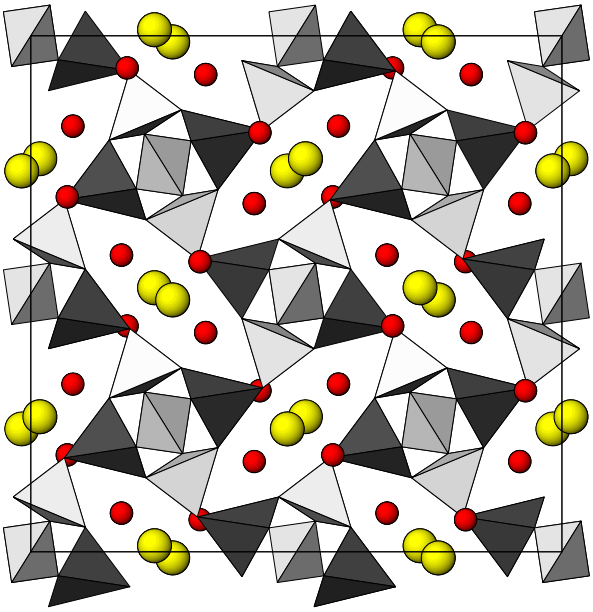

2.365 GPa

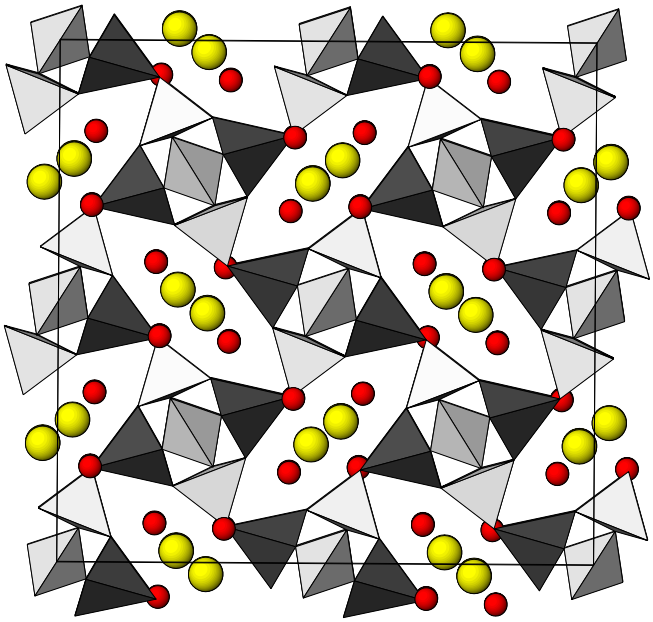

2.731 GPa

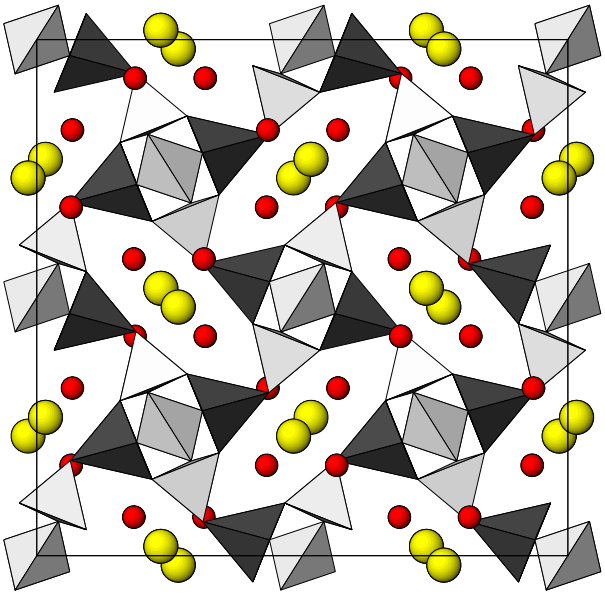

2.729 GPa*

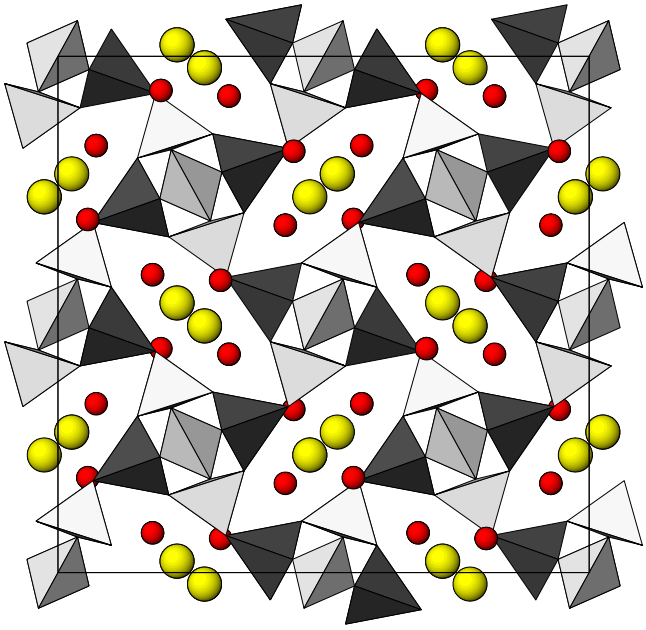

2.895 GPa

1.3.2 Tetragonal Na-GaSi-NAT

†Data series collected using mounting tape, rather than a diamond anvil cell.

*Data series collected during a pressure release step.

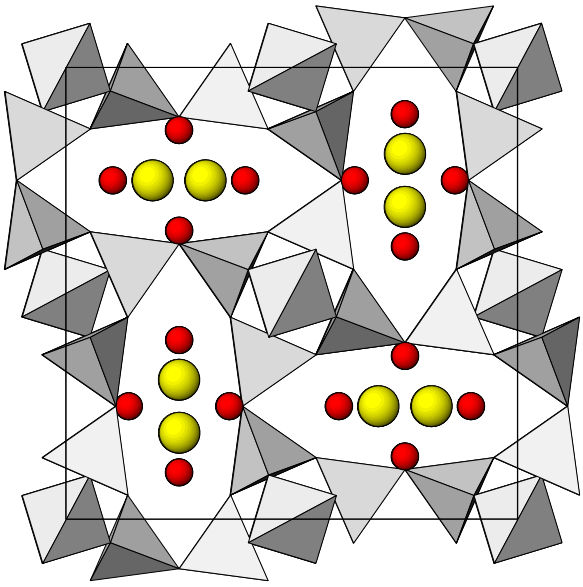

0 GPa†

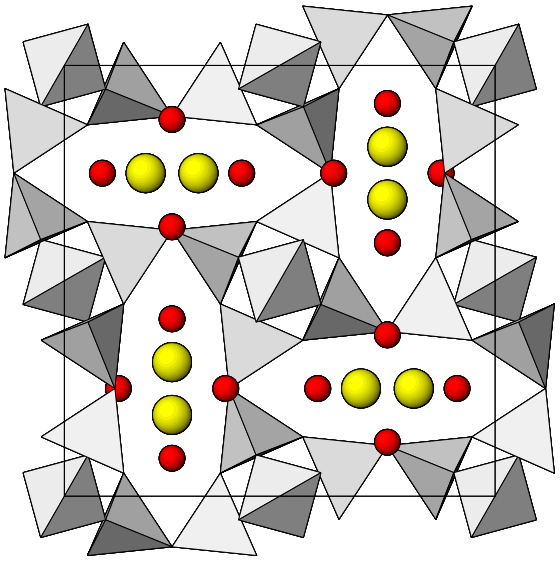

0 GPa*

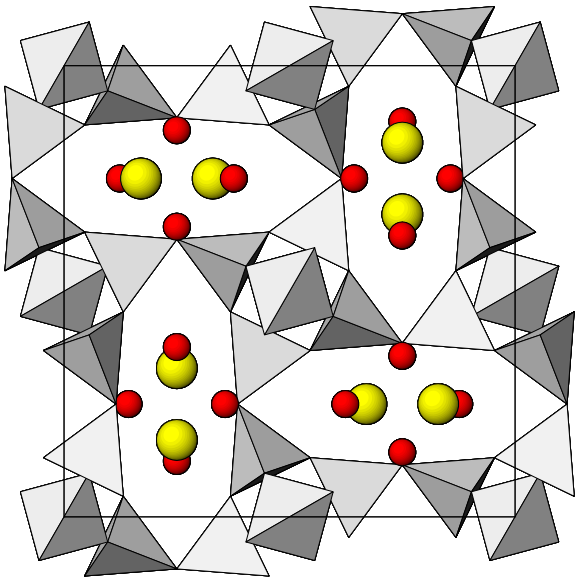

0.3567 GPa

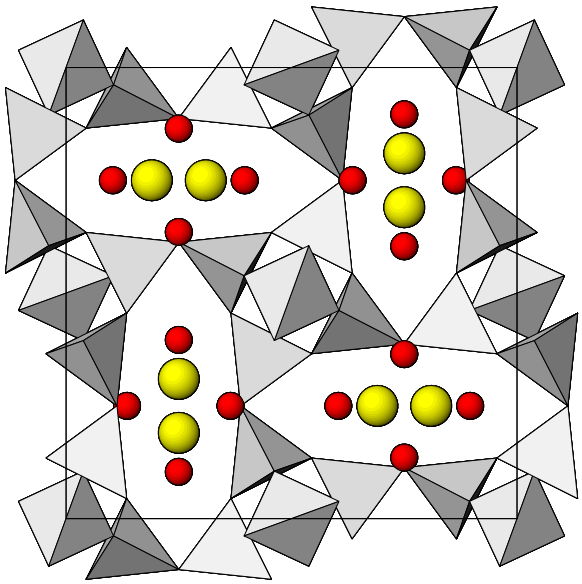

0.7270 GPa*

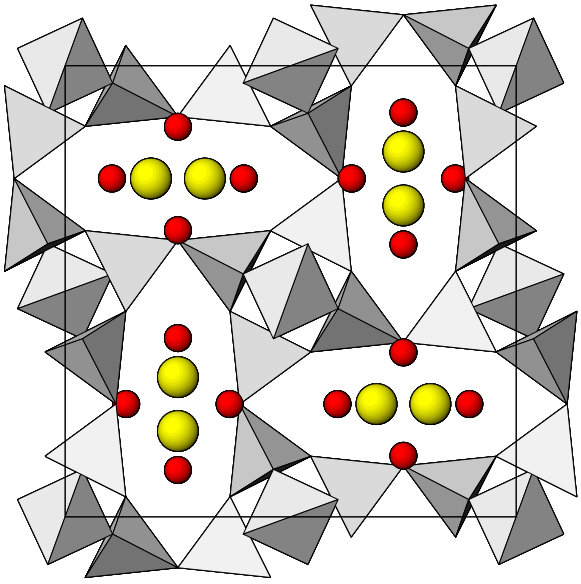

1.0717 GPa

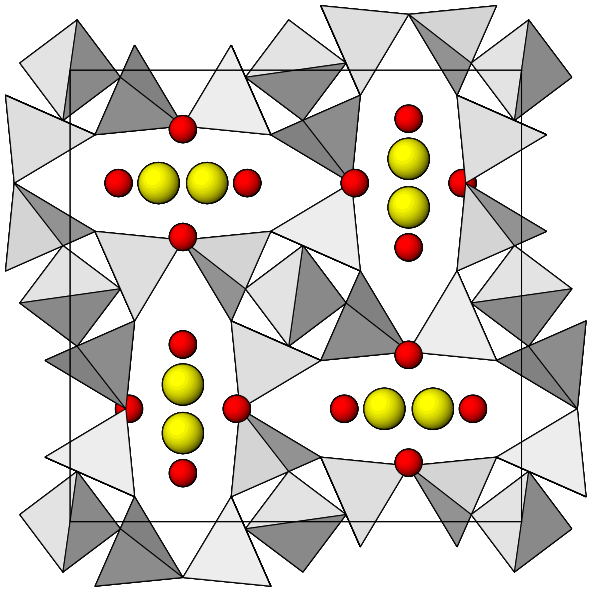

1.6360 GPa

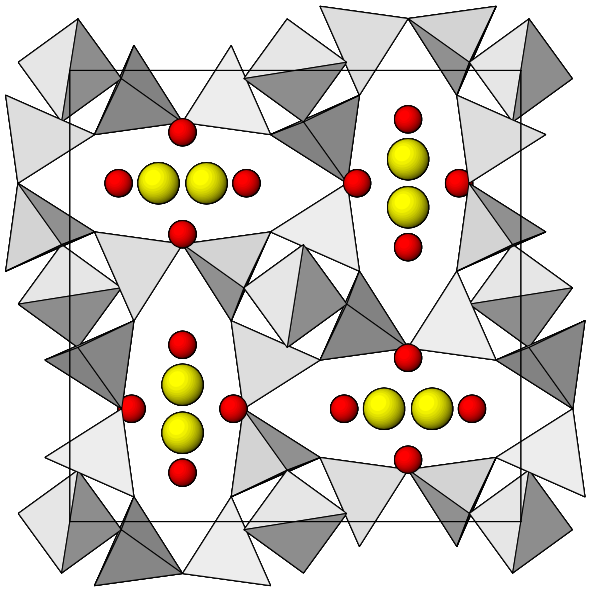

1.98 GPa

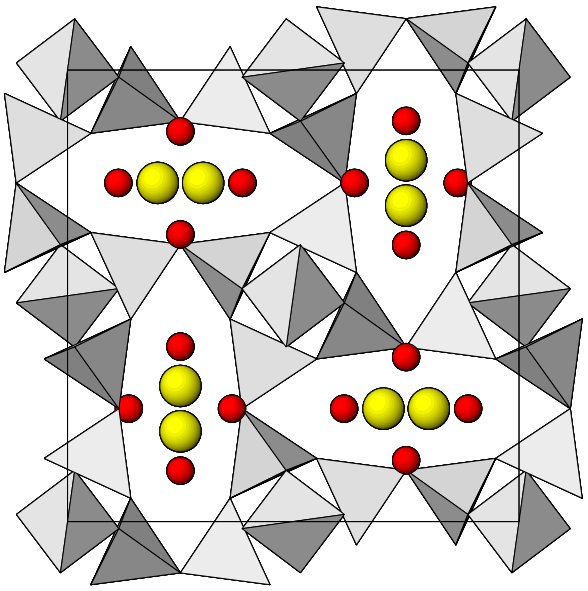

2.36 GPa

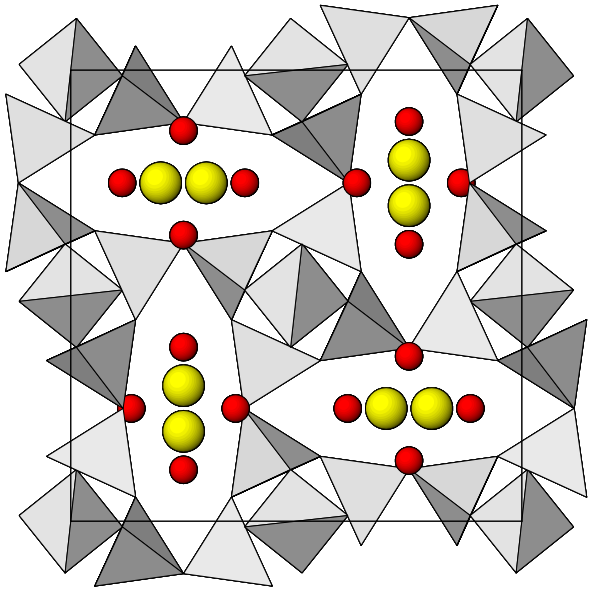

2.631 GPa

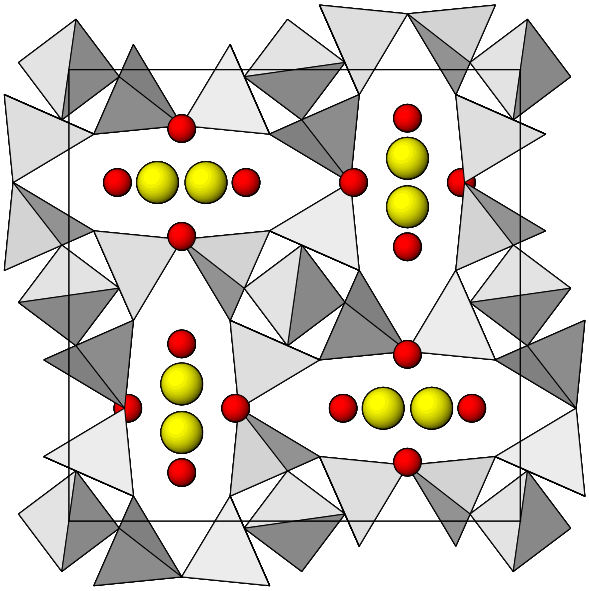

3.2549 GPa

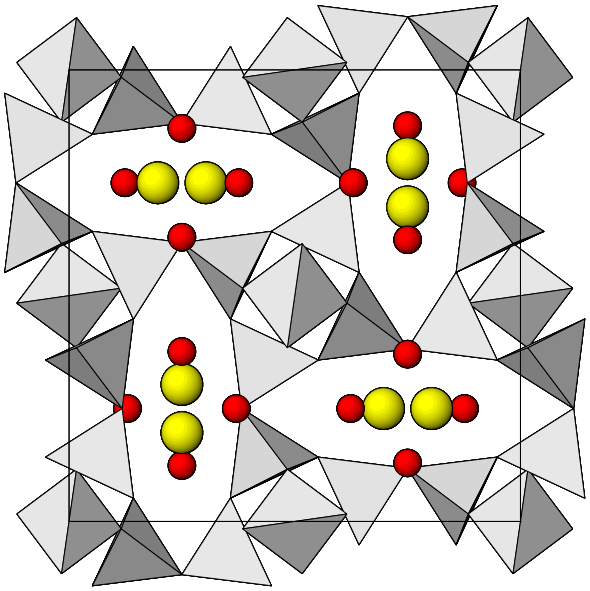

3.449 GPa*

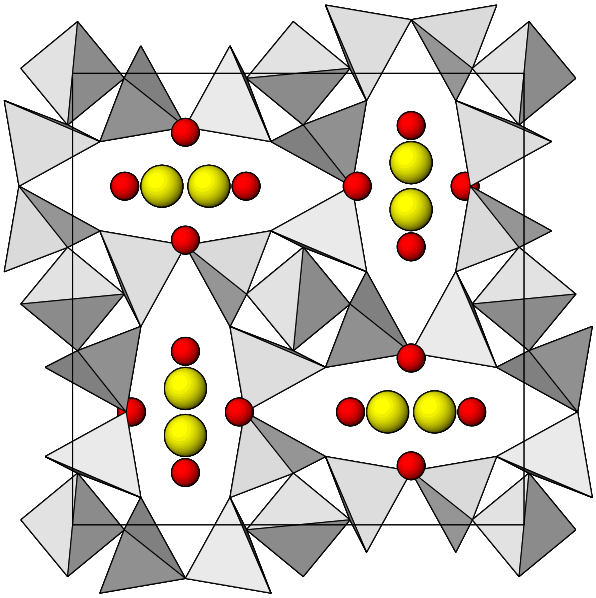

3.8260 GPa

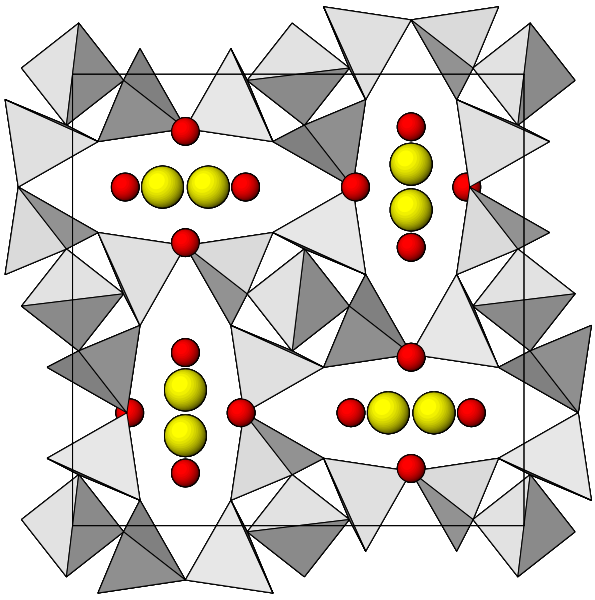

4.1996 GPa*

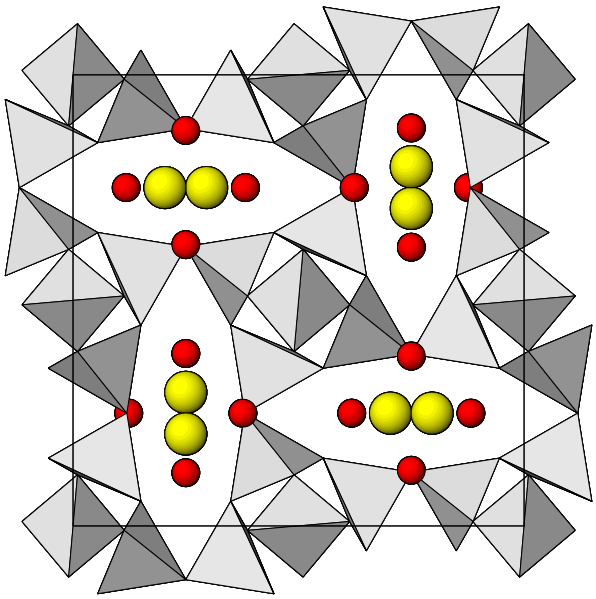

4.9790 GPa*

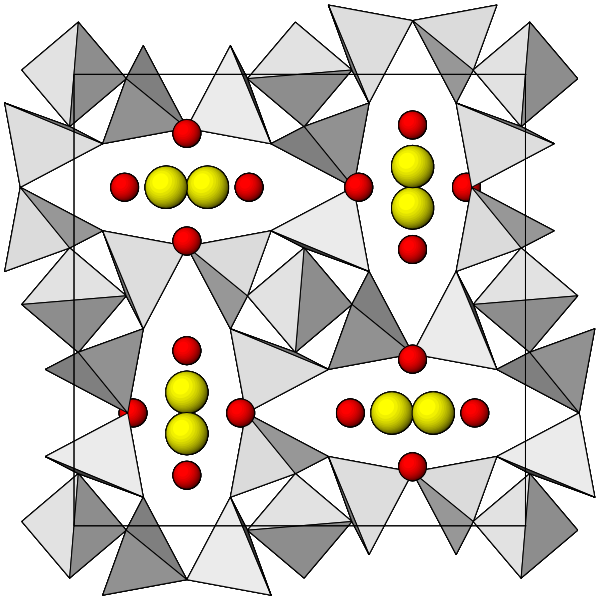

5.1080 GPa